



Norwegian University
of Life Sciences

Master's Thesis 2023 30 ECTS
Faculty of Science and Technology

Exploring evapotranspiration as part of H2O-project: Model calibration and data evaluation

Martin Jonatan Økland
Environmental Physics and Renewable Energy

Abstract

The atmosphere's mass is about 5.1480×10^{18} kg where water vapor amounts to about 0.25 %. This tiny fraction of water vapor is a key greenhouse gas, and is essential in the hydrological, meteorological and biological processes. An important component in the land-atmosphere domain is evapotranspiration (evaporation and transpiration together). For about 75 years, studies have been conducted to give good predictive evapotranspiration models. However, results show that different models yield different accuracy in their spatiotemporal application.

As part of the Norwegian Meteorological Institute's project; Hydrometeorology to Operations (H2O), this thesis will study evapotranspiration to evaluate evapotranspirational models, Priestley-Taylor and Penman-Monteith, and evaluate evapotranspirational data from remote sensing and pan evaporation.

Five versions of the Priestley-Taylor (PT) model were evaluated, of which four were hourly-based. One of the models used the standard α of 1.29. One model was based on the approach from Cristea et al. (2013) to calculate α . The two other hourly-based models required programming with curve-fitting, where one used curve-fitting to calculate α and γ , while the other one used curve-fitting for α only. The fifth PT model was daily-based with an α value calculated by curve-fitting. The best PT model had α values between 0.2755 and 0.3789 with an RMSE compared to measurements of 0.0043.

Four versions of the Penman-Monteith (PM) model were evaluated, of which two were daily-based and two were hourly-based. The first daily-based PM model calculated actual evapotranspiration directly and resulted in significant underestimations. The other PM models calculated reference evapotranspiration before being multiplied by a crop coefficient. The second daily-based and the first hourly-based PM models used a crop coefficient of 0.9, while the second hourly-based PM model used curve-fitting to calculate a suitable crop coefficient of 0.588. The best PM model was the hourly-based with the calibrated crop coefficient, resulting in an RMSE value of 0.0039.

Remote sensing measurements were evaluated by comparing them to eddy-covariance measurements. The remote sensing measurements were about 30-40 % greater than the eddy-covariance measurements. It was however not found out if this is a systematic error or just a coincidence.

Pan evaporation measurements were evaluated by converting them into estimates of actual evapotranspiration and comparing them to eddy-covariance measurements. Crop coefficients of 0.9 and 0.588 were used in this conversion. It was found that on an hourly basis, the conversion using a crop coefficient of 0.588 yielded the most accurate result compared to eddy-covariance measurements.

This thesis has proven that an hourly-based PM model with crop coefficient of 0.588 is more accurate than a PT model with α of between 0.2755 and 0.3789. It has also been proven that the literature-based PM model is more accurate than the literature-based PT model. The overall conclusion of all evaluations is that more extended time series' are needed to reach a conclusive answer. However, the results seem promising as proof of concept that calibrating evapotranspirational models could yield valuable predictions, and that data from remote sensing and pan evaporation could be reliable.

Sammendrag

Massen til atmosfæren er omtrent $5,1480 \times 10^{18}$ kg hvorav vanndamp utgjør rundt 0,25 %. Denne lille andelen vanndamp er en viktig drivhusgass, og er avgjørende for hydrologiske, meteorologiske og biologiske prosesser. En viktig komponent i land-atmosfære koblingen er fordampning og transpirasjon (evapotranspirasjon). I omtrent 75 år har det blitt utført forsøk på å finne gode prediktive modeller for evapotranspirasjon. Resultatene viser imidlertid at ulike modeller gir ulik nøyaktighet i deres geografiske og tidsmessige anvendelse.

Som del av Meteorologisk Institutt sitt prosjekt, "Hydrometeorology to Operations" (H2O), skal denne avhandlingen studere evapotranspirasjon for å evaluere evapotranspirasjonsmodeller, Priestley-Taylor og Penman-Monteith, samt vurdere evapotranspirasjonsdata fra fjernmåling og fordampningskar.

Fem versjoner av Priestley-Taylor (PT)-modellen ble evaluert, hvorav fire var timebaserte. En av modellene brukte standard α -verdi på 1,29. En modell var basert på tilnærmingen fra Cristea et al. (2013) for å beregne α . De to andre timebaserte modellene krevde programmering med kurvetilpasning, der den ene brukte kurvetilpasning for å beregne både α og γ , mens den andre kun brukte kurvetilpasning for α . Den femte PT-modellen var dagsbasert med en α -verdi beregnet ved kurvetilpasning. Den beste PT-modellen hadde α -verdier mellom 0,2755 og 0,3789 med en RMSE sammenlignet med målinger på 0,0043.

Fire versjoner av Penman-Monteith (PM)-modellen ble evaluert, hvorav to var dagsbaserte og to var timebaserte. Den første dagsbaserte PM-modellen beregnet faktisk fordampning direkte og resulterte i betydelig underestimert. De andre PM-modellene beregnet referansefordampning før de ble multiplisert med en avlingskoeffisient. Den andre dagsbaserte og den første timebaserte PM-modellen brukte en avlingskoeffisient på 0,9, mens den andre timebaserte PM-modellen brukte kurvetilpasning for å beregne en egnet avlingskoeffisient på 0,588. Den beste PM-modellen var den timebaserte med kalibrert avlingskoeffisient, noe som resulterte i en RMSE-verdi på 0,0039.

Fjernmålinger ble evaluert ved å sammenligne dem med eddy-kovariansmålinger. Fjernmålingene var omtrent 30-40 % høyere enn eddy-kovariansmålingene. Det ble imidlertid ikke fastslått om dette skyldes en systematisk feil eller om det bare var en tilfeldighet.

Målinger fra fordampningskar ble evaluert ved å konvertere dem til estimer av faktisk fordampning og sammenligne dem med eddy-kovariansmålinger. Avlingskoeffisienter på 0,9 og 0,588 ble brukt i denne konverteringen. Det ble funnet ut at på timebasis ga konverteringen med en avlingskoeffisient på 0,588 det mest nøyaktige resultatet sammenlignet med eddy-kovariansmålinger.

I denne avhandlingen har det blitt bevist at en timebasert PM-modell med en avlingskoeffisient på 0,588 er mer nøyaktig enn en PT-modell med α -verdier mellom 0,2755 og 0,3789. Det har også blitt bevist at den litteraturbaserte PM-modellen er mer nøyaktig enn den litteraturbaserte PT-modellen. Den overordnede konklusjonen av alle evalueringene er at det trengs lengre tidsserier for å komme fram til en endelig konklusjon. Imidlertid virker resultatene lovende som en bevisføring av konseptet om at kalibrering av evapotranspirasjonsmodeller kan gi verdifulle prediksjoner, og at data fra fjernmåling og fordampningskar kan være pålitelige.

Preface and Acknowledgments

Closing into an end on my studies in Environmental Physics and Renewable Energy at the Norwegian University of Life Sciences (NMBU), this thesis is my final work here. Not only does this work mark the end of my studies, but it is also a contribution to the Norwegian Meteorological Institute's project; Hydrometeorology to Operations.

I wish to thank Mareile Astrid Wolff, Laura Ehrnsperger and Bikas Chandra Bhattarai for their guidance, feedback and support. Your questions and feedback have been valuable in finding out what to look into, as my knowledge within meteorology was very limited before starting this thesis.

Special thanks to Eika Sportssenter for being a fantastic gym so that I could keep my mind sane.

I wish to thank my friends since my first year at the university; Erik Lovén, Atle Hanssen, Oskar Leknes and Andreas Ranje. I don't know where I would be without you. I also want to thank my mother and my girlfriend for listening to all my problems.

Lastly, I wish to thank myself for coming this far. The journey has had its ups and downs. With good discipline from home and a lot of stubbornness, I managed to pull my stupid ass through five years of academia.

Martin J. Økland

Martin J. Økland

Ås, 15.05.2023

Contents

Abstract	i
Sammendrag	ii
Preface	iii
1 Introduction	1
1.1 Background	1
1.2 Motivation	2
1.2.1 Hydrometeorology to operations (H2O)	2
2 Theory	4
2.1 Energy balance in the land-atmosphere system	4
2.1.1 Ground and sensible heat fluxes	5
2.2 Wind	9
2.3 Water vapor and latent heat	11
2.4 Evapotranspiration	13
2.5 Potential ET and Actual ET	15
2.5.1 Estimation of Potential Evapotranspiration	15
2.5.2 Estimation of Actual Evapotranspiration	17
2.6 Evapotranspirational measurements	19
2.6.1 Eddy covariance instrument	19
2.6.2 Pan evaporation measurement	21
2.6.3 Remote sensing	22
3 Methods and Materials	24
3.1 Meteorology during measuring period	24
3.2 Meteorological parameters correlation	25
3.3 Creating and evaluating Priestley-Taylor models	25
3.4 Creating and evaluating Penman-Monteith models	27
3.5 MODIS data	27
3.6 Pan evaporation measurements from Søråsjordet	28
4 Results	30
4.1 Presenting the data	30
4.1.1 Evapotranspiration	30
4.1.2 Pan evaporation	30
4.1.3 Accumulated ET, Evaporation and Precipitation	30
4.1.4 Net radiation	32
4.1.5 Ground heat flux	33
4.1.6 Air temperature	33
4.1.7 Air pressure	33
4.1.8 Vapor pressure deficit	33
4.1.9 Relative humidity	33
4.1.10 Precipitation	34
4.1.11 Daylight	34

4.2	Evaluation of parameter correlation	34
4.3	Evaluation of Priestley-Taylor	37
4.4	Evaluation of Penman-Monteith model	43
4.5	Evaluation of MODIS	46
4.6	Evaluation of pan evaporation measurements	47
5	Discussion	54
5.1	Explaining the raw data	54
5.1.1	Evapotranspiration	54
5.1.2	Pan evaporation	54
5.2	Priestley-Taylor models	55
5.3	Penman-Monteith models	56
5.4	Priestley-Taylor vs Penman-Monteith	57
5.5	MODIS	57
5.6	Pan evaporation and thoughts on the ET models	58
6	Conclusion	60
6.1	Evapotranspiration models	60
6.2	MODIS	60
6.3	Pan evaporation measurements	60
6.4	Future outlook	61
Appendix A: Meteorological parameters		66
	Evapotranspiration	66
	Pan evaporation	69
	Net radiation	72
	Ground heat flux	75
	Air temperature	78
	Air pressure	81
	Vapor pressure deficit	84
	Relative humidity	87
	Precipitation	90
	Daylight	93
Appendix B: ET models		96
B1:	PT models	96
	PT1	96
	PT2	99
	PT3	102
	PT4	105
	PT daily	108
B2:	PM models	109
	PMhourly1	109
	PMhourly2	112
	PMdaily2 and daily resolution of PMhourly1 and PMhourly2	115
	PMdaily1	116
Appendix C: Pan vs EC		117

Pan evaporation hourly	117
Reference evapotranspiration hourly	120
Actual evapotranspiration hourly, $k_c=0.9$	123
Actual evapotranspiration hourly, $k_c=0.588$	126

List of Figures

1	Energy fluxes	5
2	Aerodynamic and Bulk surface resistance in plant canopy	7
3	wind speed profile with eddies	10
4	Wind components in time	11
5	P_{sat} vs T	13
6	Plant stomata	14
7	Water balance in the LA system	14
8	α vs RH and U	17
9	Eddy-Covariance instrument	20
10	Flux-tower with eddies	21
11	MOD16 algorithm	23
12	Eddy-Flux tower	25
13	3D figure of evaporation pan	28
14	Accumulated ET, Evaporation and Precipitation 2021	31
15	Accumulated ET, Evaporation and Precipitation 2022	31
16	Accumulated Precipitation and Evaporation since 1997	32
17	Scatterplot: R_n vs ET	35
18	Scatterplot: u_2 vs ET	35
19	Scatterplot: RH vs ET	36
20	Scatterplot: G vs ET	36
21	Plot: PT1 vs EC	37
22	Plot: PT2 vs EC	38
23	Plot: PT1 and R_n	39
24	Plot: PT3 vs EC	39
25	Plot: PT4 vs EC	40
26	Plot: PT3, R_n and daylight	41
27	Plot: Comparison of all PT models and EC	41
28	Plot: PM hourly $kc=0.9$ vs EC	44
29	Plot: PM hourly $kc=0.588$ vs EC	44
30	Plot: Comparison of PM models vs EC (daily resolution)	45
31	Plot: first PM model vs EC	46
32	Plot: MODIS vs EC	47
33	Plot: Daily pan evaporation vs EC	48
34	Plot: Daily reference evapotranspiration vs EC	49
35	Plot: Daily estimated evapotranspiration $kc=0.9$ vs EC	50
36	Plot: Daily estimated evapotranspiration $kc=0.588$ vs EC	51
37	Plot: Comparing ET_{a1} and ET_{a2}	52
38	Plot: Hourly ET_{pan} vs ET_a June 2021	52
39	Plot: ET June 2021	66
40	Plot: ET July 2021	66
41	Plot: ET August 2021	67
42	Plot: ET June 2022	67
43	Plot: ET July 2022	68
44	Plot: ET August 2022	68
45	Plot: Evaporation June 2021	69

46	Plot: Evaporation July 2021	69
47	Plot: Evaporation August 2021	70
48	Plot: Evaporation June 2022	70
49	Plot: Evaporation July 2022	71
50	Plot: Evaporation August 2022	71
51	Plot: Net radiation June 2021	72
52	Plot: Net radiation July 2021	72
53	Plot: Net radiation August 2021	73
54	Plot: Net radiation June 2022	73
55	Plot: Net radiation July 2022	74
56	Plot: Net radiation August 2022	74
57	Plot: Ground heat flux June 2021	75
58	Plot: Ground heat flux July 2021	75
59	Plot: Ground heat flux August 2021	76
60	Plot: Ground heat flux June 2022	76
61	Plot: Ground heat flux July 2022	77
62	Plot: Ground heat flux August 2022	77
63	Plot: Air temperature June 2021	78
64	Plot: Air temperature July 2021	78
65	Plot: Air temperature August 2021	79
66	Plot: Air temperature June 2022	79
67	Plot: Air temperature July 2022	80
68	Plot: Air temperature August 2022	80
69	Plot: Air pressure June 2021	81
70	Plot: Air pressure July 2021	81
71	Plot: Air pressure August 2021	82
72	Plot: Air pressure June 2022	82
73	Plot: Air pressure July 2022	83
74	Plot: Air pressure August 2022	83
75	Plot: VPD June 2021	84
76	Plot: VPD July 2021	84
77	Plot: VPD August 2021	85
78	Plot: VPD June 2022	85
79	Plot: VPD July 2022	86
80	Plot: VPD August 2022	86
81	Plot: Relative humidity June 2021	87
82	Plot: Relative humidity July 2021	87
83	Plot: Relative humidity August 2021	88
84	Plot: Relative humidity June 2022	88
85	Plot: Relative humidity July 2022	89
86	Plot: Relative humidity August 2022	89
87	Plot: Accumulated precipitation June 2021	90
88	Plot: Accumulated precipitation July 2021	90
89	Plot: Accumulated precipitation August 2021	91
90	Plot: Accumulated precipitation June 2022	91
91	Plot: Accumulated precipitation July 2022	92
92	Plot: Accumulated precipitation August 2022	92

93	Plot: Daylight June 2021	93
94	Plot: Daylight July 2021	93
95	Plot: Daylight August 2021	94
96	Plot: Daylight June 2022	94
97	Plot: Daylight July 2022	95
98	Plot: Daylight August 2022	95
99	Plot: PT1 June 2021	96
100	Plot: PT1 July 2021	96
101	Plot: PT1 August 2021	97
102	Plot: PT1 June 2022	97
103	Plot: PT1 July 2022	98
104	Plot: PT1 August 2022	98
105	Plot: PT2 June 2021	99
106	Plot: PT2 July 2021	99
107	Plot: PT2 August 2021	100
108	Plot: PT2 June 2022	100
109	Plot: PT2 July 2022	101
110	Plot: PT2 August 2022	101
111	Plot: PT3 June 2021	102
112	Plot: PT3 July 2021	102
113	Plot: PT3 August 2021	103
114	Plot: PT3 June 2022	103
115	Plot: PT3 July 2022	104
116	Plot: PT3 August 2022	104
117	Plot: PT4 June 2021	105
118	Plot: PT4 July 2021	105
119	Plot: PT4 August 2021	106
120	Plot: PT4 June 2022	106
121	Plot: PT4 July 2022	107
122	Plot: PT4 August 2022	107
123	Plot: PT daily 2021	108
124	Plot: PT daily 2022	108
125	Plot: PMhourly1 June 2021	109
126	Plot: PMhourly1 July 2021	109
127	Plot: PMhourly1 August 2021	110
128	Plot: PMhourly1 June 2022	110
129	Plot: PMhourly1 July 2022	111
130	Plot: PMhourly1 August 2022	111
131	Plot: PMhourly2 June 2021	112
132	Plot: PMhourly2 July 2021	112
133	Plot: PMhourly2 August 2021	113
134	Plot: PMhourly2 June 2022	113
135	Plot: PMhourly2 July 2022	114
136	Plot: PMhourly2 August 2022	114
137	Plot: PM daily 2021	115
138	Plot: PM daily 2022	115
139	Plot: PMdaily1 2021	116

140	Plot: PMdaily1 2022	116
141	Plot: ET from EC and Pan evaporation June 2021	117
142	Plot: ET from EC and Pan evaporation July 2021	117
143	Plot: ET from EC and Pan evaporation August 2021	118
144	Plot: ET from EC and Pan evaporation June 2022	118
145	Plot: ET from EC and Pan evaporation July 2022	119
146	Plot: ET from EC and Pan evaporation August 2022	119
147	Plot: ET from EC and reference ET June 2021	120
148	Plot: ET from EC and reference ET July 2021	120
149	Plot: ET from EC and reference ET August 2021	121
150	Plot: ET from EC and reference ET June 2022	121
151	Plot: ET from EC and reference ET July 2022	122
152	Plot: ET from EC and reference ET August 2022	122
153	Plot: ET from EC and estimated ET ($k_c = 0.9$) June 2021	123
154	Plot: ET from EC and estimated ET ($k_c = 0.9$) July 2021	123
155	Plot: ET from EC and estimated ET ($k_c = 0.9$) August 2021	124
156	Plot: ET from EC and estimated ET ($k_c = 0.9$) June 2022	124
157	Plot: ET from EC and estimated ET ($k_c = 0.9$) July 2022	125
158	Plot: ET from EC and estimated ET ($k_c = 0.9$) August 2022	125
159	Plot: ET from EC and estimated ET ($k_c = 0.588$) June 2021	126
160	Plot: ET from EC and estimated ET ($k_c = 0.588$) July 2021	126
161	Plot: ET from EC and estimated ET ($k_c = 0.588$) August 2021	127
162	Plot: ET from EC and estimated ET ($k_c = 0.588$) June 2022	127
163	Plot: ET from EC and estimated ET ($k_c = 0.588$) July 2022	128
164	Plot: ET from EC and estimated ET ($k_c = 0.588$) August 2022	128

List of Tables

1	Terrain roughness for Momentum	8
2	Crop coefficients	19
3	Meteorological conditions during measuring period	24
4	Spearman's rank correlation coefficients values of meteorological parameters vs ET .	36
5	α and γ values for the first four PT models	42
6	α and γ values of the fifth PT model	42
7	RMSE values of PT models	43
8	RMSE values of PM models	46
9	RMSE values of pan evaporations vs EC	53

Acronyms

EC eddy-covariance

ET Evapotranspiration

H2O Hydrometeorology to Operations

LA Land-Atmosphere

LAI Leaf area index

LSMs land-surface models

MODIS Moderate Resolution Imaging Spectroradiometer

NWP Numerical weather predictions

PM Penman-Monteith

PT Priestley-Taylor

RMSE root-mean-squared-error

List of Symbols

Symbol	Explanation	Unit
A	Power available for evaporation	MW/m ²
a	Acceleration	m/s ²
b_1	Coefficient	-
b_2	Coefficient	-
b_3	Coefficient	1/(m/s)
$c1$	Coefficient	-
$c2$	Coefficient	-
$c3$	Coefficient	1/(m/s)
c_{aw}	Mole fraction of water vapor in air	-
c_{aw}^*	Mole fraction of water vapor in saturated air	-
c_p	Heat capacity	MJ/(kg °C)
D	Vapor pressure deficit	kPa
dz	Height or depth	m
d	Zero plane displacement height	m
E	Rate of evaporation	mm/s
F	Force	N
F_D	Drag force	N
E_{pan}	Pan evaporation	mm/h or mm/day
e^0	Saturation vapor pressure	kPa
e_a	Actual vapor pressure	kPa
ET_0	Reference evapotranspiration	mm/h or mm/day
ET_a	Actual evapotranspiration	mm/h or mm/day
ET_p	Potential evapotranspiration	mm/h or mm/day
G	Ground heat flux	W/m ²
g_a	Aerodynamic conductance	m/s
g_c	Soil conductivity	W/(m °C)
g_s	Bulk surface conductance	m/s
H	Sensible heat flux	W/m ²
k	Von Karman's constant	-
k_c	Crop coefficient	-
k_p	Pan coefficient	-
LAI_{active}	Active leaf area index	-
m	Mass	kg
P	Air pressure	kPa
R	Ideal gas constant	J/(K mol)
R_n	Net radiation	W/m ²
r_a	Aerodynamic resistance	s/m
r_l	Stomatal resistance	s/m
r_s	Bulk surface resistance	s/m
RH	Relative humidity	%

T	Temperature	$^{\circ}\text{C}$
T_a	Air temperature	$^{\circ}\text{C}$
T_s	Soil temperature	$^{\circ}\text{C}$
t	Time	s
U	Wind speed	m/s
U_{t0}	Wind speed at initial time	m/s
U_{t1}	Wind speed at end time	m/s
U_z	Wind speed at height z	m/s
u_z	Wind speed at height z	m/s
u_*	Friction velocity	m/s
x	Distance	m
z	Height above ground	m
z_h	Height of relative humidity measurement	m
z_m	Height of wind measurement	m
z_{oh}	Roughness governing heat and vapor	m
z_{om}	Roughness governing momentum	m
α	Constant in Priestley-Taylor equation	-
γ	Psychrometric constant	kPa/ $^{\circ}\text{C}$
Δ	Slope of saturation-to-vapor-pressure	kPa
ϵ	molecular weight ratio [vapor/dry air]	-
λ	Latent heat of vaporization	MJ/kg
$\lambda_{w(T)}$	Latent heat of vaporization at temperature T	MJ/kg
μ_w	Chemical potential of water vapor in air	J/mol
μ_{w*}	Standard chemical potential of water vapor	J/mol
ρ	Density	kg/m ³
ρ_a	Air density	kg/m ³

1 Introduction

1.1 Background

On average, the total mass of the atmosphere is 5.1480×10^{18} kg, whereas water vapor amounts in the range of 1.27×10^{16} kg (Trenberth & Smith, 2005). Although water is only 0.25 % of the atmosphere in weight, it plays a significant role as a greenhouse gas to keep our planet warm, and in the water (or hydrological) cycle. There is a consensus in the scientific community that human activity has warmed the climate. The Intergovernmental Panel on Climate Change mentions this in their assessment report (Masson-Delmotte et al., 2021). With an increasing global mean temperature, the hydrological cycle is believed to increase (Genfo et al., 1991; Trenberth, 1999). This means the evaporation rates will increase, and the atmosphere can hold more water. Thus increasing the favor of intense rainfall events.

Knowledge about evaporation and transpiration is crucial to better understanding the climate and its variations and giving good predictions about future hydrological cycles. With better predictions, water resource managers can take proper actions, irrigation requirements can be adjusted, and river forecasts will be improved (Blaney & Criddle, 1962; Xu & Singh, 2001; Jackson et al., 2001). Evapotranspiration (ET) is also important in the ecological domain, as it gives clues about plant activity and the energy balance in an ecosystem (Currie, 1991; O'Brien, 1993).

Since ET models reflect the water and energy balance of a local or regional system, it is possible to get an idea of how much water there is in the local ecosystem. This could help prevent water damage to infrastructure because of the ability to predict heavy rain. It would also be possible to take action before a drought since it would be possible to know how much water is leaving the soil.

Studies have been done for about 75 years in the search for good predictive ET models, some with higher complexity and depending on more variables than others. ET models were mainly developed to predict crops' water balance, so optimized irrigation systems could be built (Barry & Blanken, 2016a; Blaney & Criddle, 1962). Studies have also compared different models to determine which will yield the most accurate predictions (Xu & Singh, 2001; Fisher et al., 2011; Gavin & Agnew, 2004).

However, results show that ET models will have varying accuracy depending on their spatiotemporal application. The considerable uncertainty and variation stem from the vegetation, as it is hard to quantify plant productivity. Transpiration from stomatal conductance in plant leaves, heterogeneous vegetation consisting of different plant species and sizes, and the fact that transpiration represents 80-90 % of terrestrial ET (Jasechko et al., 2013), are some of the reasons why predicting ET poses challenges. Another issue is the available meteorological data one can use to calculate ET. Many models are therefore based on empirical constants that represent plant productivity, since it is hard to quantify. The models would then only depend on variables that are easy to measure (i.e air temperature, air pressure, daylight hours, latitude, etc).

A commonly used model that requires only a few measurements is the Priestley-Taylor model. It is a radiation-based model. It estimates ET, consists of primarily empirical constants, and depends on variables such as air temperature, air pressure and irradiation. The more advanced Penman-Monteith model is a combination-type model. Besides meteorological data as the Priestley-Taylor needed, this model also requires information about the surface (i.e vegetation and surroundings)

1.2 Motivation

As mentioned in the previous section, ET models have a high variance in their spatiotemporal application. Empirical constants used in equations may be adjusted to make ET models fit better for their application. Some studies have adjusted these constants depending on their spatial and temporal application, resulting in higher accuracy models.

For example, the study by Cristea et al. (2013) looked into how to improve the accuracy of the Priestley-Taylor model in the USA by using linear regression depending on relative mean relative humidity and mean wind speed to find more appropriate values for the empirical constant α (will be explained further in the theory section). From their results, adjusting α reduced the model median root-mean-squared-error (RMSE) value from 1 to 0.78-0.85.

Another study by Gavin & Agnew (2004) used Penman-Monteith and Priestley-Taylor models to model actual, reference and equilibrium evaporation from a temperate wet grassland. Using two different values for α (1.25 and 0.80) to represent the wetness level of the surface in the Priestley-Taylor model, reliable estimates of actual evaporation were achieved when compared to Bowen ratio energy balance data with RMSE.

As mentioned in the previous section, knowledge about ET is essential to understand the climate and hydrological cycles better. ET models also play an important role in land-surface models (LSMs). With improved understanding and modeling of the hydrological activities (i.e improved ET models), LSMs could provide reliable estimates of surface- and groundwater fluxes. This could, in turn, facilitate early warning of flash floods, agricultural drought and give more precise Numerical weather predictions (NWP). So far, no applicable ET models are explicitly calibrated for the Norwegian climate.

1.2.1 Hydrometeorology to operations (H2O)

NWP depends on atmospheric variables such as irradiation, wind, humidity and air temperature. Despite advances over the past few decades, predicting intense local rainfall remains challenging. Currently, NWPs do not fully consider the coupling between the atmosphere and the components on land (i.e soil moisture and temperature, land biosphere, terrestrial snow, ET, lake temperature, etc). NWPs without the Land-Atmosphere (LA) coupling are believed to fall short of their ability to predict short-range forecasts and hydrological forecasts (what happens to the water after precipitation).

In 2020 the Norwegian Meteorological Institute started a campaign called Hydrometeorology to Operations (H2O) which aims to develop world-leading NWPs which will be integrated across the LA domain. Emphasis is put on the LA coupling and soil hydrology so that reliable hydrometeorological forecasts can be warnings for enhanced preparedness can be delivered.

As part of the H2O project, this thesis will study ET in the LA domain to increase our understanding of ET data in the Norwegian climate, and if it is possible to achieve beneficial results from ET models. The observations for this study originate from the meteorological station at Søråsjordet located in Ås, Viken county, Norway. The reason for choosing this meteorological site is because it has a close connection to the Norwegian University of Life Sciences (NMBU), the meteorological station has a eddy-covariance (EC) instrument with two years of flux measurements, a long time series of pan evaporation measurements, long term meteorological measurements stretching back to 1859 in which the surroundings have remained almost consistent, and the area around the site

is an agricultural field.

To achieve the objective of this thesis, the following subjects are investigated:

- 1. Evaluating and adapting typically used parameters of ET-models like Penman-Monteith and Priestley-Taylor, and compare to the EC-measurements for use in Norwegian Climate.** Five types of Priestley-Taylor models are evaluated: One with literature values from Priestley & Taylor (1972), one with a calculated approach from Cristea et al. (2013) and three using curve-fitting to find best-suited values, of which one is based on daily resolution. Four types of Penman-Monteith models are evaluated: Two based on daily resolution, where one calculates evapotranspiration directly and one through calculating reference evapotranspiration first. Two other Penman-Monteith models are based on hourly resolution and calculate reference evapotranspiration first, but the two use different crop coefficient values.
- 2. Compare the EC measurements with MODIS-based satellite data.**
- 3. Evaluate the long-term pan evaporation measurements from Søråsjordet by comparing the EC measurements with a two-year parallel.** The pan evaporation measurements are converted to estimations of actual evapotranspiration. Two series of estimated actual evapotranspiration are calculated, where the difference is the choice of crop coefficient. One crop coefficient value is derived from one of the Penman-Monteith models.

2 Theory

2.1 Energy balance in the land-atmosphere system

For a better understanding of ET, looking into the source and the different energy states in the LA system is crucial. The core energy source for this system is the incoming solar radiation, which on annual average irradiates $\sim 1361 \text{ W/m}^{-2}$ to the top of our atmosphere (Kopp & Lean, 2011). The electromagnetic wavelength range of this incoming radiation is 200-2500 nm (96.3 % of the radiation) (Newport-Corporation, n.d.). Radiation that reaches the surface has to pass through the atmosphere, which will absorb and scatter the radiation spectrum. Oxygen and nitrogen absorb short waves, blocking radiation with wavelengths below 190 nm. The absorption of short waves turns oxygen into ozone, which absorbs longer ultraviolet waves (200-300 nm) and weakly absorbs visible light. Water vapor, carbon dioxide and oxygen also absorb near-infrared radiation. If it is a cloudless day and the zenith angle is zero (the Sun is directly above a point on the Earth's surface), the solar irradiance is effectively reduced from $\sim 1361 \text{ W/m}^{-2}$ at the top of the atmosphere to $\sim 1050 \text{ W/m}^{-2}$ when it reaches the surface (Newport-Corporation, n.d.).

When there is a net radiation surplus (usually during daytime), the energy must be dispersed at the surface through conduction, convection, phase change, and storage. In the LA system, heat is transported into deeper soil layers mainly by conduction, which is the ground heat flux, G . Whereas the dominant heat transportation through air happens by convection, which is the sensible heat flux, H , and phase change is the latent heat flux, λE , where λ is the latent heat of vaporization and E is the rate of evaporation. The equation of energy balance can therefore be written as

$$R_n = G + H + \lambda E + \left(\rho c_p \frac{\Delta T}{\Delta t} dz \right), \quad (1)$$

where R_n is the net radiation. Figure 1 shows these fluxes with their representative positive directions. The last term, which is in the bracket, represents the energy storage, where ρ is the density of either air or soil, c_p is the specific heat capacity of either air or soil, $\Delta T/\Delta t$ is the rate of temperature change, and dz is the depth beneath or height above of the surface area where the radiation is dispersed. When searching for the ET, the λE term in equation 1 must be found to calculate ET.

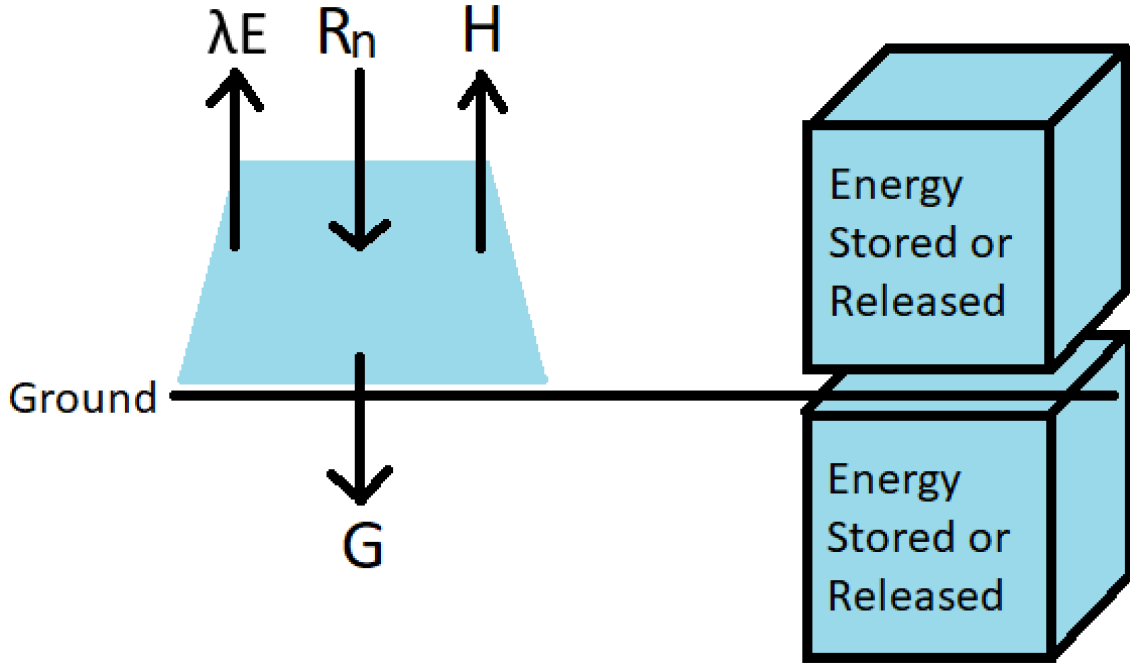


Figure 1: *The arrows in this figure represent the given positive direction of the different energy fluxes. As one can see, energy surplus will be stored in the air and the soil, and released if the net radiation is too low.*

2.1.1 Ground and sensible heat fluxes

Radiation not reflected from the surface or absorbed by vegetation will be converted into heat energy for the soil, also known as ground heat flux. The composition of the individual soil compounds and water content determines the conductivity of the soil. Sand, for example, has a high conductivity since it consists of mostly quartz minerals, whereas organic soils have a low conductivity. The porosity of the ground also determines the conductivity since air works as an insulator. However, if the pores are filled with water (i.e high soil moisture), the conductivity increases (Barry & Blanken, 2016a). The ground heat flux, G , from equation 1 is given by equation 2, where g_c is the conductivity of the soil, and $\Delta T/\Delta z$ is the vertical temperature gradient of the soil.

$$G = -g_c \frac{\Delta T_s}{\Delta z} \quad (2)$$

The ground heat flux is a crucial component of the surface energy balance (eq. 1) as it affects the exchange of heat and moisture with the laminar boundary layer (thin layer of air right above the surface shown in fig. 2). The ground heat flux is also a parameter used in the Penman-Monteith equation (eq. 19, 20, 22), which will be further explained in section 2.5.2.

Another essential component of the lower surface level, which is also a parameter of the Penman-Monteith equation (eq. 19), is the bulk surface conductance, g_s , also known as stomatal conductance, and is described by equation 3, where r_s is the bulk surface resistance (which will be explained further in the paragraph before equation 4).

$$g_s = r_s^{-1} \quad (3)$$

This conductance describes a plant's ability to exchange gases with the boundary layer. The stomates on a plant are responsible for the transpiration of a plant. Water vapor is "exhaled" from the stomates during transpiration while carbon dioxide is "inhaled". This process will be explained in more detail in section 2.2. As the stomates' opening increases, the bulk surface conductance increases. The environmental factors influencing the conductance are irradiation, temperature, humidity and wind speed. The conductance is made into a "bulk" because it is difficult to separate whether the water vapor comes from soil evaporation or plant transpiration.

As shown in equation 3, the inverse of bulk surface conductance, g_s , is the bulk surface resistance, r_s . The term bulk surface "resistance" comes from the analog of Ohm's law in electricity. Current or flux is proportional to a potential difference and inversely proportional to resistance, making it applicable to water vapor diffusing through the stomata of plant leaves (Lhomme, 1991). The bulk surface resistance is calculated by eq.4, where r_l is bulk stomatal resistance and LAI_{active} is active sunlit leaf area (Allen et al., 1998).

$$r_s = \frac{r_l}{LAI_{active}} \quad (4)$$

Since it would be impossible to measure the stomatal resistance of each individual leaf, the bulk stomatal resistance, r_l , is the average resistance of all leaves. This resistance varies between crops, crop management, and how far into the growing season the crop is. It is also influenced by climate and water availability. If a crop is water stressed, the resistance increases (Allen et al., 1998). Leaf area index (LAI) is dimensionless and is expressed as the fraction of leaf area (only the upper side) per ground area, and the part of the leaf area that contributes to surface heat and vapor transfer is the active LAI. From Allen et al. (1998), it is said that LAI values differ widely between crops, but is usually in the range of 3-5 for mature crops.

An example for calculating the bulk surface resistance of well-watered grass crop can be found in Allen et al. (1998), Box 5. Here the Assumption is that the LAI of grass is given as; $LAI = 24h$, where h is the height of the grass in m. Further, LAI_{active} is given as; $LAI_{active} = 0.5LAI$, assuming that only the upper half of dense clipped grass actively contributes to the surface heat and vapor transfer. It is assumed that the stomatal resistance, r_l , of well-watered grass is 100 s/m and that the crop height, h , is 0.12 m. From these assumptions, it is concluded that the bulk surface resistance of well-watered grass with a height of 0.12 m is 70 s/m.

Figure 2 shows where in the plant canopy aerodynamic resistance (will be explained in the next paragraph) and bulk surface resistance are.

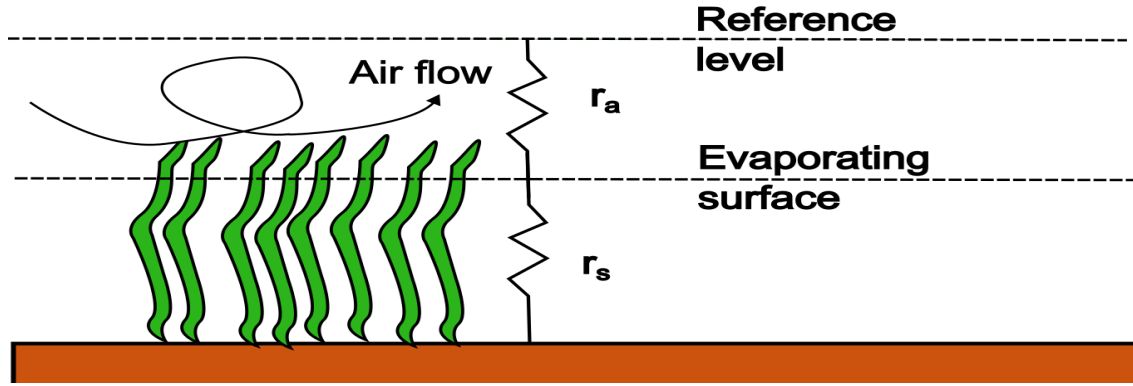


Figure 2: The figure shows where the bulk surface and aerodynamic resistance are in the plant canopy. The Evaporating surface is the same as the laminar boundary layer.

Radiant energy absorbed by vegetation and soil but not transformed into latent heat flux will increase the surface temperature of the vegetation and soil, contributing to an increase in sensible heat flux. Latent heat loss is highest in energy-limited water-rich ecosystems, for example, irrigated systems, since these are usually well-watered crops. Latent heat loss decreases as available water decreases (which will increase the sensible heat flux).

The heat from the vegetation and/or soil is transferred through conduction to the laminar boundary layer, and then transported into the atmosphere by convection. There are two types of convection; free and forced. When an air mass by the surface is heated, its density is decreased. Due to buoyancy, the less dense air will rise and displace cooler air, and the cooler air will sink to replace the warmer air mass. Forced convection refers to the phenomenon where air is compelled to rise due to surface irregularities. In the LA system, surface roughness is essential for the sensible heat flux. Convection depends on turbulence, which depends on aerodynamic conductance, g_a . Aerodynamic conductance increases with greater surface roughness (Monson & Baldocchi, 2014a). Some typical estimations of surface roughness, z_{om} are displayed in table 1. The inverse of aerodynamic conductance is the aerodynamic resistance, r_a , and is calculated by equation 5.

$$r_a = \frac{\ln\left(\frac{z_m-d}{z_{om}}\right) \ln\left(\frac{z_h-d}{z_{oh}}\right)}{k^2 u_z} \quad (5)$$

Here, z_m is the height of the wind measurement, z_h is the height of the humidity measurement, d is the zero plane displacement height, z_{om} is the roughness length governing momentum transfer, z_{oh} is the roughness governing the transfer of heat and vapor, k is von Karman's constant (0.41), and u_z is the wind speed at the measuring height z .

Roughness length governing momentum, z_{om} is the height at which the wind speed profile would be assumed to be zero due to surface roughness. The following logarithmic equation gives the wind speed profile;

$$U_z = \frac{u_*}{k} \ln(z/z_{om}) \quad (6)$$

where U_z is the wind speed at height z , u_* is the friction velocity, which provides the wind's tendency to transfer momentum on the surface, create shear stress and produce turbulence. k is

Table 1: *Some examples of surface roughness estimations depending on the landscape. The table is inspired from Barry & Blanken (2016a).*

Terrain roughness for Momentum		
Class	Roughness [m]	Description
Sea	0.0002	Open water, snow-covered flat plain, featureless desert. Free fetch of several kilometers
Smooth	0.005	Featureless landscape, with little to none vegetation. Marshes, snow-covered open country
Open	0.03	Level country with low vegetation and isolated obstacles. Grass, tundra
Roughly open	0.1	Low crops or plant cover. Moderately open with occasional obstacles. Isolated trees, low buildings
Rough	0.25	High crops or crops of varying height. Scattered obstacles. Buildings, tree belts
Very rough	0.5	Intensely cultivated. Large farms and forest clumps. Bushland. Urban areas with low buildings
Skimming	1.0	Covered with large similar obstacles. Forests. Dense urban areas without significant building height variations
Chaotic	+2	Irregular distribution of large obstacles. Dense urban with mix of low and high buildings. Forests with clearings

von Karman’s constant, and z is the height. The rougher the surface, the higher the point where U will equal zero. The theoretical height at which U becomes zero as a function of $\ln(z)$ is known as the roughness length, z_{om} . The greater the value of z_{om} , the rougher the surface, and the higher the point above ground U becomes zero (Monson & Baldocchi, 2014b). From Barry & Blanken (2016b) and Allen et al. (1998), the roughness length for a well-watered grass canopy is estimated to be $0.1h$, where h is the crop height.

The zero plane displacement height, d , is the height at which the mean wind speed is zero due to roughness elements such as plants, trees, buildings and other obstacles on the surface. When looking at actual canopied surfaces, reductions of U_z will reach zero at a height above the predicted z_{om} (Monson & Baldocchi, 2014b). From Barry & Blanken (2016b) and Allen et al. (1998), zero plane displacement height for a well-watered grass canopy is estimated to be $2/3$ of the crop height, h .

Roughness height governing heat and vapor, z_{oh} is the height at which temperature and vapor profiles are assumed to be zero. The roughness height governing heat and vapor depends on the surface roughness governing momentum, z_{om} . From Allen et al. (1998), the roughness height governing heat and vapor for well-watered grass is estimated to be $0.1z_{om}$.

A limitation of this equation is that it is only valid for neutral stable conditions for short time scales (hourly or less). Since it is challenging to measure d , z_{om} and z_{oh} , empirical equations have been developed to estimate these parameters (as mentioned in the previous paragraph). It is also possible to use the estimations in table 1 for an estimated value of z_{om} .

Following the calculations from Allen et al. (1998), Box 4, it is possible to get an estimate of aerodynamic resistance for well-watered grass, dependent on wind speed. Assuming that zero

plane displacement height, d , is $2/3h$, roughness length governing momentum, z_{om} , is $0.123h$, roughness height governing heat and vapor, z_{oh} is $0.1z_{om}$, crop height, h is 0.12m, and that the height of wind speed and humidity measurements, z_m and z_h are 2 m. The estimate for the aerodynamic resistance, r_a , becomes $208/u_2$, where as mentioned, u_2 is the measured wind speed at 2 m.

2.2 Wind

Wind is essentially an air mass that is being moved by a force. Newton's second law of motion can explain it;

$$F = ma \quad (7)$$

where m is the mass of the air and a is the acceleration of the air mass, and F is the force applied on the air mass. The opposing forces of the force that is accelerating the air mass, are pressure and friction. Since the air pressures on Earth's surface are not in containers, they will try to reach an equilibrium. This pressure difference will therefore create a force that accelerates the atmospheric masses from high to low pressure. The atmospheric mass encounters flow resistance due to accelerated air molecules colliding with slower air molecules within the mass itself. The acceleration from the difference in air pressure including resistance can be stated as;

$$a = - \left(\frac{\Delta P}{\rho_a x} + \frac{F_D}{m} \right) \quad (8)$$

where a is still the acceleration, ΔP is the pressure difference between two points, ρ_a is the air density, x is the distance between the two pressure points, F_D is the resistance as drag force which causes deceleration, and m is the mass.

The drag is caused by friction at the molecular scale, and acts therefore as viscosity. In the domain where the air is in layers and the flow of air is mostly laminar, the molecular viscosity is an essential factor. However, in turbulent flows, a larger scale of interactions is the critical factor determining the shear stresses (Monson & Baldocchi, 2014b). Momentum can be transferred and shear be caused due to parcels of air interacting with adjacent layers. These air parcels are called wind eddies and create eddy viscosity, the turbulence that opposes the inertial forces propelling the flow. The eddies increase in size with the height above ground, and because of the inherent instability of the eddies, they will decompose into smaller eddies as they move with the flow. When large eddies decompose they transfer their energy. As they become smaller, they will eventually be so small that their energy is consumed as work against viscosity and kinetic energy becomes heat. Figure 3 shows how the eddies look in a wind speed profile for a longitudinal wind, u . The figure also shows the composition of the eddy with longitudinal wind, u , and vertical wind, w .

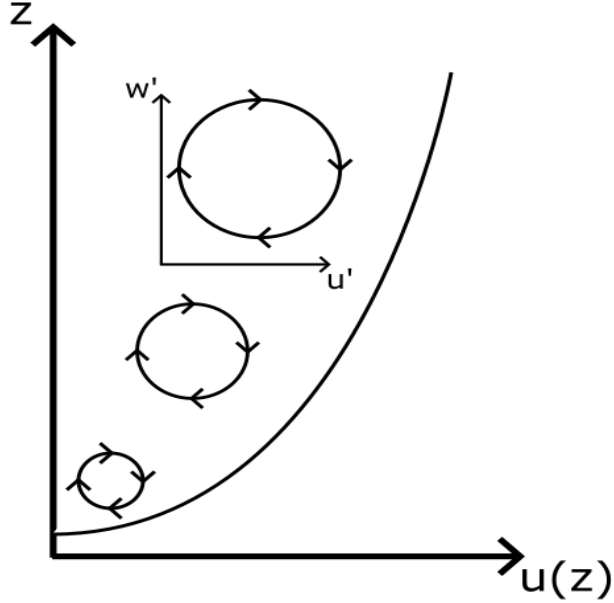


Figure 3: *The figure shows a standard wind speed profile with parcels of eddy turbulence.*

Since ΔP will change during the course of time, the wind speed will also change with time. The wind speed during the course of time can be represented as;

$$U_{t1} = U_{t0} + a\Delta t \quad (9)$$

where U_{t1} is the wind speed at time $t1$, U_{t0} is the wind speed at time $t0$, which is the wind before the state of ΔP changed. Δt is the difference in time.

The wind speed U is a composite wind speed that can be decomposed into three wind components in Cartesian coordinates. Along the x-axis is the longitudinal wind velocity, u , along the y-axis is the latitudinal wind velocity, v , and along the z-axis is the vertical wind velocity, w . The magnitude of each component will vary with time, and therefore also their contribution to mean wind speed velocity, periodic wave velocity, and random fluctuating velocity.

The mean wind velocity reflects the "quasi-constant" components, regional pressure gradients, and local near-surface pressure gradients. Energy and mass are advected along these pressure gradients. Since these pressure gradients do not change significantly in their magnitude or distribution during the time span to derive the mean wind velocity, they are quasi-constant.

Time-dependent variance with a periodicity of a few hours around the mean wind velocity is known as the periodic wave velocity. These waves are often not explicitly considered in the analyses of turbulent transport. These waves tend to occur during stable thermal stratification at night. Waves that are regular in their periodicity will have no net directional transport.

Random fluctuating velocity reflects motions in short time scales such as seconds and minutes. These are turbulences, and can be caused by instabilities in the flow. The random fluctuating component is responsible for the turbulent transport of heat, energy and mass between the surface and atmosphere. The different wind velocity components are shown in figure 4.

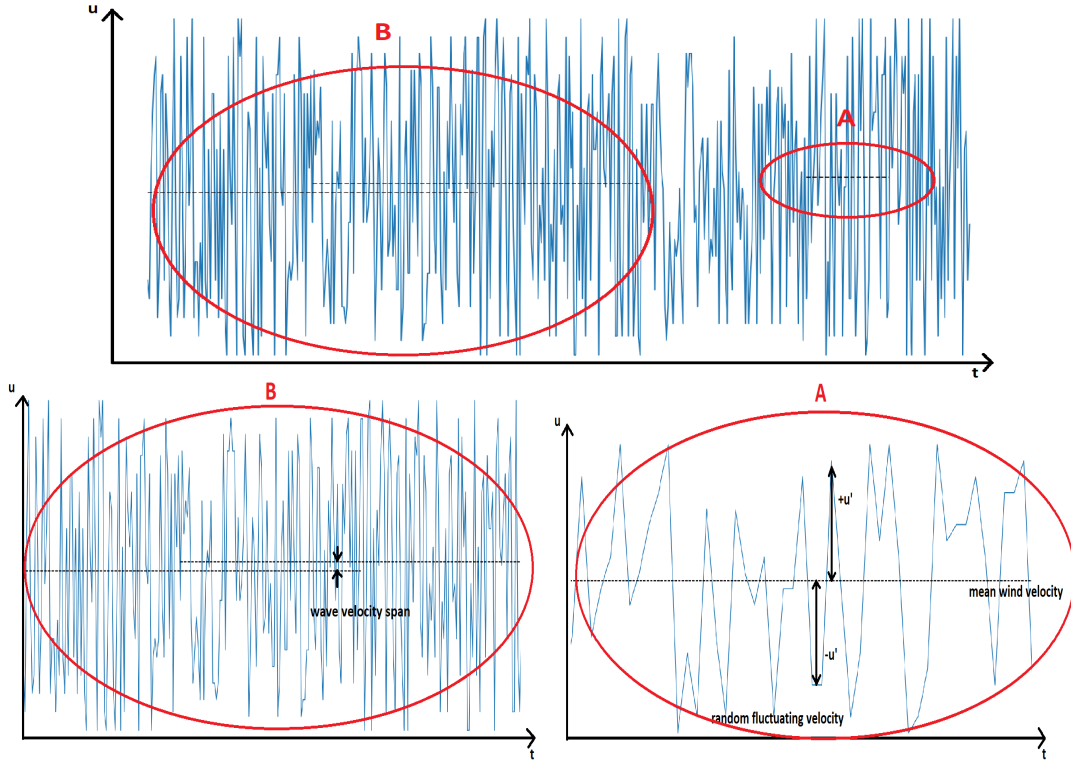


Figure 4: The figure shows the longitudinal wind velocity u as a time series. Circle B shows the mean wind velocities of the two different periods from the wave-like pattern. Circle A shows the mean wind velocity in a short time span with the random fluctuations.

2.3 Water vapor and latent heat

The latent heat flux, λE , is dependent on the amount of energy that can be used for evaporation (eq. 1 and fig. 1), and the concentration of water vapor that is in the laminar boundary layer. The energy drives the phase change from liquid water to water vapor, and the concentration of water vapor drives the flux of energy and mass from the surface. The relation that defines the chemical potential of water vapor in terms of mole fraction is given as;

$$\mu_w = \mu_w^* + RT \ln \frac{c_{aw}}{c_{aw}^*} \quad (10)$$

where μ_w and μ_w^* are chemical potentials for water vapor (the first in a sample of air and the second is standard value). c_{aw} is the mole fraction of water vapor in the sample of air, and c_{aw}^* is the saturated mole fraction of water vapor in the air sample. R and T are the ideal gas constant (8.314 J/(K mol)) and air temperature respectively. From equation 10, one can see that as the mole fraction of water increases (evaporation happens), the chemical potential of water vapor in the air increases. As water evaporates, the water molecules do not contain higher kinetic energy as the temperature does not change. It is only the chemical potential of the water molecules that changes.

Even though the phase change is not due to temperature changes, it does not mean that the air temperature above a wet surface does not affect the evaporation rate. Changes in μ_w can be caused by a change in c_{aw}^* . The value of c_{aw} is related to air temperature, and this relation

comes from the fact that as air temperature changes, its capacity to hold water changes. As the ground absorbs radiant energy, the air above the ground will heat up through sensible heat flux, H , and consequently, its capacity to hold water will increase. This relation can be derived from the Clausius-Clapeyron relation. The derived form of the Clausius-Clapeyron relation is given as;

$$\frac{dc_{aw}^*}{dT} \approx \frac{\lambda_{w(T)}c_{aw}^*}{RT^2} \quad (11)$$

where c_{aw}^* is the saturated mole fraction of water vapor in the air, or in other words; air's capacity to hold water vapor. $\lambda_{w(T)}$ is the latent heat of vaporization (temperature dependent). R is the ideal gas constant, and T is the air temperature. This equation assumes that water vapor acts as an ideal gas and that the specific molar volume of water vapor is large enough compared to liquid water so that the difference can be ignored. Assuming that $\lambda_{w(T)}$ is constant in a narrow range of temperature changes in the plant-atmosphere domain, $\lambda_{w(T)}$ becomes λ_w . Using calculus and the assumption, the Clausius-Clapeyron relation becomes;

$$c_{aw}^*(2) = c_{aw}^*(1) e^{-\frac{\lambda_w}{R\Delta T}} \quad (12)$$

This equation shows that the air's capacity to hold water vapor increases exponentially as temperature increases. This equation also shows that with a rise in temperature, T , the air's vapor holding capacity, c_{aw}^* increases by 7 % per °C. Since these derived forms of the Clausius-Clapeyron relation are hard to work with, a more empirical relation is used. The empirical relation is given as;

$$c_{aw}^* = \frac{c1}{P} e^{\frac{c2T}{T+c3}} \quad (13)$$

where the temperature T is in °C, the air pressure P is in Pa, and the coefficients $c1$, $c2$ and $c3$ are 611 Pa, 17.502, and 240.97 °C. If the saturation vapor pressure is given by; $e^0 = c_{aw}^* P$, equation 13 becomes equation 17.

For small spans of air temperature, the relation between saturation vapor pressure and temperature becomes approximately linear. The slope from this relation is referred to as the saturation-to-vapor pressure slope, which is Δ from equation 16. Figure 5 shows the relation between saturation vapor pressure and temperature.

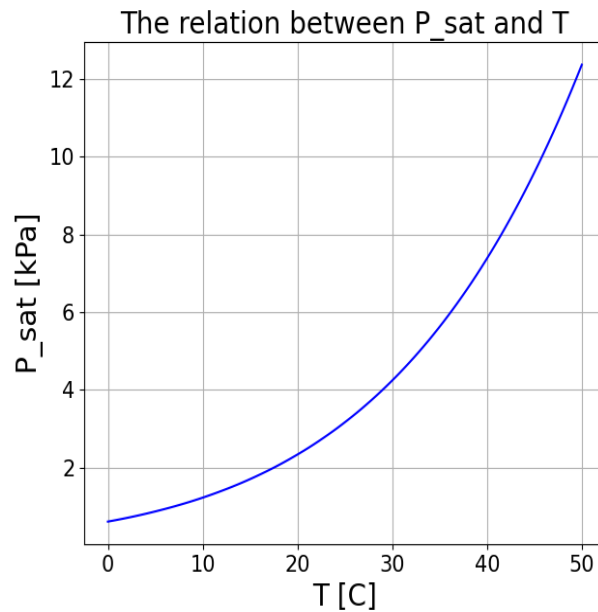


Figure 5: *The figure shows the relation between saturation vapor pressure and temperature.*

2.4 Evapotranspiration

Evapotranspiration is the process that consists of evaporation from soil and wet surfaces, and transpiration through plant leaves. ET returns about 2/3 of precipitation into the atmosphere (Chen & Liu, 2020). Sublimation is not included in the context of ET, since it is a phase change from solid water to water vapor, not liquid water to water vapor. Vapor from evaporation is derived from sources such as open waters (i.e oceans, lakes, rivers, puddles, etc.), water on objects (i.e vegetation, buildings and soil surface), or measuring devices. Transpiration is the process where vegetation "breathes in" carbon dioxide from the surrounding air through its stomates located on leaves, needles or stems (depending on the plant). While consuming carbon dioxide, stomates also tend to release water as vapor, since the air in the intercellular spaces of the leaf is usually saturated or near saturated (Gates, 1968). Nutrients in the soil are dissolved in water, and consumed by the plants through their roots. Only a tiny fraction of the water consumed stays within the plant, while most of it is transpired. A simplified drawing of a plant with its stomates is shown in figure 6.

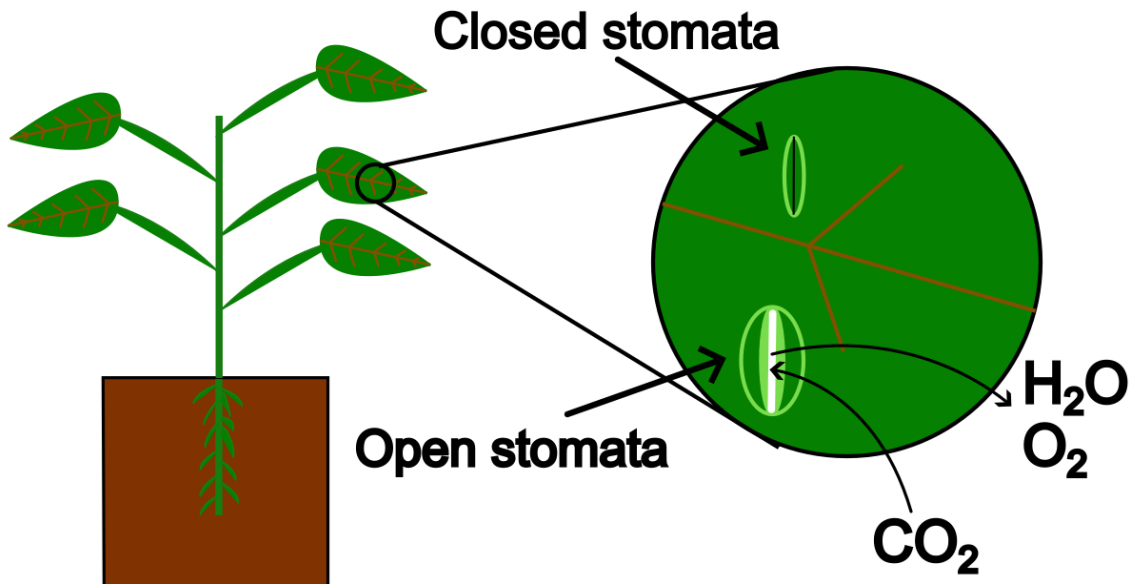


Figure 6: A drawing of a plant with a zoom-in on the leaf to show the stomata.

We use the term "evapotranspiration" because once the water vapor is released into the air, it is hard to distinguish how much of the vapor is from evaporation, and how much is from transpiration. A simple figure of evapotranspiration and water balance at surface level in the LA system is shown in figure 7. From the figure, one can see that evapotranspiration occurs where there is vegetation.

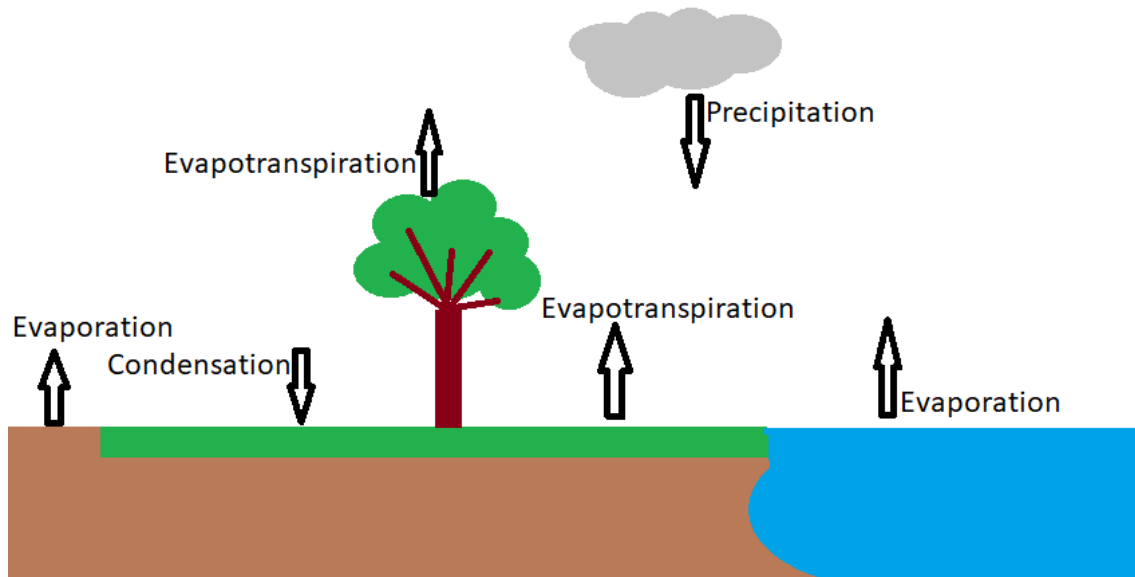


Figure 7: A simplification of the water balance in the LA domain.

As we know, phase-shifting liquid water into water vapor requires tremendous amounts of energy (2256 kJ/kg) due to the strong hydrogen bonds between water molecules. This increases with orders of magnitude if there are impurities in the water (Marek & Straub, 2001). The required energy for evaporation is provided by heat or radiation. However, evaporation will not happen if the surrounding air is saturated, and there is no wind to facilitate the transportation of water

molecules in the air. Thus, the main climatic influences on evaporation are solar radiation (directly or indirectly as air temperature), relative humidity of the air, and air transportation in the form of wind. Transpiration depends on the type of vegetation in the area of interest. The ground or soil characteristics determine the retention of precipitation inputs in the form of soil moisture. Overall, these three controls of ET can alter depending on the spatiotemporal scale and the eco-climate system.

2.5 Potential ET and Actual ET

When looking at ET, it is essential to distinguish between potential evapotranspiration, ET_p , and actual evapotranspiration, ET_a . With knowledge about the available energy, it is possible to calculate ET_p since it represents how much ET is theoretically expected from the amount of energy in the system if available water is not a limiting factor. This measure of ET is vital for farmers, so they know how much irrigation is needed for their crops to avoid drought or waterlogged soils (Fisher et al., 2011). Also, ET_p models rely on meteorological measurements that are easy to acquire. A simple way to measure ET_p is to use evaporation pans, since the measurement would be pure evaporation without being dependent on plant productivity. A parameter similar to potential evapotranspiration, ET_p , is reference evapotranspiration, ET_0 . Reference evapotranspiration, ET_0 , can be obtained by calculation from evaporation pan measurements. Reference evapotranspiration, ET_0 , is a measure of how much evapotranspiration is theoretically expected from a well-irrigated surface with a grass reference crop (Allen et al., 1998).

ET_a is the actual amount of water lost into the atmosphere through both evaporation and transpiration. Thus, ET_a represents the actual water balance of a system, and varies depending on soil, vegetation and wind (Fisher et al., 2011). One thing to note is that ET_a will never exceed ET_p as ET_p is the highest possible rate of ET if water is not limited. For example, in a desert, the value of ET_p will be significant because the air is dry, and plenty of energy is available for evaporation. However, the value of ET_a will be close to zero, since the system has almost no water to evaporate.

Studies have been done to find values of evaporation and evapotranspiration by eddy-covariance measurements and by estimated calculations. One of these studies is the thesis by Rutger (2002). The location of the study was in the sub-arctic area around the Tana basin in the north of Norway and Finland. Here, it was found that evaporation values were 59 mm between 23. June to 27. July 1999 and 57 mm between 5. June to 23. July 2000. The estimated evapotranspiration values were calculated to be 74 mm between 22. June to 2. August 1999 and 75 mm between 5. June to 23. July 2000. Another study done in Alaska found evapotranspirational values of about 21.5 mm/week in July 2013 and 17 mm/week in August 2013 (Ruaruen et al., 2015).

2.5.1 Estimation of Potential Evapotranspiration

As mentioned in the introduction, a simple equation to calculate ET_p is the Priestley-Taylor equation, which is given by;

$$ET_p = \alpha \frac{\Delta}{\Delta + \gamma} R_n \quad (14)$$

This equation is based on radiation, or more precisely, net radiation, R_n , temperature and air pressure. The empirical constant in this equation is α . Δ is the slope of saturation-to-vapor

pressure and is shown in equation 16, and γ is the psychrometric constant and is shown in equation 15.

The constant α depends on the water saturation level of the surface, which means that α would be greater for a saturated surface than for an unsaturated surface. In the study by Priestley and Taylor (1972), different values of α were found even though an effort was put to get values for saturated surfaces only. These values ranged from 1.33 to 1.08. Priestley and Taylor also did calculations to get values of α above bodies of water. The resulting values of α ranged from 1.30 to 1.20. From these results, Priestley and Taylor concluded that the best overall mean estimate (for land and water) value for α is 1.26. This value of 1.26 will be referred to as "literature value" in this thesis.

The psychrometric constant γ from equation 14 is air pressure dependent. The psychrometric constant is called a "constant", because it has negligible variations when used on a local and short time-series scale. It is also constant if mean air pressure is used (Allen et al., 1998). The equation for the psychrometric constant is given as;

$$\gamma = \frac{c_p P}{\epsilon \lambda}, \quad (15)$$

where c_p is the specific heat of air at constant air pressure. The specific heat of air, c_p , depends on the composition of the air. Different sources have different values for the specific heat of air. In Allen et al. (1998) it is given as 1.013 kJ/(kg °C). In Barry & Blanken (2016c) it is given as 1003.5 J/(kg K). And in (TETB, n.d.) it is given as 1.006 kJ/(kg K) at 18 °C. λ is the latent heat of vaporization of water, and on average will have a value of 2450 kJ/kg (Allen et al., 1998). P is the air pressure, and ϵ is the molecular weight ratio between water vapor and dry air (which is 0.622) (Allen et al., 1998). On average, the psychrometric constant would be somewhere in the region of 0.066 kPa/°C.

In equation 14, Δ is the saturation-to-vapor pressure slope. This is the reason why the PT equation is dependent on air temperature. From Allen et al. (1998), Δ is given by this equation;

$$\Delta = \frac{4098e^0}{(T_a + 237.3)^2}, \quad (16)$$

$$e^0 = 611e^{\frac{17.27T_a}{T_a+237.3}}, \quad (17)$$

where e^0 is the saturation vapor pressure in Pa at the given air temperature, T_a , in °C (Allen et al., 1998). Note that the coefficients in equation 17 and equation 13 from section 2.3 are different. $c1$ is still the same in both equations, $c2$ is 17.502 in eq. 13 and 17.27 in eq. 17, and $c3$ is 240.97 in eq. 13 and 237.3 in eq. 17).

Since the best mean estimate of α is 1.26, and the value comes from estimates of saturated surfaces, this model falls short when used in arid areas with low soil moisture, where the actual value of α would be lower. Areas with a lot of wind, plenty of water in the soil and low air humidity will have a higher value of α than 1.26. Therefore, to solve this issue, α should be adjusted to make the PT model fit better for the region it is applied to. The psychrometric constant γ should also be adjusted for the location of application, to make the PT model as precise as possible. In the

study by Cristea et al. (2013), the value of α has been site-calibrated in order to improve the performance of the PT model. In the study by Cristea et al. (2013), multiple linear regressions, with mean annual relative humidity, RH , mean annual wind speed, U , and coefficients b_1 , b_2 and b_3 were used in equation 18 to determine α .

$$\alpha = b_1 + b_2RH + b_3U \quad (18)$$

From Cristea et al. (2013), the coefficients b_1 , b_2 and b_3 are 2.214, $-1.526 RH^{-1}$ and $0.079 (m/s)^{-1}$ respectively. From this study, it was found that α could vary between 1.09 and 1.68 depending on the site. Values of Δ and γ were calculated using the procedures from Allen et al. (1998), which are the same procedures as mentioned in this theory. The paper from Cristea et al. (2013) also mentions that there are many other papers that have tried to site calibrate the value of α , which have resulted in values ranging from 0.6 to 2.47. The papers are listed in Table 1 in Cristea et al. (2013). A plot of the α values obtained from equation 18 with annual mean relative humidity in the range 0.40 to 0.80 and annual mean wind speed in the range 1 to 5 m/s, is shown in figure 8.

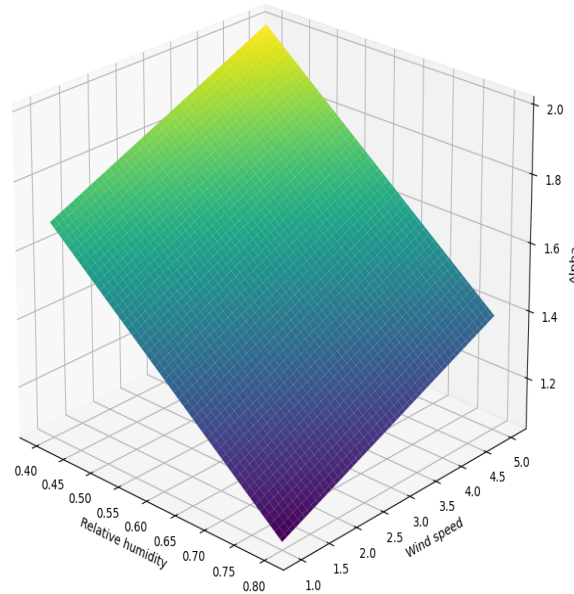


Figure 8: *The figure shows the relation between α values and relative humidity and wind speed.*

2.5.2 Estimation of Actual Evapotranspiration

Actual evapotranspiration, ET_a , is dependent on more variables than potential evapotranspiration, ET_p , and is therefore more troublesome to calculate. Not only does the energy in the system determine ET_a (which is enough to calculate ET_p), but also the available water in the system, the weather, and plant productivity. One way to calculate ET_a is to use the Penman-Monteith (PM) equation. This equation has different modifications depending on if it is supposed to calculate daily or hourly values.

One of the variations of PM is the daily-based equation that calculates ET_a directly and depends on the variables on the ground (i.e bulk surface resistance and aerodynamic resistance, eq. 4 and 5). The equation is given as;

$$ET_a = \frac{\Delta At + (\rho_a c_p D)/g_a}{\Delta + \gamma(1 + g_s/g_a)} \quad (19)$$

where Δ is the saturation-to-vapor pressure slope (eq. 16), t is the time-span in seconds (86400 s in a day), A is the energy available for evaporation which is given as; $R_n - G$, where R_n is net radiation and G is ground heat flux. ρ_a and c_p are density and heat capacity of air respectively. D is the vapor pressure deficit. g_a and g_s are aerodynamic- and bulk surface conductance respectively, which means that they are the inverse of aerodynamic resistance and bulk surface resistance (eq. 5 and 4). γ is the psychrometric constant, and is given by equation 15. This Penman-Monteith equation is gathered from Barry & Blanken (2016a).

Another approach to calculate ET_a , is to first calculate reference evapotranspiration, ET_0 . ET_0 can be calculated by the daily-based PM equation, given as;

$$ET_0 = \frac{0.408\Delta At + \gamma \frac{900}{T_a + 273} u_2 (e^0 - e_a)}{\Delta + \gamma(1 + 0.34u_2)} \quad (20)$$

where Δ is the saturation-to-vapor pressure slope (eq. 16), A is energy available for evaporation, which is defined as $R_n - G$, where from equation 1 R_n is the net radiation and G is the ground heat flux. t is the time span in seconds (for this equation it is the number of seconds in a day, $t = 86400$ s), T_a is the mean air temperature throughout the day, u_2 is the mean wind speed throughout the day measured at 2m. γ is the psychrometric constant given by equation 15. e^0 is the saturation vapor pressure at temperature T_a , given by equation 17. And e_a is the actual vapor pressure, and is given as;

$$e_a = e^0 \frac{RH}{100} \quad (21)$$

where RH is the mean relative humidity. The difference between saturation vapor pressure, e^0 , and actual vapor pressure, e_a is known as the vapor pressure deficit, D , or VPD .

One can also calculate ET_a on an hourly basis. Again, first, the reference evapotranspiration, ET_0 , has to be calculated. The hourly based PM equation to calculate ET_0 is given as;

$$ET_0 = \frac{0.408\Delta At + \gamma \frac{37}{T_a + 273} u_2 (e^0 - e_a)}{\Delta + \gamma(1 + 0.34u_2)} \quad (22)$$

where Δ is saturation-to-vapor pressure slope, and A , u_2 and T_a are now hourly mean values. t is the number of seconds in an hour ($t = 3600$ s). γ is the psychrometric constant. e^0 is the saturation vapor pressure at temperature T_a (eq. 17). And e_a is the actual vapor pressure (eq. 21).

Calculating reference evapotranspiration, ET_0 , it is multiplied with a crop coefficient, k_c , to get actual evapotranspiration ET_a . The crop coefficient, k_c is an empirical constant that can be found in tables (for example Table 12 in Allen et al. (1998)). A summary of Table 12 from Allen et al. (1998) can be viewed in table 2. Note that the values in table 2 are under the assumption that the

soil is properly irrigated so that the crop is not water stressed. The equation calculating actual evapotranspiration, ET_a , from reference evapotranspiration, ET_0 is given as;

$$ET_a = ET_0 k_c \quad (23)$$

In order to measure ET_a , advanced measuring equipment is needed, such as an eddy-covariance instrument.

Table 2: A summary of Table 12 from Allen et al. (1998). Cool season grasses are types of grass that are bluegrass, ryegrass and fescue. k_c ini is the crop coefficient at the beginning of the growth period. k_c mid is the crop coefficient in the middle of the growth period. k_c end is the crop coefficient at the end of the growth period.

Crop coefficients				
Crop type	k_c ini	k_c mid	k_c end	Maximum crop height [m]
Small vegetables	0.70	0.90-1.05	0.75-1.00	0.3-0.6
Vegs - Solanum	0.60	1.05-1.15	0.70-0.90	0.6-0.8
Vegs - Cucumber	0.40-0.60	0.85-1.00	0.60-0.90	0.3-0.4
Roots and Tubers	0.30-0.50	0.80-1.20	0.30-0.95	0.4-1.5
Legumes	0.40-0.50	1.00-1.15	0.30-1.10	0.4-1.0
Perennial Vegetables	0.40-0.60	0.85-1.15	0.30-1.10	0.2-0.8
Fibre crops	0.35	0.40-1.20	0.4-0.70	1.2-1.5
Oil crops	0.35	1.00-1.15	0.25-0.55	0.3-2.0
Cereals	0.30-1.05	1.00-1.20	0.25-1.05	1.0-4.0
Forages	0.40-0.95	0.50-1.20	0.50-1.15	0.1-1.2
Turf grass - cool season	0.90	0.95	0.95	0.10
Sugar cane	0.40	1.25	0.75	3.0
Tropical fruits and trees	0.50-1.10	0.30-1.20	0.30-1.15	0.6-8.0
Grapes and Berries	0.30	0.70-1.05	0.50-0.85	1.5-5.0
Fruit trees	0.40-1.00	0.45-1.20	0.45-1.05	2.0-10
Wetlands temperate climate	0.30-1.05	1.10-1.20	0.30-1.10	0.3-2.0
Open water <2 m depth subhumid climate tropics	-	1.05	1.05	-
Open water >5 m depth clear of turbidity temperate climate	-	0.65	1.25	-

2.6 Evapotranspirational measurements

2.6.1 Eddy covariance instrument

Eddy-covariance is a real-time sensor-based measurement of gasses. The measuring instrument consists of a three-axis sonic anemometer that measures the speed and direction of the wind, and an infrared gas analyzer that measures gas concentrations. A simplified figure of an open path EC instrument used to gain data for this study is shown in figure 9. The measurements are taken with a high frequency (10-20 Hz), and calculated into means of 30-minute intervals.

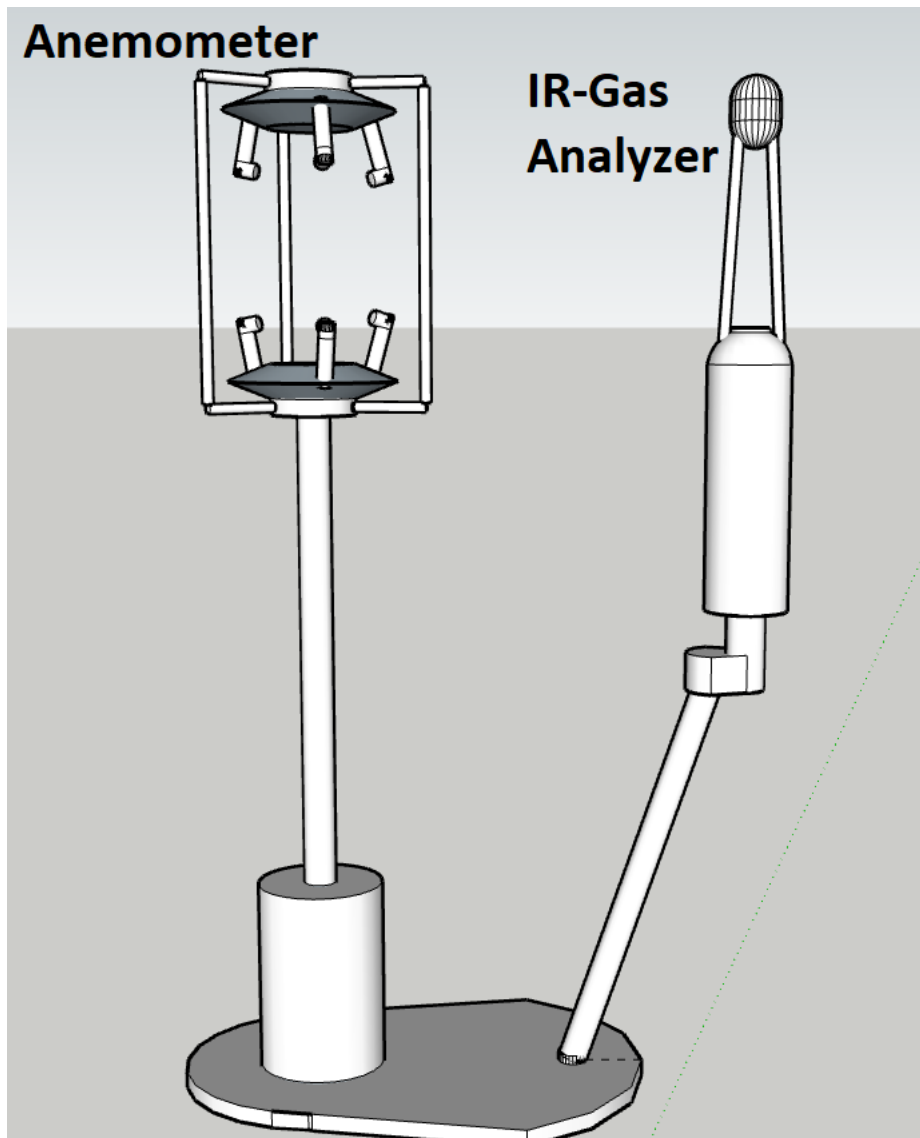


Figure 9: *Simple 3D drawing of an open-path eddy covariance instrument LICOR LI-7500S. The anemometer is located to the top left, and the infrared gas analyzer is on the top right.*

One way to understand how the measuring works, is to imagine that the gasses the EC instrument measures are within a particular space. Inside this space, there are numerous rotating eddies (currents) that transport these gasses. The vertical component of the moving gasses is the flux that is of interest. Figure 10 shows a simple descriptive figure of how the eddies pass the eddy-flux tower that measures the eddies carrying water vapor.

By having information about the wind and the concentration of water vapor, the EC instrument calculates a mean of all the measurements to come to a net value of the flux. After these calculations, it is possible to tell how much of these gasses are absorbed into or released from the soil and vegetation (Chatterjee & et.al, 2017).

The mounting height of the eddy-covariance instrument should be chosen considering the ecosystem where it is installed. From Aubinet et al. (2012), the mounting height of the EC-instrument over grassland should be $h_m > [d+4(h_c-d)]$ where h_c is the mean canopy height and should be less than or

equal to 1.75 m. d is the zero plane displacement height. Over forested or more complex ecosystems, the mounting height should be $h_m \approx d + 4(h_c - d)$. For the most accurate EC measurements of an area, the land has to be flat and consist of homogeneous vegetation. Environmental conditions need to be steady as well (Chatterjee & et.al, 2017). As mentioned in the previous section, the EC instrument is used to measure actual evapotranspiration ET_a . In order to measure potential evapotranspiration ET_p , an evaporation pan can be used.

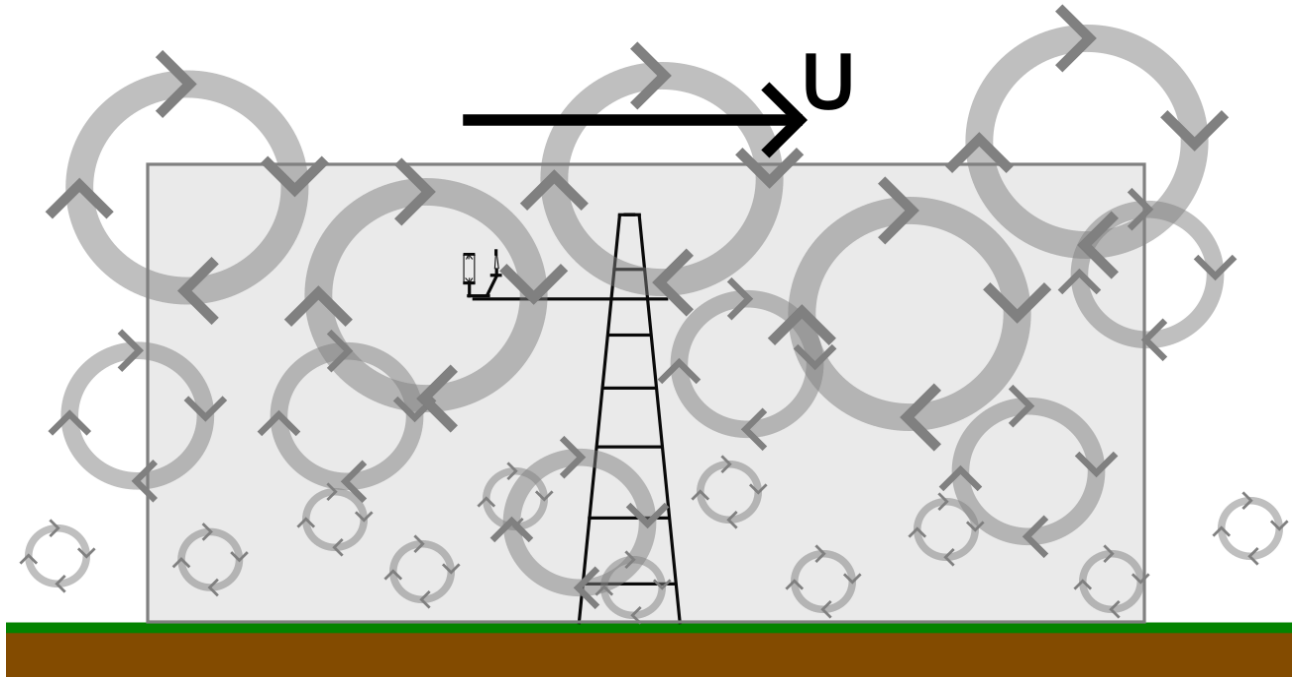


Figure 10: A flux-tower measuring the eddies carrying water vapor molecules.

2.6.2 Pan evaporation measurement

An evaporation pan is an instrument that measures evaporation, ET_{pan} . This way of measuring evaporation and estimating evapotranspiration has been important for farmers, water and irrigation managers, and water resource project planning as it gives an idea about the water budget in the local area and an indication of crop water usage (Smajstrla et al., 2000). Today, the data gathered from long time series of pan evaporation plays an important role in the study of climate change, and data can also be compared with modern EC instruments to find out how well this type of measurement performs (which will be done in this thesis).

There are different kinds of evaporation pans used throughout the world, and there are ways to convert measurements between these pans. The different pans have different ways of installation, and there are about 50 different equations to estimate reference evapotranspiration, ET_0 , depending on different assumptions and different meteorological data requirements (Grismer et al., 2002). One of the many pan standards is the Class A evaporation pan used in the USA, set by the National Weather Service. The Class A pan is a cylindrical tub made of galvanized steel with a diameter of 120.7 cm and depth of 25 cm, which rests on a level wooden base, and is enclosed by chains to avoid animals drinking from the pan (Farnsworth et al., 1982; Smajstrla et al., 2000).

The general equation for the reference evapotranspiration, ET_0 , from pan evaporation, ET_{pan} , is given as;

$$ET_0 = k_p E_{pan}, \quad (24)$$

where k_p is the pan coefficient and E_{pan} is the amount of evaporation from the pan. The pan coefficient k_p is a correction factor and depends on the meteorological and spatial conditions surrounding the evaporation pan. Several equations have been made in order to estimate a value for the pan coefficient, where many of them depend on daily mean relative humidity, daily mean wind speed and fetch distance (Grismer et al., 2002). One of these equations for the Class A pan coefficient that only depends on relative humidity, RH , as shown in equation 25 (Eagleman, 1967). For the Class A pan, the pan coefficient varies between 0.35 and 0.85.

$$k_p = 0.56 + 0.00275RH \quad (25)$$

After calculating the reference evapotranspiration, ET_0 , the actual evapotranspiration, ET_a can be calculated by equation 23. The crop coefficient in equation 23 is a coefficient that depends on the type of vegetation, and how far into the growing season the crop is.

2.6.3 Remote sensing

Remote sensing is a way to acquire data from areas and objects by measuring reflected and emitted radiation using sensors (from radars, airplanes or satellites). The sensors detect and record emitted energy from the surface, either passively (measuring reflected energy from the Sun on Earth's surface) or actively (measuring reflected energy from the satellite on the Earth's surface). There are three common classes of satellite orbits; low-Earth orbit which is from 160 to 2,000 km above Earth's surface, medium-Earth orbit which is from 2,000 to 35,500 km above Earth, and high-Earth orbit which is above 35,500 km above Earth's surface. The most commonly used orbit for remote sensing is the low-Earth orbit with a polar-orbiting path (satellite orbits the Earth from pole to pole) while the Earth rotates. This allows satellites to gain data for the entire globe rapidly (NASA, n.d.).

Resolution from satellites determines the quality of the data gathered from the sensors, and varies depending on the orbit and the type of sensor. The four types of resolutions are; radiometric, spatial, spectral and temporal. *Radiometric resolution* is the bit resolution, which indicates how many potential digital values a pixel can have. The higher the radiometric resolution, the easier it is to distinguish slight differences in energy. *Spatial resolution* is the surface area each pixel covers. The finer the spatial resolution (pixel covers the lowest possible amount of surface area), the higher the detail of an image. *Spectral resolution* is the number of wavelength bands a sensor can discern. A normal photo camera has 3 spectral bands that capture the wavelengths of visible light (red, green and blue). Sensors on satellites can be multispectral with up to 10 wavelength bands, or even hyperspectral with hundreds to thousands of wavelength bands including the infrared, ultraviolet or even x-ray range. The more and narrower bands, the finer the spectral resolution. *Temporal resolution* depends on a satellite's orbit and its swath width. The resolution is the time it takes for a satellite to revisit an observational area. The temporal resolution of polar satellites can vary from 1 to 116 days. Temporal and spatial resolution are often inverse of each other due to the fact that to acquire a high spatial resolution, the swath width has to be narrow, meaning that the temporal resolution will have to be low, and vice versa (NASA, n.d.).

Two satellites launched by NASA for remote sensing are Terra Satellite Platform, which launched in 1999, and Aqua, which launched in 2002. Both satellites use a Moderate Resolution Imaging Spectroradiometer (MODIS) sensor. The satellites are part of a project to remote sense photosynthesis and evapotranspiration for all biomes in a 15-year period. The University of Montana was tasked with developing software and algorithms for the MODIS-based satellites (UMT, n.d.-a). The algorithm for remote sensing evapotranspiration is MOD16. It has a spatial resolution of 1 km² and a temporal resolution of 8 days (dataset in 8-day intervals). Evapotranspiration from the MOD16 algorithm is based on the Penman-Monteith equation, and it needs inputs from the satellite’s measurements and meteorological measurements from the ground to calculate this. A flowchart of the algorithm is shown in figure 11. The dataset for evapotranspiration calculated by the MOD16 algorithm has to be multiplied by 0.1 to get the real ET values (UMT, n.d.-b), and the ET values are summations of the 8-day interval (W.R et al., 2021).

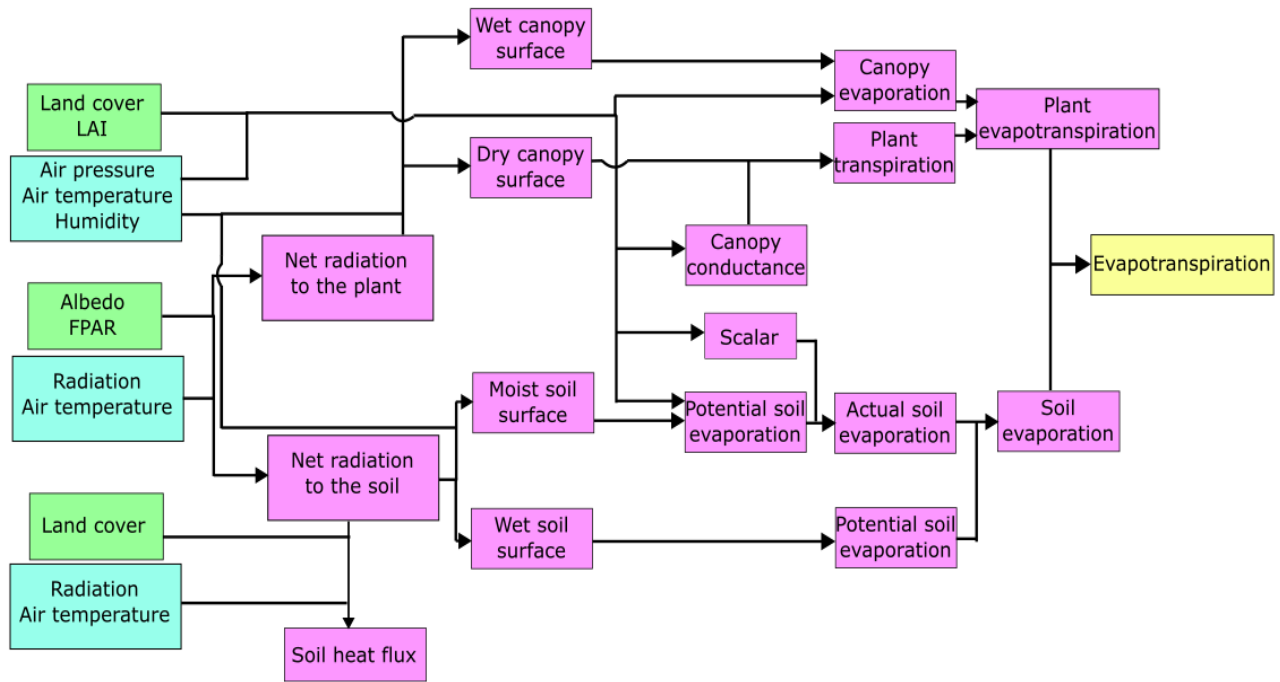


Figure 11: Flowchart of the MOD16 algorithm to calculate actual ET. The green boxes are remote sensing inputs with 8 day intervals. The blue boxes are meteorological inputs with daily intervals. The purple boxes are intermediate algorithm calculations, which are done on daily basis. The yellow box is the final algorithm output in 8 day resolution. FPAR stands for Fraction of Absorbed Photosynthetically Active Radiation. Figure is inspired from W.R et al. (2021).

3 Methods and Materials

The dataset provided for the analysis and evaluation of the Penman-Monteith and Priestley-Taylor model, consists of several measurements from different meteorological instruments obtained from Søråsjordet. Søråsjordet is an agricultural site of about 500 acres (the meteorological site disposes 12 acres) in Ås, Viken county, Norway. Its coordinates are N59°39'37" E10°46'54" and it is located 93.9m above sea level. The vegetation is relatively homogeneous and consists mostly of short grass, and the field is relatively plane (slope of 1% towards southwest) (NMBU, 2009). The data used in the evaluation spans from the 29th of June 2021 to the 27th of September 2021 and the 16th of June 2022 to the 25th of August 2021. These time periods were chosen because of missing ET measurements in the beginning of June for both years, and at the end of August in 2022. There were also some NaN values in these timelines that had to be removed, and there were dates with precipitation that had to be handled.

The eddy covariance instrument used for ET measurements at Søråsjordet is an open-path infrared gas analyzer (LICOR LI-7500DS). The EC instrument was mounted at a height of 6m (see figure 12). Since the EC instrument is an open-path gas analyzer kind, it means that air is not sucked into a sampling chamber, but is directly sampled, making measurements during precipitation invalid, since droplets will obstruct the measurement path.

3.1 Meteorology during measuring period

The year 2021 was warmer and drier than the normal. For the whole country, the mean temperature was 1.1 °C above the normal, and the precipitation was 15 % less than the normal (Grinde et al., 2021). 2022 was also warmer than normal, with a mean temperature for the whole country of 0.7 °C above the normal. Even though the precipitation for the country as a whole was 15 % above the normal, the eastern part of the country had a summer that was classified as "very dry" or "extremely dry" (Mamen et al., 2022).

Measurements from Søråsfeltet station indicate that the temperature during summer 2021 in Ås was higher than normal. The driest month in 2021 was August, with a total accumulated precipitation of 3.6 mm. This is 3.74 % of the normal value of 96.3 mm. July had a total accumulated precipitation of 90.3 mm, 8.2 mm more than the normal value. June had 58.4 % less precipitation than the normal of 76.9 mm (Wolff & Grimenes, 2022). In the summer of 2022, the mean temperature of July was 16.6 °C, which is 0.2 °C lower than the normal, while the mean temperature of June and August were 1.3 °C and 0.8 °C higher than the normal respectively. June was drier than normal, with 5.5 mm less accumulated precipitation than normal. July had a total accumulated precipitation of 93.6 mm, 11.5 mm more than normal. August 2022 had only 1/3 of its normal precipitation (Wolff, 2023). The mean temperature and precipitation of summers 2021 and 2022 with the monthly normal are summarized in table 3.

Table 3: *Monthly mean temperatures and total accumulated precipitation.*

	2021			2022			Normal		
	June	July	August	June	July	August	June	July	August
Temperature[°C]	16.2	18.9	15.5	15.8	16.6	16.5	14.5	16.8	15.7
Precipitation[mm]	32.0	90.3	3.6	71.4	93.6	24.6	76.9	82.1	96.3



Figure 12: A picture of the eddy-covariance instrument (marked with the red ring) mounted on the eddy-flux tower.

3.2 Meteorological parameters correlation

Looking at the Priestley-Taylor and Penman-Monteith equations (eq. 14, 19, 20 and 22) it is possible to see what kind of meteorological parameters they depend on. Before working on these equations, a quick investigation of the parameters and their correlation to evapotranspiration was done. Scatter plots of net radiation R_n , wind speed U , relative humidity RH and ground heat flux G compared to ET were made to show how the parameters correlate to ET. Spearman's rank correlation coefficient with the p-value was calculated for each parameter. From the Priestley-Taylor equation (eq. 14), one can see that there should be a linear correlation between R_n and ET, so a linear regression was also done for this parameter.

3.3 Creating and evaluating Priestley-Taylor models

The analysis of the dataset and the evaluation of the ET models were performed with the programming tool Python 3.8. Some datasets were in intervals of 10 minutes, and some were in intervals of 30 minutes. To make a consistent dataframe from these datasets, the 10-minute datasets had

to be turned into 30-minute datasets. Depending on the parameter, the values were either turned into mean values or summation of three 10-minute data points. For example; air temperature and wind speed were turned into mean values, while precipitation was summed. None valid values in the datasets were marked with the value "-9999" beforehand, which is the logger's way of marking an invalid measurement. These values were replaced with NaN values. Ultimately, all datasets were saved into one dataframe, and the time resolution was changed to one-hour.

A dataframe with a daily resolution was also generated to analyze how the Priestley-Taylor model would react to daily values. Mean daily and daily summed values were generated accordingly, depending on the parameter.

As stated in the theory, the value of α should be adjusted to get good models for the spatiotemporal application. Four different PT models were created, and compared. One model based on Priestley & Taylor (1972), where α is (as mentioned in section 2.3.1) the mean estimated value of 1.26. This model will be named "PT1".

A second model based on the approach from Cristea et al. (2013), where α is calculated based on local variables as mean relative humidity and mean wind speed, and calculated with equation 18. This model will be named "PT2". Since both of these approaches (PT1 and PT2) have no set value of γ , the value of γ was calculated with equation 15.

The third PT model calculated α and γ using Python's "scipy.optimize curve_fit" function. The curve_fit function takes in the model function, the independent variables (in this case, irradiation and air temperature), and the y-data (measured ET-values). The function returns the best-fit parameters (α and γ) by the least-squares method. Different values of α and γ were calculated for each month and whether there was daylight. This model will be named "PT3".

In the fourth PT model, curve fitting was used for α only, while γ was calculated using equation 15. Again, different values of α were created depending on the month and daylight. This model will be named "PT4".

For both curve-fitting models (PT3 and PT4), irradiation, temperature and ET values were used as data for the two months of the consecutive years. This means that data for both June 2021 and June 2022 were used together to calculate α and γ values for June. The same goes for July and August. This approach was chosen to make the values of α and γ as general as possible by using as large datasets as possible. To make the models as precise as possible, extreme ET values above 1 mm/h and below -0.2 mm/h, and data that coincide when precipitation above 1 mm were removed from the y-data during the curve-fitting. The removal of data at the same time as when there is precipitation is because of the limitation of the EC instrument.

A fifth PT model based on daily values was created in the same manner as PT4. Curve fitting was used to calculate values for α depending on the month, and data for both 2021 and 2022 was used. The difference is that extreme values and times with precipitation were not removed, since daily values would not be as affected by these incidents. The model made from this approach will be named "PT5".

After creating the five models, they were each compared with the ET measurements, visually with plots, mathematically by calculating the mean difference between model and measurements, and statistically through root-mean-squared error. All comparisons were made with data with no precipitation, except for PT5.

3.4 Creating and evaluating Penman-Monteith models

The datasets used for the Penman-Monteith modeling are the same as the ones used to create and evaluate the Priestley-Taylor models. The cleanup of these datasets is done in the same manner as for the datasets used in the PT modeling. Values in 10-minute temporal resolution were turned into 30-minute resolution, and invalid values were turned into NaN values. All datasets were then saved as one dataframe. The time resolution of the dataframe was then changed to one-hour resolution.

To calculate actual evapotranspiration and reference evapotranspiration with the daily PM equations (eq. 19 and 20), the hourly dataframe was transformed into a dataframe with a daily resolution. For the reference evapotranspiration, the crop coefficient was chosen as $k_c = 0.9$, based on table 2. This value is for cool-season turf grass, which is a type of grass that grows at higher latitudes, such as bluegrass, ryegrass and fescue. Estimated actual evapotranspiration from using equation 19 and equation 20 with $k_c = 0.9$ was plotted with EC measurements. The results were also compared to EC measurements by calculating the mean difference and RMSE. Data for both 2021 and 2022 were used in the comparison. The PM models from these approaches are named "PMdaily1" for equation 19 and "PMdaily2" for equation 20 with $k_c = 0.9$.

The PM model based on equation 22, was calculated using the hourly dataframe, and with two different crop coefficients. One as $k_c = 0.9$, which is for cool season turf grass according to table 2. Another PM model used a crop coefficient calculated using the built-in function in Python "scipy.optimize curve_fit", to find a more fitting crop coefficient. To get a reasonable estimate of a crop coefficient value, times with precipitation were removed from the dataframe used in the curve-fitting to calculate the crop coefficient. Data for both 2021 and 2022 was used in the calculation. The results for both approaches were then plotted, and mean difference and RMSE values between model values and EC measurements were calculated. The mean difference and RMSE are calculated for the data without precipitation, to avoid errors that might occur due to the limitation of the EC instrument. The PM model from the approach with a crop coefficient of 0.9 is named "PMhourly1" and the PM model from the approach of calculating a crop coefficient using curve fitting is named "PMhourly2".

3.5 MODIS data

As the theory mentions, the MODIS algorithm calculates actual evapotranspiration using the Penman-Monteith equation. It needs inputs from the satellite's measurements and meteorological measurements from the ground to calculate this. The ground measurements needed are air pressure, air temperature, air humidity, and radiation. From the sensors on the satellite, the inputs are the type of land cover, leaf area index and albedo.

For the evaluation of the remote sensing from MODIS, actual evapotranspiration data from MODIS is compared to evapotranspiration measurements from the EC instrument. The EC data was summed into 8-day accumulated values, because the data from MODIS has a 8-day temporal resolution (W.R et al., 2021).

While looking into the datasets it was noticed that the timelines between the MODIS data and EC data were offset. Before calculating the differences between MODIS data and EC data, the measurements from EC were offset with -3 days for the 2021 data and +2 days for the 2022 data, so that the values from MODIS and the EC instrument would be on the same dates. Dates not

common between MODIS and EC were removed before calculating the differences.

3.6 Pan evaporation measurements from Søråsjordet

The evaporation pan used at Søråsjordet is a pan that has been developed and built at the Norwegian University of Life Sciences. The evaporation pan does the measurements automatically. Evaporation is measured in mm with an uncertainty of ± 0.1 mm. The evaporation is measured with a floater that measures the height of the water in the pan, and the pan is buried into the ground. Automatic corrections are made in case of precipitation by subtracting the measured precipitation from the measured water level in the pan. If there is little water left in the pan, the pan is refilled. The time index of the measurements are in Norwegian normal time, or Central European Time (CET). Figure 13 shows a drawn figure of the pan. Measurements are not done between November and March due to the possibility of the water freezing (NMBU, 2014).

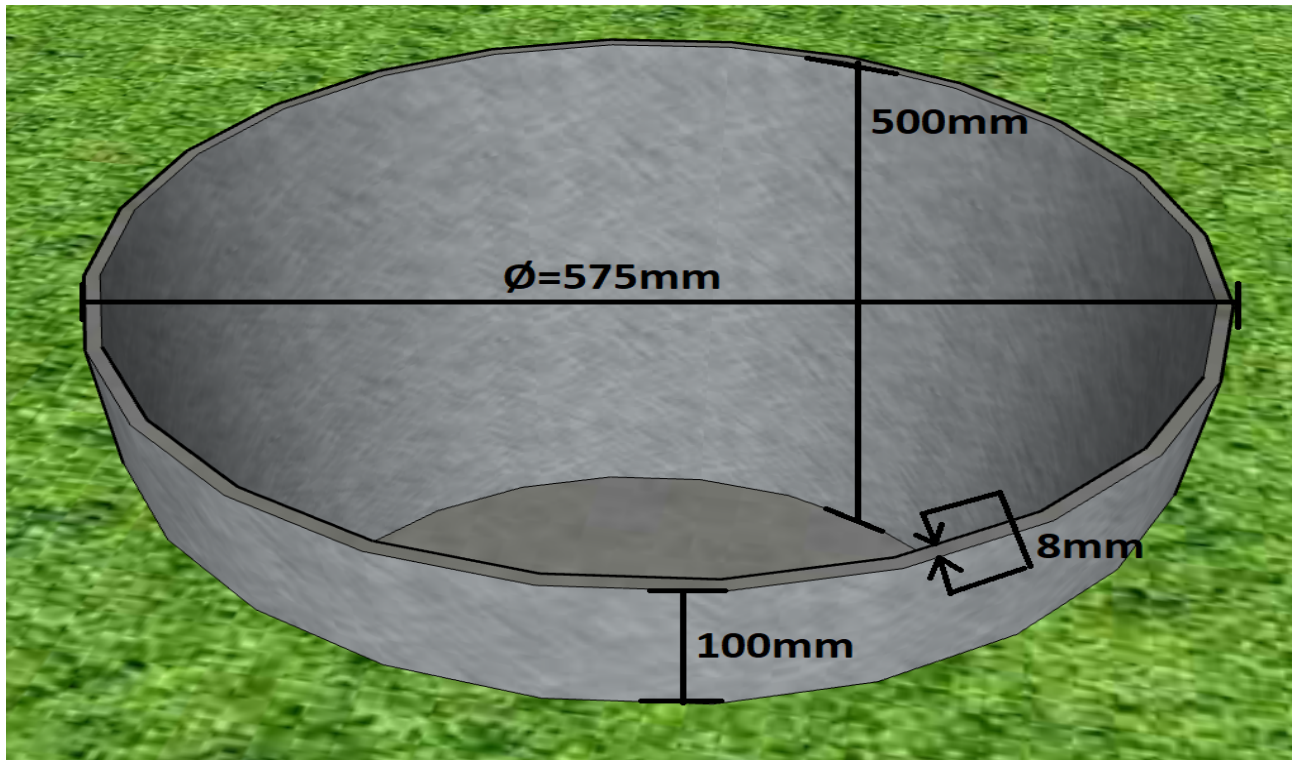


Figure 13: A simplified 3D figure of the evaporation pan used at Søråsfeltet.

The pan evaporation measurements, ET_{pan} , was first compared with the eddy-covariance measurements, ET_a , visually to see how much they coincide with each other. Hourly and daily values of ET_{pan} were compared to ET_a values from the EC instrument. Periods with missing data from the EC instrument were removed (ref. section 3.3), and coinciding pan measurements were also removed. Extreme outliers in the pan measurements were also removed. The dates of these measurements are mentioned in section 4.1.2 and discussed in section 5.1.2. Since the pan measurements were in CET, and the measurements from the EC instrument were in Central European Summer Time (CEST), the time index of the pan measurements were shifted with -1 hour.

Reference evapotranspiration, ET_0 , was calculated from the pan measurements, ET_{pan} , by equation 24 . The pan coefficient was calculated with equation 25 using hourly relative humidity values.

The reference evapotranspiration, ET_0 was compared to EC measurements, ET_a (both hourly and daily). After that, estimates of actual evapotranspiration were calculated using equation 23. The first estimates of actual evapotranspiration, ET_{a1} , were calculated using a crop coefficient, k_c , of 0.9 (which is for cool season turf grass, ref. table 2). The second estimates of actual evapotranspiration, ET_{a2} were calculated using the crop coefficient found from the curve-fitting approach for the Penman-Monteith model PMhourly2 (ref. section 3.4). The idea behind using the crop coefficient from the PMhourly2 model, was to see if the estimates of ET_{a2} would be more accurate than the estimates of ET_{a1} . RMSE values were calculated when comparing ET_a from the EC instrument with ET_{pan} , ET_0 , ET_{a1} and ET_{a2} .

4 Results

4.1 Presenting the data

As there are six plots for each parameter (one for each summer month of 2021 and 2022), the plots for this sub-section have to be looked up in Appendix A.

4.1.1 Evapotranspiration

When looking into the figures 39 to 44, there are some distinguishing features. First of all, the daily oscillation is very much apparent. It is possible to see that ET is going on during the daytime, and little to no ET during nighttime. It is possible to see that most ET values are between 0 mm/h and 0.4 mm/h.

The summer of 2021 had 4 days where the ET was above 0.4 mm/h, while the summer of 2022 had 22 days where the ET was above 4 mm/h. In 2021 the ET increased slightly from June into about the 5th of July, and then it slowly decreased again from about the 17th of July throughout August. For 2022 it looks more as if the ET is more stable with peaks at about 0.4 mm/h through June and July, except for the extremes on the 13th of July and 25th of July. August 2022 has a lower ET, with peak values between 0.2 and 0.3 mm/h.

There are extreme dips in ET in 2021. These happen between the 10th and 11th of July, the night between the 14th and 15th of July, and the night between the 10th and 11th of August. Extreme dips in ET during 2022 occurred between the 27th and 28th of June, between the 31st of July and the 1st of August, the night between the 2nd and 3rd of August, and the 11th of August.

4.1.2 Pan evaporation

As with the ET data, the pan evaporation has a daily oscillation, which can be seen in figures 45 to 50. One can observe spikes in evaporation happening during daytime, and less evaporation during nighttime. Most spikes are in the range between 0.25 and 0.5 mm/h.

The summer of 2021 had about 18 days where the measured evaporation was above 0.5 mm/h, while the summer of 2022 had about 20 days where the measured evaporation was above 0.5 mm/h. Extremes with measured evaporation above 1 mm/h happened on the 21st and 31st of July 2021, the 16th and 17th of August 2021, the 18th, 29th and 30th of July 2022, and the 22nd and 26th of August 2022.

Low daytime peak values (below 0.2 mm/h) occurred on the 10th of July 2021, 26th of June 2022, 21st of July 2022, and 18th of August 2022.

4.1.3 Accumulated ET, Evaporation and Precipitation

The plots of accumulated evapotranspiration and precipitation have different beginnings of measurement and ends of measurement, the only month that can be compared between 2021 and 2022 is July. From the plots in figure 14 and 15, one can see that the accumulated evapotranspiration in July 2021 was about 70 mm and about 90 mm in July 2022. The accumulated precipitation was about 90 mm for both July 2021 and July 2022. The accumulated evaporation in July 2021 was about 130 mm and about 120 mm in July 2022.

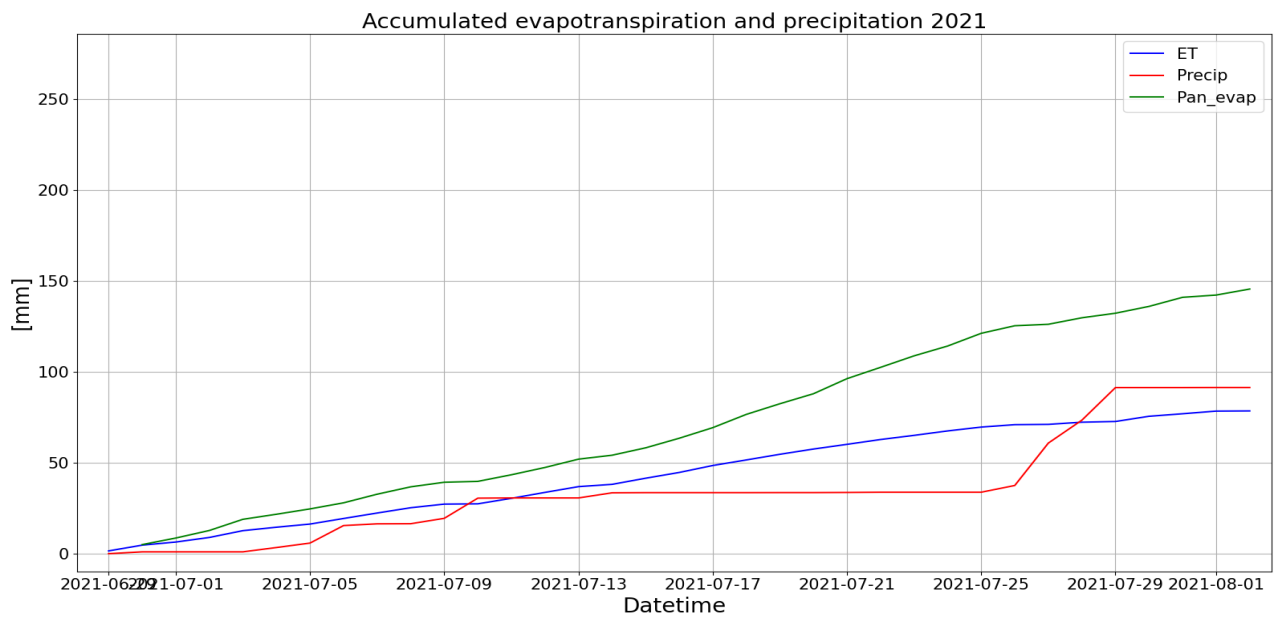


Figure 14: *Daily accumulated evapotranspiration (blue), precipitation (red) and pan evaporation (green) during summer 2021.*

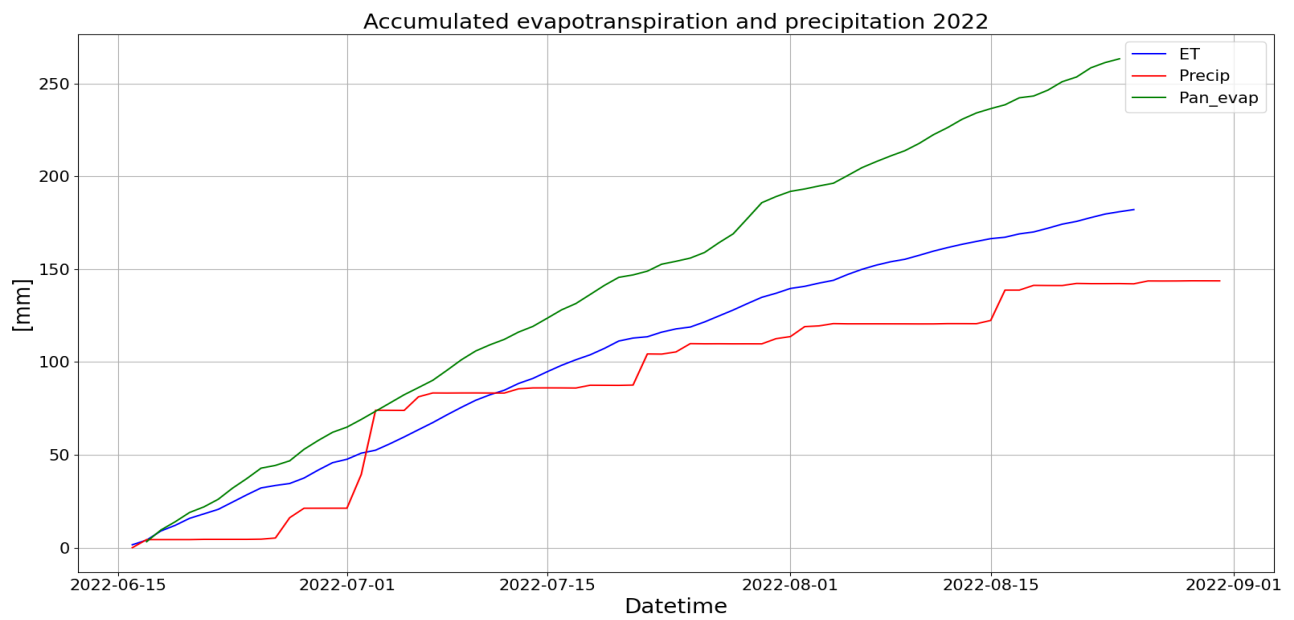


Figure 15: *Daily accumulated evapotranspiration (blue), precipitation (red) and pan evaporation (green) during summer 2022.*

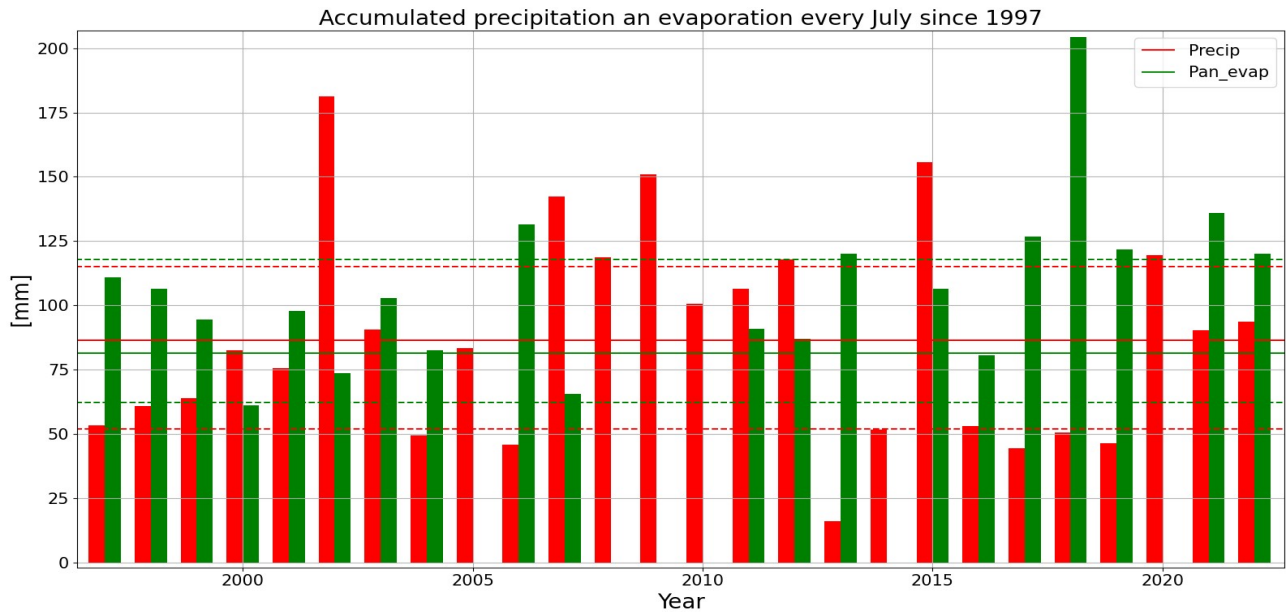


Figure 16: *Every July's accumulated precipitation (red) and pan evaporation (green) between 1997 and 2021. Mean precipitation (red line) and mean pan evaporation (green line). 75 and 25 percentiles as dashed lines.*

The plot in figure 16 shows the accumulated precipitation and evaporation for each month of July since 1997. The straight horizontal lines are mean values and the dashed lines are 25 and 75 percentiles. One can see that there are some missing data, since the evaporation values for 2005, 2008, 2009 and 2010 are zero. The mean evaporation line in the plot is excluding these zero values. Excluding the zero evaporation values, the evaporation values do not vary that much, as the 25 percentile is at about 85 mm and the 75 percentile is at 120 mm. There is one extreme deviation in 2018, where the evaporation was just above 200 mm. Thus, the measured values in July 2021 and 2022 are within the higher range of normal evaporation. The accumulated precipitation has a lot of variation for each July, except for 2016, 2017, 2018 and 2019. The accumulated precipitation for each year has a 75 percentile at about 115 mm and a 25 percentile at about 50 mm. The accumulated precipitation from July 2021 and 2022 is about at the mean for the accumulated precipitation in each July since 1997.

4.1.4 Net radiation

Looking into the figures from figure 51 to figure 56, as with the ET, the daily oscillations are very apparent. It is visible that there is positive net radiation during daytime, and slight negative net radiation during nighttime. It is possible to see that for both 2021 and 2022, most net radiation peaks are in the range between 400 and 500 W/m². There are some days where the peak values are below 300 W/m², which might indicate days with overcast.

Some extreme low values occurred on the 10th of July 2021, 27th of July 2021, 29th of July 2021, 22nd of July 2022, and 25th of July 2022.

4.1.5 Ground heat flux

Exploring the plots from figure 57 to figure 62, there is a daily oscillation as with ET and net radiation. As with net radiation, the values of ground heat flux are positive during the daytime and negative during the nighttime. Taking the theory from section 2.1 into account, it is a logical trend, as the soil will consume and store thermal energy during daytime, and release stored thermal energy during nighttime.

Most of the peak values of ground heat flux appear to be between 30 to 60 W/m², while most of the negative dips are at about -20 W/m². This is true for both summers of 2021 and 2022.

Some low peaks occur on the 10th of July 2021, 27th of July 2021, 29th of July 2021, 1st of August 2021, 27th of August 2021, 22nd of July 2022, and 25th of July 2022. These dates are the same as the ones mentioned in the previous section, when low peaks of net radiation were mentioned.

4.1.6 Air temperature

The plotted air temperature data from figure 63 to figure 68 show daily oscillation, with high temperature during daytime and low temperature during nighttime. From the plot in figure 64 of July 2021, one can see that the month was very warm, with 24 days where the measured temperature was above 20 °C. Compared to July 2022, one can see in the plot in figure 67 that it had 17 days with a measured temperature above 20 °C. Of the warm days in July 2021, 9 days had measured temperatures above 25 °C, while July 2022 had only one day with a measured air temperature above 25°C. All days in the summer of 2021 and 2022 have temperatures above 15 °C during daytime.

4.1.7 Air pressure

In contrast to the previous parameters that have been looked into, air pressure does not oscillate on a daily basis. This can be viewed in the plots in figures from figure 69 to figure 74. Most of the measured air pressures are between 99.5 kPa and 101 kPa. Very low air pressure (below 99 kPa) occurred between the 29th of July 2021 and the 2nd of August 2021, between the 18th and 19th of August 2021, and between the 25th and 26th of July 2022. Something noticeable for all plots is that almost all measured air pressures are below the average sea-level atmospheric pressure, which is approximately 101.3 kPa.

4.1.8 Vapor pressure deficit

Looking at the plots from figure 75 to figure 80, there is a noticeable daily oscillation, with peaks during daytime and dips during nighttime. Right of the bat, one can see measuring errors between the 27th and 28th of June 2022 and between the 2nd and 3rd of August 2022, where the vapor pressure deficit drops below 0 kPa. Most of the peaks of measured vapor pressure deficit occur in the range between 1 and 2 kPa. Some noticeable high values (above 2 kPa) occurred on the 3rd, 14th and 25th of July 2021, and on the 12th and 14th of August 2022.

4.1.9 Relative humidity

The relative humidity plots from figure 81 to figure 86 show an daily oscillation. However, compared to all the other parameters that had daily oscillations with peaks during daytime and dips during

nighttime, the relative humidity is the inverse of that, with peaks during nighttime and dips during daytime (most of the time). Noticeable features are the two long-lasting values of 100 % relative humidity during the 27th and 28th of June 2022, and between the 2nd and 3rd of August 2022. From the previous section, these dates are also the dates with measuring errors of vapor pressure deficit. Low values (below 30 %) of relative humidity occurred on the 18th and 20th of June 2022, the 23rd of July 2022, and the 8th, 9th, 11th and 23rd of August 2022.

4.1.10 Precipitation

Looking at the accumulated precipitation plots from figure 87 to figure 92, one can see that the total accumulated precipitation for July 2021 and July 2022 was about 90 mm. It is also visible that August 2021 was very dry with only about 3.6 mm of precipitation. July 2021 had a dry period between the 15th and 26th. August 2022 had a dry period between the 5th and 16th.

4.1.11 Daylight

Looking at the daylight plots from figure 93 to figure 98, one can see that the amount of daylight is longer than the number of hours without daylight. This should not be a surprise since the measurements are during the summer in the northern hemisphere. A (slightly) noticeable feature on the plots of July 2021 and 2022 is that the number of hours without daylight is more extended by the end of the month, than at the beginning of the month. This should be expected as the amount of daylight should decrease after the 21st of June.

4.2 Evaluation of parameter correlation

The scatterplot in figure 17 shows a linear correlation between net radiation, R_n , and evapotranspiration, ET . The result from the linear regression shows a strong linear correlation between net radiation and evapotranspiration as the R^2 value is 0.710. The regression line between ET and R_n has the equation; $ET = 0.0359 + 0.0007R_n$. The Spearman's rank correlation coefficient is 0.866 with a p-value of 0.0. The scatterplot in figure 18 shows the correlation between wind speed, U , and evapotranspiration, ET . A noticeable feature from the plot is that for wind speeds below 4 m/s, there is a tighter gathering of ET values around zero. The Spearman's correlation coefficient is 0.527 with a p-value of 0.0. The scatterplot in figure 19 shows the correlation between relative humidity, RH , and evapotranspiration, ET . From the plot, it is visible that there is a lot of scattering for values of RH below 75 %. One can also see some linearity on the top part of the scatterplot, and that ET decreases with increasing RH . The Spearman's rank correlation coefficient is -0.575 with a p-value of 0.0. The scatterplot in figure 20 shows the correlation between ground heat flux, G , and evapotranspiration, ET . One can see in the plot that there is a tight gathering of ET values around zero for G values below 20 W/m². There is a lot of scattering in the plot, but a noticeable increase in the ET values as the G values increase. The Spearman's rank correlation coefficient is 0.751 with a p-value of 0.0. Table 4 lists the Spearman's rank correlation coefficients.

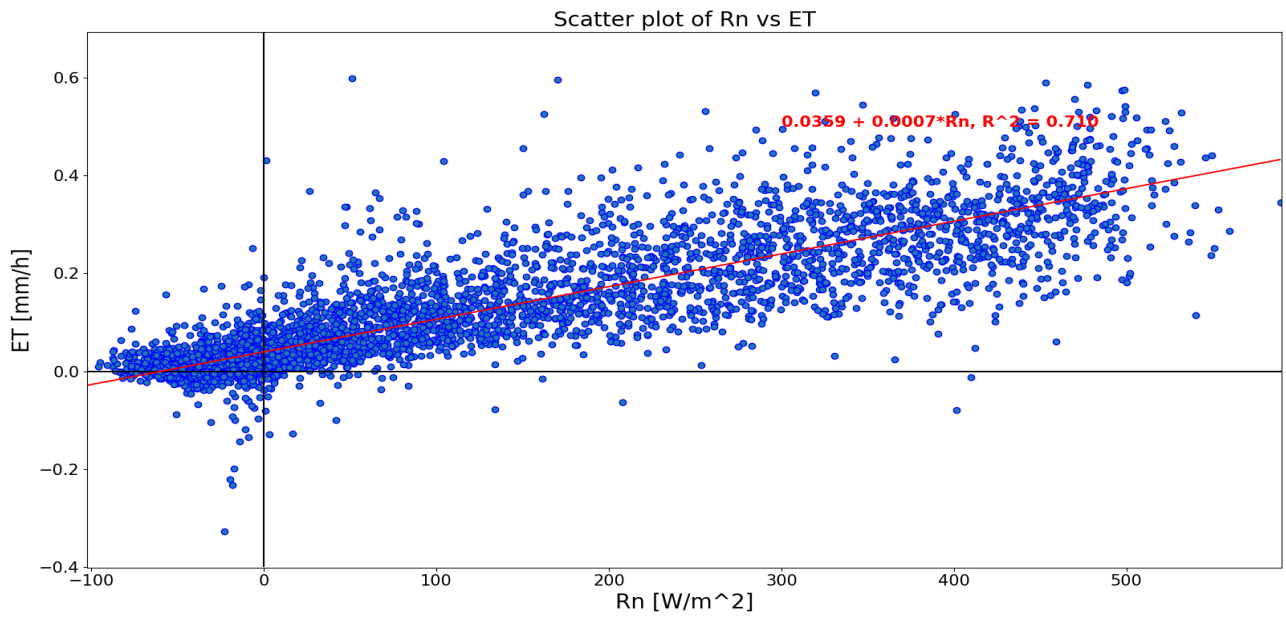


Figure 17: Scatter plot of net radiation R_n vs evapotranspiration with the regression line in red.

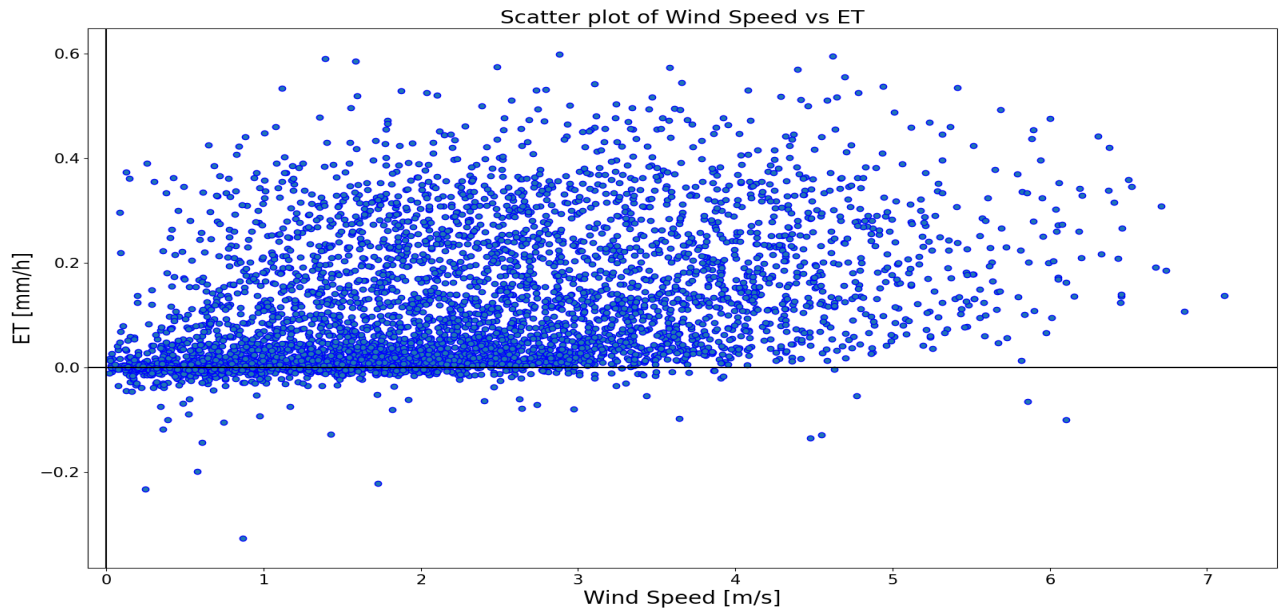


Figure 18: Scatter plot of wind speed vs evapotranspiration.

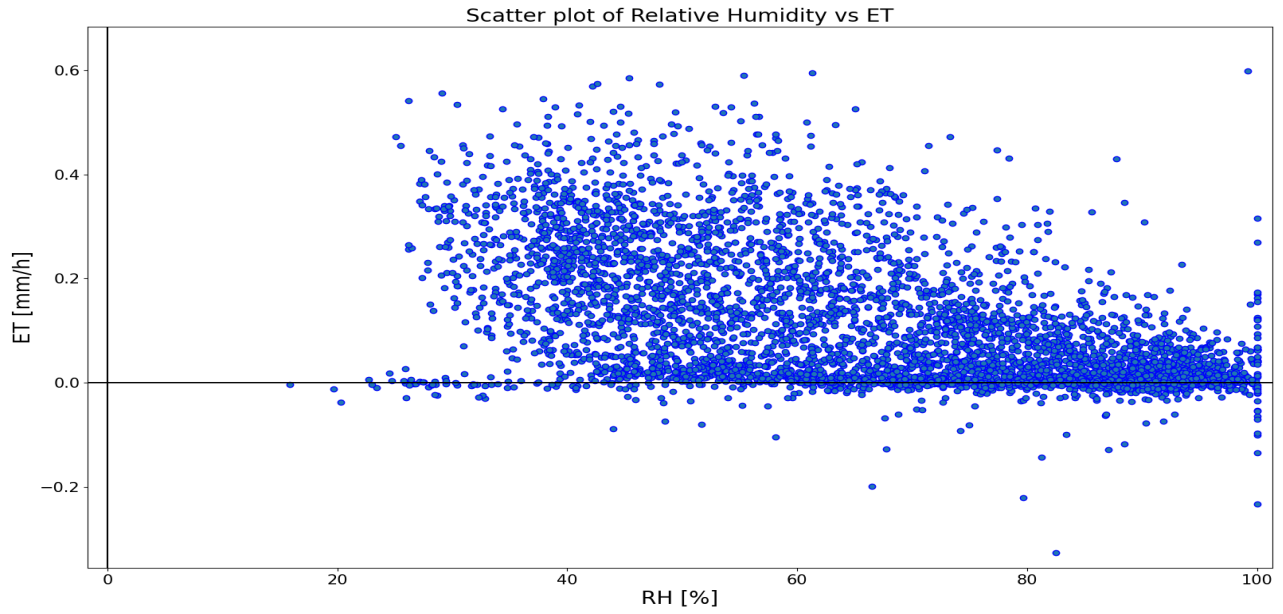


Figure 19: *Scatter plot of relative humidity vs evapotranspiration.*

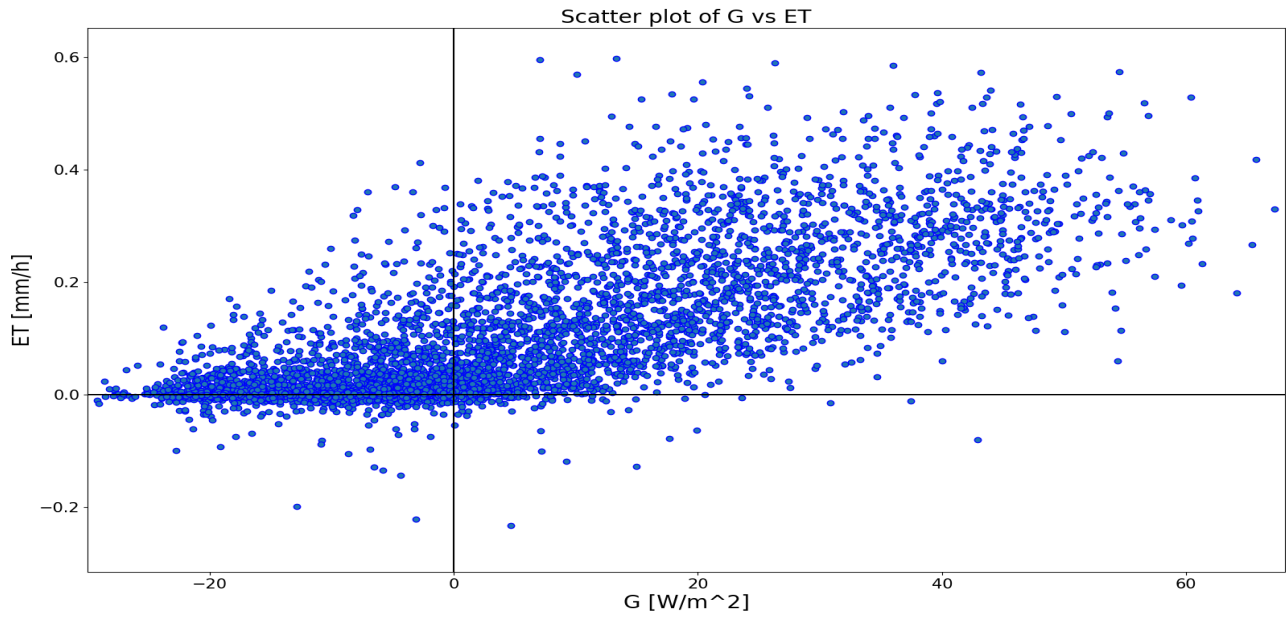


Figure 20: *Scatter plot of ground heat flux, G , vs evapotranspiration.*

Table 4: *Spearman's rank correlation coefficient values of different meteorological parameters compared to evapotranspiration, ET . R_n is net radiation, U is wind speed, RH is relative humidity, and G is ground heat flux.*

Spearman's rank correlation coefficients				
Parameter	R_n	U	RH	G
Coeff	0.866	0.527	-0.575	0.751

4.3 Evaluation of Priestley-Taylor

The five PT models mentioned in section 3.3 were compared with EC measurements of actual evapotranspiration, ET_a . To visually show how the PT models perform they were plotted. Since there are six plots for each model (one for each summer month in 2021 and 2022), the full plots can be viewed in Appendix B1, while small sections of the plots will be shown here.

The PT-model with literature value $\alpha = 1.26$ is shown in figure 21 and in Appendix B1 from figure 99 to figure 104. The PT-model using the approach from Cristea et al. (2013) to calculate α is shown in figure 22 and in Appendix B1 from figure 105 to figure 110. The PT model using curve-fitting to calculate values for α and γ is shown in figure 24 and in Appendix B1 from figure 111 to figure 116. And the PT model using curve-fitting to calculate values for only α is shown in figure 25 and Appendix B1 from figure 117 to figure 122. The last PT model, which is based on daily values and uses curve-fitting to calculate only α is shown in figure 27. The four previous PT models are also shown with daily values in figure 27, so all models can be visually compared. The α and γ values for each model are displayed in tables 5 and 6.

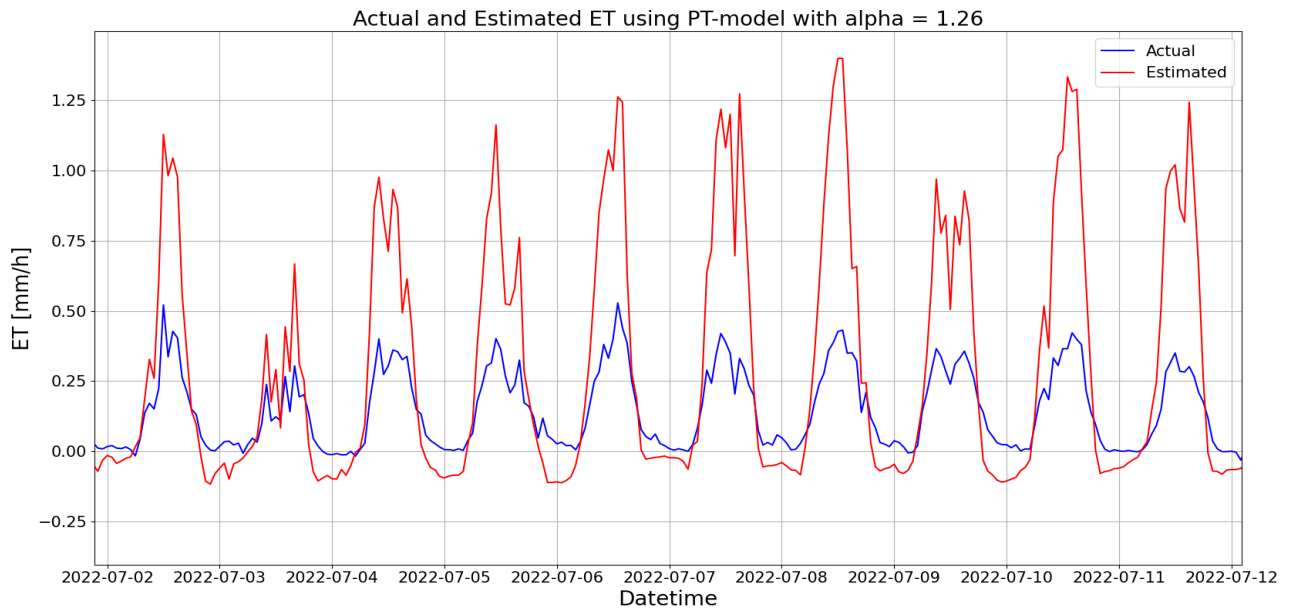


Figure 21: Comparison of measured ET -values (in blue) and the estimated ET -values (in red) from the PT1 model. This is just a section of the whole timeline plot where each point represents an hour.

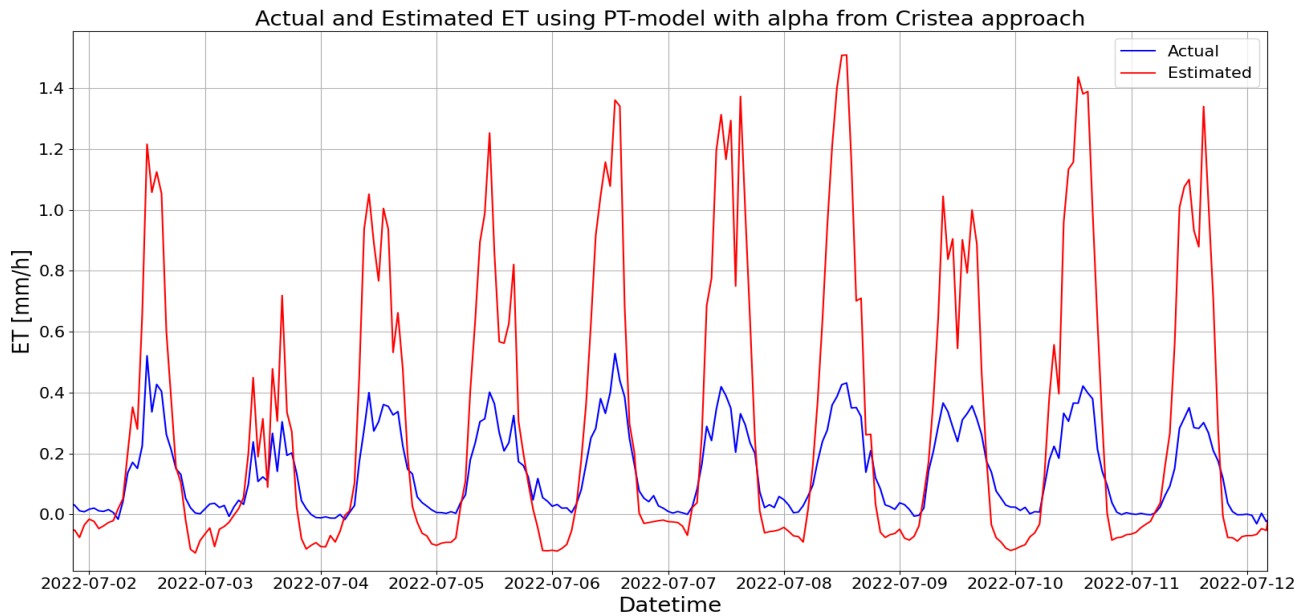


Figure 22: Comparison of measured ET -values (in blue) and the estimated ET -values (in red) from the PT2 model. This is just a section of the whole timeline plot where each point represents an hour.

Some noticeable features in both PT1 and PT2 are that both models tend to overestimate evapotranspiration during the daytime. Another feature is the estimation of more negative evapotranspiration during nighttime compared to the measurements. Both models have a similar trend compared to the measurements. The plot from figure 21 is plotted together with net radiation, R_n in figure 23, to display how the model correlates with net radiation. As shown in figure 23, the deep slopes with negative values in both PT1 and PT2 correlate with the negative values of net radiation. From the full plots from figure 99 to figure 110 in Appendix B1, one can see that the estimated ET is close to the measured ET on the following dates; 10th, 27th and 29th of July 2021, 27th of June 2022, and 22nd of July 2022. There is also a low estimation of ET on the 25th of July 2022.

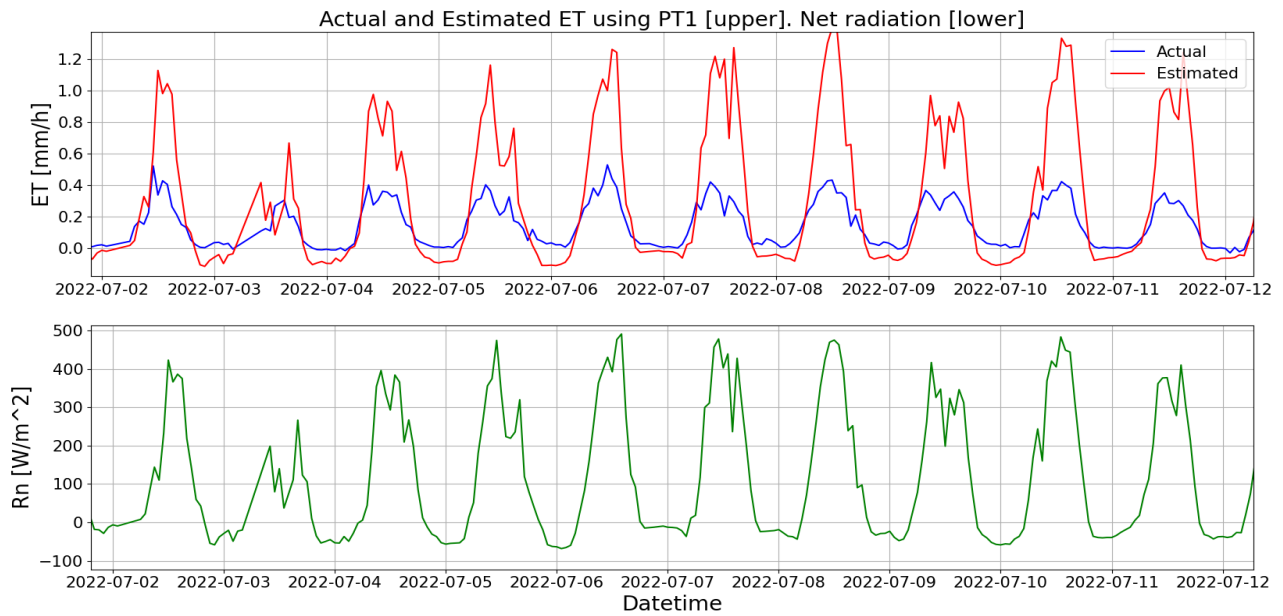


Figure 23: Comparison of measured ET-values (in blue) and the estimated ET-values (in red) from the PT1 model in the upper plot. Net radiation measurements (in green) in the lower plot.

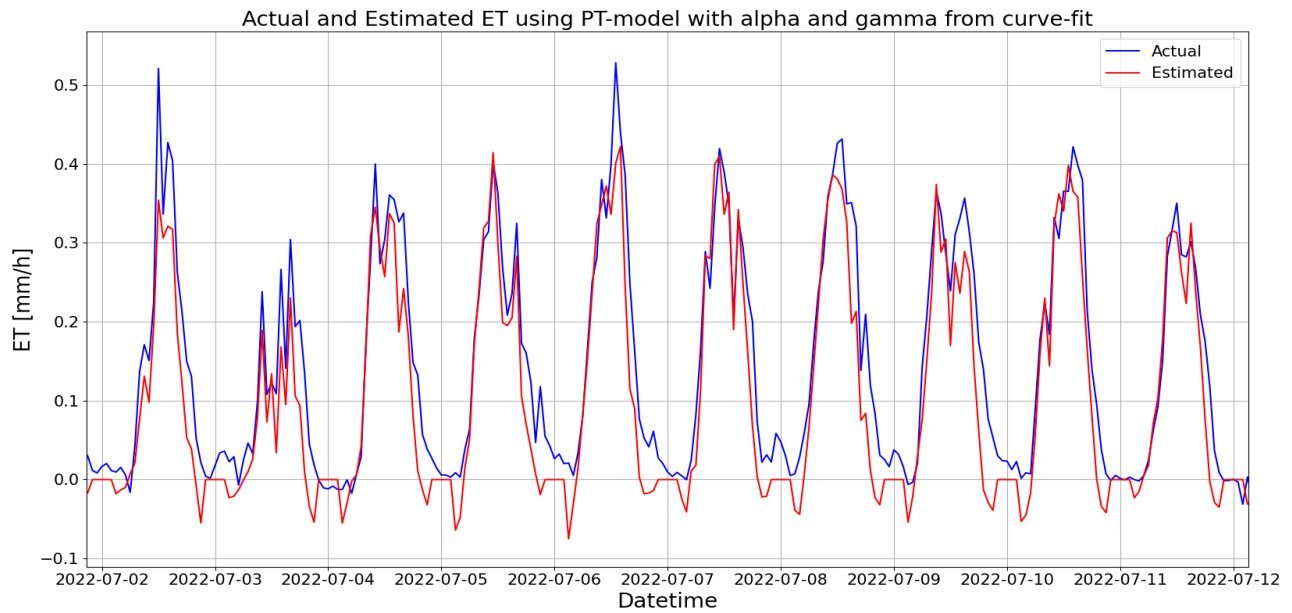


Figure 24: Comparison of measured ET-values (in blue) and the estimated ET-values (in red) from the PT3 model. This is just a section of the whole timeline plot where each point represents an hour.

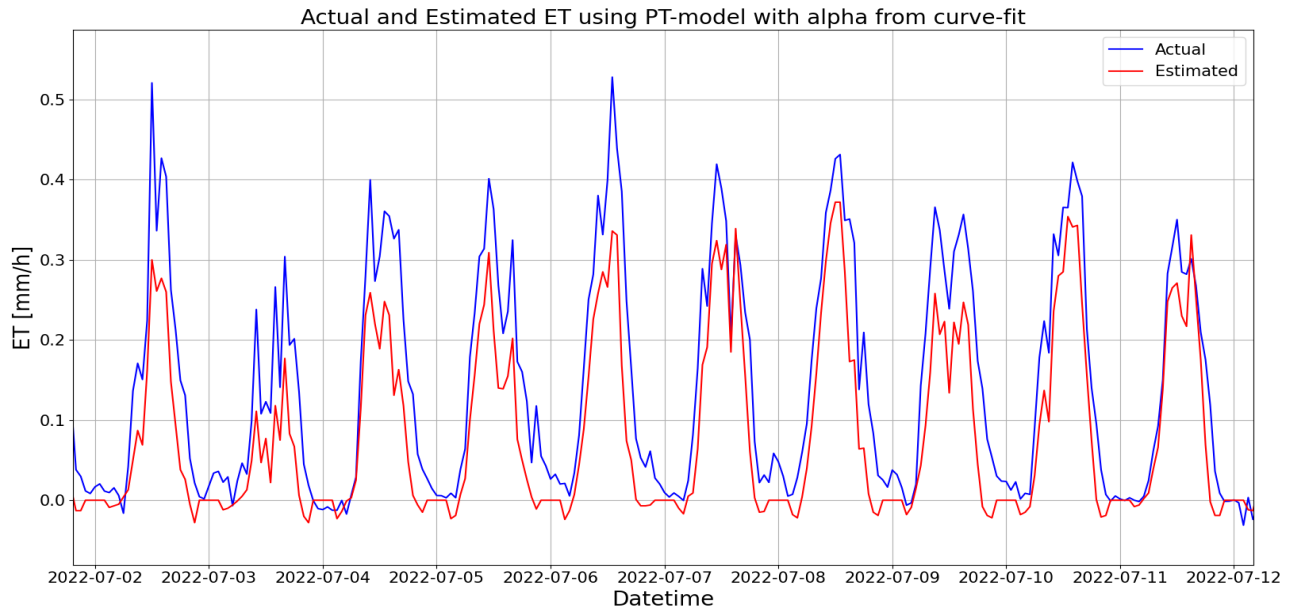


Figure 25: Comparison of measured *ET*-values (in blue) and the estimated *ET*-values (in red) from the *PT4* model. This is just a section of the whole timeline plot where each point represents an hour.

Noticeable features from the plots of *PT3* and *PT4* are that the estimated evapotranspiration will often be underestimated during daytime. The other noticeable feature is that both models will have two "fangs" during nighttime, one at the beginning and one at the end of the night. Figure 26 shows the correlation between the estimated values from *PT3*, the net radiation, R_n , and if daylight is registered. These plots show that the net radiation becomes negative at 20:00 and stays negative until 05:00 the next day. The value of daylight is not "True" (in a binary language) at 22:00, and is not "True" until 03:00 the next day. The two dips in the estimated evapotranspiration values occur at 21:00 and 03:00 the next day. Another interesting feature in the full plots from figure 111 to figure 122 in Appendix B1 are estimated *ET* values that are much lower than the measured *ET* values. This occurs on the following dates: the 27th of June 2022, and the 13th, 22nd and 25th of July 2022.

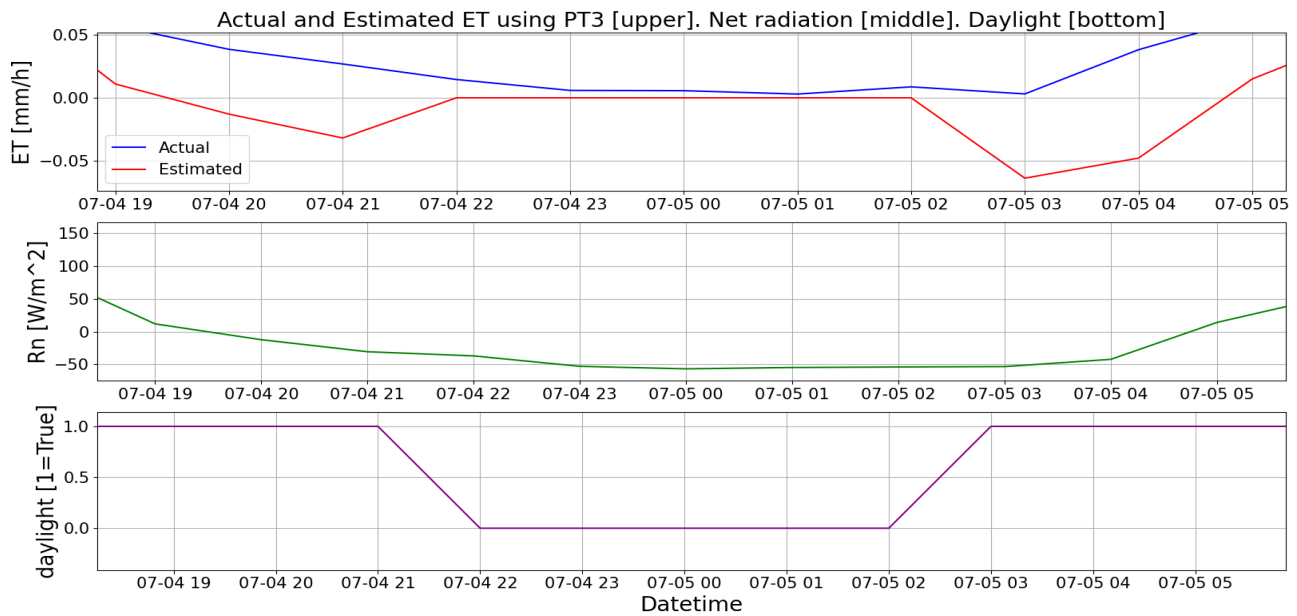


Figure 26: Comparison of measured ET-values (in blue) and the estimated ET-values (in red) from the PT3 model in the upper plot. Net radiation (in green) in the middle plot. Daylight value (in purple) in the lower plot.

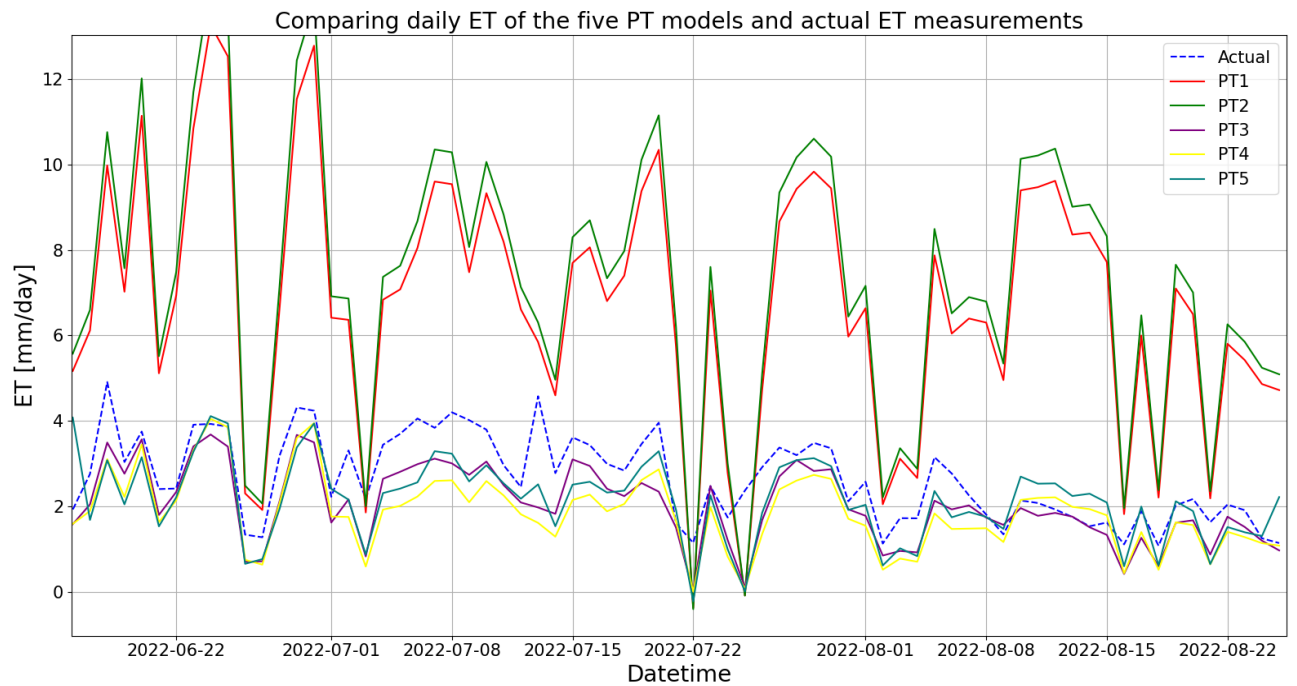


Figure 27: Comparison of measured ET-values (in blue) and the estimated ET-values from PT1 (red), PT2 (green), PT3 (purple), PT4 (yellow) and PT5 (teal). This is just a section of the whole timeline plot where each point represents a day.

From the plot in figure 27, one can see that the PT1 and PT2 will often overestimate ET values, ranging from a factor of two to a factor of five. PT3 and PT4 will sometimes over- and underestimate ET values compared to EC measurements. However, the deviation from the measurements

is minuscule compared to PT1 and PT2, with a difference ranging from 0 to 2 mm/day. The daily PT model (PT5) has a similar deviation from the measurements of PT3 and PT4. A noticeable trend is that the ET values from PT1 and PT2 are closer to EC measurements when the measured values drop. The differences in the dropping ET values can range from 0 to about 4 mm/day. By looking into the full plots in Appendix B1 from figure 123 to figure 124, one can see that the daily PT model (PT5) will often overestimate ET values in 2021, and often underestimate ET values in 2022.

From the full plots in Appendix B1 from figure 123 to figure 124, one can see that the dates that have low estimated ET values in all PT models, and which make PT1 and PT2 estimate ET values closer to EC measurements, happen on the following dates; 10th, 27th and 29th of July 2021. 2nd of August 2021. 26th and 27th of June 2022. 3rd, 22nd and 25th of July 2022. 2nd, 4th, 16th, 18th and 21st of August 2022. By comparing these dates with the net radiation plots and precipitation plots in Appendix A (fig. 51-56 and 87-92) and looking into figure 27, which is a section of the time-series, one can see that the dates mentioned are the same dates as when the net radiation is low, and when there is precipitation.

Table 5: α and γ values for the first four PT models.

α and γ values								
Daylight								
Model	PT1		PT2		PT3		PT4	
Month	α	γ	α	γ	α	γ	α	γ
June	1.26	64.46-66.72	1.359	64.46-66.72	0.0010	0.0260	0.3789	65.27-66.24
July	1.26	64.46-66.72	1.359	64.46-66.72	0.0006	-0.0432	0.3350	64.46-66.34
August	1.26	64.46-66.72	1.359	64.46-66.72	0.0004	-0.0489	0.2755	64.53-66.69
No daylight								
Model	PT1		PT2		PT3		PT4	
Month	α	γ	α	γ	α	γ	α	γ
June	1.26	64.46-66.72	1.359	64.46-66.72	-69.79	57060	-0.0807	65.33-66.17
July	1.26	64.46-66.72	1.359	64.46-66.72	-102.0	62822	-0.1083	64.48-66.38
August	1.26	64.46-66.72	1.359	64.46-66.72	-7.945	13933	-0.0382	64.53-66.67

Table 6: α and γ values for the daily based PT model

α and γ values for PT5		
Month	α	γ
June	11.03	65.33-66.17
July	12.12	64.52-66.31
August	11.12	64.76-66.66

From table 5, one can see that the calculated value for α using the approach from Cristea et al. (2013) with equation 18, the value is 0.099 higher than the literature value of 1.26. The α values for PT3 and PT4 are negative at night. The values of α for PT3 during daytime are in the 10^{-4} order of magnitude, while the γ values are in the 10^{-2} order of magnitude. Also, the values of γ for PT3 are negative during the daytime in July and August. Values of γ for PT3 during nighttime are in the 10^4 order of magnitude. Values of α for PT4 are in the 10^{-1} order of magnitude during

daytime. The γ values for PT1, PT2 and PT4 range between 64 and 67 kPa/°C. For PT5, the values of α are in the range of about 11 and 12, and the values of γ are in the range of about 64 and 67 kPa/°C.

The root-mean-squared error analysis on these models is listed in table 7. This analysis found that the approach of using curve-fitting to find values for α and γ , also known as PT3, yields the highest accuracy with an RMSE value of 0.0032. The approach of the model PT4 yielded the second-best accuracy with an RMSE value of 0.0043. The approach of the model PT3 yielded the worst accuracy with an RMSE value of 0.2312. Model PT1 yielded the second-worst accuracy with an RMSE value of 0.1898. Since PT5 is based on daily values its RMSE and mean difference value are not comparable to the other models.

Table 7: *RMSE and mean difference values of the five Priestley-Taylor models. For PT1-PT4 the mean difference is in mm/h, while for PT5 it is mm/day.*

Comparison method		
Model	RMSE	Mean diff
PT1	0.1898	0.280
PT2	0.2312	0.309
PT3	0.0032	0.039
PT4	0.0043	0.045
PT5	0.7518	0.672

4.4 Evaluation of Penman-Monteith model

The four PM models mentioned in section 3.4 were compared with EC measurements of actual evapotranspiration, ET_a . To visually show how the PM models perform they were plotted. Since there are six plots for each model (one for each summer month in 2021 and 2022), the full plots can be viewed in Appendix B2, while small sections of the plots will be shown here.

The plots comparing EC measurements and PM-model using equation 22 and crop coefficient of 0.9 are shown in figure 28 and in Appendix B2 from figure 125 to figure 130. By using curve-fitting to calculate a more suitable value for the crop coefficient, the PMhourly2 model uses a crop coefficient of 0.588. The plots comparing EC measurements and PM-model using equation 22 and crop coefficient 0.588 are shown in figure 29 and in Appendix B2 from figure 131 to figure 136. The PMhourly1 model and PMhourly2 model are made into daily resolution and plotted together with PMdaily2 and EC measurements in figure 30 and in Appendix B2 from figure 137 to figure 138. Because the PMdaily1 model has such a significant error, it is plotted separately in figure 31 and in Appendix B2 from figure 139 to figure 140. The daily values estimated from PMdaily1 are in the 10^{-1} mm/day order of magnitude.

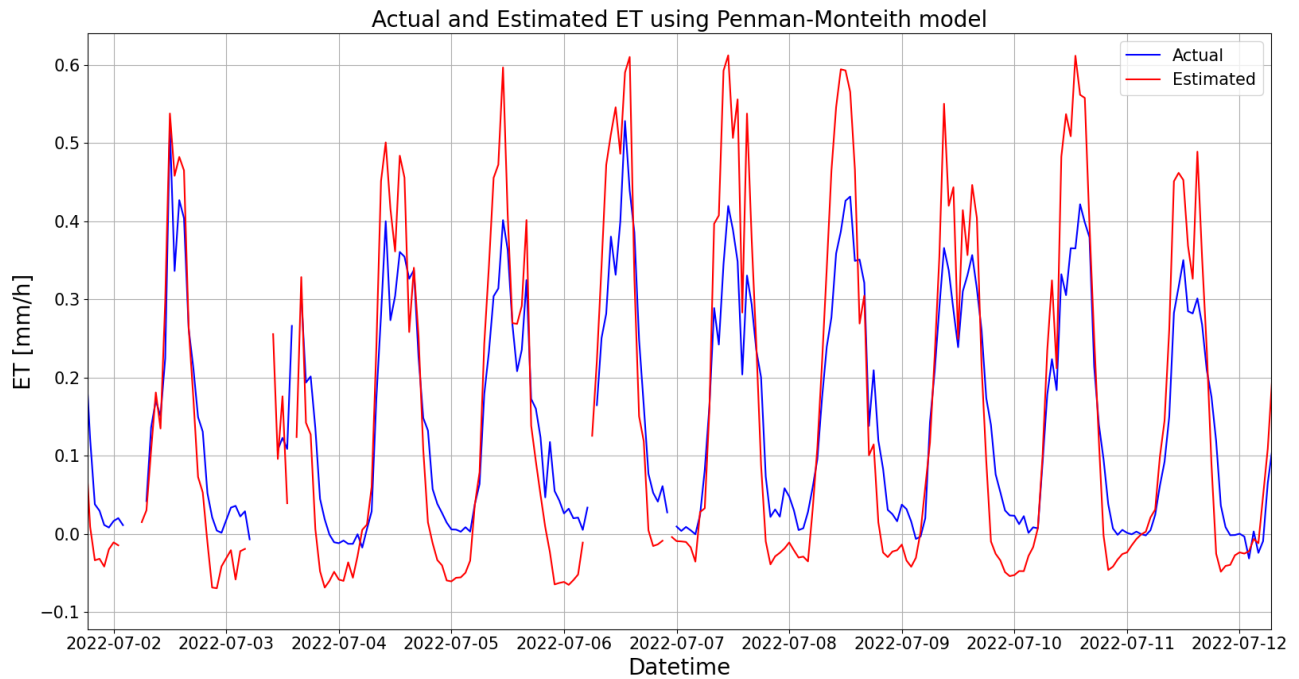


Figure 28: Comparison of measured *ET*-values (in blue) and the estimated *ET*-values (in red) from the *PMhourly1* model. This is just a section of the whole timeline plot where each point represents an hour.

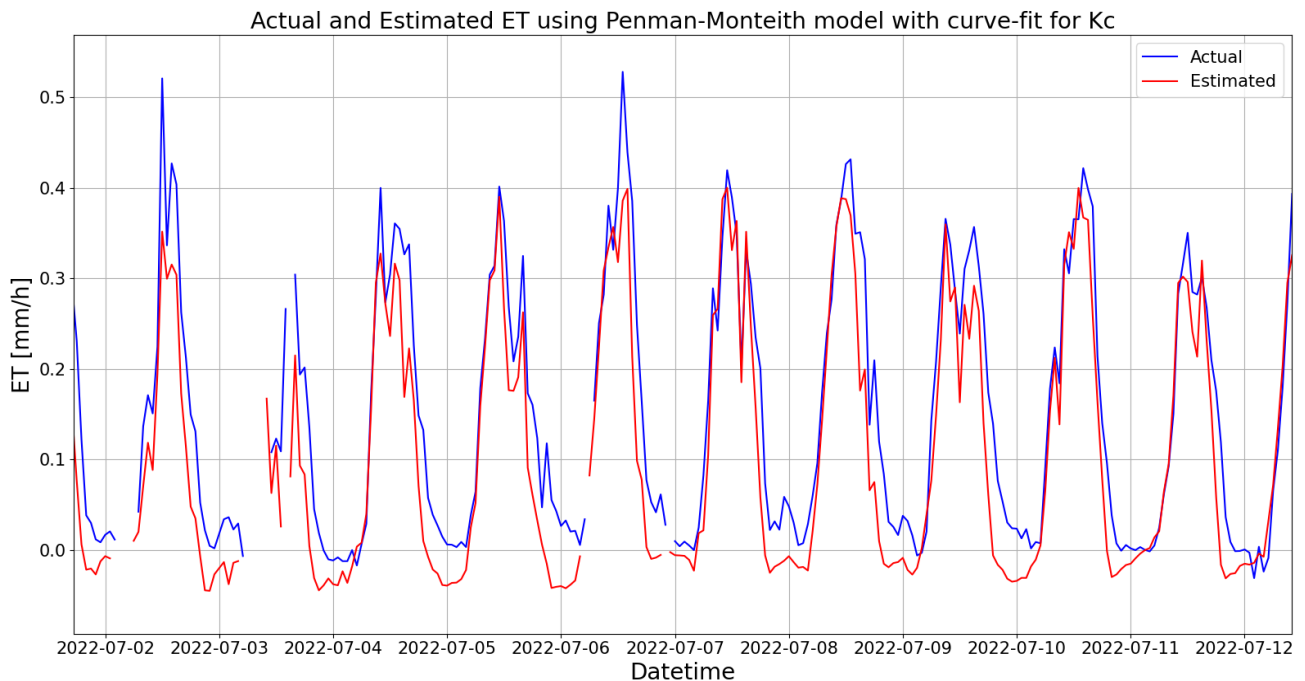


Figure 29: Comparison of measured *ET*-values (in blue) and the estimated *ET*-values (in red) from the *PMhourly2* model. This is just a section of the whole timeline plot where each point represents an hour.

As one can see from the plot in figure 30, the *PMhourly1* model tends to overestimate *ET* values

during daytime, and underestimate ET values during nighttime. One can also see some parts where there is missing data. One can also see that the PMhourly1 model follows the trend of the EC measurements.

From the plot in figure 29, one can see that the estimated values from the PMhourly2 model fit better to the measurements compared to PMhourly1. One can also see that the PMhourly2 model tends to underestimate ET values compared to the EC measurements. One can also see that the PMhourly2 model also underestimates ET values during the night, but not as much as the PMhourly1 model. In the plot, one can see the same missing values as in the PMhourly1 model.

In Appendix B2 from figure 125 to figure 136 one can see that both PMhourly1 and PMhourly2, have some dates with very low values of ET. These are the following dates; 10th, 27th and 29th of July 2021. 26th and 27th of June 2022. 1st, 3rd, 22nd and 25th of July 2022. And nights to the 3rd, 16th, and 18th of August 2022. These dates are the same as the PT models estimated with low ET values. There is no need to show the net radiation plot and precipitation plot with the PM models, as the correlation on the dates mentioned is the same for PM models as with the PT models.

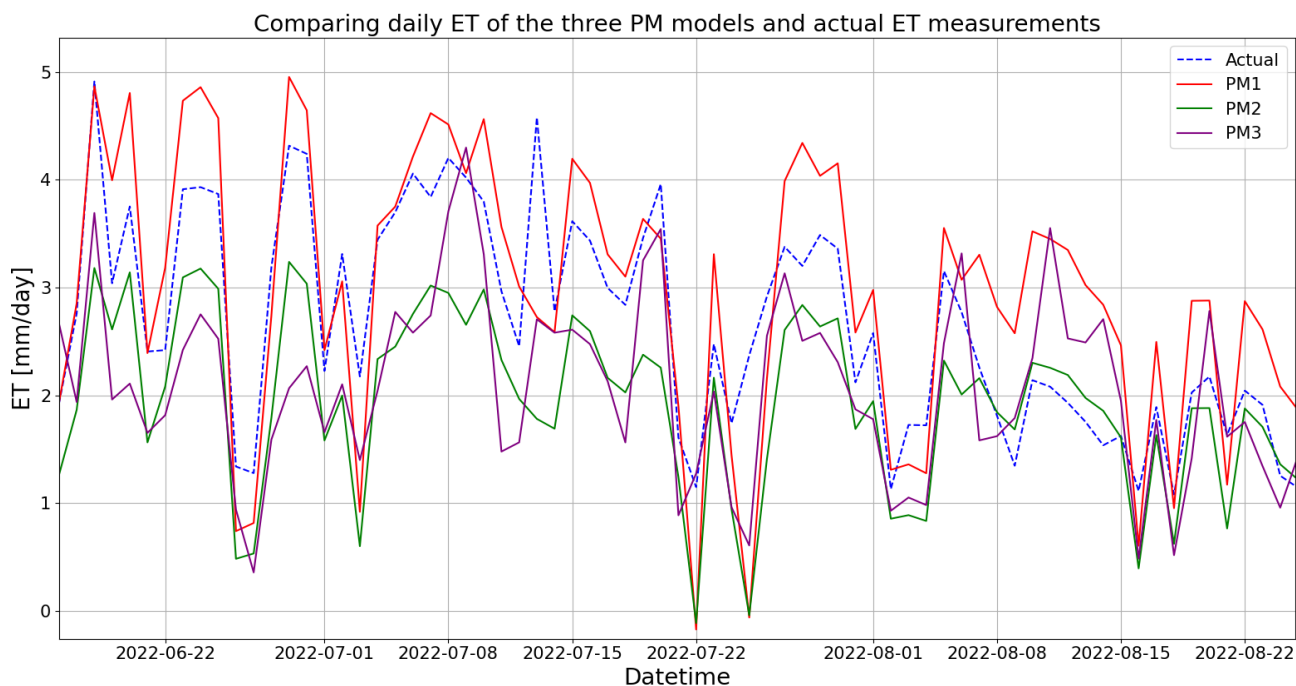


Figure 30: Comparison of measured ET-values (in blue) and the estimated ET-values from PMhourly1 (red), PMhourly2 (green), and PMdaily2(purple). This is just a section of the whole timeline plot where each point represents a day.

From the plots in figure 30 and in Appendix B2 from figure 137 to figure 138, one can see that the PMdaily2 model (PM3 in the figures) is, for the most part, underestimating the daily ET values. The same is true for the PMhourly2 model (PM2 in figures). On a daily scale, the PMhourly1 model (PM1) tends to overestimate the ET values.

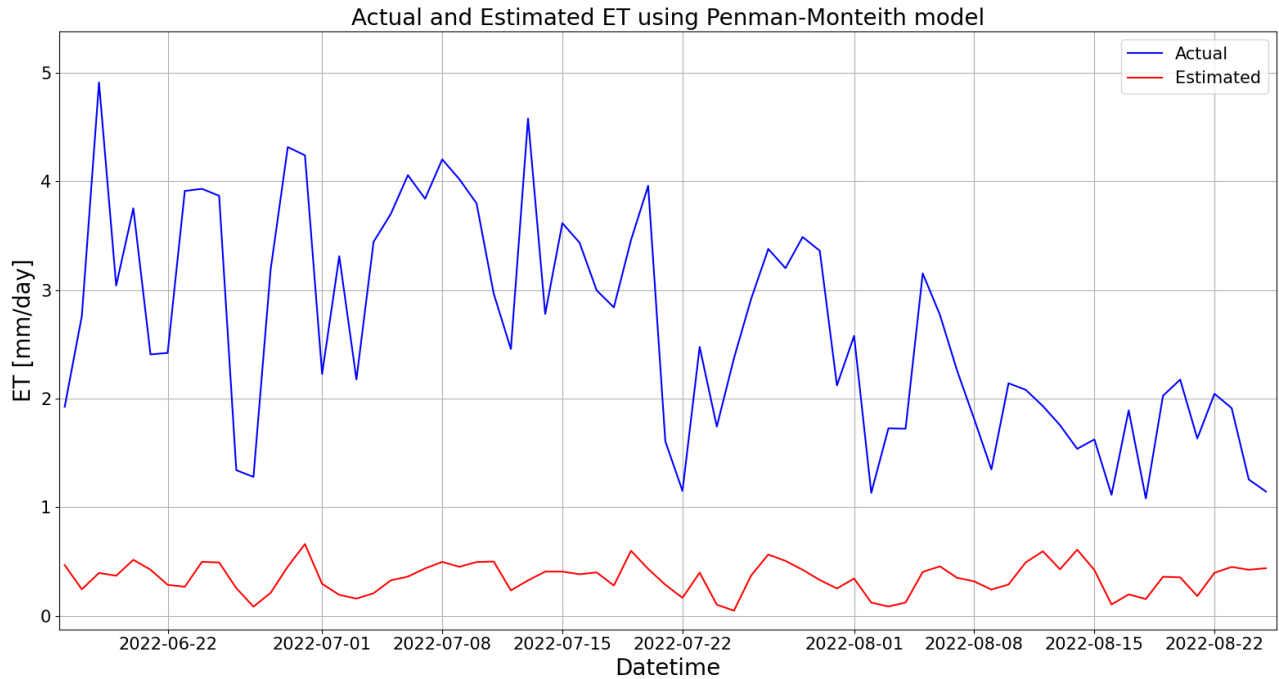


Figure 31: Comparison of measured ET-values (in blue) and the estimated ET-values from PM-daily1 (red). This is just a section of the whole timeline plot where each point represents a day.

The results from doing root-mean-squared error analysis and calculating the mean difference of each model are summarized in table 8. The PMhourly1 model compared to EC measurements resulted in an RMSE value of 0.0108 and a mean difference of 0.074 mm/h. The PMhourly2 model compared to EC measurements resulted in an RMSE value of 0.0039 and a mean difference of 0.044 mm/h, which is better than the PMhourly1 model. The PMdaily2 model compared to EC measurements resulted in an RMSE value of 0.8759 and a mean difference of 0.778 mm/day. The PMdaily1 model compared to the EC measurements resulted in an RMSE value of 5.7660 and a mean difference of 2.220 mm/day.

Table 8: RMSE and mean difference values of the four Penman-Monteith models. For the hourly models the mean difference is in mm/h, while it is mm/day for the daily models.

Comparison method		
Model	RMSE	Mean diff
PMdaily1	5.7660	2.220
PMdaily2	0.8759	0.778
PMhourly1	0.0108	0.074
PMhourly2	0.0039	0.044

4.5 Evaluation of MODIS

The plot comparing the measurements from MODIS and the EC instrument is shown in figure 32. As shown in the plot, there is an offset of three days between the data points from MODIS and the EC instrument in 2021, and an offset of two days in 2022. This offset is due to a difference in what date the summation of 8 days starts and ends between MODIS data and EC data. The plots show

that the ET values from MODIS are always higher than those from the EC instrument. However, both the MODIS and EC data have a similar trend in the way that the ET values are high in July and decrease throughout August. After offsetting the timelines of the EC measurements, the difference between MODIS and EC measurements of actual ET in 2021 were calculated to be between 3.2 and 9.8 mm/8days. In 2022, the difference between MODIS and EC measurements were calculated to be between 0.5 and 9.9 mm/8days. The mean difference in 2021 was therefore 6.2 mm/8days and 4.6 mm/8days in 2022. This means the MODIS data overestimates EC measurements by about 30-40 %. The RMSE values between MODIS and EC data for 2021 and 2022 are 44 and 33.

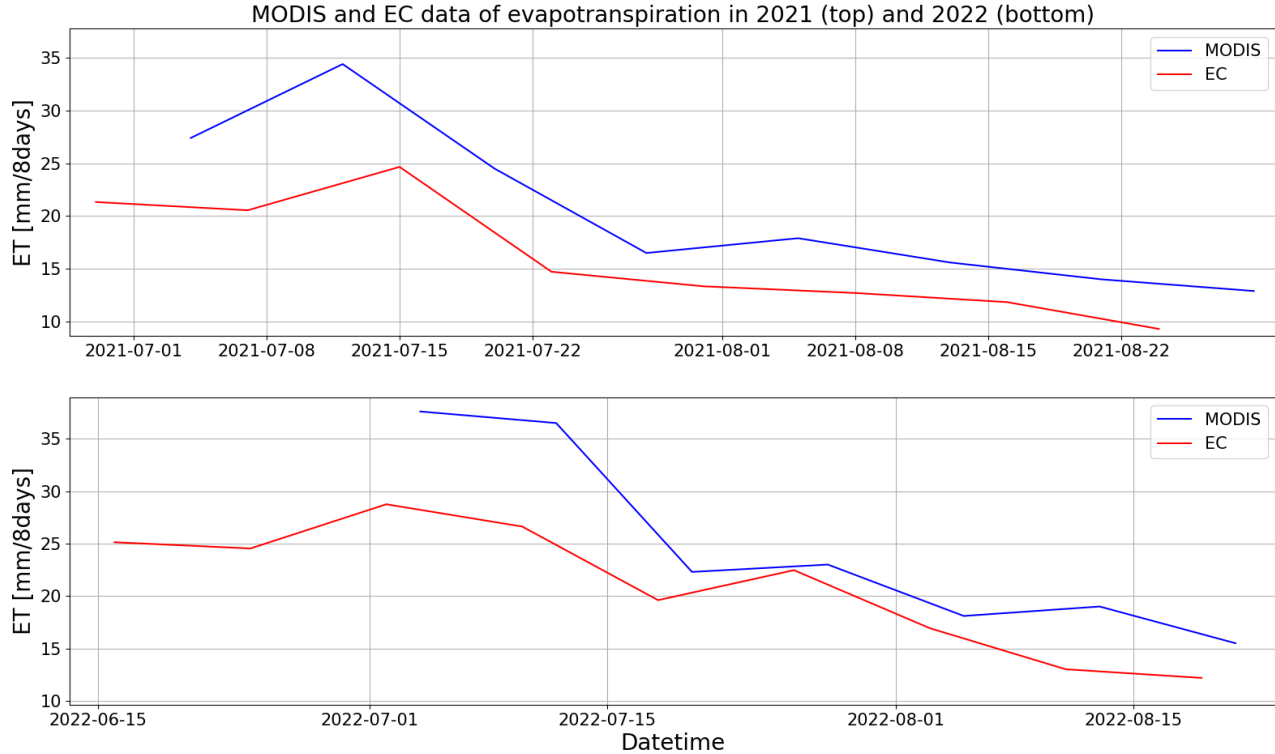


Figure 32: The plot shows ET values from MODIS (blue) and EC instrument (red)

4.6 Evaluation of pan evaporation measurements

The pan evaporation measurements were compared with EC measurements visually by plotting them. The plots are presented in hourly and daily resolution, where full plots in hourly resolution can be found in Appendix C. The daily pan evaporation, ET_{pan} , and daily ET_a from the EC instrument for 2021 and 2022 are shown in figure 33, while the hourly values are shown in Appendix C from figure 141 to figure 146. The daily reference evapotranspiration, ET_0 , and ET_a from the EC instrument for 2021 and 2022 are shown in figure 34, while the hourly values shown in Appendix C from figure 147 to figure 152. The daily estimates of actual evapotranspiration, ET_{a1} , using crop coefficient 0.9, and ET_a from the EC instrument for 2021 and 2022 are shown in figure 35, while the hourly values are shown in Appendix C from figure 153 to figure 158. The daily estimates of actual evapotranspiration, ET_{a2} , using crop coefficient 0.588, and ET_a from the EC instrument for 2021 and 2022 are shown in figure 36, while the hourly values are shown in Appendix C from figure 159 to figure 164.

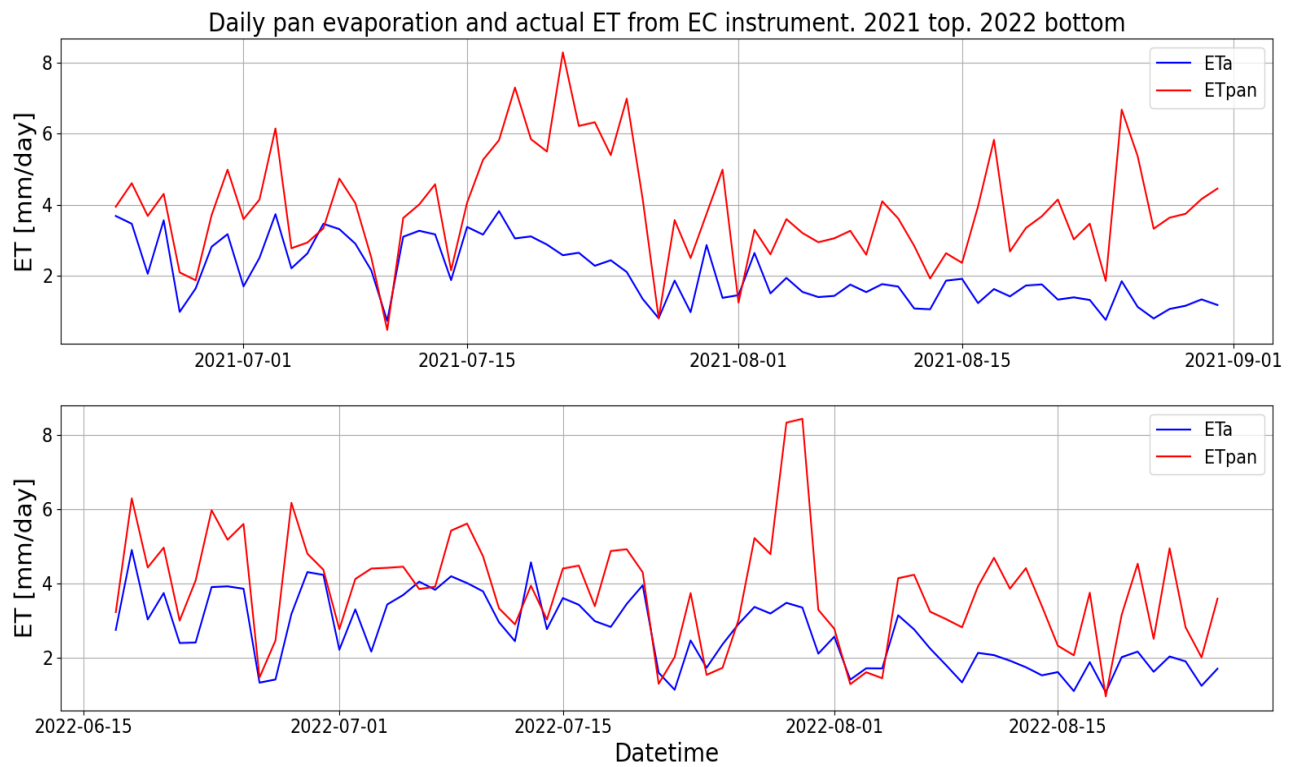


Figure 33: Comparison of measured ET -values (in blue) and the pan evaporation values (red). The plot on top is for 2021 and the bottom plot is for 2022. Time resolution is in days.

From figure 33 the plot of ET_{pan} in both 2021 and 2022 is greater than ET_a , with a few exceptions. In 2021 the mean value of ET_{pan} was 3.88 mm/day while ET_a had a mean value of 2.07 mm/day. ET_{pan} had a maximum of 8.23 mm/day and a minimum of 0.48 mm/day in 2021. ET_a had a maximum of 3.83 mm/day and a minimum of 0.74 mm/day in 2021. In 2022 ET_{pan} had a mean value of 3.81 mm/day while ET_a had a mean value of 2.68 mm/day. Maximum and minimum in 2022 for ET_{pan} were 8.44 mm/day and 0.97 mm/day, and 4.91 mm/day and 1.08 mm/day for ET_a . Interesting features of the ET_{pan} plot in 2021 are the values above above 6 mm/day in the middle of July, and the increasing difference between ET_{pan} and ET_a throughout August. In 2022 and interesting feature of the ET_{pan} plot is the peak in the end of July.

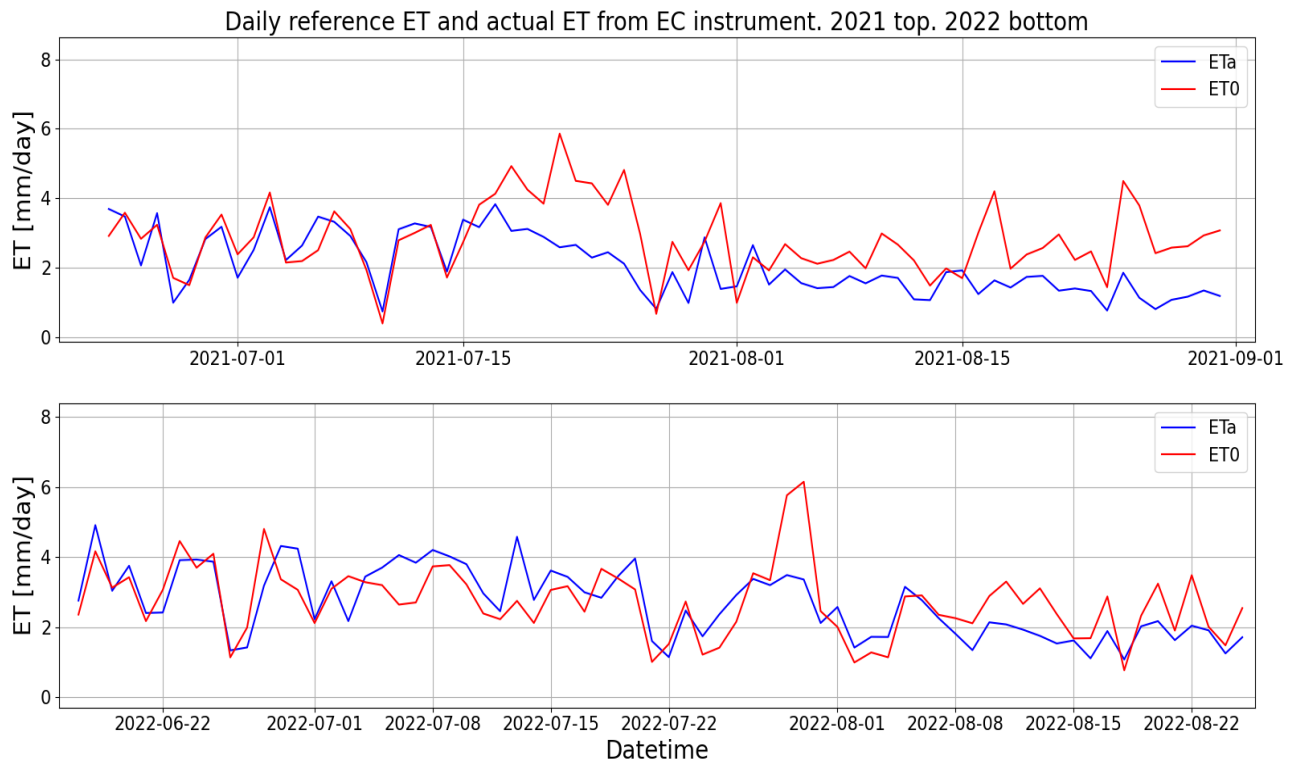


Figure 34: Comparison of measured ET -values (in blue) and the reference evapotranspiration values (red). The plot on top is for 2021 and the bottom plot is for 2022. Time resolution is in days.

Figure 34 shows that reference evapotranspiration, ET_0 is closer to ET_a values compared to ET_{pan} . The mean of ET_0 in 2021 was 2.81 mm/day and the maximum and minimum were 5.86 mm/day and 0.39 mm/day. The mean of ET_0 in 2022 was 2.74 mm/day and the maximum and minimum were 6.15 mm/day and 0.77 mm/day. These results show that the mean of ET_0 was 0.74 mm/day more than ET_a in 2021 and 0.06 mm/day more in 2022. As with the plots of ET_{pan} , there are values above 4 mm/day of ET_0 from the middle of July in 2021, and an increase in difference between ET_0 and ET_a throughout August in 2021. ET_0 has a peak in the end of July in 2022.

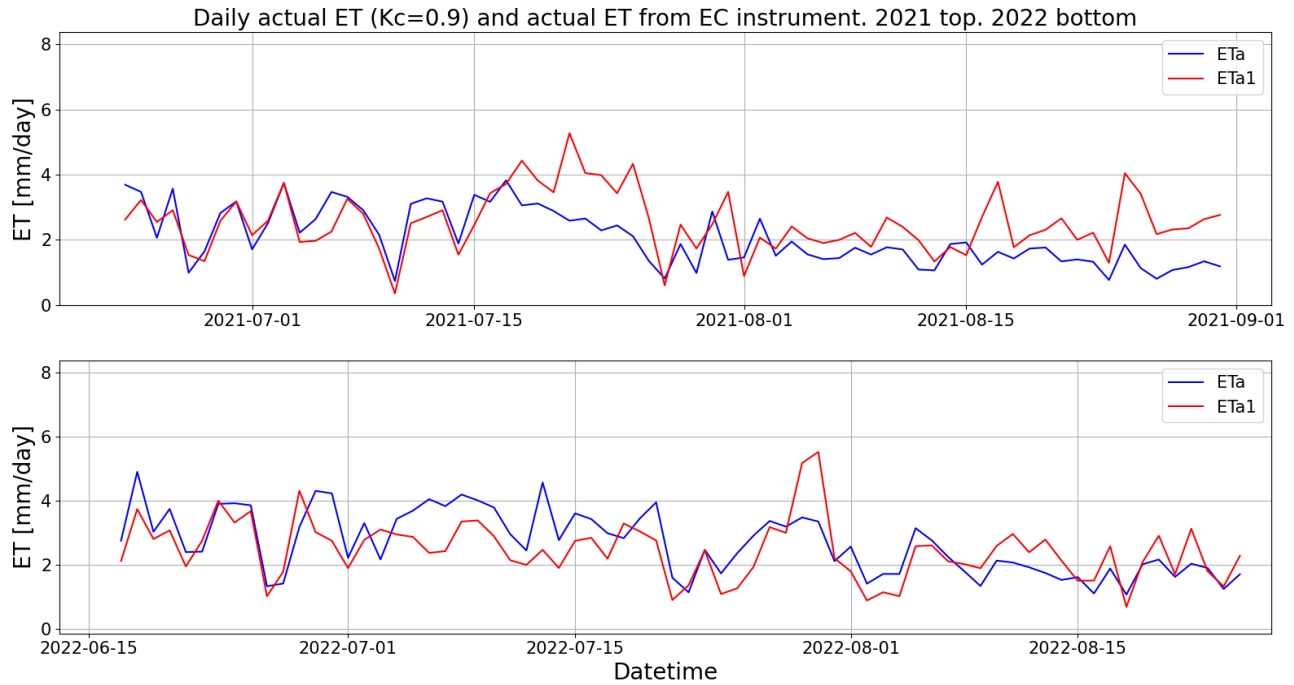


Figure 35: Comparison of measured ET -values (in blue) and the estimated evapotranspiration ($k_c=0.9$) values (red). The plot on top is for 2021 and the bottom plot is for 2022. Time resolution is in days.

Figure 35 shows the daily estimates of actual evapotranspiration, ET_{a1} , with crop coefficient 0.9. As one can see, the values of ET_{a1} are lower than pan evaporation ET_{pan} and lower than reference evapotranspiration, ET_0 . The ET_{a1} values fit better with the ET_a values from the EC instrument, especially in the beginning of July 2021. The mean values of ET_{a1} were 2.53 mm/day in 2021 and 2.47 mm/day in 2022. The maximum and minimum values were 5.27 mm/day and 0.35 mm/day in 2021, and 5.53 mm/day and 0.70 mm/day in 2022. Compared to ET_a , the means of ET_{a1} were 0.46 mm/day more in 2021 and 0.21 mm/day less in 2022. As with ET_{pan} and ET_0 , there are high values of ET_{a1} in the second half of July in 2021, an increasing difference between ET_{a1} and ET_a throughout August 2021, and a peak in the end of July 2022.

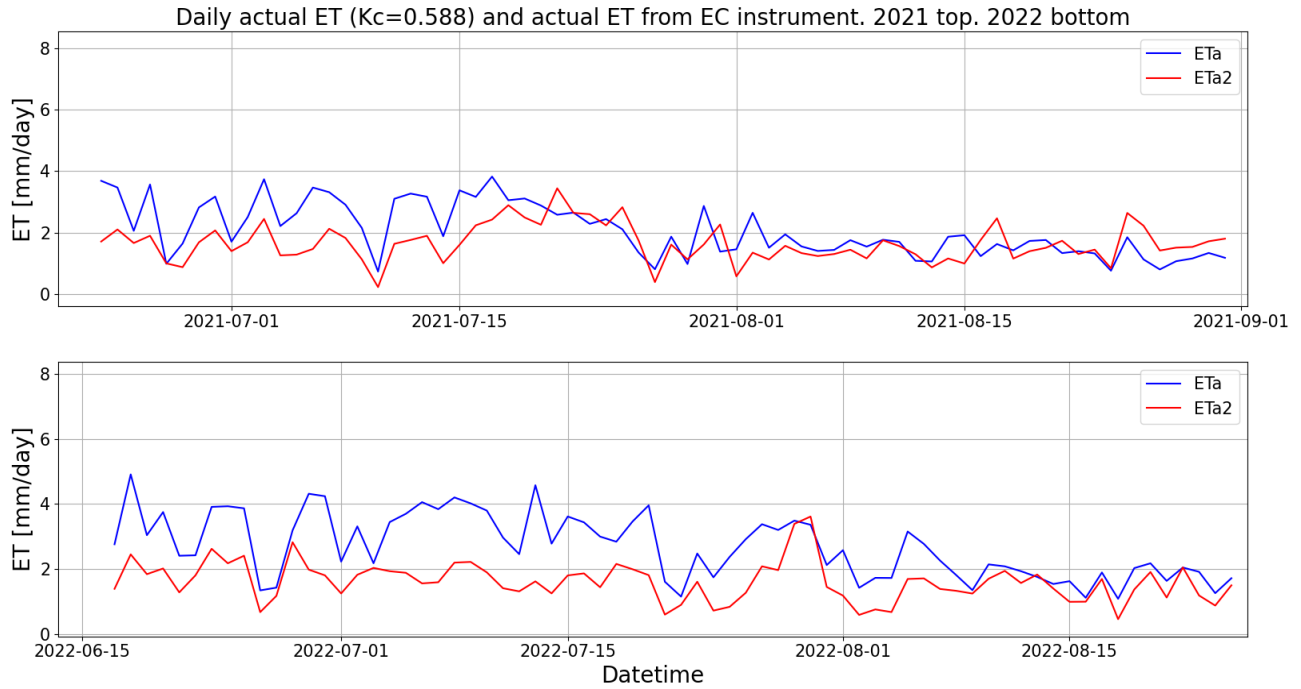


Figure 36: Comparison of measured ET -values (in blue) and the estimated evapotranspiration ($k_c=0.588$) values (red). The plot on top is for 2021 and the bottom plot is for 2022. Time resolution is in days.

From figure 36, it is shown that the daily estimates of actual evapotranspiration with crop coefficient 0.588, ET_{a2} , are below ET_a values in June and the first half of July in 2021, but after about the 20th of July, the ET_{a2} values fit better with the ET_a values. In the plot of ET_{a2} in 2022, one can see that ET_{a2} values are always below ET_a , but that the difference between ET_{a2} and ET_a is lower in August. The mean of ET_{a2} in 2021 was 1.65 mm/day and 1.61 mm/day in 2022. The maximum and minimum of ET_{a2} were 3.44 mm/day and 0.23 mm/day in 2021, and 3.61 mm/day and 0.45 mm/day in 2022. Compared to the means of ET_a , the means of ET_{a2} were 0.42 mm/day less in 2021 and 1.07 mm/day less in 2022.

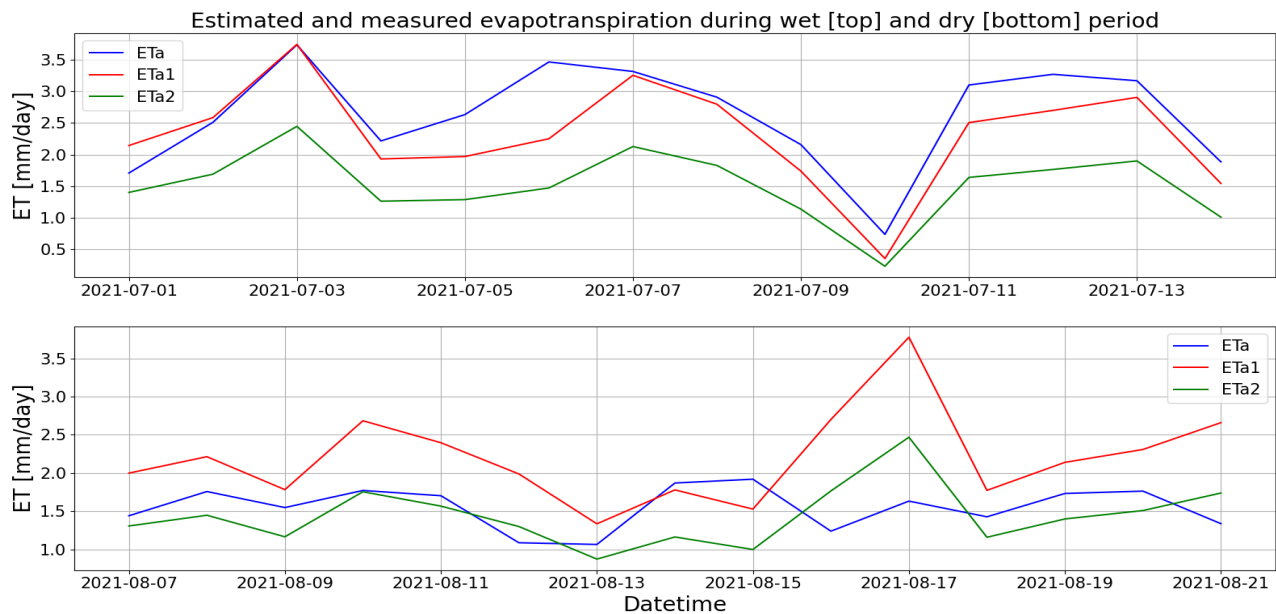


Figure 37: Comparison between ET_{a1} (red) and ET_{a2} (green) with ET_a (blue) during wet (top) and dry (bottom) period.

Figure 37 shows how ET_{a1} and ET_{a2} values are compared to the measured ET_a values during a dry and wet period. In the figure one can see that ET_{a1} values are closer to ET_a values during the wet period compared to ET_{a2} values, while the ET_{a2} values are closer to ET_a values during the dry period compared to ET_{a1} values.

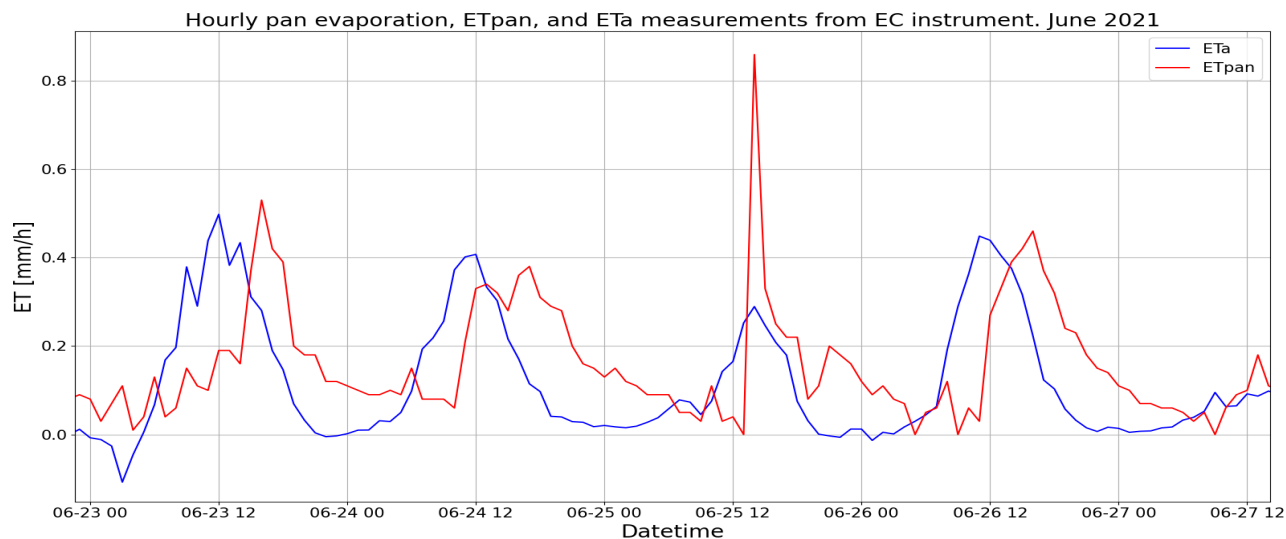


Figure 38: Zoomed in hourly plot of ET_{pan} (red) and ET_a (blue) in June 2021

Figure 38 is one of the plots with hourly resolution from Appendix C. The plot shows that in an hourly resolution, there is a difference between the peak values of ET_a and ET_{pan} , even after the time index of the pan data has been shifted with -1 hour. One can see that the ET_a peaks occur at about 12 and the ET_{pan} peaks are up to 3 hours behind.

The results from doing the root-mean-squared error analysis on the pan evaporation measurements, ET_{pan} , reference evapotranspiration, ET_0 , and estimated evapotranspiration, ET_{a1} and ET_{a2} , compared to eddy-covariance measurements, ET_a , are summarized in table 9. From the table, one can see that the estimated actual evapotranspiration using the modified crop coefficient, ET_{a2} , yielded a higher accuracy in 2021 with RMSE values of 0.0087 in the hourly resolution and 0.7368 in the daily resolution, compared to the estimated actual evapotranspiration using the crop coefficient of 0.9, ET_{a1} , which yielded RMSE values of 0.0113 in the hourly resolution and 0.9768 in the daily resolution. For 2022, the estimations of actual evapotranspiration using crop coefficient 0.9, ET_{a1} , was slightly better than estimations of actual evapotranspiration using crop coefficient 0.588, ET_{a2} . ET_{a1} yielded RMSE values of 0.0171 in the hourly resolution and 0.6499 in the daily resolution, while ET_{a2} yielded also 0.0171 in the hourly resolution, but 1.6814 in the daily resolution.

Table 9: *RMSE values where evaporation measurements, ET_{pan} , reference evapotranspiration, ET_0 , and estimated evapotranspiration, ET_{a1} and ET_{a2} , have been compared to evapotranspiration measurements, ET_a , from the EC instrument.*

RMSE values				
Comparison	Time scale: Hourly		Time scale: Daily	
	Year 2021	Year 2022	Year 2021	Year 2022
ET_{pan} vs ET_a	0.0200	0.0240	4.9914	2.3963
ET_0 vs ET_a	0.0129	0.0179	1.4230	0.6728
ET_{a1} vs ET_a	0.0113	0.0171	0.9768	0.6499
ET_{a2} vs ET_a	0.0087	0.0171	0.7368	1.6814

5 Discussion

5.1 Explaining the raw data

5.1.1 Evapotranspiration

By comparing the ET data with precipitation data, one can see that in many instances where there are extreme measurements of ET (both positive and negative), there is also an increase in accumulated precipitation, which means that there is precipitation happening during these extreme measurements. As mentioned in section 3, ET measurements done when there was precipitation are removed when calculating the accuracy of models compared to ET measurements, because of the errors that might occur. And this error is shown in the comparison between ET and accumulated precipitation data.

While comparing ET data with net radiation data, one can observe that there are low net radiation values in many instances with low peak ET values. And high ET values when the net radiation values are high. This fact coupled with the result from the correlation analysis in section 4.2 implies that net radiation is a strong driving force for evapotranspiration.

The values of accumulated evapotranspiration in July were about 70 mm and 90 mm in 2021 and 2022 respectively. As mentioned in the theory, the thesis by Rutger (2002) estimated evapotranspiration values to be 74 mm between the 22nd of June to 2nd of August 1999 and 75 mm between the 5th of June to 23rd of July 2000 in the sub-arctic area. Even though the values from Rutger (2002) are lower, they are in the same order of magnitude, and one has to take the difference between sub-arctic and temperate climates into consideration. From Ruairuen et al. (2015) ET values were found to be about 21.5 mm/week in July 2013 and 17 mm/week in August 2013, which is very similar to the values found in this study, as 70 mm and 90 mm of ET in July would be about 17.5 mm/week and 22.5 mm/week.

5.1.2 Pan evaporation

The diary of the pan measurements says that the grass at the meteorological station was cut and that a diffuse was adjusted on the 21st of July 2021, which could explain the spike in the evaporation measurements that day. The spike on the 31st of July 2021 occurred for unknown reasons, since there is no information about that day in the diary, and there are no abnormal meteorological measurements that day. The spike on the 16th of August 2021 could be explained as a measuring error since there was precipitation that day, and from the diary it says that the pan was refilled. For the 17th of August 2021, there is no information in the diary, nor any reasonable explanation in the meteorological data for the spike.

The spike that occurred on the 18th of July 2022 could be explained by several factors that could lead to a measuring error. From the diary it says that the grass was cut, the pan was refilled and that a diffuse was adjusted. There was also precipitation that day. On the 29th of July 2022, the highest net radiation during July was recorded, and from the diary it says that there was an error on the mechanical thermometer. These instances could explain the spike on the 29th of July 2022. For the spike on the 30th of July 2022, there is no explanation to be drawn, not from the diary, nor the meteorological data. From the diary it says that the grass was cut and that the evaporation pan was refilled, which can explain the spike on the 22nd of August 2022. The evaporation pan was refilled on the 26th of August 2022, which can explain the spike that day.

On the 10th of July 2021, the measured net radiation was low, and there was precipitation during that day, which explains the low evaporation. On the 26th to 27th of June 2022, the measured net radiation was low, there was precipitation, and the relative humidity was high, which explains the low evaporation. No explanation was found for the low evaporation value on the 21st of July 2022. The measured net radiation on the 18th of August 2022 was a little low (about 250 W/m² peak value), but not enough to explain the low evaporation measured that day. Nor are there other meteorological data that could explain this low-measured evaporation.

Rutger (2002) got values of evaporation of 59 mm between 23rd of June to 27th of July 1999, and 57 mm between 5th of June to 23rd of July. These values are about half of the accumulated evaporation from this study.

In figure 16 one can see that the evaporation in 2018 was extremely high compared to other years. This is because the the period from May-July had a mean air temperature of 17.6 °C, which is 3.9 °C more than the normal. The precipitation was also extremely low with 167 mm in May-July compared to the normal of 209 mm, and about one third of the precipitation came during one day (58.4 mm on the 17th of June) (Wolff et al., 2019). The mean temperature in July 2018 was 20.5 °C, which is 1.6 °C more than in July 2021 and 3.7 °C more than in July 2022.

5.2 Priestley-Taylor models

The values of γ in the two first PT models (PT1 and PT2) are within the range of what is expected from the literature (from the theory section; about 66 Pa/°C). Something surprising is that the calculated value of α using equation 18 yielded a model less accurate than simply using the literature-given value of 1.26. One reason might be that the study done by Cristea et al. (2013) was done in the USA, and the coefficients in equation 18 are unsuitable for the Norwegian climate. Another explanation could be that the study by Cristea et al. (2013) used mean annual relative humidity and mean annual wind speed. In contrast, the mean relative humidity and mean wind speed during summer were used in this study.

The results showed that the most accurate PT models were gained from using Python's "scipy.optimize curve_fit". This is because the values of α (and γ for PT3) are specifically tailored for the ET measurements made, and will therefore obviously yield the highest accuracy when compared with the measurements they were made from. The values of α (and γ for PT3) gained from this approach are in a range that has not been seen in any literature while doing this study. The model PT4, where curve-fitting was used only to find values for α and equation 15 to find values for γ yielded less accuracy than PT3. However, the α values during daytime for PT4 are more reasonable than for PT3, and the γ values for PT4 are within a reasonable range compared to the 66 Pa/°C that has been mentioned in the theory section. The negative α values during the night for both PT3 and PT4 do not make any sense physically. If one looks into equations for PT (eq. 14), Δ (eq. 16) and γ (eq. 15), one can see that Δ and γ will always remain positive. So the only way for ET to be negative is if net radiation R_n is negative. α can therefore not be negative during the night, and these negative values should rather be replaced by zero. And since γ can not be negative, the negative daytime γ values for PT3 also do not make any sense. All in all, the PT3 model should be discarded. A solution, however, would be to set a limiting range of values for the curve-fitting function.

The α values obtained from curve fitting with daily mean values (PT5 model) are about ten times larger than the literature value of 1.26. When looking at the RMSE values, it seems as if the PT5

model yields the worst results, however, this is because the values used in the RMSE analysis are much larger since they are daily values instead of hourly values (as for PT1-PT4). From the daily plot with all PT models, it is visually clear that PT5 outperforms PT1 and PT2.

As mentioned in the methods section, due to the limitation on the ET measurements when there is precipitation, data points were removed if they belonged to times when precipitation was above 1 mm. When comparison between model and measurement was done, these data points were still not included. Henceforth, it is essential to consider this fact when looking at the accuracy results of the five PT models.

Looking into the meteorological monthly overview of the years 2021 and 2022, it turns out that both years had June and August that were unusually warm and dry at the location where the data for this study is gathered (Grinde et al., 2021; Mamen et al., 2022; Wolff & Grimenes, 2022; Wolff, 2023). This in turn could imply that the values for α and γ from curve-fitting are potentially useless in more "normal" conditions. These dry and warm summers could also explain why the two models from the literature (PT1 and PT2) overestimated the ET values. As mentioned in section 2.5.1, an α value of 1.26 is a mean estimate of well-watered (saturated) soil and bodies of water. From Priestley & Taylor (1972), it is also said that lower values of α are expected if the soil is not saturated. A case of low α values also occurred in the study by Kustas et al. (1996). In the study mentioned, the α value was found to vary between 1 and 0.6. The conditions mentioned in the study are similar to those in this study, as both had a dry period in the summer.

The Priestley-Taylor model is a potential evapotranspiration model, it does not consider if there is enough water in the system. It only takes energy as a parameter. This would explain the overshooting of both literature-based models. The dry summers is a reasonable explanation for the low α values in the model PT4, since a low α value means that there is significant canopy resistance (De Bruin, 1983).

Since the comparison is made with EC measurements, the PT models are compared with actual evapotranspiration, ET_a , but the PT equation is for potential evapotranspiration, ET_p . It could be possible to convert ET_a to ET_p by dividing ET_a by an empirical stress factor. The stress factor represents water availability and the canopy-atmosphere coupling (Peng et al., 2019). This was unfortunately not done in this study.

5.3 Penman-Monteith models

By comparing the PMhourly1 and PMhourly2 models with the EC measurements, it is clear that the PMhourly2 model yielded the highest accuracy, since it has an RMSE value of 0.00393 compared to 0.01082 for the PMhourly1 model. From the plots in figures 28, 29 and 30 it is possible to see that the PMhourly1 model will often overestimate evapotranspiration while PMhourly2 will often underestimate evapotranspiration. From the plot in figure 30, it is also visible that the PMdaily2 model tends to underestimate evapotranspiration.

As with the PT3 and PT4 models, the meteorological conditions during the summers of 2021 and 2022 must be considered. It might be that the modified crop coefficient for the PMhourly2 model is 0.588 because of the warm and dry conditions, and that a crop coefficient of 0.9, as used in the PMhourly1 model is more suitable during "normal" meteorological conditions. According to the paper by Allen et al. (1998), if the soil surface is dry, the crop coefficient can drop as low as 0.1.

Much time and effort have been spent figuring out why the PMdaily1 model performs poorly.

The Python code used to calculate the ET_a estimates have been checked by supervisors and other students, however, an error could not be located. Therefore, the reason for this poor performance is unknown.

5.4 Priestley-Taylor vs Penman-Monteith

Since the PT and PM models are compared to EC measurements, it is also possible to compare them. By looking at the RMSE values, the best hourly model is PT3, with an RMSE of 0.0032. However, as mentioned in the discussion about the PT models, PT3 will yield the best ET estimates, since both γ and α were calculated with curve fitting. PT3 will be discarded.

The best model, with an RMSE value of 0.0039, is the PMhourly2 model, which is the hourly PM model with a modified crop coefficient. As with the PT4 model, it might be that the modified crop coefficient is the reason for the good result, but that the model is not as good during normal meteorological conditions.

When looking at the models purely based on literature, the PMhourly1 model yields the best result with an RMSE value of 0.0108 compared to PT1 with an RMSE value of 0.1898. This result should be expected as the Penman-Monteith equation reflects the actual evapotranspiration and is dependent on more variables than the Priestley-Taylor equation, which is supposed to calculate the potential evapotranspiration, and depends on only available energy.

Comparing the two daily-based models, PT5 and PMdaily2 show that PT5 yields a higher accuracy with an RMSE value of 0.7518 compared to 0.8759 from PMdaily2. This result could be explained by the fact that the value of α was calculated using curve fitting for the PT5 model, while the PMdaily2 model used the literature-given crop coefficient of 0.9.

5.5 MODIS

As mentioned in the results, actual ET from MODIS is greater than actual ET measurements from the EC instrument by about 30-40 %. A study by Degano et al. (2021) trying to compare MODIS data of potential evapotranspiration and actual evapotranspiration had issues with the MODIS data systematically overestimating potential evapotranspiration at about 65%. However, they found that there was both over- and underestimation for the actual evapotranspiration, depending on the geographical zone where the values were compared (Degano et al., 2021). Compared to Degano et al. (2021), a similar trend is the decreasing difference between MODIS data and ground measurements towards the end of the growth stage. From Degano et al. (2021) the trend is only valid in the following zones; Undulating Pampa, Laboulaye and Junín. However, the ground measurements from Degano et al. (2021) have higher values of ET than the MODIS data. A speculation that the study by Degano et al. (2021) got overestimations when comparing MODIS ET_p data with ground measurements and good results when comparing MODIS ET_a data with ground measurements is that the study by Degano et al. (2021) did not use an EC instrument to measure the actual evapotranspiration, but used the Penman-Monteith equation similar to equation 20 to calculate the ET_a . The MODIS algorithm also uses Penman-Monteith to calculate ET_a . This could explain the good results between MODIS ET_a and ground ET_a , and the overestimation between MODIS ET_p and ground ET_a .

Another study comparing MODIS data with EC measurements is Hu et al. (2015). The results from Hu et al. (2015) have similarities in the MODIS and EC values of actual evapotranspiration

over grassland. The grassland from Hu et al. (2015) was in the Netherlands, and the ET_a values from MODIS were ranging from over 30 to over 20 mm/8days during summer. From the results, the ET_a values in this study were ranging at about 35 to 15 mm/8days. The EC measurements from Hu et al. (2015) were below MODIS values, and ranged at around 20 mm/8days. From the results in this thesis, the EC measurements of ET_a were ranging somewhere between 25 and 10 mm/8days. Another similarity to the findings in Hu et al. (2015) is that the land cover is grassland and that the ET_a values from MODIS and the EC instrument decrease towards the end of the summer.

As mentioned in the results, the data between MODIS and EC were offset to each other in time. This was said to be due to the difference in the start and end date of the 8-day summation between these two. This will also mean that the EC and MODIS measurements will have summed some different days in the 8-day interval. In 2021 the ET_a value from MODIS was summed by three days before the 8-day summation from the EC instrument. In 2022, the ET_a value from MODIS was summed by two days later compared to the 8-day summation from the EC instrument.

Since the time series of EC measurements is only for two summers, it is hard to conclude if there is a systematic overestimation from the MODIS data, or if it is just a coincidence.

5.6 Pan evaporation and thoughts on the ET models

Looking at the daily plots from section 4.6 of the pan measurements (figure 33), ET_{pan} , compared to the EC measurements, ET_a , it is shown that the evaporation from the pan measurements is always larger than the evapotranspirational measurements from the EC instrument. The pan can evaporate water if there is enough energy and the surrounding air is not saturated by water vapor. Evapotranspiration will be lower than the evaporation from the pan, because evaporating water from the soil requires more energy (ref. section 2.4), and the vegetation will also hold on to more water if it is water stressed.

The feature with high values of ET_{pan} after the 15th of July in 2021 can be explained by the high air temperatures (ref. figure 64) and low relative humidity (ref figure 82) during daytime and nighttime in that period. The feature with the increasing difference between ET_{pan} and ET_a throughout August can be explained by the increase in air temperature throughout August (ref figure 65), and the low amount of precipitation, that decreases the evapotranspiration (ref. section 4.1.10). The feature with the peak ET_{pan} value at the end of July 2022 does not have a meteorological explanation, which means that it might just have been some measuring errors. Many of the times, when the ET_{pan} values are close to ET_a values, are the exact times when there has been precipitation. One can see this because the ET_{pan} are close to ET_a values when both of them are low. Low values come from low net radiation since precipitation comes in clouds, as well as increased relative humidity because of the moisture in the air.

A study by Liu et al. (2019) did an analysis on changes in actual evapotranspiration and pan evaporation and their influencing factors, from 1998 to 2005. Their results for 2002 have some similarities with the findings in this thesis. In 2002, Liu et al. (2019) had the highest values of pan evaporation (about 450 mm) and the lowest values of actual evapotranspiration (about 250 mm) during summer compared to other years. Liu et al. (2019) also calculated the lowest crop coefficient (mean k_c of about 0.7) in the summer of 2002 compared to other years. The similarity here is the high values of pan evaporation and low values of actual evapotranspiration, which makes ET_{a2} more accurate than ET_{a1} , where ET_{a2} uses a crop coefficient of 0.588 compared to

ET_{a1} which uses a crop coefficient of 0.9. The summer of 2002 where the study by Liu et al. (2019) was conducted was drier than normal (precipitation: 180.3 mm compared to 304.8 mm in 2001, 355.6 mm in 2003, 330.2 mm in 2004).

An interesting result is the comparison between the RMSE values of ET_{a1} and ET_{a2} . Table 9 shows that ET_{a2} yields estimates closer to the ET_a values measured by the EC instrument in 2021. In one way, this goes to show that the calibrated crop coefficient of 0.588 is more suitable to use when the meteorological conditions are drier than normal (ref. section 3.1). Table 9 also shows that ET_{a1} had values closer to ET_a in 2022. From figure 37 one can also visually see that ET_{a1} is more suitable for wet conditions while ET_{a2} is more suitable for dry conditions. From section 3.1 it was mentioned that the conditions in 2022 were wetter than in 2021, which could explain why using a crop coefficient of 0.9 yielded better results in 2022. These results show that the crop coefficients in Table 12 from Allen et al. (1998) might not be valid for dry conditions.

The results from the comparison of ET_{a1} and ET_{a2} also build up the statement mentioned in section 5.4 about the calibrated evapotranspirational models. The summer of 2021 was drier than normal, and could therefore make the calibrated models unreliable during normal conditions.

The temporal difference between the peak values of ET_{pan} and ET_a can be explained by the temporal difference between peak net radiation and peak air temperature. If one compares the figures 38, 51 and 63, one can see that the peak net radiation is at about 12, which is the same time as the peak values of ET_a . The peak air temperature values can lag up to four hours after the peak net radiation, which explains why the peak ET_{pan} values can lag behind the peak ET_a values.

6 Conclusion

6.1 Evapotranspiration models

Taking the results and discussions from the evaluation of the Priestley-Taylor and Penman-Monteith models, it has been shown that the crop coefficient calibrated ($k_c = 0.588$) PM model is the most accurate hourly-based ET model with an RMSE value of 0.00039, and the second most accurate ET model being the α calibrated ($\alpha = 0.2755-0.3789$) PT model with an RMSE value of 0.0043. It has also been shown that the hourly PM with a literature-based crop coefficient of 0.9 yields a more accurate result than the hourly Priestley-Taylor with a literature-based α value of 1.26, which is expected, since the Penman-Monteith equation is more advanced as it includes water vapor and wind.

The good performances of both the calibrated PM model and the calibrated PT model should not be considered ground truth as they are based on limited data. The limitation is that both calibrations were done for two summer periods that were warmer and drier than usual, which can lead to faulty results under "normal" conditions. The negative values in PT4 should be replaced by zero. The PT3 model should be discarded.

The Penman-Monteith equation from Barry & Blanken (2016a) (eq. 19), has proven to perform poorly. The reason for this is unknown.

Overall, longer time series' are needed to evaluate all evapotranspirational models introduced in this thesis properly. Using data from only two summers is not enough to come to a conclusive answer as weather can be significantly different on a year-to-year basis. A 10-year series or longer would be ideal. Despite this limitation, the results seem promising as a proof of concept.

6.2 MODIS

The results found that the MODIS data overestimate values of actual evapotranspiration by about 30-40 % compared to the EC measurements. It has also been found out that this type of overestimation has happened over grassland in the Netherlands as well in the study by Hu et al. (2015). If it is found that this is a systematic overestimation every summer at high latitudes over grassland, it would maybe be reasonable to assume that the MODIS algorithm could need improvements. Since the timeline of the EC measurements is only over two summers, it is not possible to conclude if this is a systematic error. It is also therefore difficult to conclude if the data from MODIS is reliable for the area of interest. If it is found that the data from MODIS is reliable, it would provide valuable information, since data from MODIS has a long time series of measurements back in time.

6.3 Pan evaporation measurements

From the comparison of the EC measurements with the pan evaporation measurements, it is clear that the pan evaporation measurements could be trusted, however, an emphasis has to be put on the choice of what crop coefficient value to use if the measurements are converted to actual evapotranspiration. Again, as with the ET models, longer time series is needed to evaluate the reliability of the measurements correctly.

6.4 Future outlook

In order to come to a conclusive answer on what α values to use in the Priestley-Taylor equation, and what crop coefficient to use in the Penman-Monteith equation, longer time series are needed. The same is true for the evaluation of these calibrated parameters. An interesting research could also be to find α and crop coefficient values for ecosystems in Norway different from the grassland studied in this thesis. If different ecosystems and sites in Norway would be studied for a suitable α value, maybe a map similar to the one presented by Cristea et al. (2013) could be made. Coupling soil moisture data with the data from this thesis could also provide useful information on how α and crop coefficient values would vary depending on the available water in the soil.

As mentioned in section 6.2, the time series between MODIS and EC data need to be longer to reach a conclusive answer on the evaluation. Something that should be looked into is if the data from MODIS systematically overestimates ET values during summer. If so, it should be easy to evaluate the reliability of the MODIS data, since a solution could be to improve the MOD16 algorithm.

The evaluation of the pan measurements has also been challenging with limited data. However, the historical data from 1997 has slight variation, which could indicate that the data is reliable, but it does have some missing values. As with the evaluation of the ET models, it would maybe be interesting to couple soil moisture with the data from this thesis, to see how the comparison between ET_a from the EC instrument and ET_{pan} from the pan measurements behaves with different values of soil moisture.

References

- Allen, R., Pereira, L., Raes, D., Smith, M., et al. (1998). Crop evapotranspiration-guidelines for computing crop water requirements-fao irrigation and drainage paper 56. *Fao, Rome, 300*(9), D05109.
- Aubinet, M., Vesala, T., & Papale, D. (2012). *Eddy covariance: a practical guide to measurement and data analysis*. Springer Science & Business Media.
- Barry, R., & Blanken, P. (2016a). *Microclimate and local climate*. 32 Avenue of the Americas, New York: Cambridge University Press. (Chapter 5)
- Barry, R., & Blanken, P. (2016b). *Microclimate and local climate*. 32 Avenue of the Americas, New York: Cambridge University Press. (Chapter 3)
- Barry, R., & Blanken, P. (2016c). *Microclimate and local climate*. 32 Avenue of the Americas, New York: Cambridge University Press. (Chapter 2)
- Blaney, H., & Criddle, W. (1962). *Determining consumptive use and irrigation water requirements* (No. 1275). US Department of Agriculture.
- Chatterjee, D., & et.al. (2017, 12). Eddy covariance technique for micrometeorological measurements. In (p. 91-103).
- Chen, J., & Liu, J. (2020). Evolution of evapotranspiration models using thermal and shortwave remote sensing data. *Remote Sensing of Environment, 237*, 111594. Retrieved from <https://www.sciencedirect.com/science/article/pii/S0034425719306145> doi: <https://doi.org/10.1016/j.rse.2019.111594>
- Cristea, N., Kampf, S., & Burges, S. (2013). Revised coefficients for priestley-taylor and makkin-hansen equations for estimating daily reference evapotranspiration. *Journal of Hydrologic Engineering, 18*(10), 1289–1300.
- Currie, D. (1991). Energy and large-scale patterns of animal-and plant-species richness. *The American Naturalist, 137*(1), 27–49.
- De Bruin, H. (1983). A model for the priestley-taylor parameter α . *Journal of Applied Meteorology and Climatology, 22*(4), 572–578.
- Degano, M., Rivas, R., Carmona, F., Niclos, R., & Sanchez, J. (2021). Evaluation of the mod16a2 evapotranspiration product in an agricultural area of argentina, the pampas region. *The Egyptian Journal of Remote Sensing and Space Science, 24*(2), 319–328.
- Eagleman, J. R. (1967). Pan evaporation, potential and actual evapotranspiration. *Journal of Applied Meteorology and Climatology, 6*(3), 482–488.
- Farnsworth, R. K., Thompson, E. S., & Peck, E. L. (1982). *Evaporation atlas for the contiguous 48 united states*. US Department of Commerce, National Oceanic and Atmospheric Administration
- Fisher, J., Whittaker, R., & Malhi, Y. (2011). Et come home: potential evapotranspiration in geographical ecology. *Global Ecology and Biogeography, 20*(1), 1–18.
- Gates, D. M. (1968). Transpiration and leaf temperature. *Annual Review of Plant Physiology, 19*(1), 211–238.

- Gavin, H., & Agnew, C. (2004). Modelling actual, reference and equilibrium evaporation from a temperate wet grassland. *Hydrological Processes*, 18(2), 229–246.
- Genfo, A. D. D., Lacin, A. A., & Ruedy, R. A. (1991). Simulations of the effect of a warmer climate on atmospheric humidity. *Nature*, 351(6325), 382–385.
- Grinde, L., Mamen, J., & Tunheim, K. (2021). Klimatologisk månedsoversikt august og sommersesongen 2021. *Meteorologisk institutt: Været i Norge*.
- Grismer, M., Orang, M., Snyder, R., & Matyac, R. (2002). Pan evaporation to reference evapotranspiration conversion methods. *Journal of irrigation and drainage engineering*, 128(3), 180–184.
- Hu, G., Jia, L., & Menenti, M. (2015). Comparison of mod16 and lsa-saf msg evapotranspiration products over europe for 2011. *Remote Sensing of Environment*, 156, 510–526.
- Jackson, R., Carpenter, S., Dahm, C., McKnight, D., Naiman, R., Postel, S., & Running, S. (2001). Water in a changing world. *Ecological applications*, 11(4), 1027–1045.
- Jasechko, S., Sharp, Z., Gibson, J., & et.al. (2013). Terrestrial water fluxes dominated by transpiration. *Nature*, 496(7445), 347–350.
- Kopp, G., & Lean, J. (2011). A new, lower value of total solar irradiance: Evidence and climate significance. *Geophysical Research Letters*, 38(1).
- Kustas, W., Stannard, D., & Allwine, K. (1996). Variability in surface energy flux partitioning during washita'92: Resulting effects on penman-monteith and priestley-taylor parameters. *Agricultural and Forest Meteorology*, 82(1-4), 171–193.
- Lhomme, J. (1991). The concept of canopy resistance: historical survey and comparison of different approaches. *Agricultural and forest meteorology*, 54(2-4), 227–240.
- Liu, Y., Chen, J., & Pan, T. (2019). Analysis of changes in reference evapotranspiration, pan evaporation, and actual evapotranspiration and their influencing factors in the north china plain during 1998–2005. *Earth and Space Science*, 6(8), 1366–1377.
- Mamen, J., Tajet, H., & Tunheim, K. (2022). Klimatologisk månedsoversikt august og sommersesongen 2022. *Meteorologisk institutt: Været i Norge*.
- Marek, R., & Straub, J. (2001). Analysis of the evaporation coefficient and the condensation coefficient of water. *International Journal of Heat and Mass Transfer*, 44(1), 39–53.
- Masson-Delmotte, V., Zhai, P., Pirani, A., Connors, S., Péan, C., . . . Zhou, B. e. (2021). Summary for policymakers. in: Climate change 2021: The physical science basis. contribution of working group i to the sixth assessment report of the intergovernmental panel on climate change. *IPCC*. (pp. 332, doi:10.1017/9781009157896.001)
- Monson, R., & Baldocchi, D. (2014a). *Terrestrial biosphere-atmosphere fluxes*. 32 Avenue of the Americas, New York: Cambridge University Pres. (Chapter 10)
- Monson, R., & Baldocchi, D. (2014b). *Terrestrial biosphere-atmosphere fluxes*. 32 Avenue of the Americas, New York: Cambridge University Pres. (Chapter 13)
- NASA. (n.d.). *What is remote sensing?* Retrieved from <https://www.earthdata.nasa.gov/learn/backgrounders/remote-sensing> (gathered: 16.03.2023)

- Newport-Corporation. (n.d.). *Introduction to solar radiation*. (url: <https://www.newport.com/t/introduction-to-solar-radiation>, gathered: 10.03.2023)
- NMBU. (2009). *Feltstasjon for bioklimatiske studier – bioklim*. (<https://www.nmbu.no/fakultet/realtek/laboratorier/bioklim/om-fagklim/node/10257>, published: 07.11.2009, updated: 23.08.2021, gathered: 24.02.2023)
- NMBU. (2014). *Nedbør, fordampning og luftfuktighet*. (<https://www.nmbu.no/fakultet/realtek/laboratorier/bioklim/maleinstrumenter/nedbor#FOR>, published: 24.06.2014, updated: 17.08.2021, gathered: 24.02.2023)
- O’Brien, E. (1993). Climatic gradients in woody plant species richness: towards an explanation based on an analysis of southern africa’s woody flora. *Journal of biogeography*, 181–198.
- Peng, L., Zeng, Z., Wei, Z., Chen, A., Wood, E., & Sheffield, J. (2019). Determinants of the ratio of actual to potential evapotranspiration. *Global change biology*, 25(4), 1326–1343.
- Priestley, C., & Taylor, R. (1972). On the assessment of surface heat flux and evaporation using large-scale parameters. *Monthly weather review*, 100(2), 81–92.
- Ruairuen, W., Fochesatto, G. J., Sparrow, E. B., Schnabel, W., Zhang, M., & Kim, Y. (2015). Evapotranspiration cycles in a high latitude agroecosystem: Potential warming role. *PloS One*, 10(9), e0137209.
- Rutger, D. (2002). *Sub-arctic hydrology and climate change: a case study of the tana river basin in northern fennoscandia* (Unpublished doctoral dissertation).
- Smajstrla, A., Zazueta, F., Clark, G., & Pitts, D. (2000). Irrigation scheduling with evaporation pans. *Bulletin*, 254.
- TETB. (n.d.). Retrieved from https://www.engineeringtoolbox.com/air-specific-heat-capacity-d_705.html (The Engineering ToolBox)
- Trenberth, K. E. (1999). Conceptual framework for changes of extremes of the hydrological cycle with climate change. *Weather and climate extremes: Changes, variations and a perspective from the insurance industry*, 327–339.
- Trenberth, K. E., & Smith, L. (2005). The mass of the atmosphere: A constraint on global analyses. *Journal of Climate*, 18(6), 864–875.
- UMT. (n.d.-a). Retrieved from <https://www.umontana.edu/numerical-terradynamic-simulation-group/project/modis/default.php> (Numerical Terradynamic Simulation Group, University of Montana)
- UMT. (n.d.-b). Retrieved from <https://www.umontana.edu/numerical-terradynamic-simulation-group/project/modis/mod16.php> (Numerical Terradynamic Simulation Group, University of Montana)
- Wolff, M. (2023). Meteorologiske data for Ås 2022. (ISBN: In print)
- Wolff, M., & Grimenes, A. (2022). Meteorologiske data for Ås 2021. (ISBN: 978-82-7636-035-6)

- Wolff, M., Thue-Hansen, V., & Grimenes, A. (2019). Meteorologiske data for Ås 2018. (ISBN: 978-82-7636-032-5)
- W.R, S., Qiaozhen, M., Maosheng, Z., & Alvaro, M. (2021). User's guide modis global terrestrial evapotranspiration (et) product (mod16a2/a3 and year-end gap-filled mod16a2gf/a3gf) nasa earth observing system modis land algorithm (for collection 6.1). (Version 1.1)
- Xu, C.-Y., & Singh, V. (2001). Evaluation and generalization of temperature-based methods for calculating evaporation. *Hydrological processes*, 15(2), 305–319.

Appendix A: Meteorological parameters

Evapotranspiration

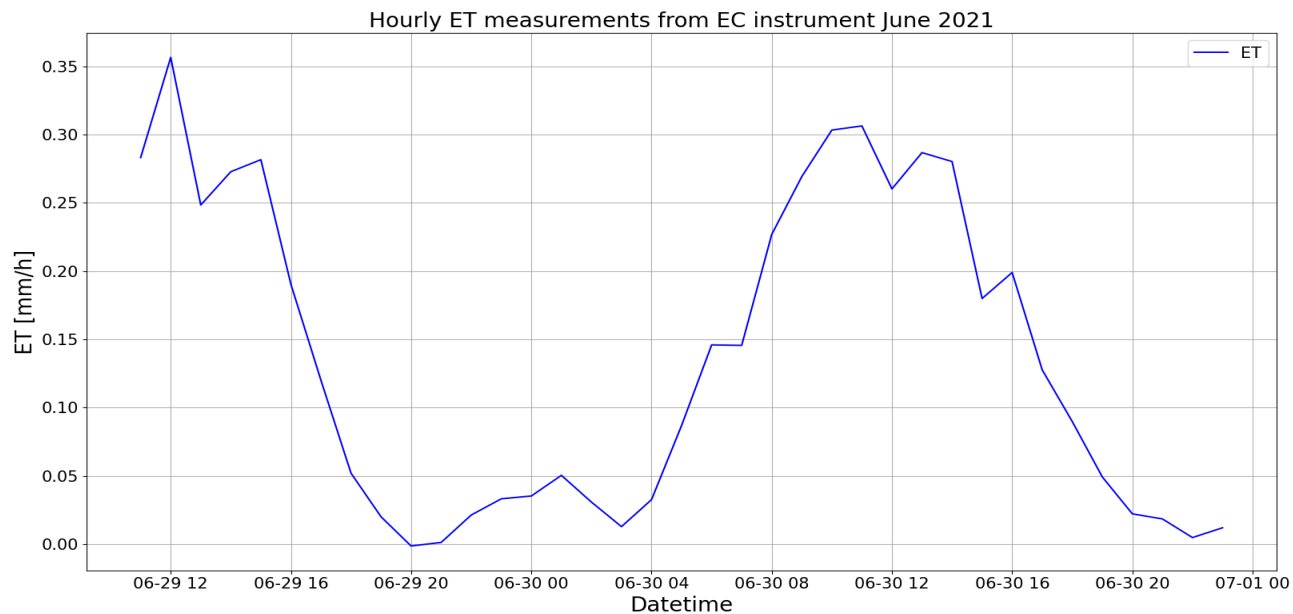


Figure 39: *Hourly evapotranspiration measurements in June 2021.*

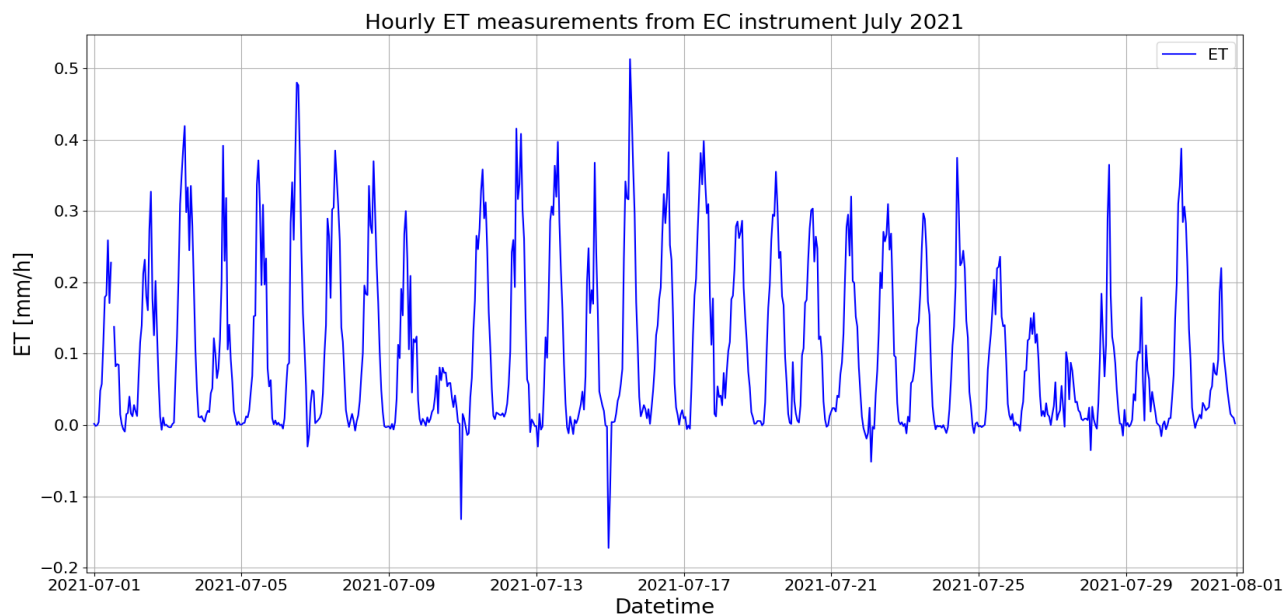


Figure 40: *Hourly evapotranspiration measurements in July 2021.*

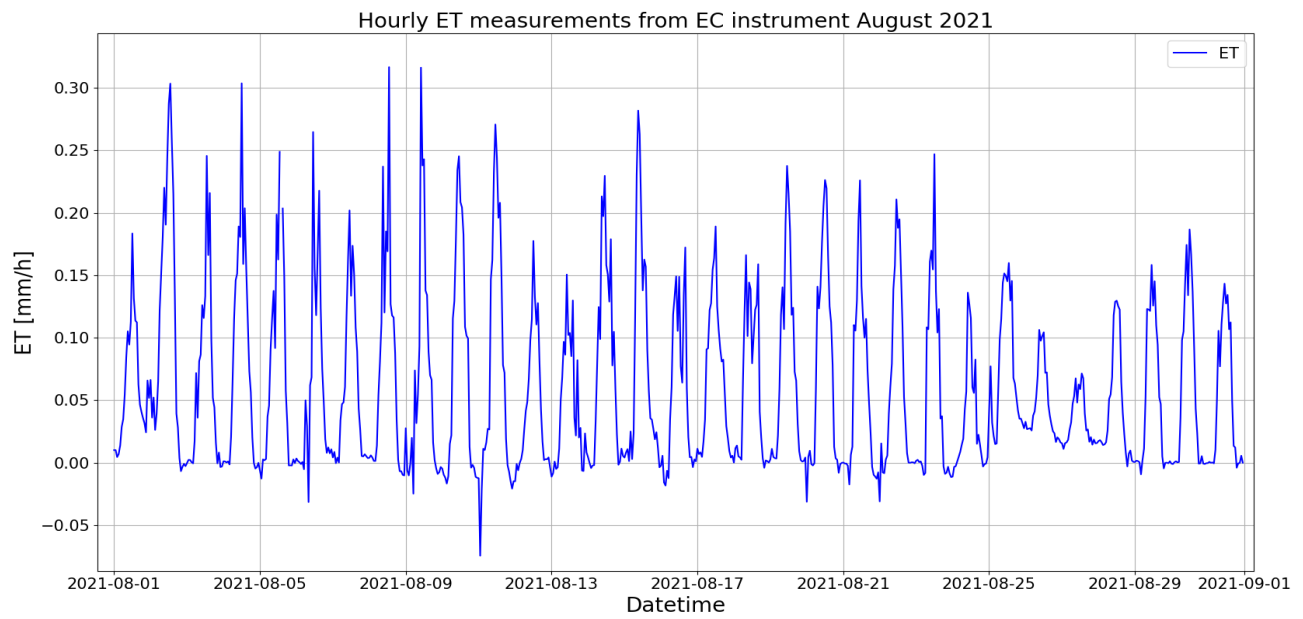


Figure 41: *Hourly evapotranspiration measurements in August 2021.*

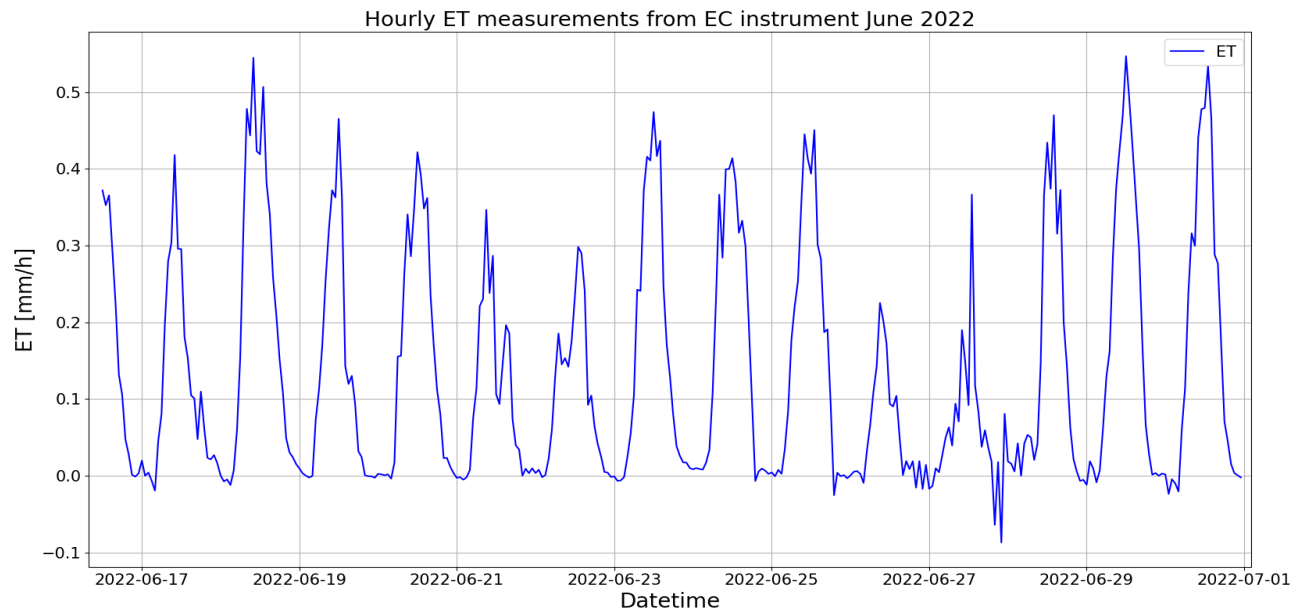


Figure 42: *Hourly evapotranspiration measurements in June 2022.*

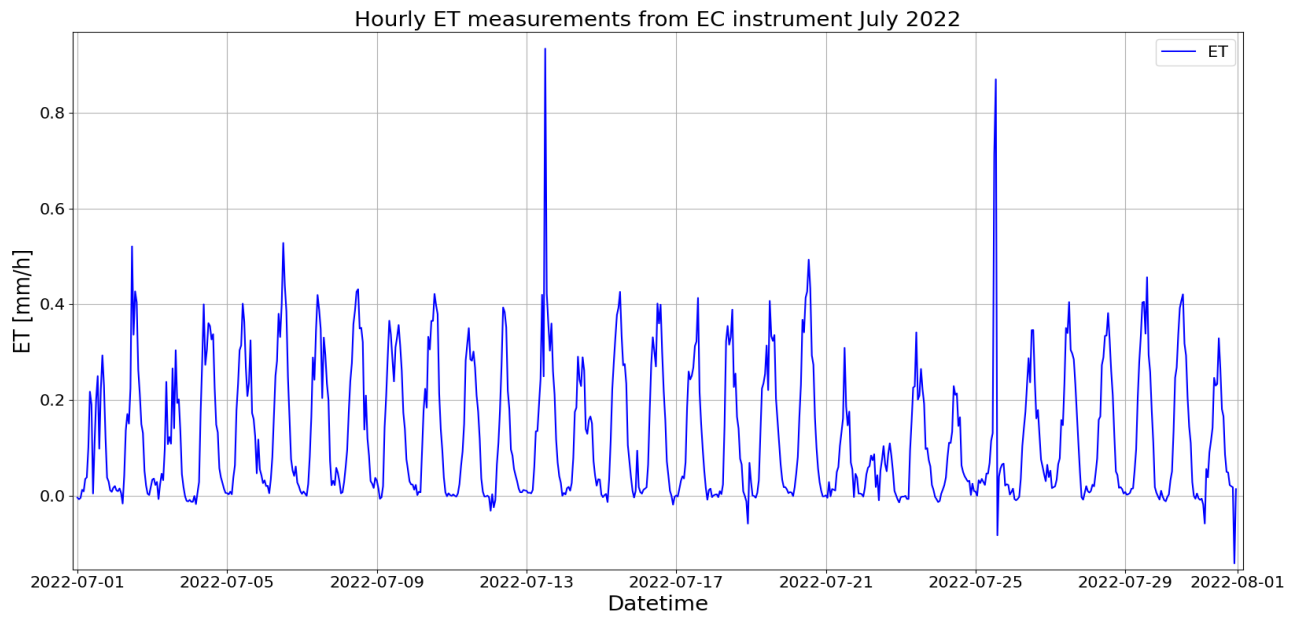


Figure 43: *Hourly evapotranspiration measurements in July 2022.*

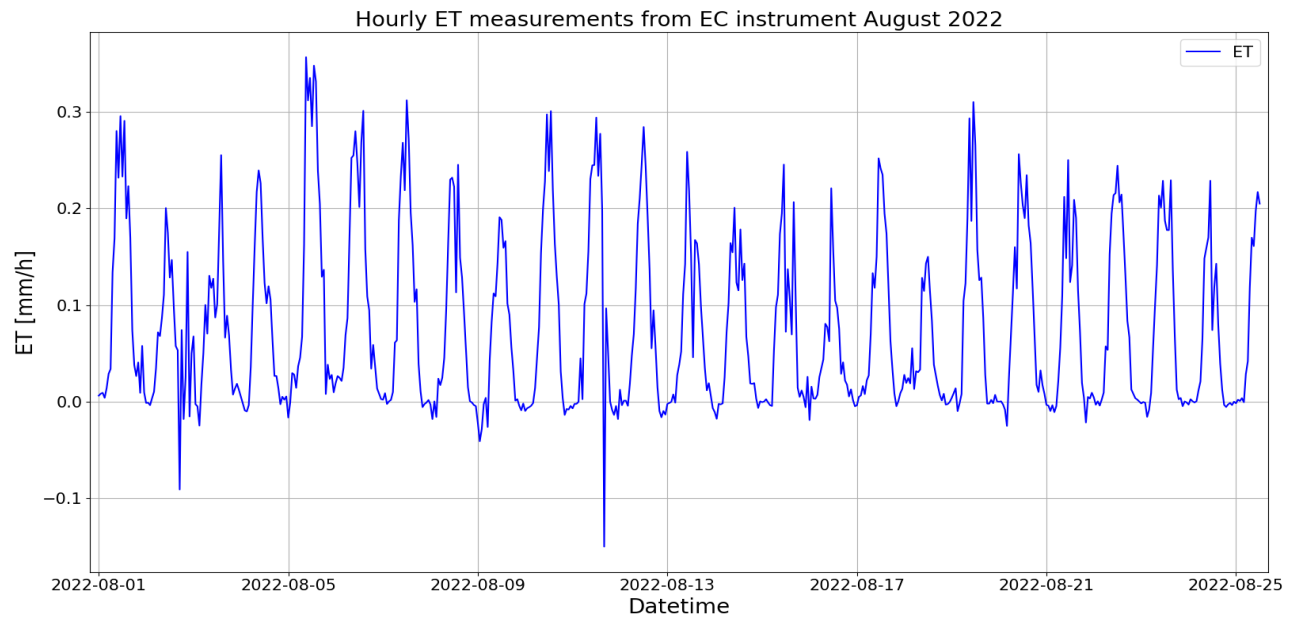


Figure 44: *Hourly evapotranspiration measurements in August 2022.*

Pan evaporation

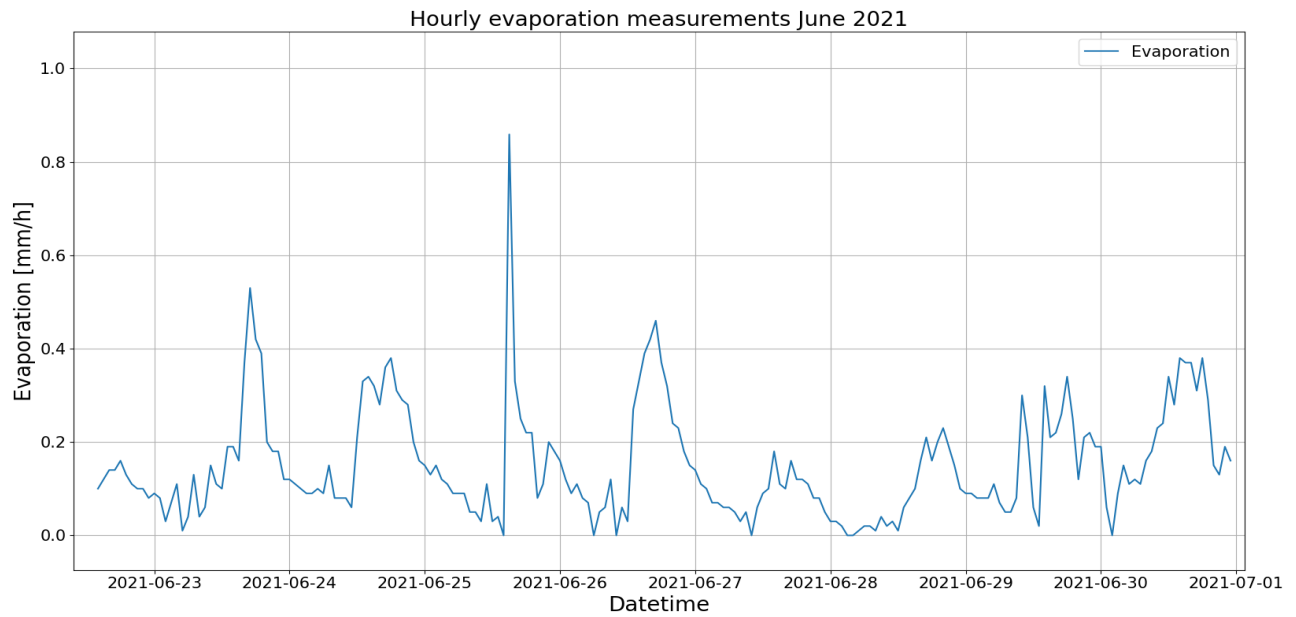


Figure 45: *Hourly pan evaporation measurements in June 2021.*

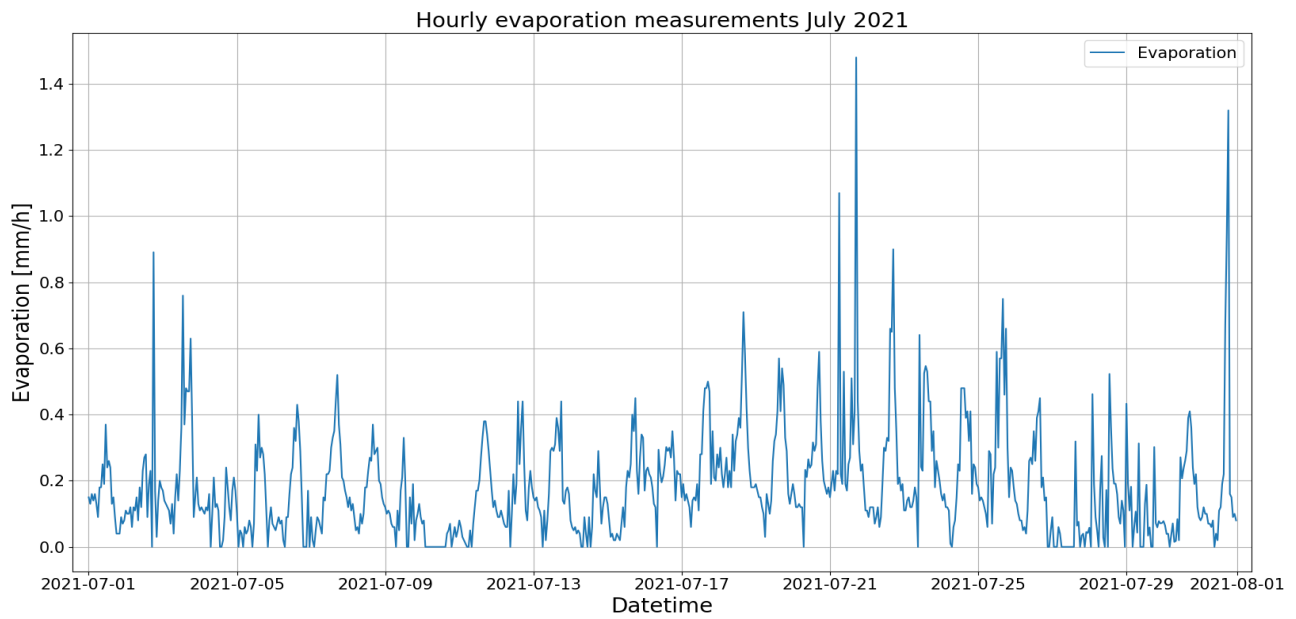


Figure 46: *Hourly pan evaporation measurements in July 2021.*

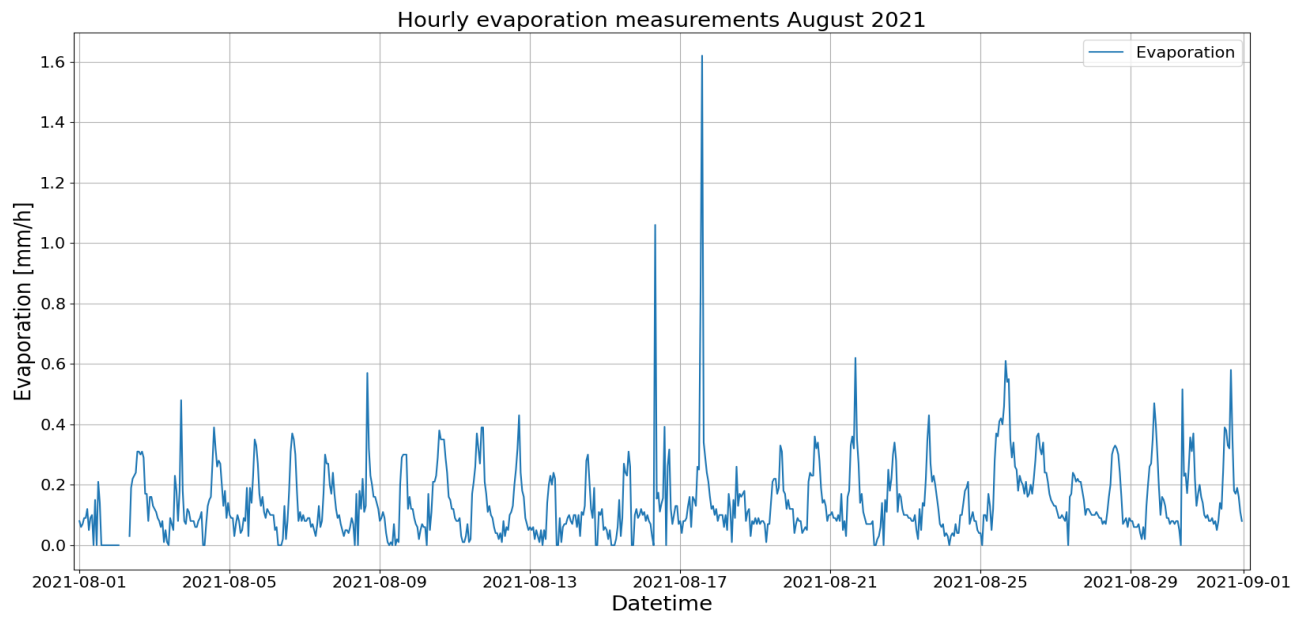


Figure 47: *Hourly pan evaporation measurements in August 2021.*

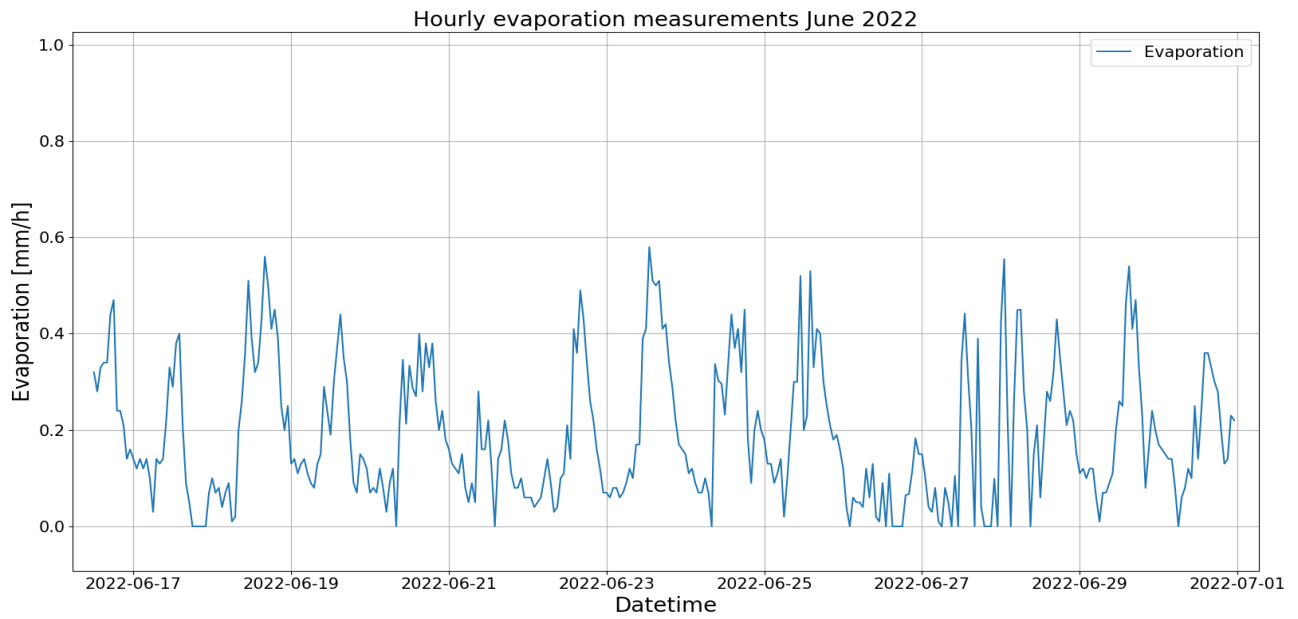


Figure 48: *Hourly pan evaporation measurements in June 2022.*

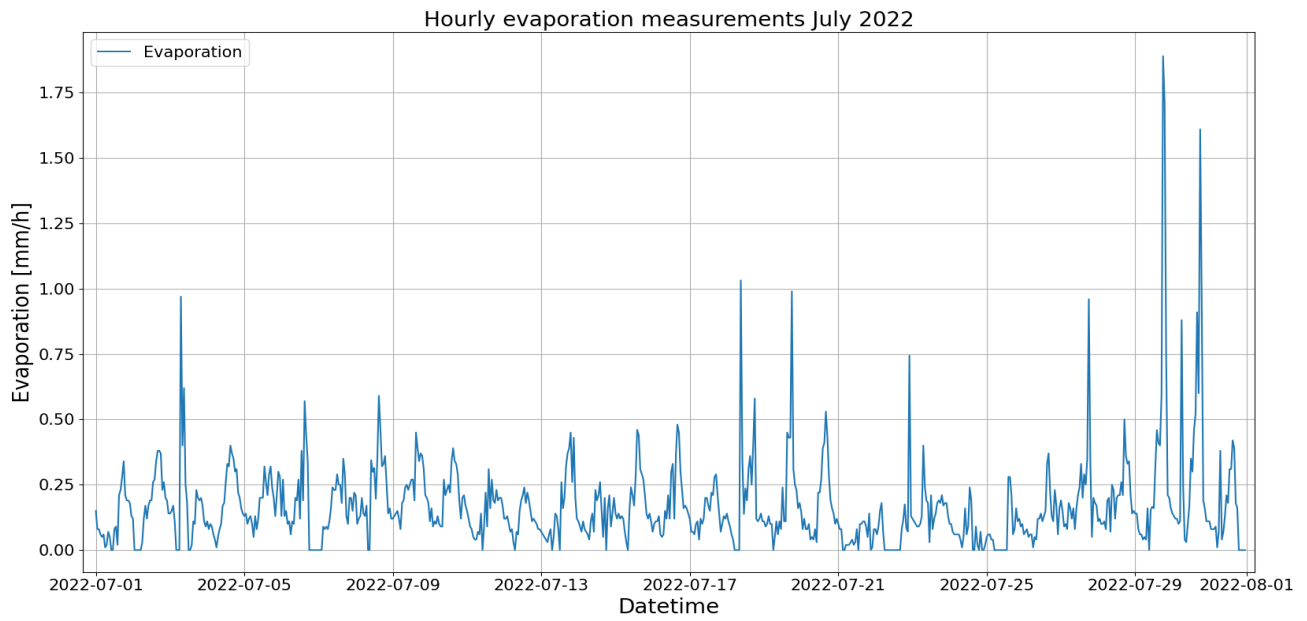


Figure 49: *Hourly pan evaporation measurements in July 2022.*

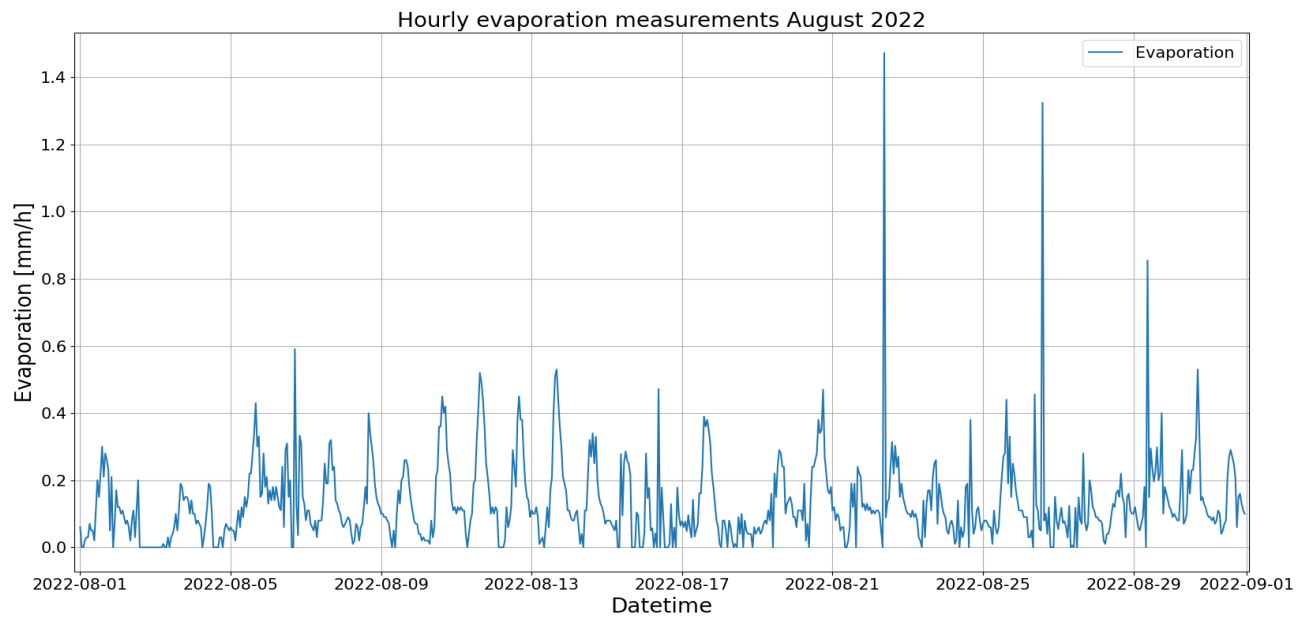


Figure 50: *Hourly pan evaporation measurements in August 2022.*

Net radiation

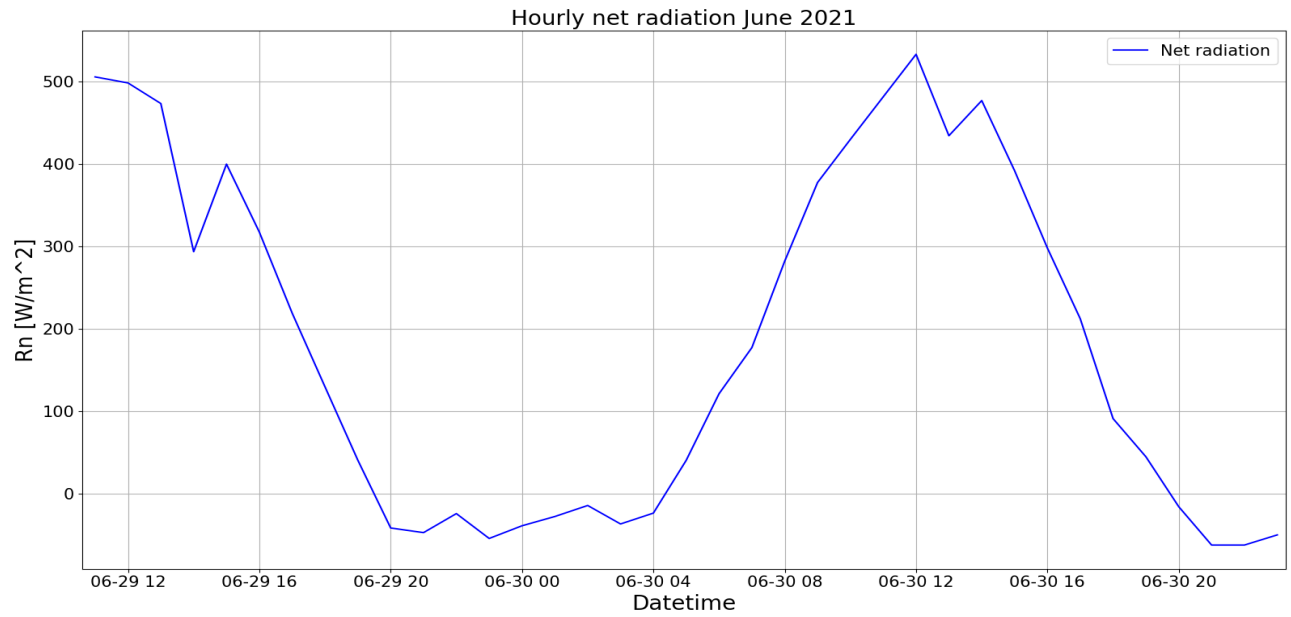


Figure 51: *Hourly measured net radiation in June 2021.*

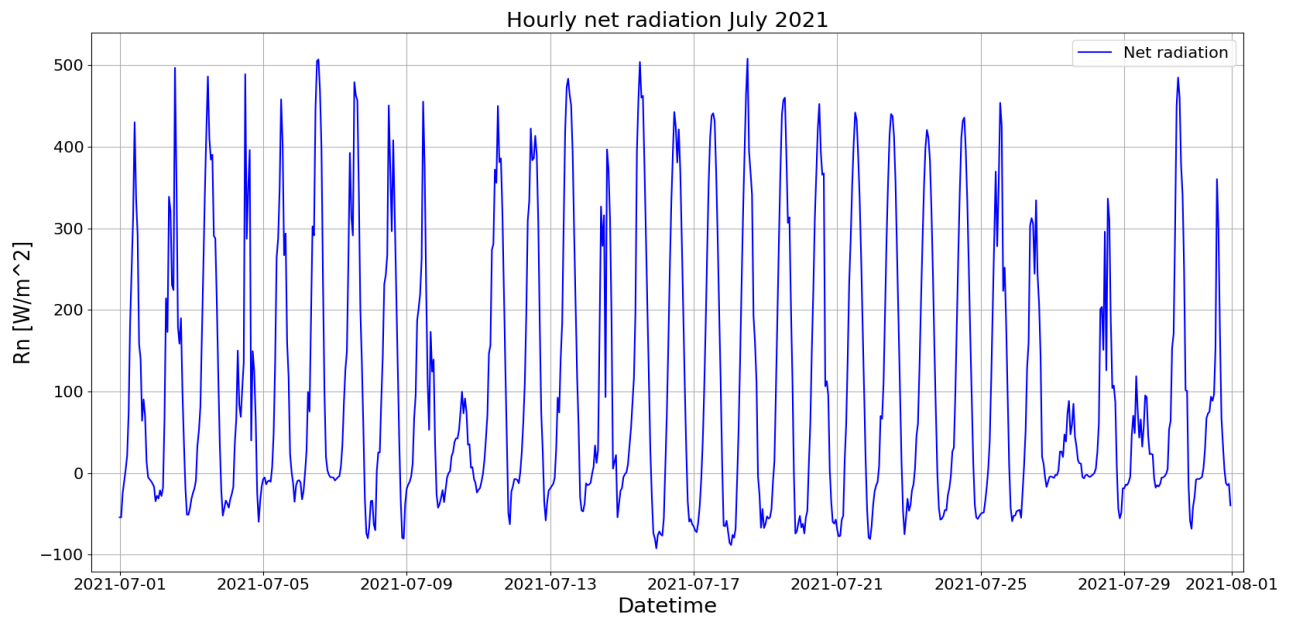


Figure 52: *Hourly measured net radiation in July 2021.*

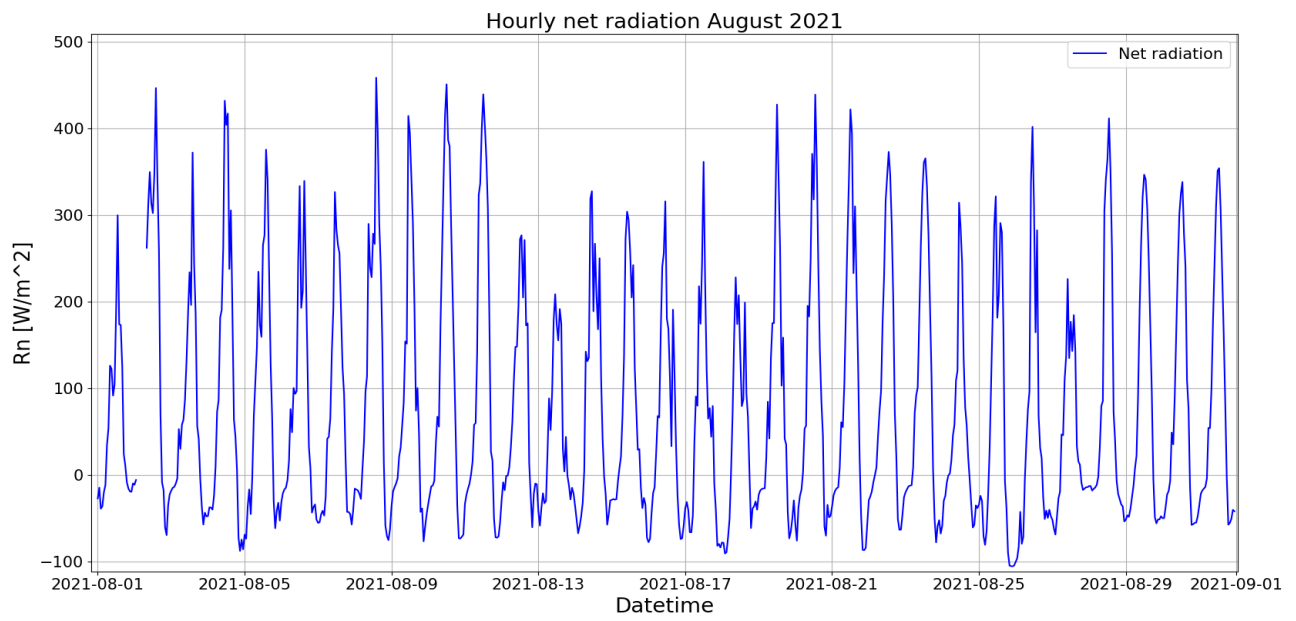


Figure 53: *Hourly measured net radiation in August 2021.*

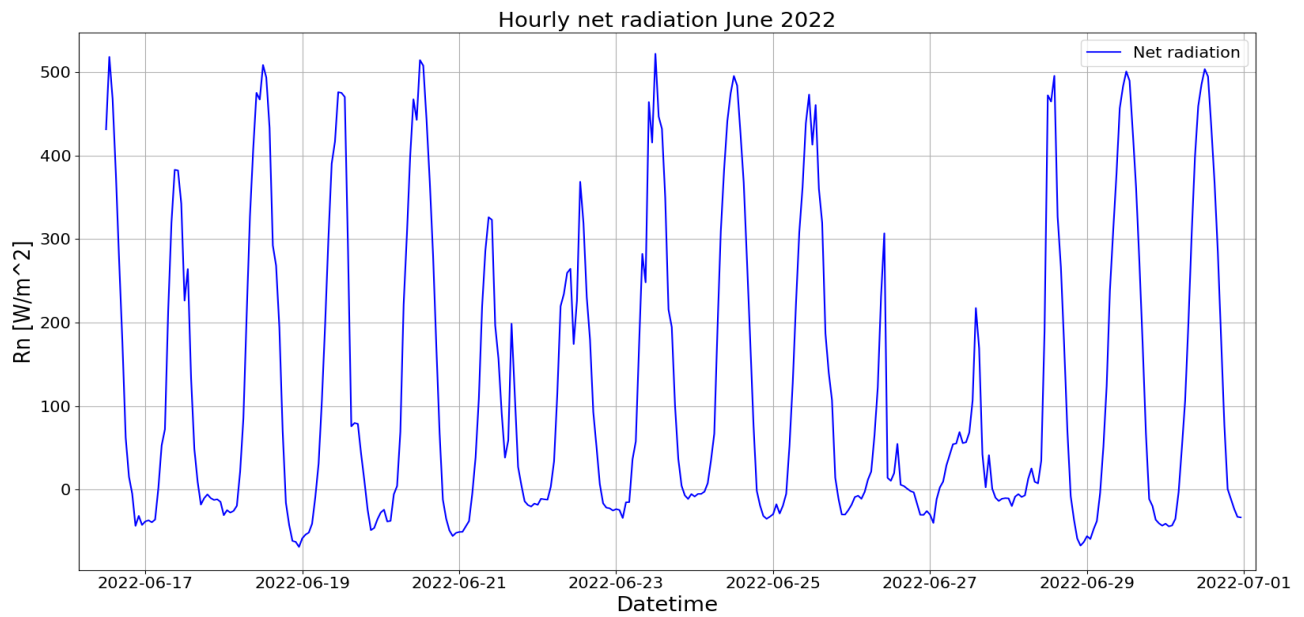


Figure 54: *Hourly measured net radiation in June 2022.*

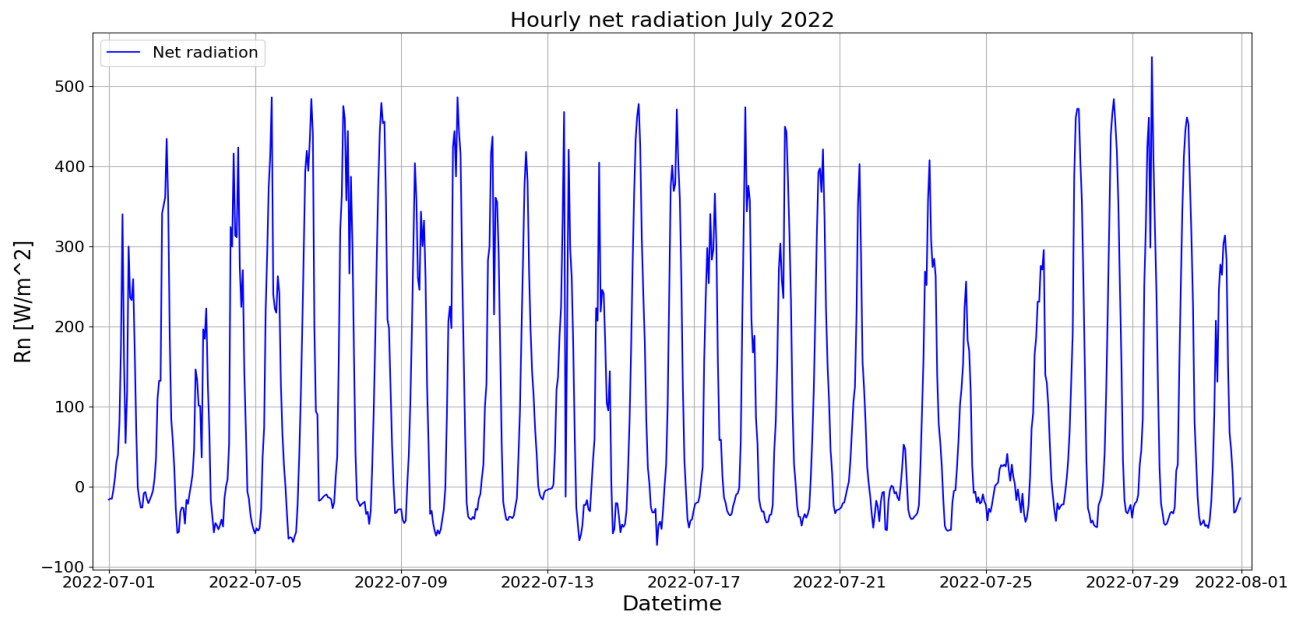


Figure 55: *Hourly measured net radiation in July 2022.*

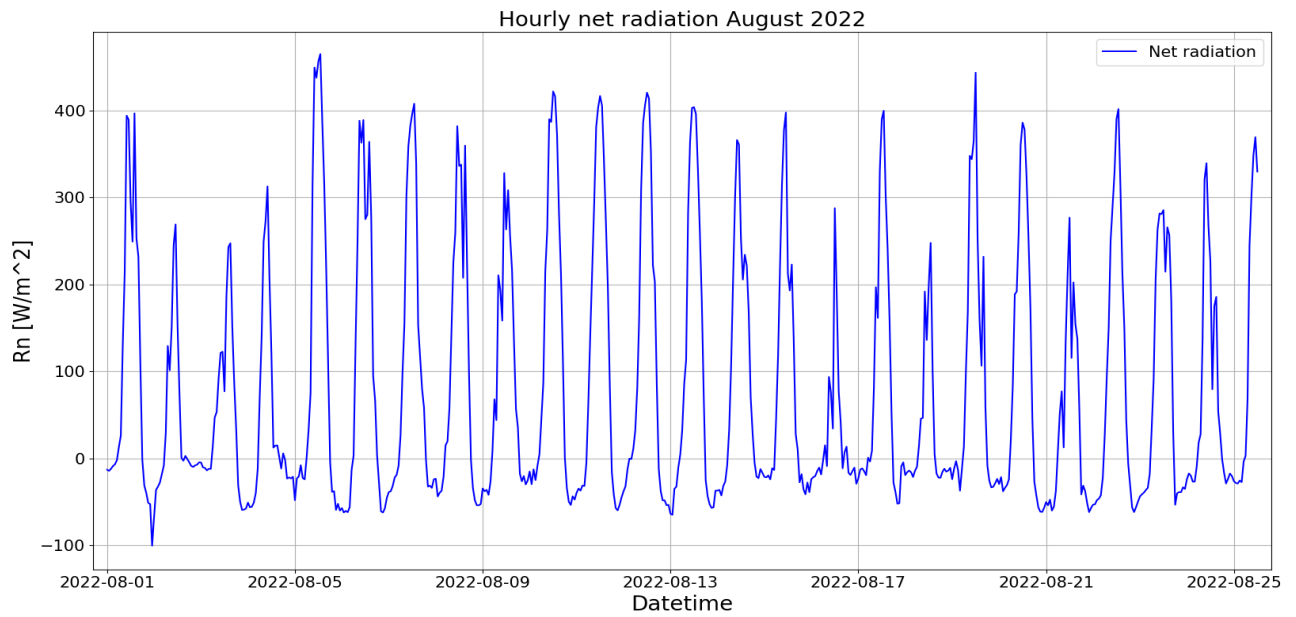


Figure 56: *Hourly measured net radiation in August 2022.*

Ground heat flux

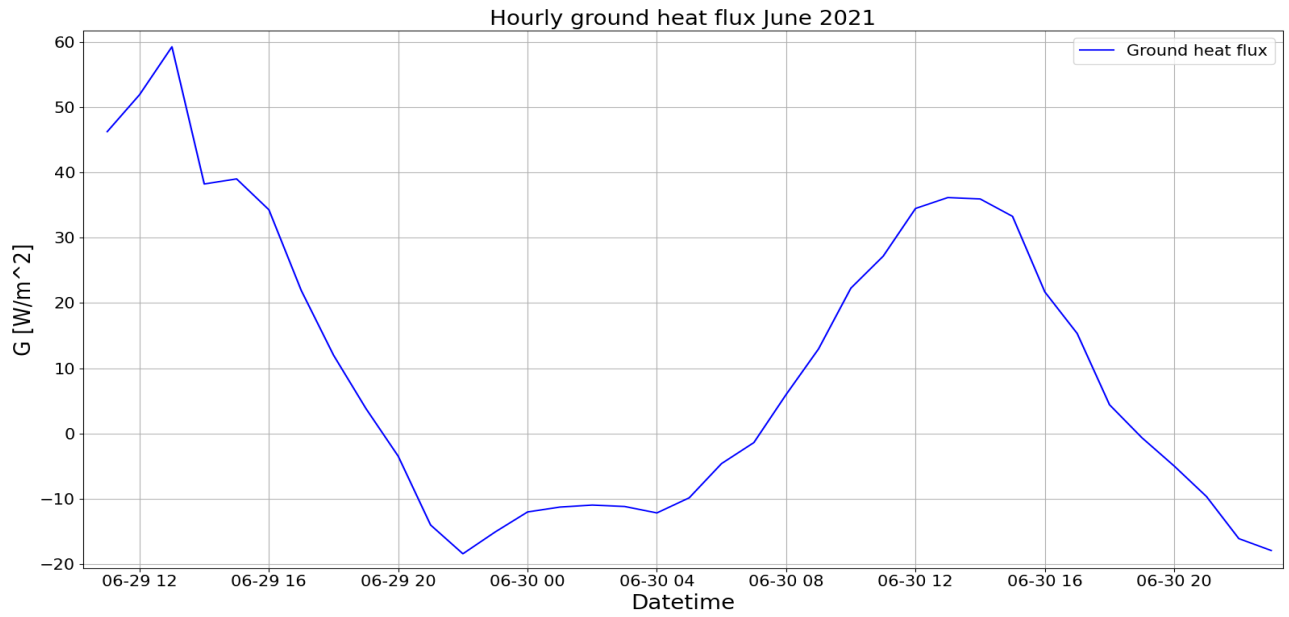


Figure 57: Hourly measured ground heat flux in June 2021.

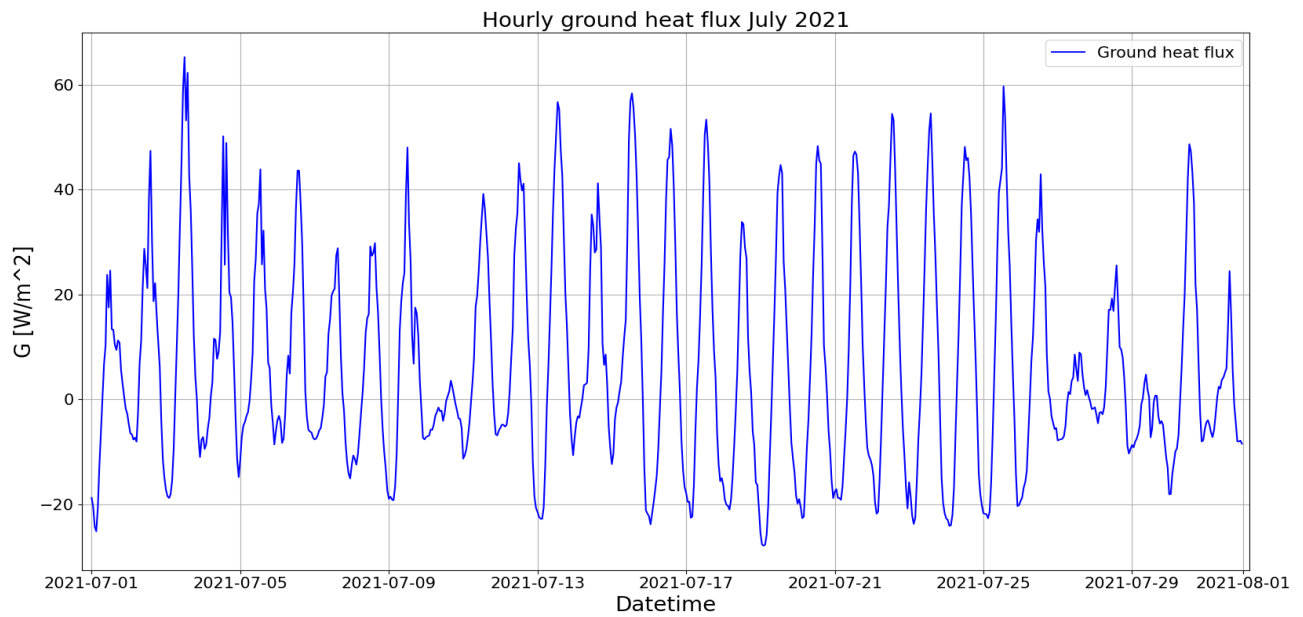


Figure 58: Hourly measured ground heat flux in July 2021.

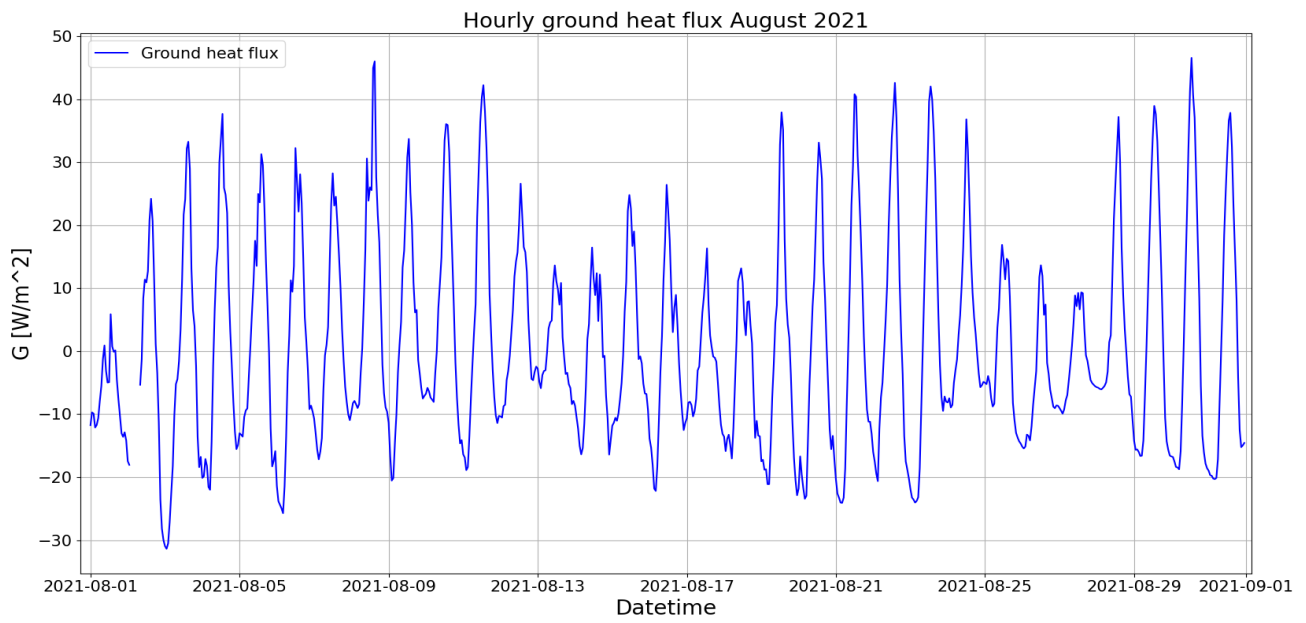


Figure 59: *Hourly measured ground heat flux in August 2021.*

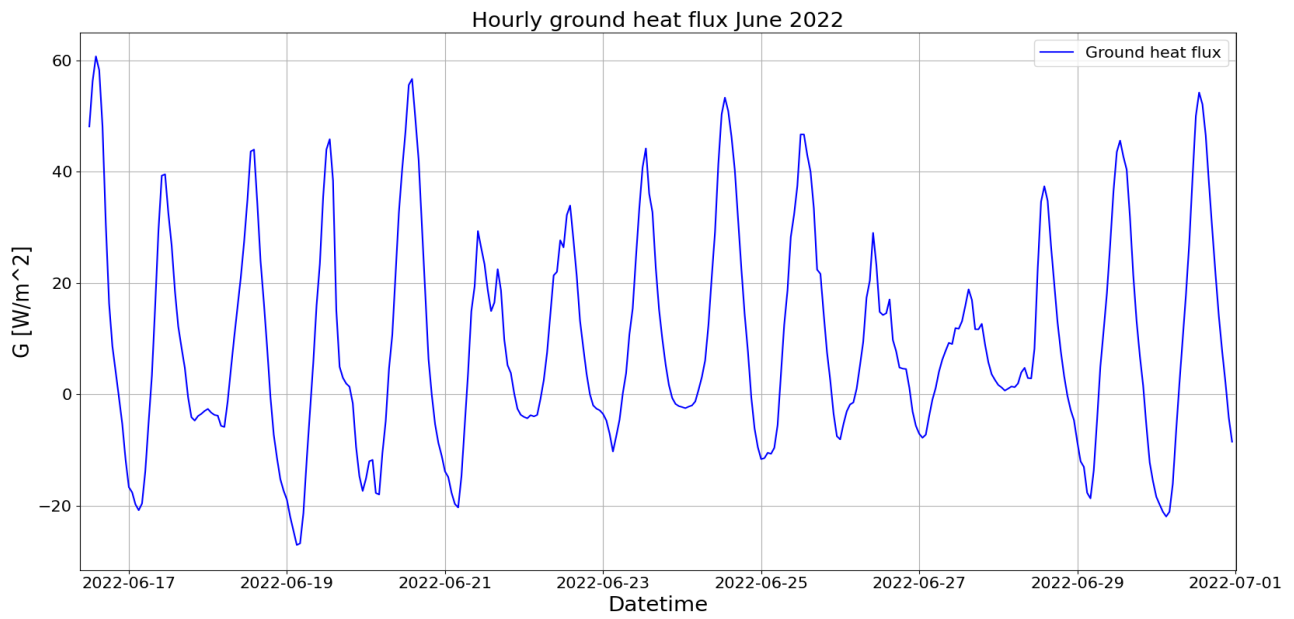


Figure 60: *Hourly measured ground heat flux in June 2022.*

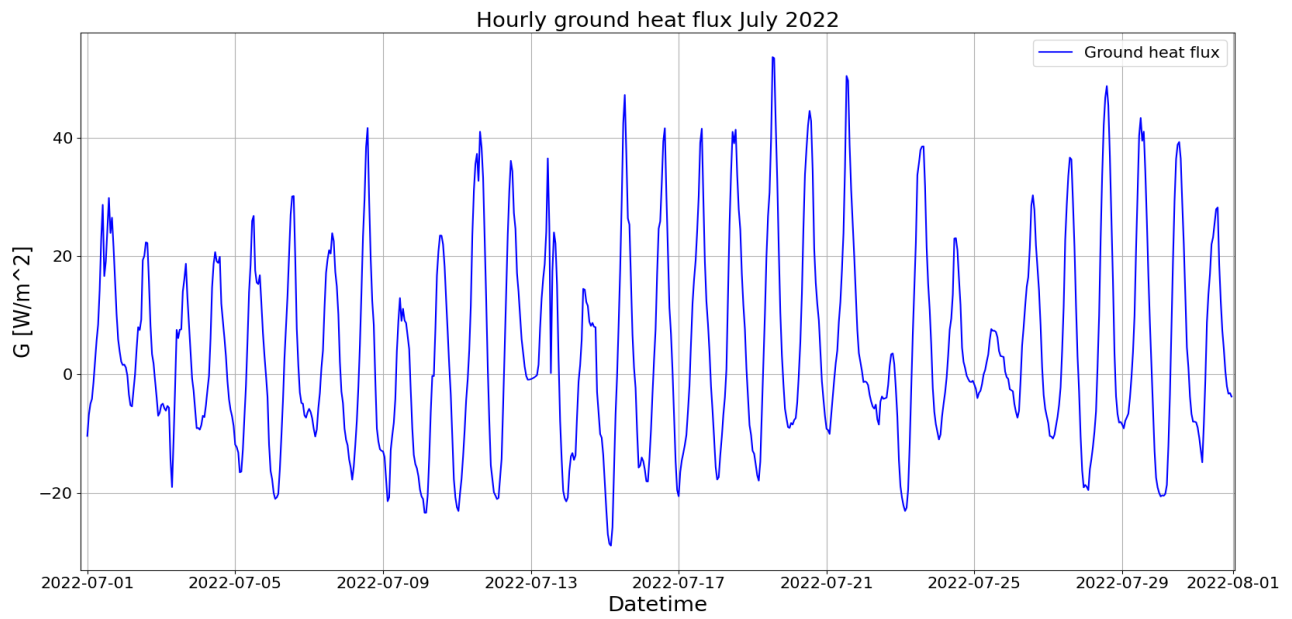


Figure 61: *Hourly measured ground heat flux in July 2022.*

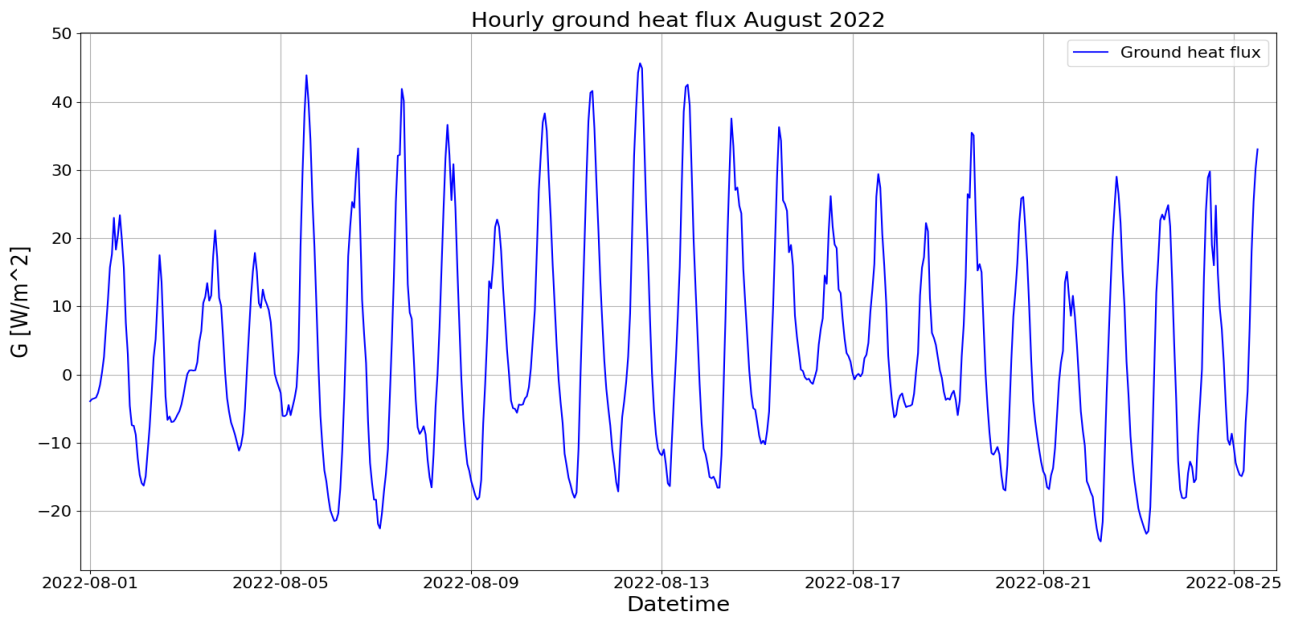


Figure 62: *Hourly measured ground heat flux in August 2022.*

Air temperature

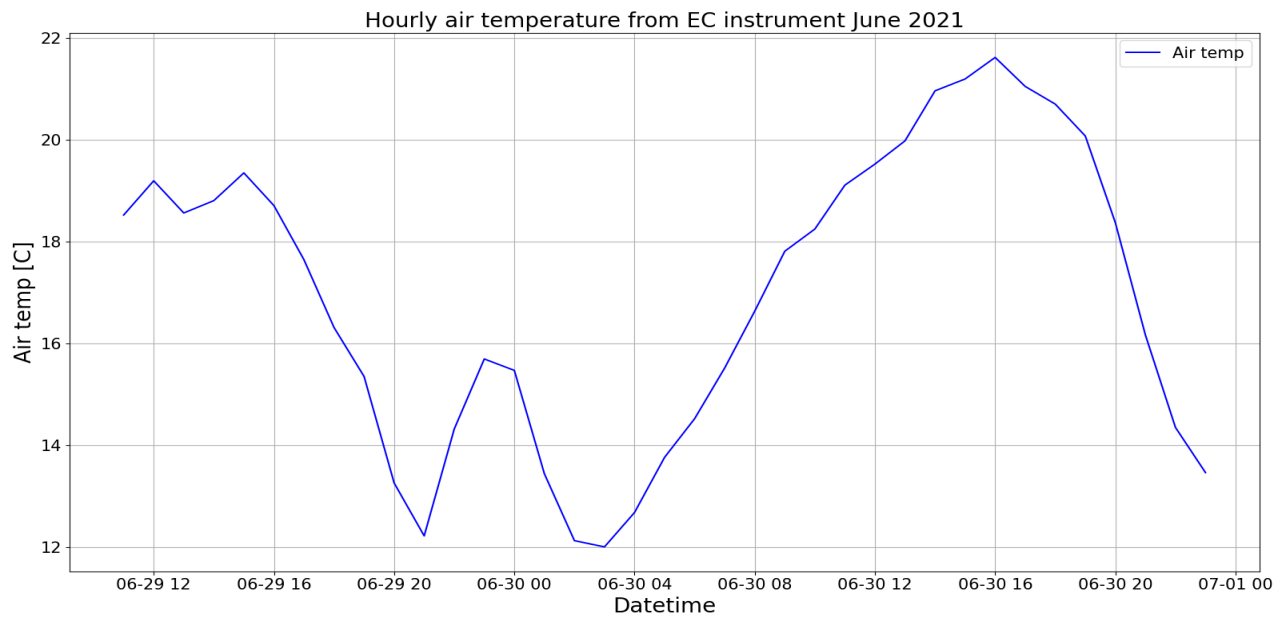


Figure 63: *Hourly measured air temperature in June 2021.*

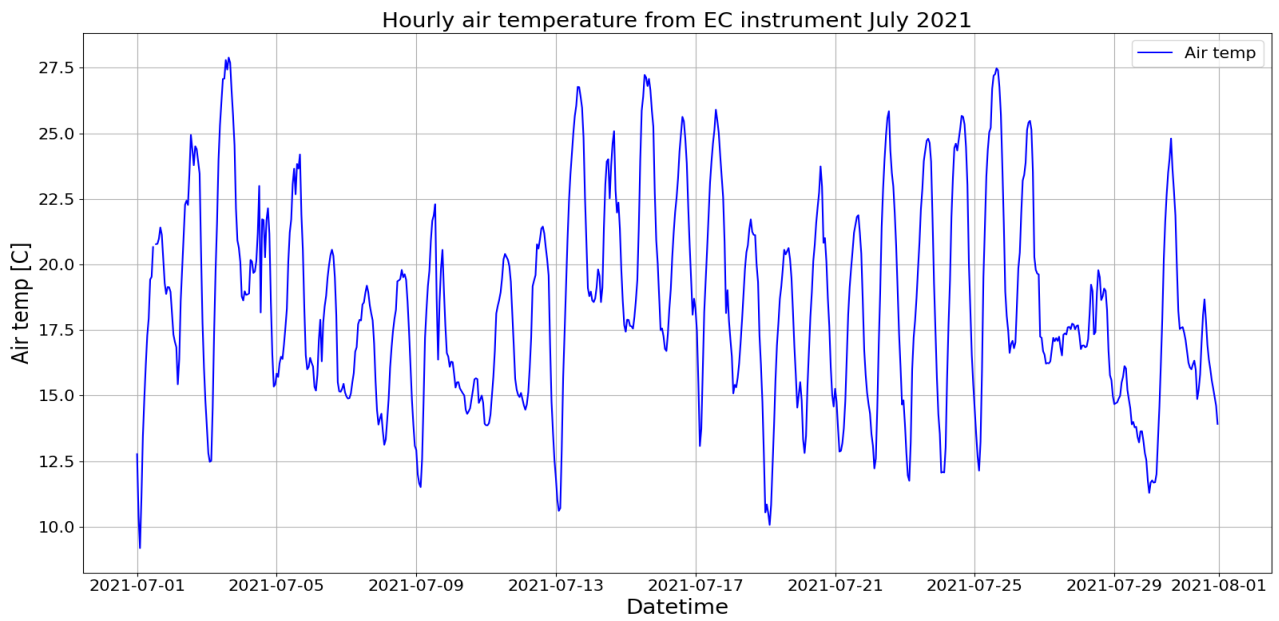


Figure 64: *Hourly measured air temperature in July 2021.*

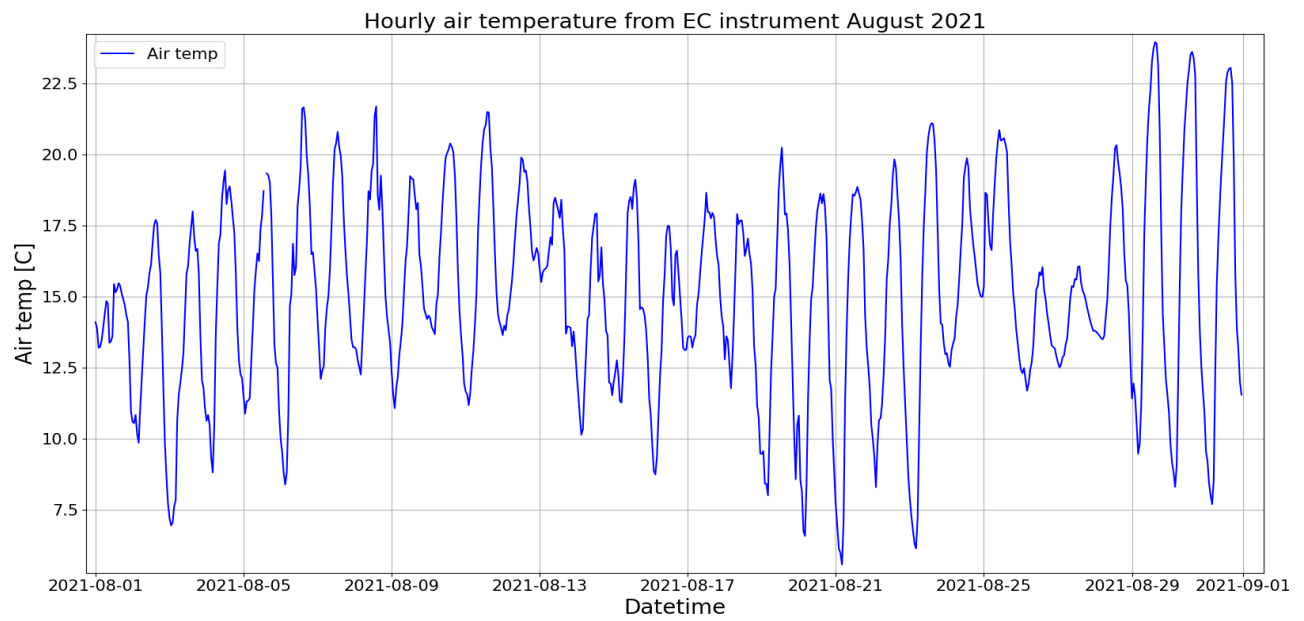


Figure 65: *Hourly measured air temperature in August 2021.*

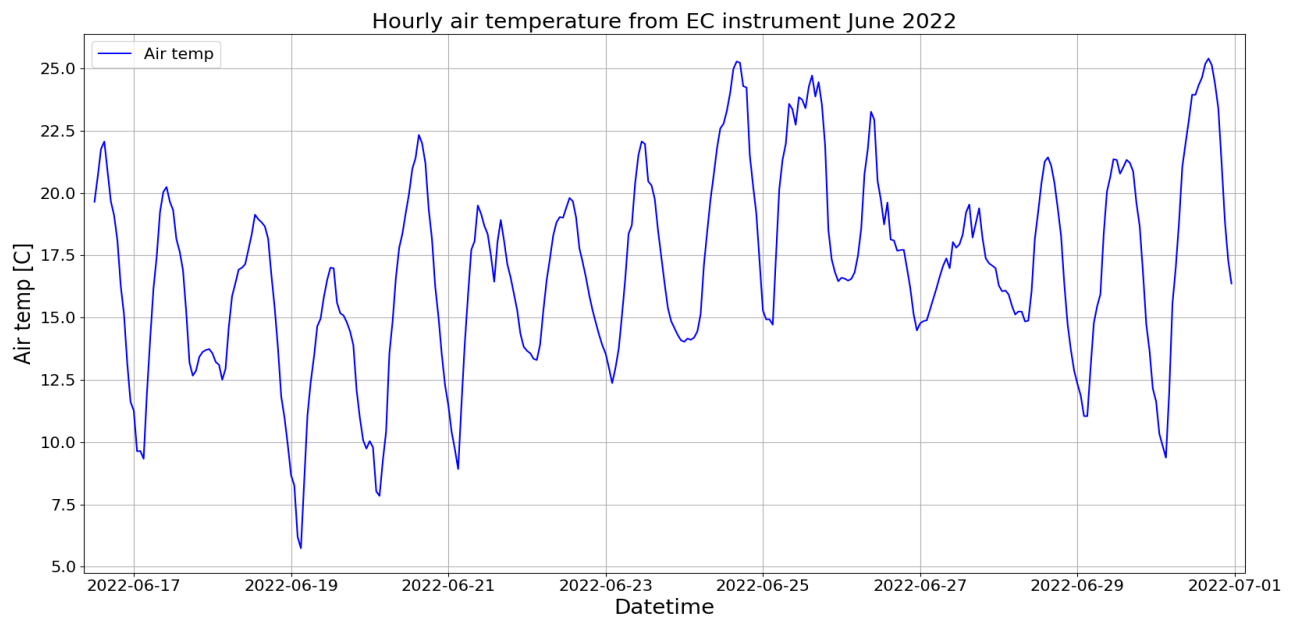


Figure 66: *Hourly measured air temperature in June 2022.*

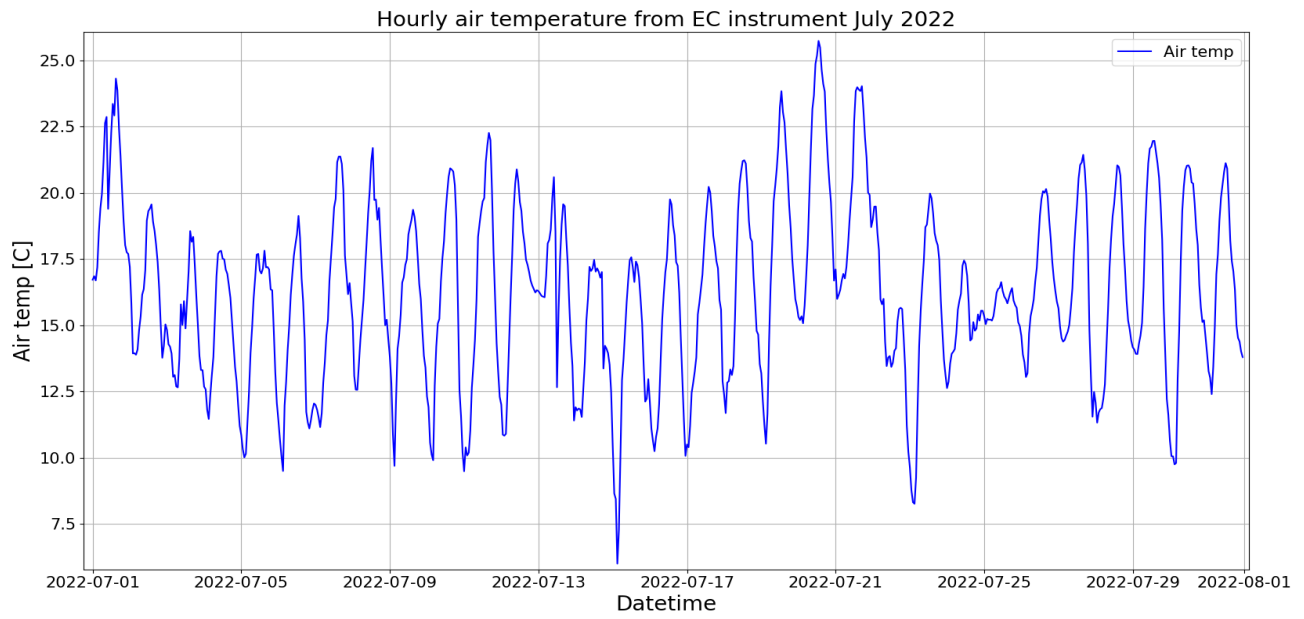


Figure 67: *Hourly measured air temperature in July 2022.*

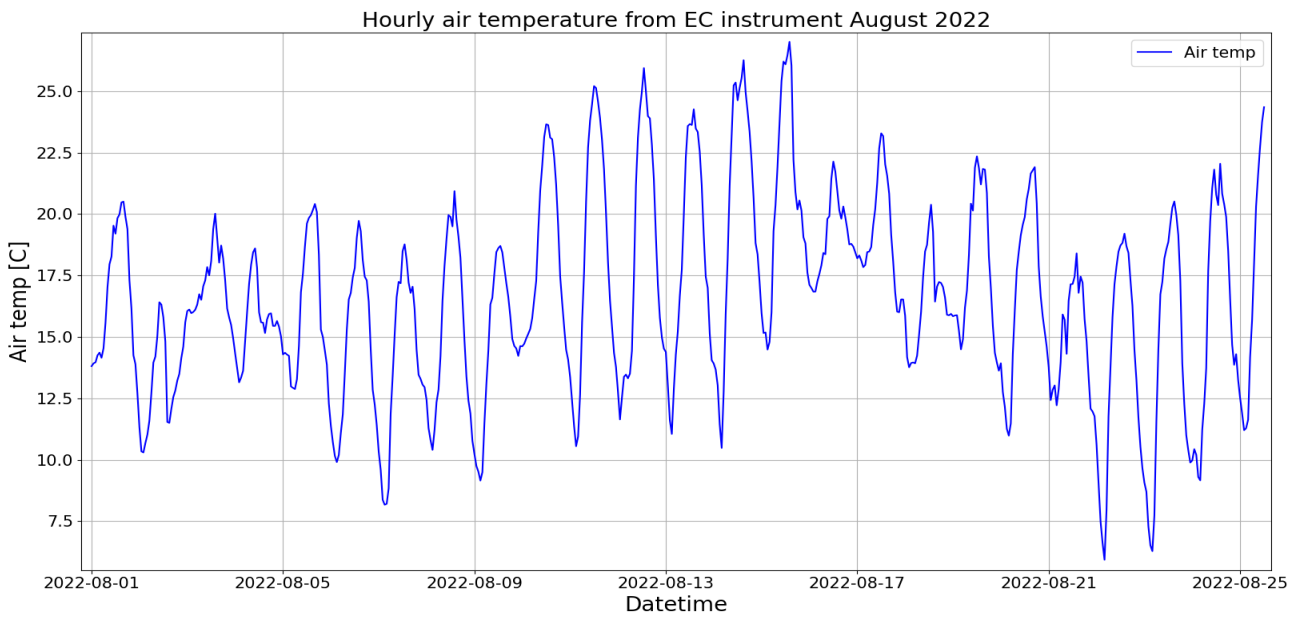


Figure 68: *Hourly measured air temperature in August 2022.*

Air pressure

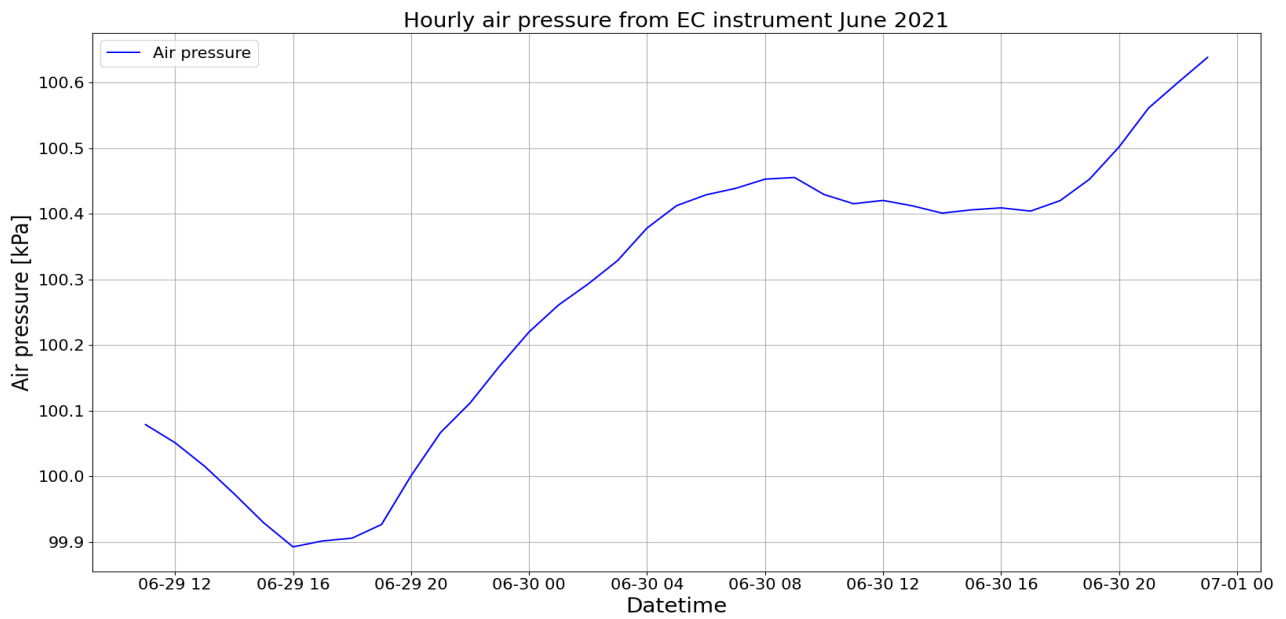


Figure 69: Hourly measured air pressure in June 2021.

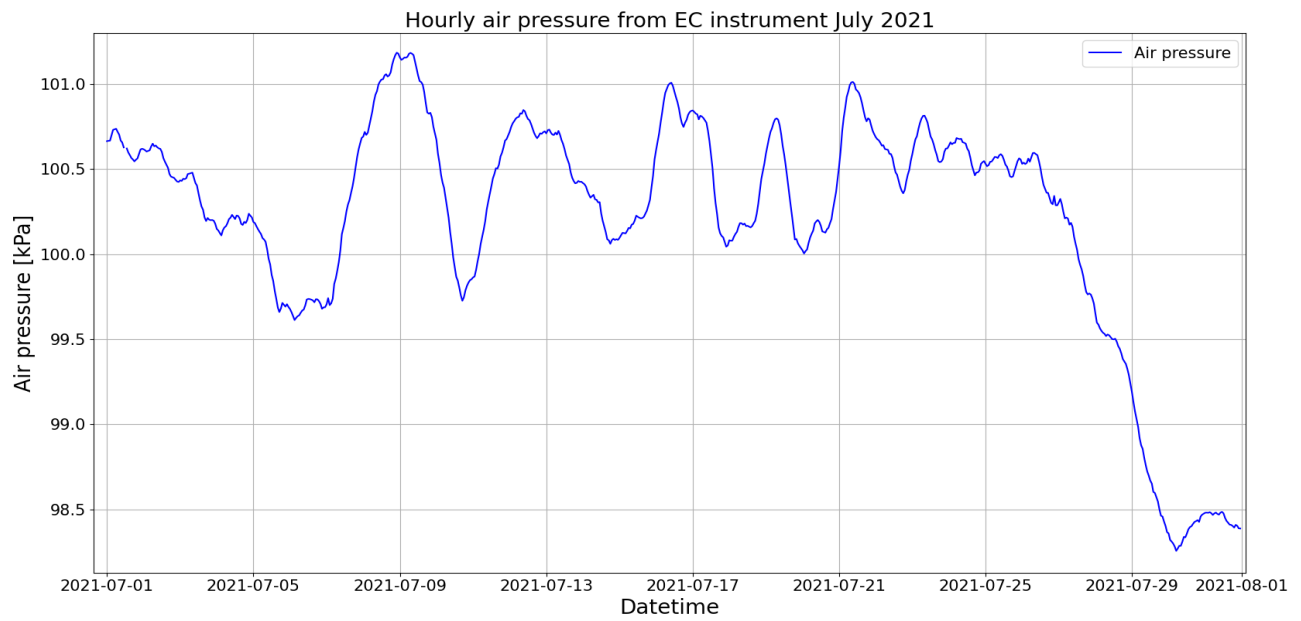


Figure 70: Hourly measured air pressure in July 2021.

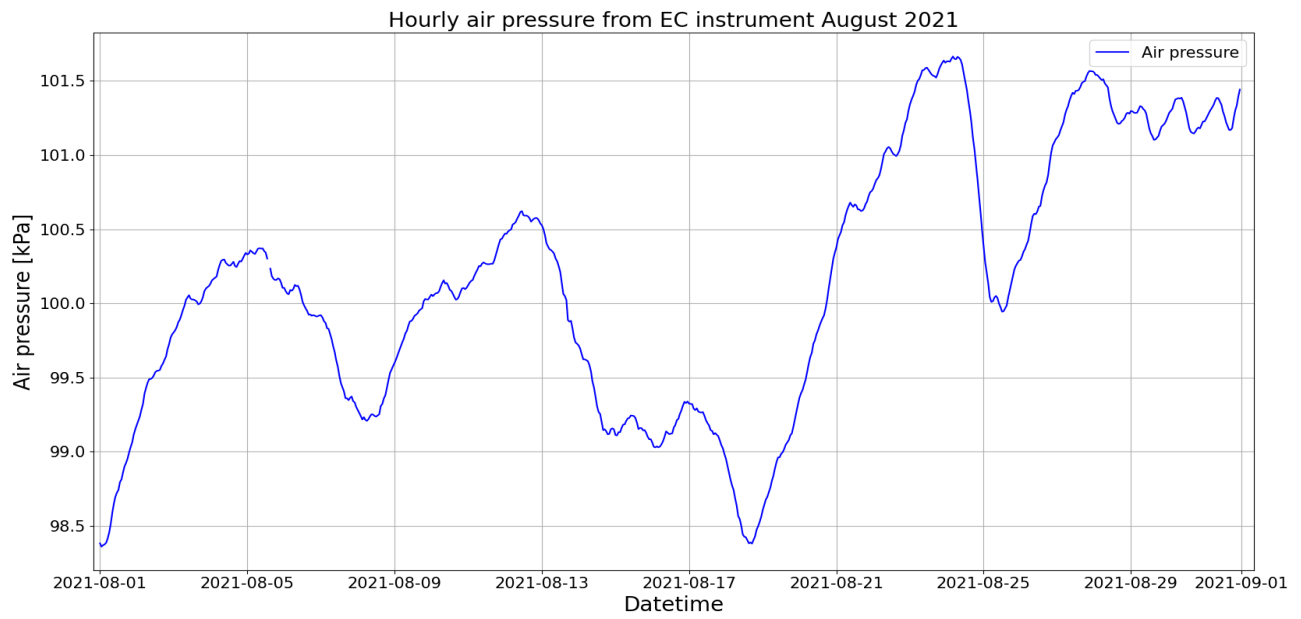


Figure 71: *Hourly measured air pressure in August 2021.*

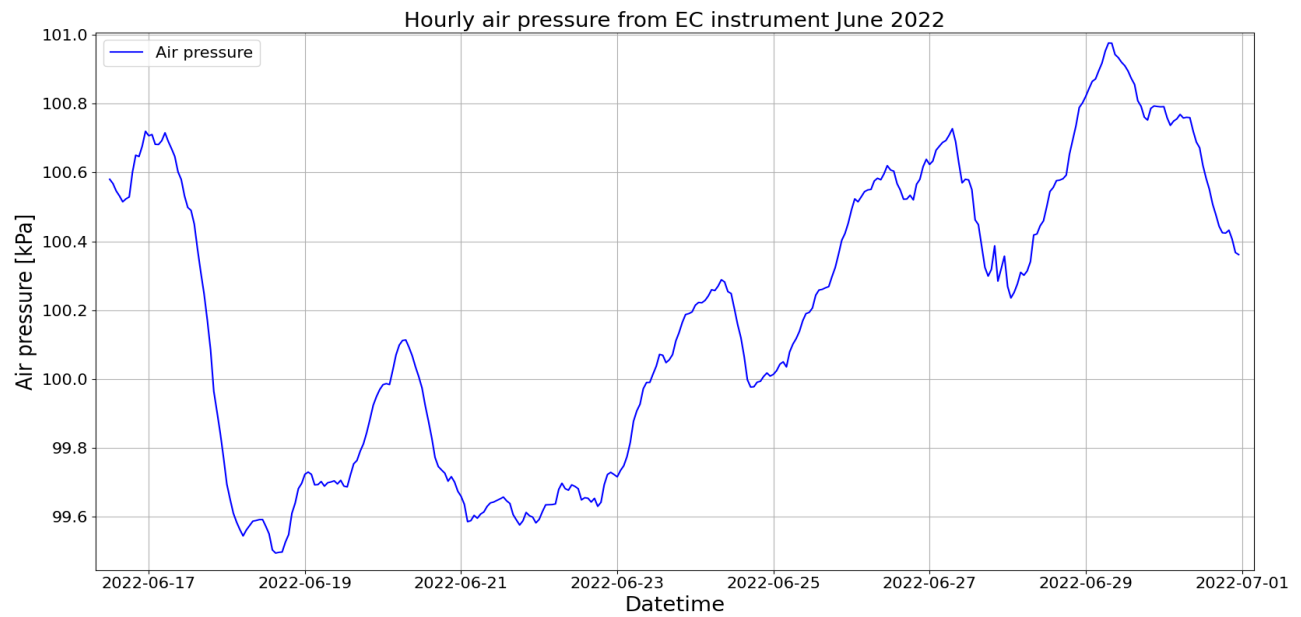


Figure 72: *Hourly measured air pressure in June 2022.*

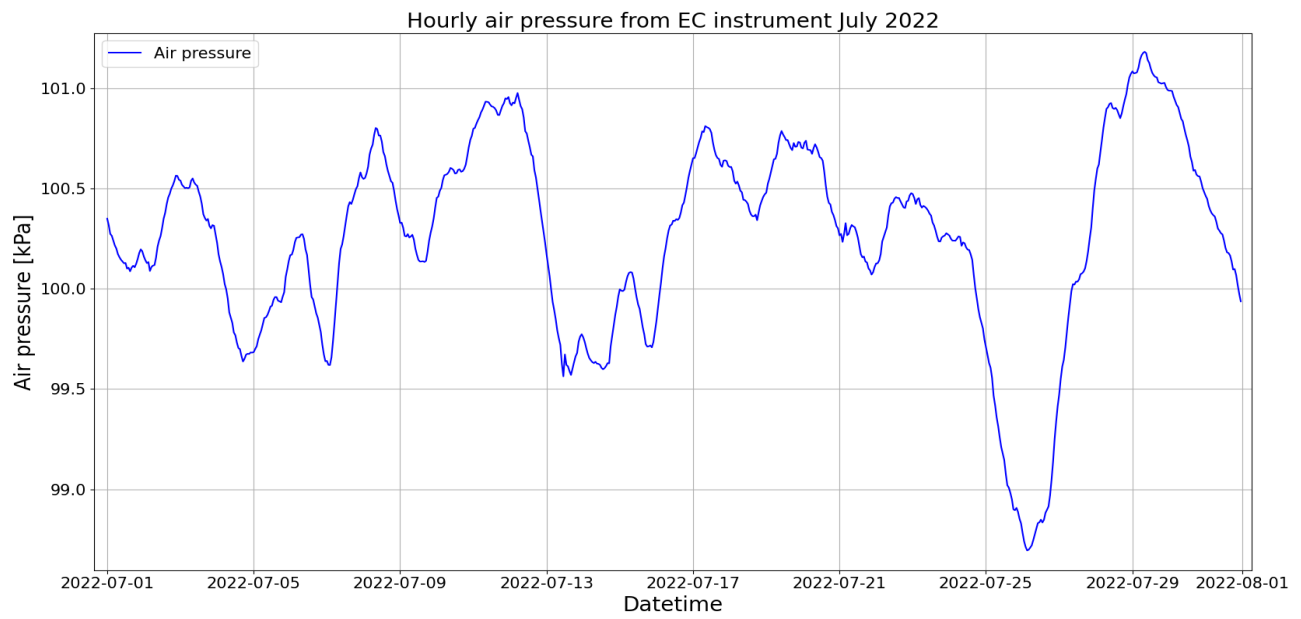


Figure 73: *Hourly measured air pressure in July 2022.*

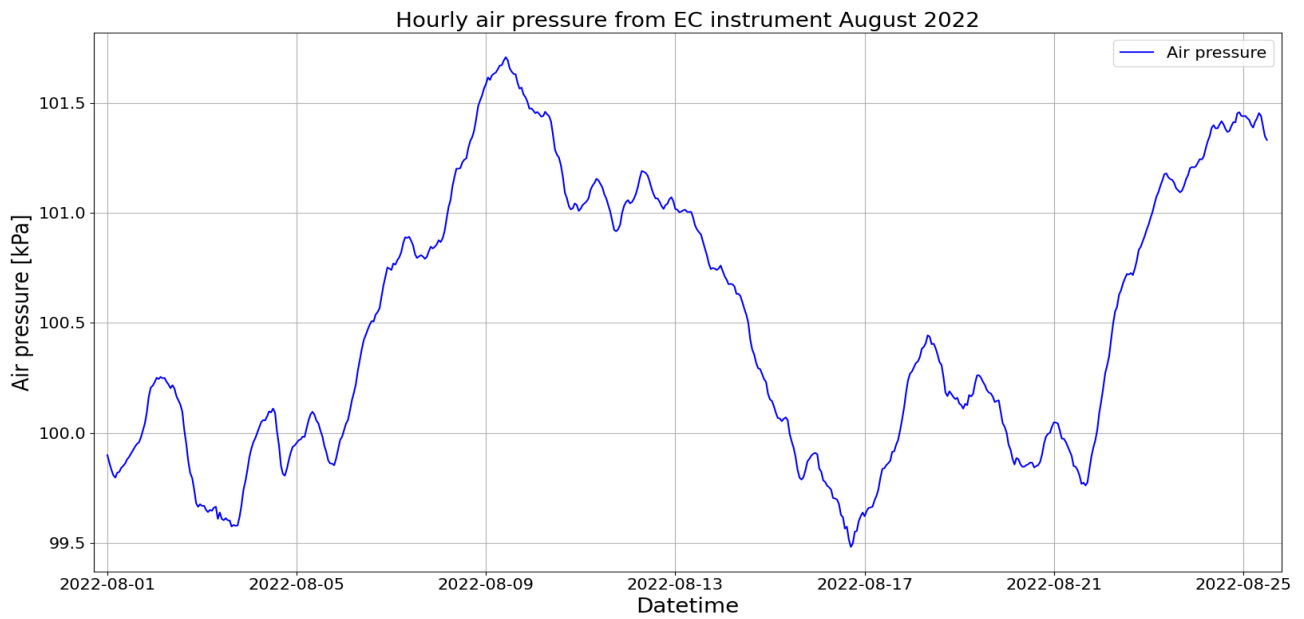


Figure 74: *Hourly measured air pressure in August 2022.*

Vapor pressure deficit

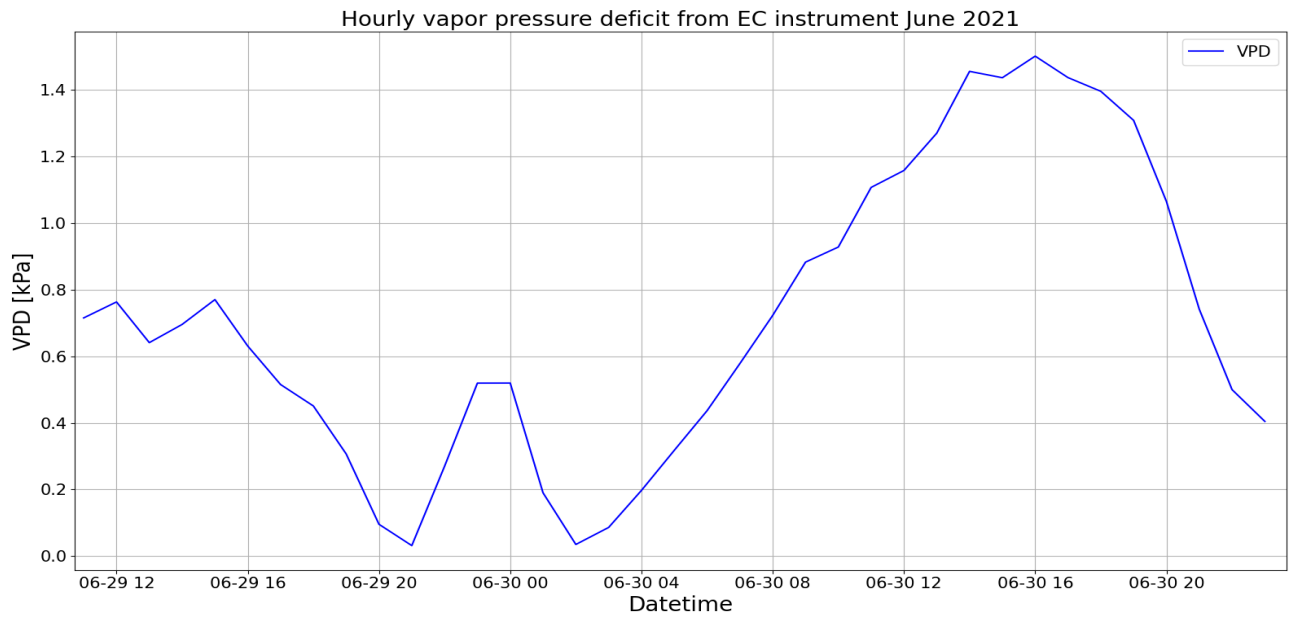


Figure 75: Hourly measured vapor pressure deficit in June 2021.

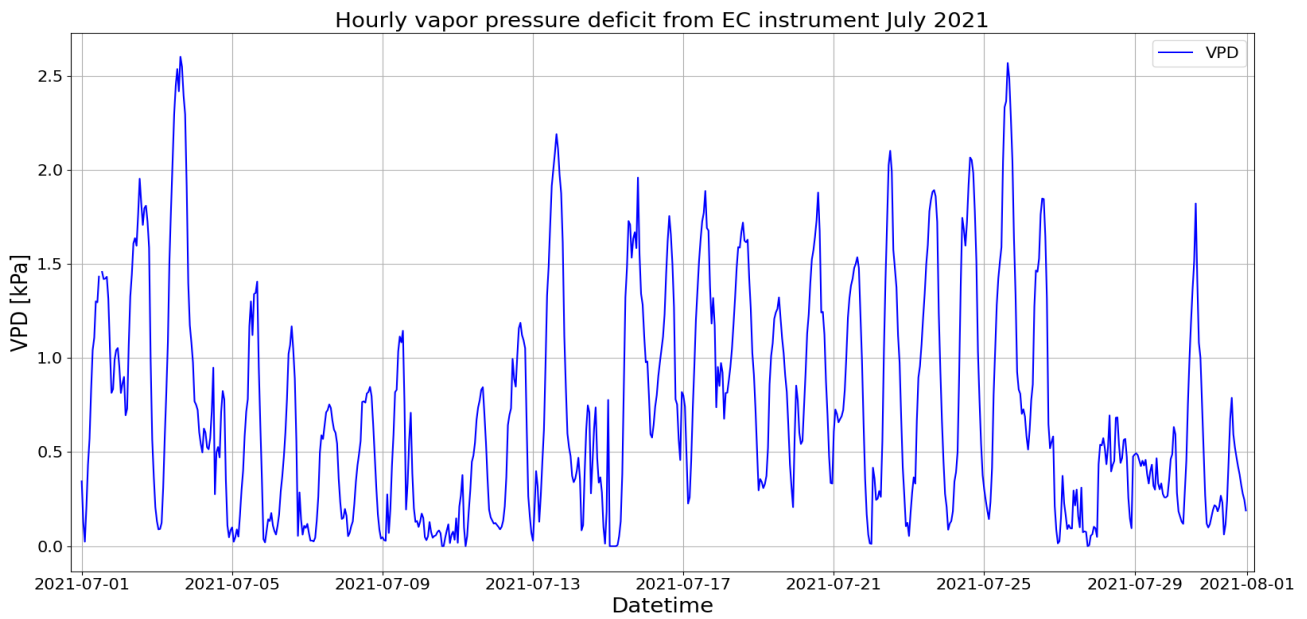


Figure 76: Hourly measured vapor pressure deficit in July 2021.

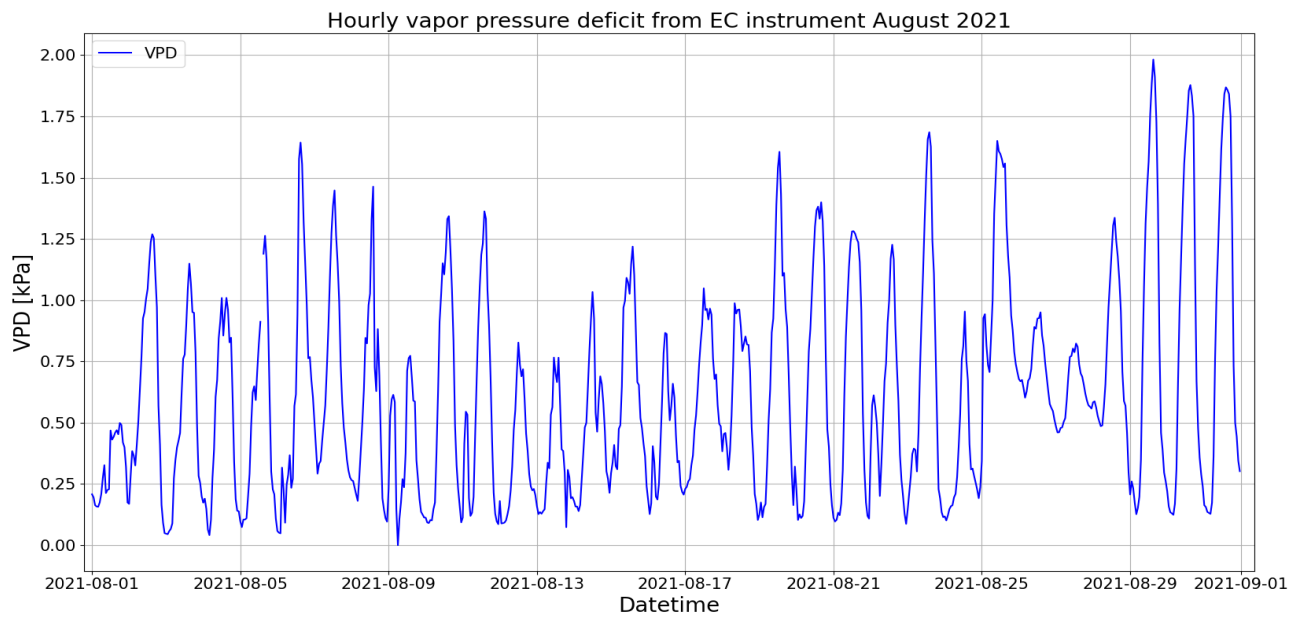


Figure 77: *Hourly measured vapor pressure deficit in August 2021.*

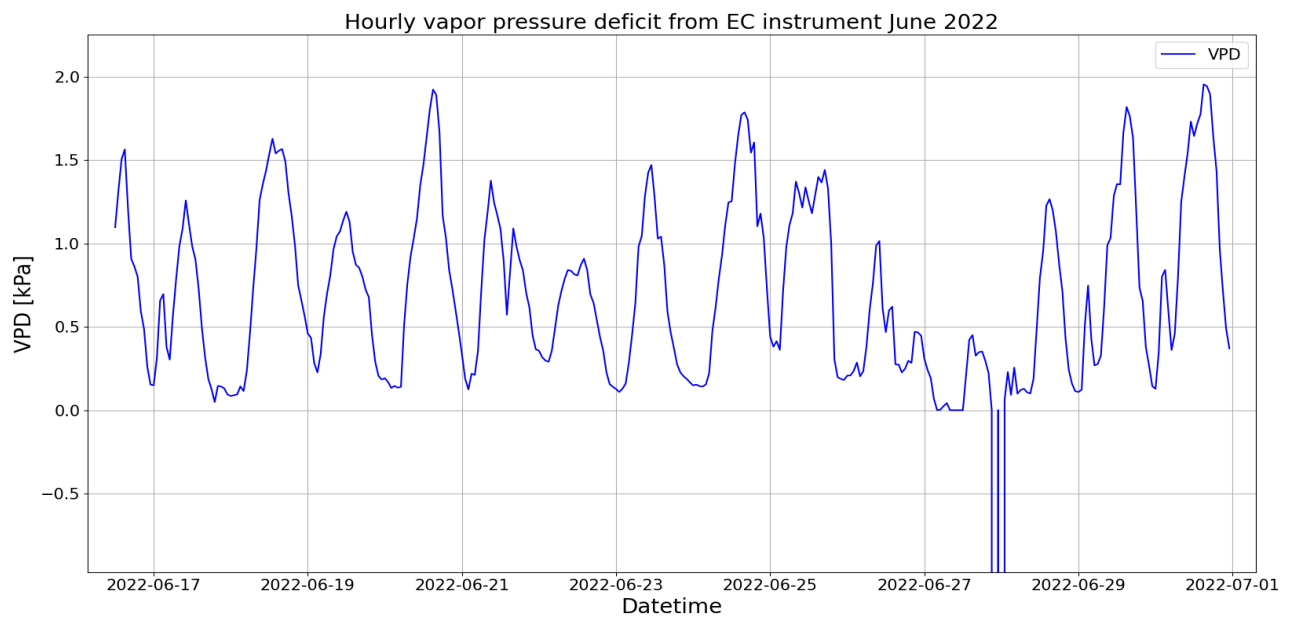


Figure 78: *Hourly measured vapor pressure deficit in June 2022.*

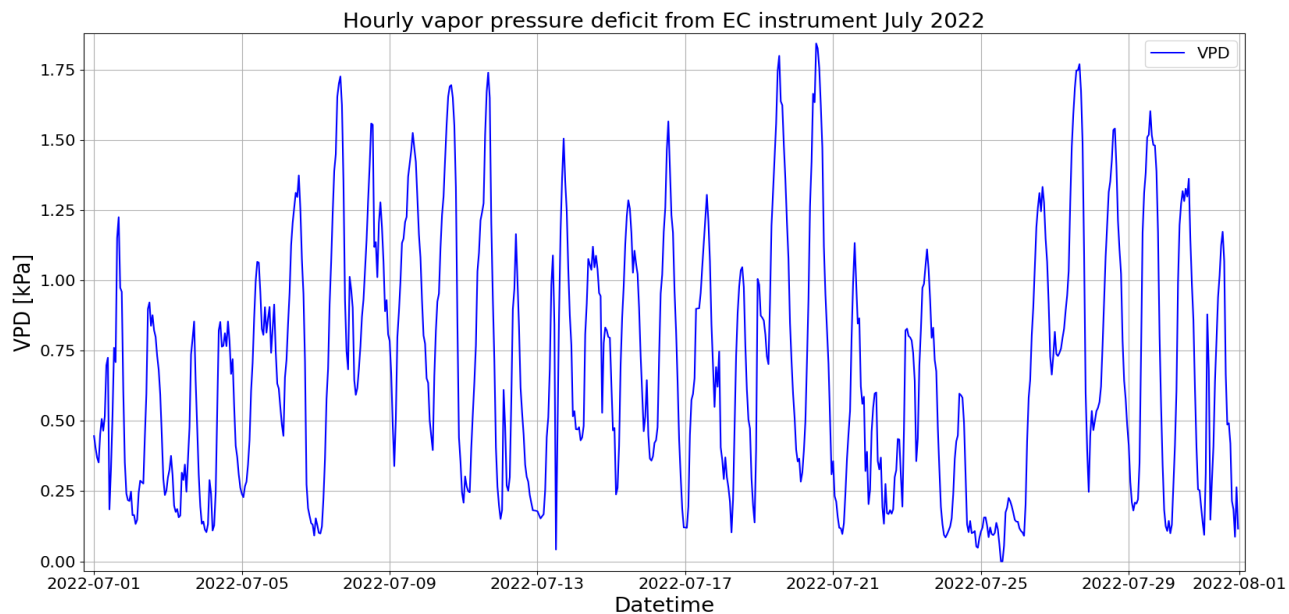


Figure 79: *Hourly measured vapor pressure deficit in July 2022.*

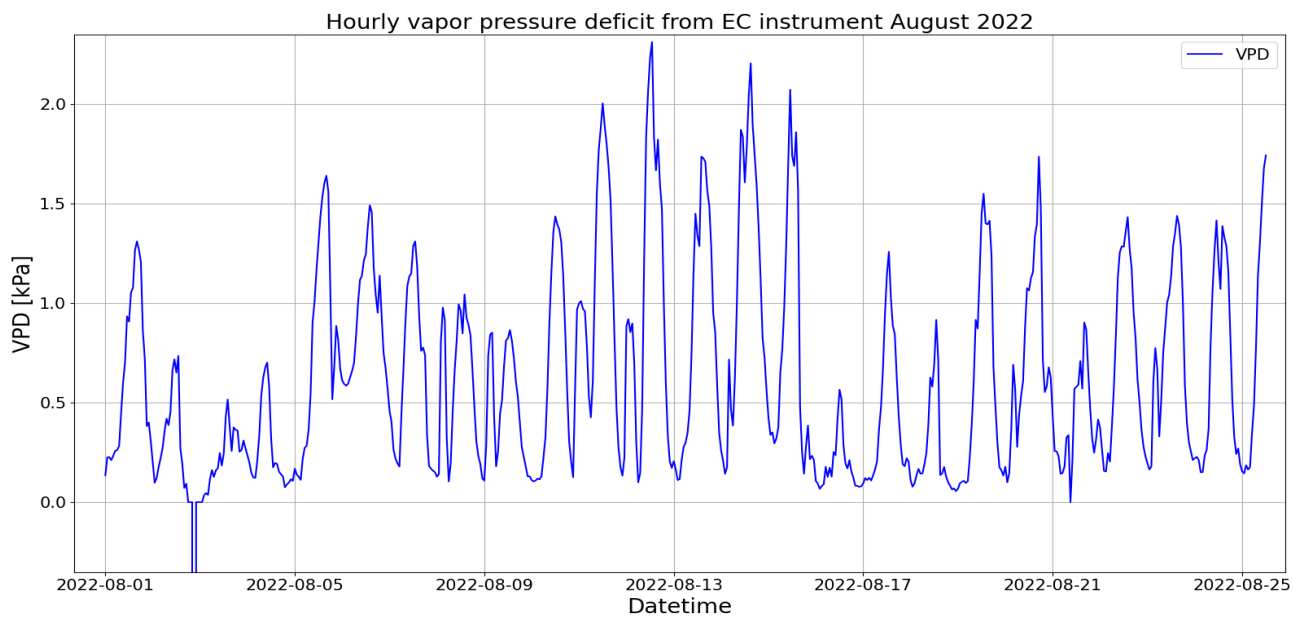


Figure 80: *Hourly measured vapor pressure deficit in August 2022.*

Relative humidity

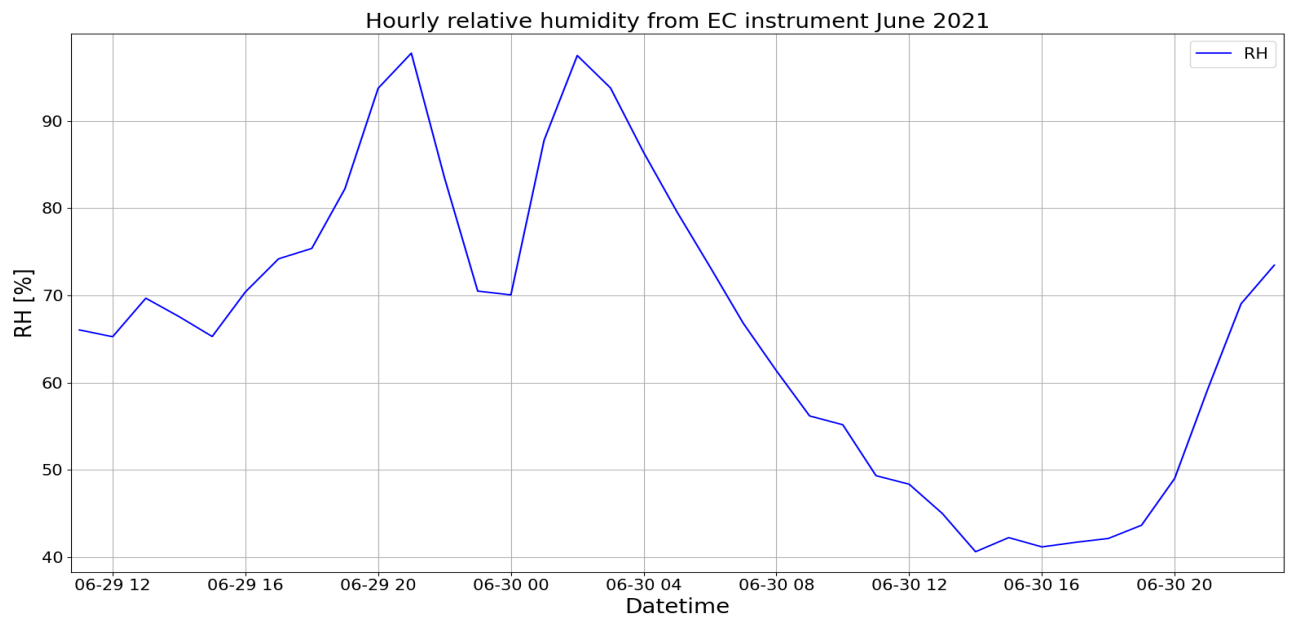


Figure 81: *Hourly measured relative humidity in June 2021.*

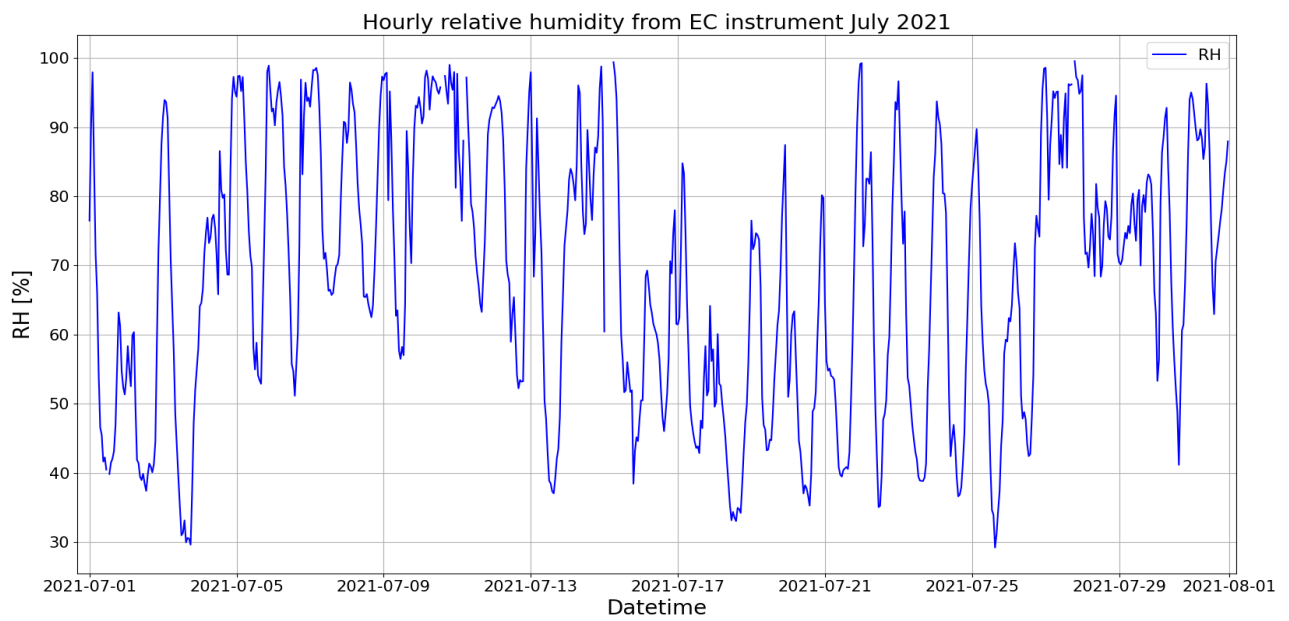


Figure 82: *Hourly measured relative humidity in July 2021.*

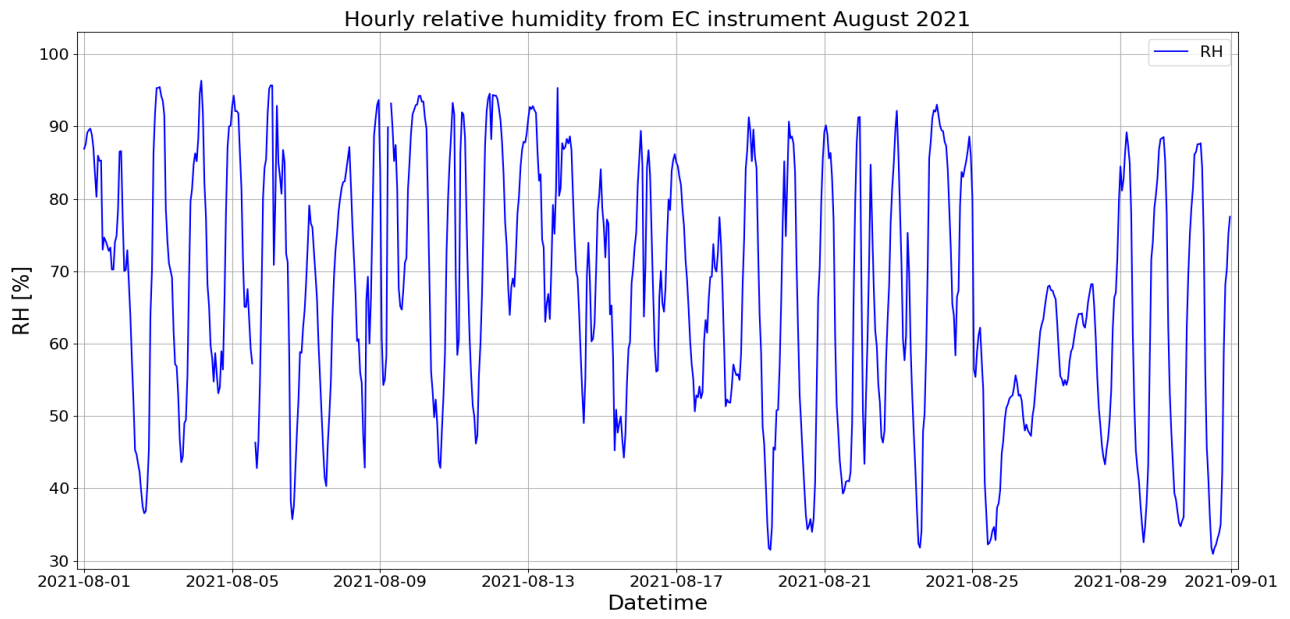


Figure 83: *Hourly measured relative humidity in August 2021.*

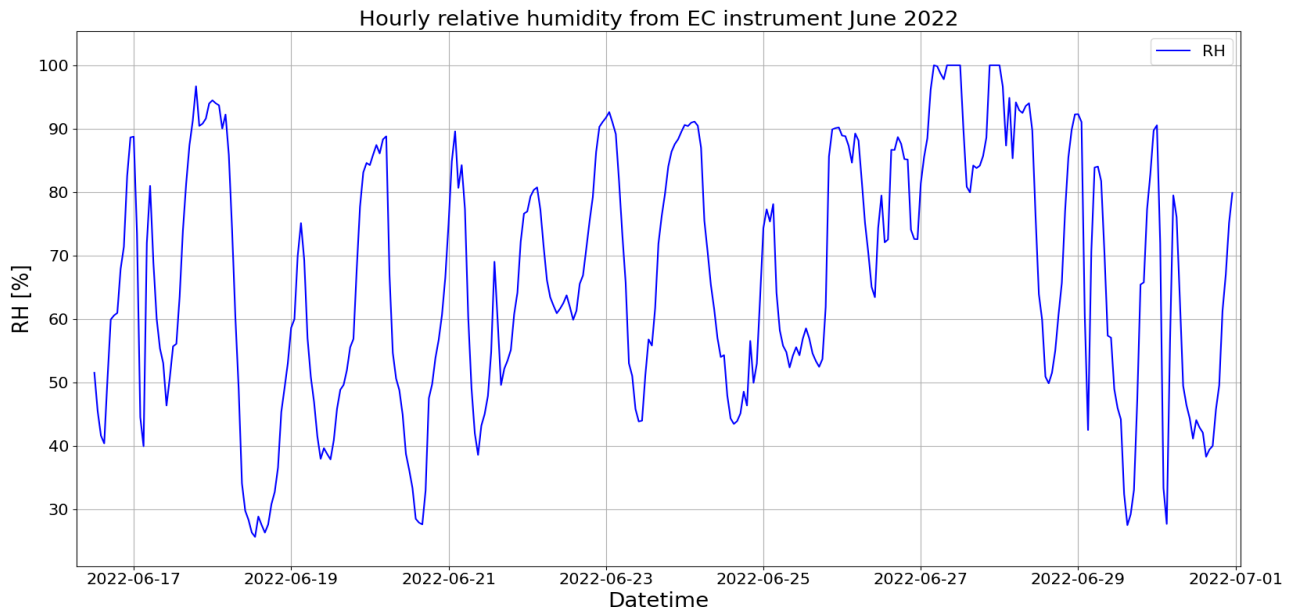


Figure 84: *Hourly measured relative humidity in June 2022.*

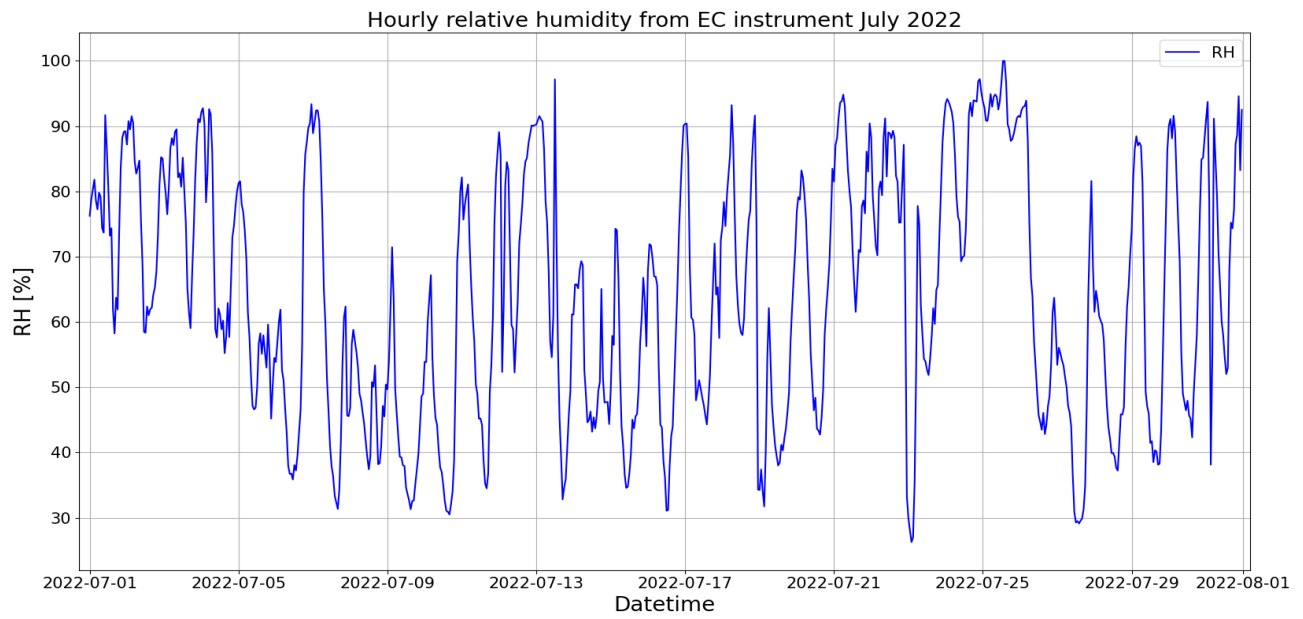


Figure 85: *Hourly measured relative humidity in July 2022.*

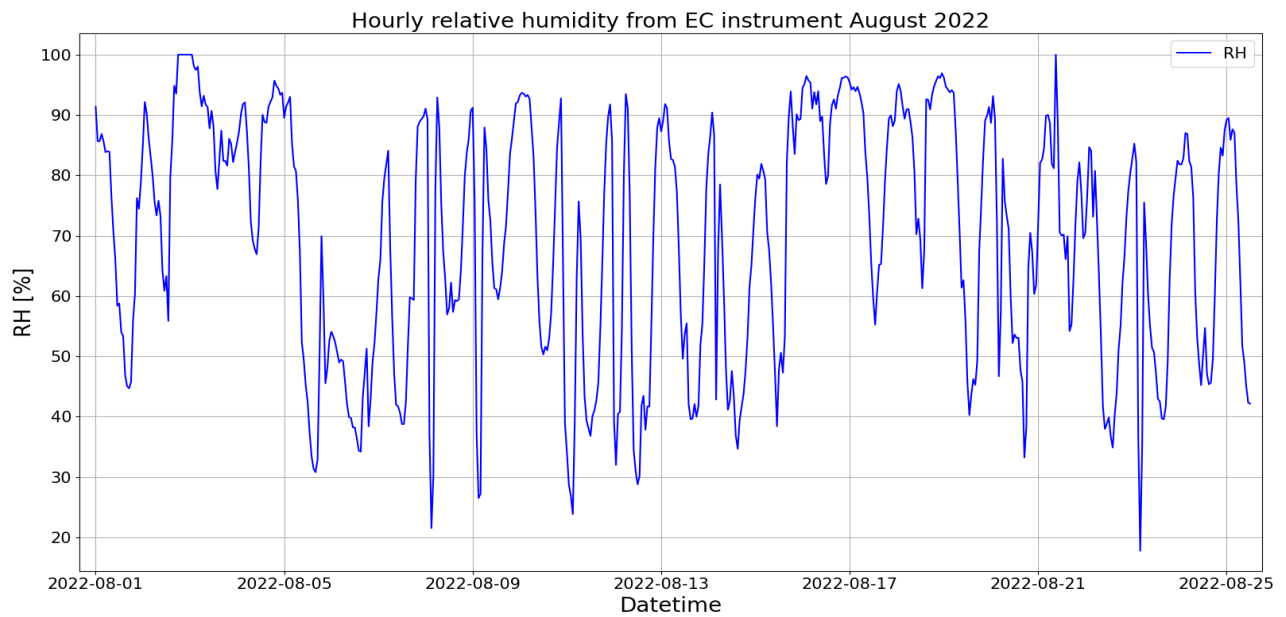


Figure 86: *Hourly measured relative humidity in August 2022.*

Precipitation

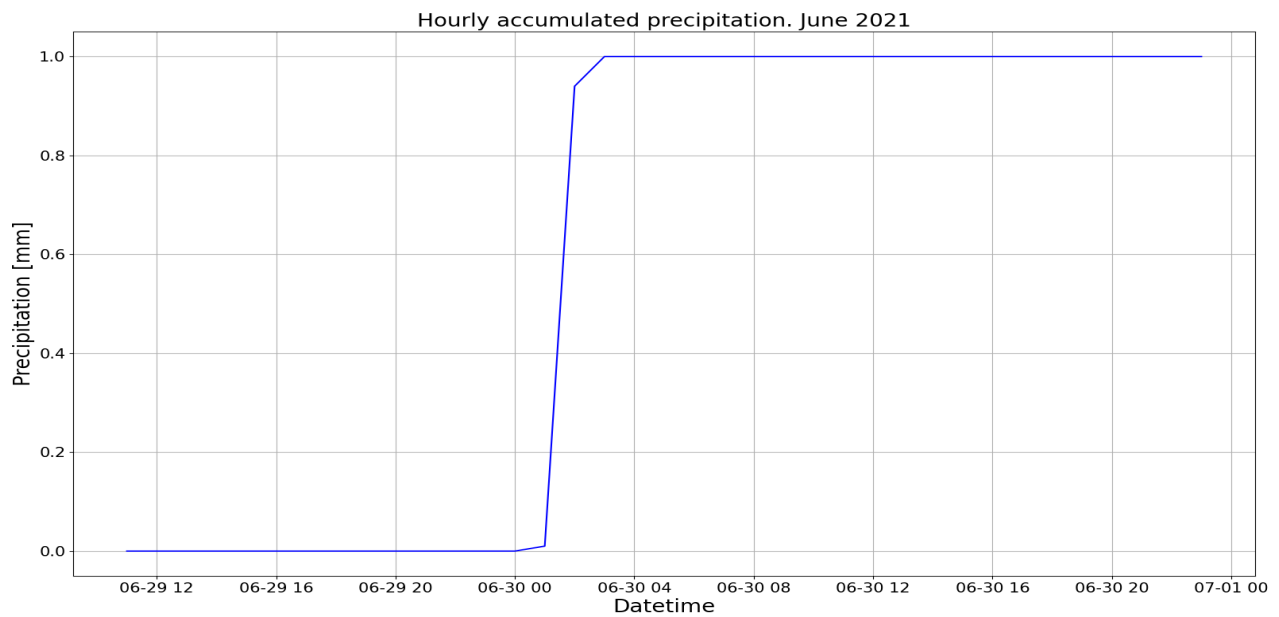


Figure 87: *Hourly accumulated precipitation in June 2021.*

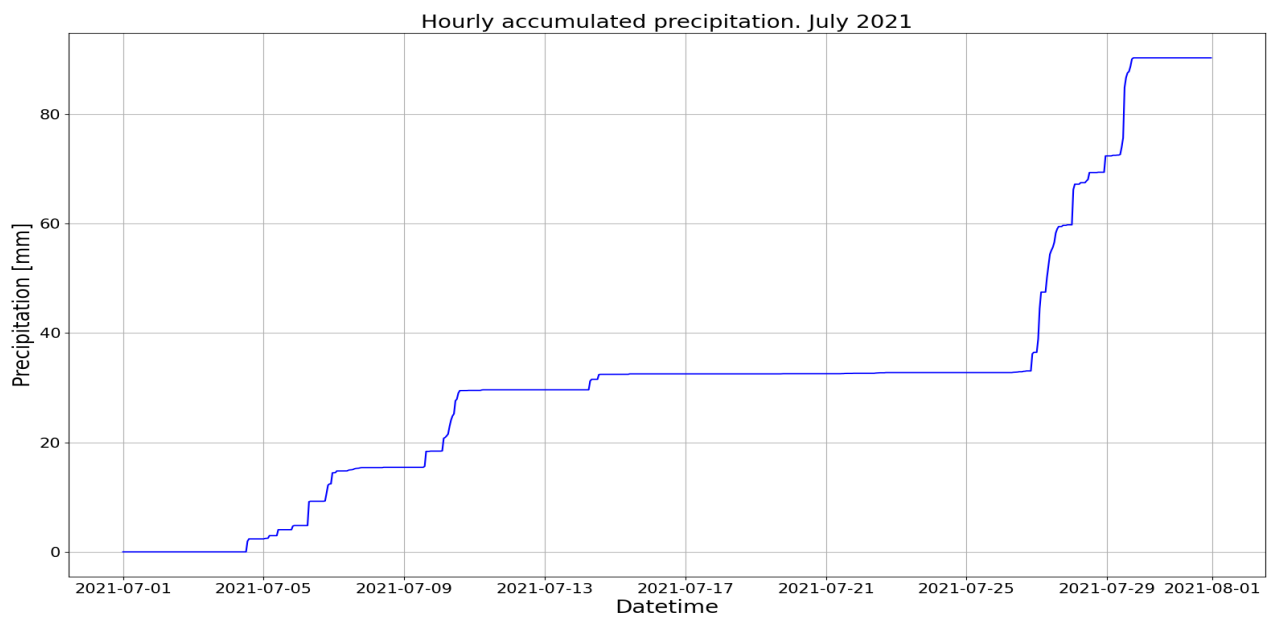


Figure 88: *Hourly accumulated precipitation in July 2021.*

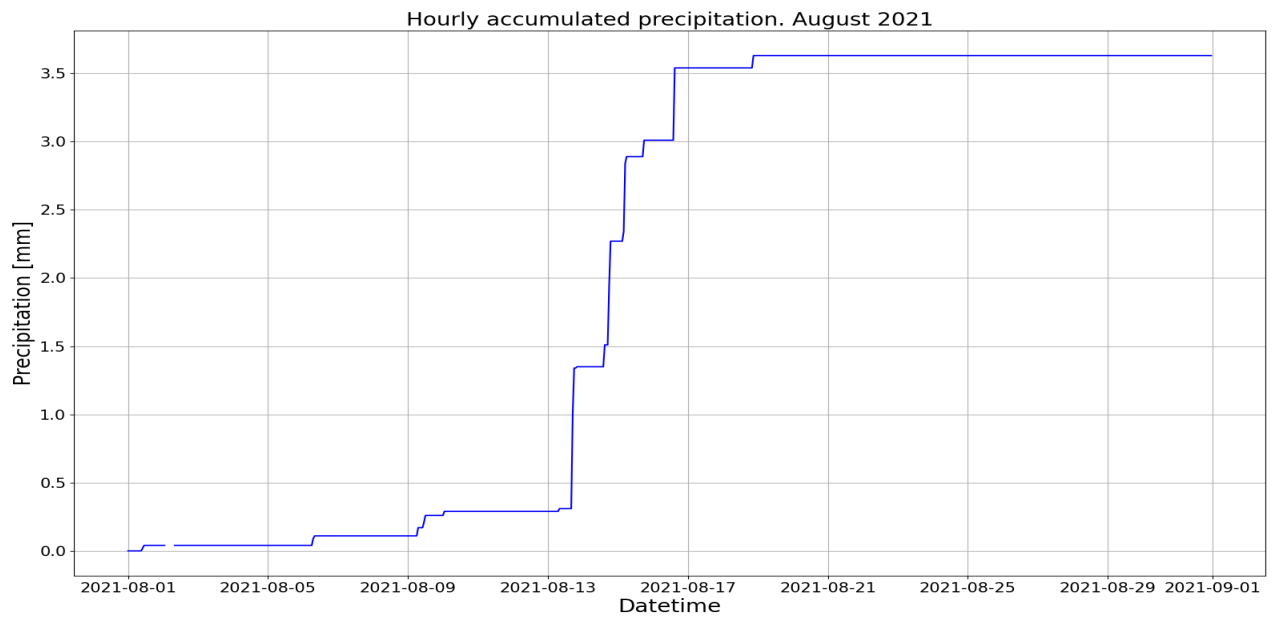


Figure 89: *Hourly accumulated precipitation in August 2021.*

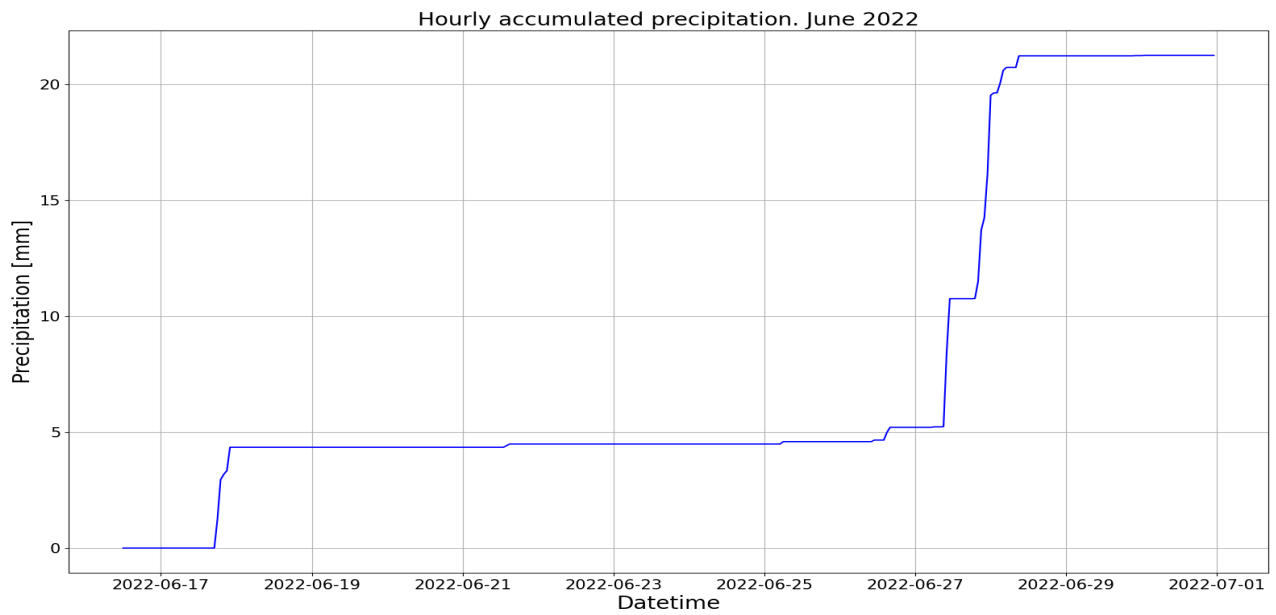


Figure 90: *Hourly accumulated precipitation in June 2022.*

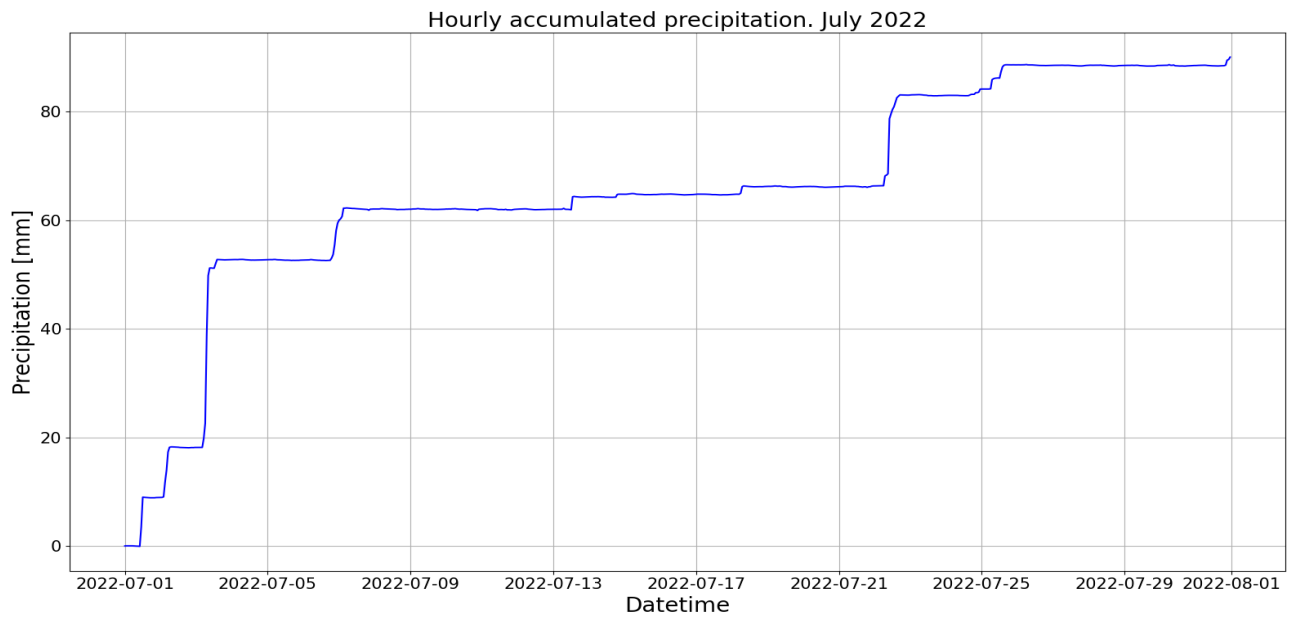


Figure 91: *Hourly accumulated precipitation in July 2022.*

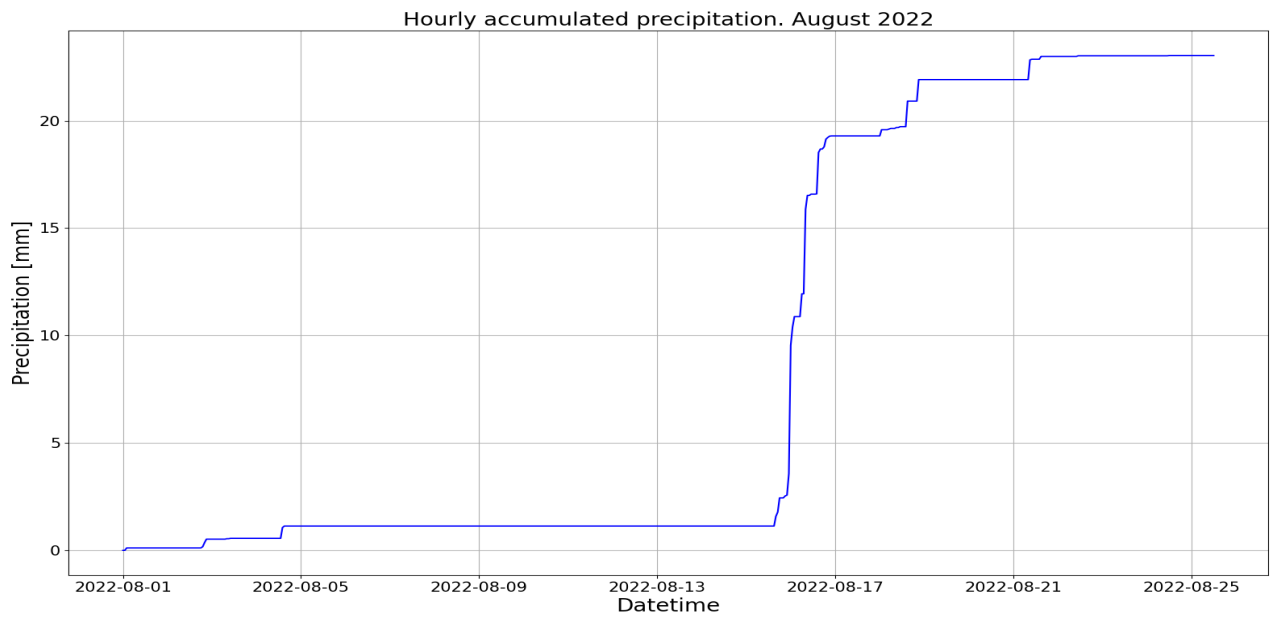


Figure 92: *Hourly accumulated precipitation in August 2022.*

Daylight

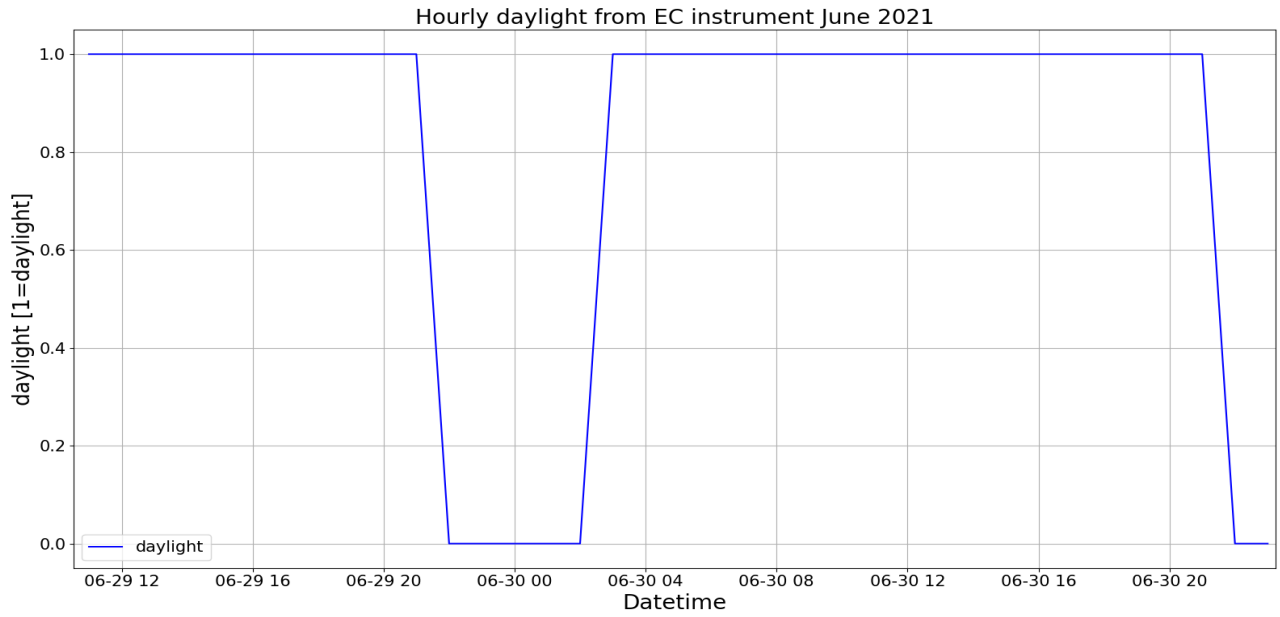


Figure 93: Hourly measurement of daylight in June 2021. Daylight at 1 and no daylight at 0.

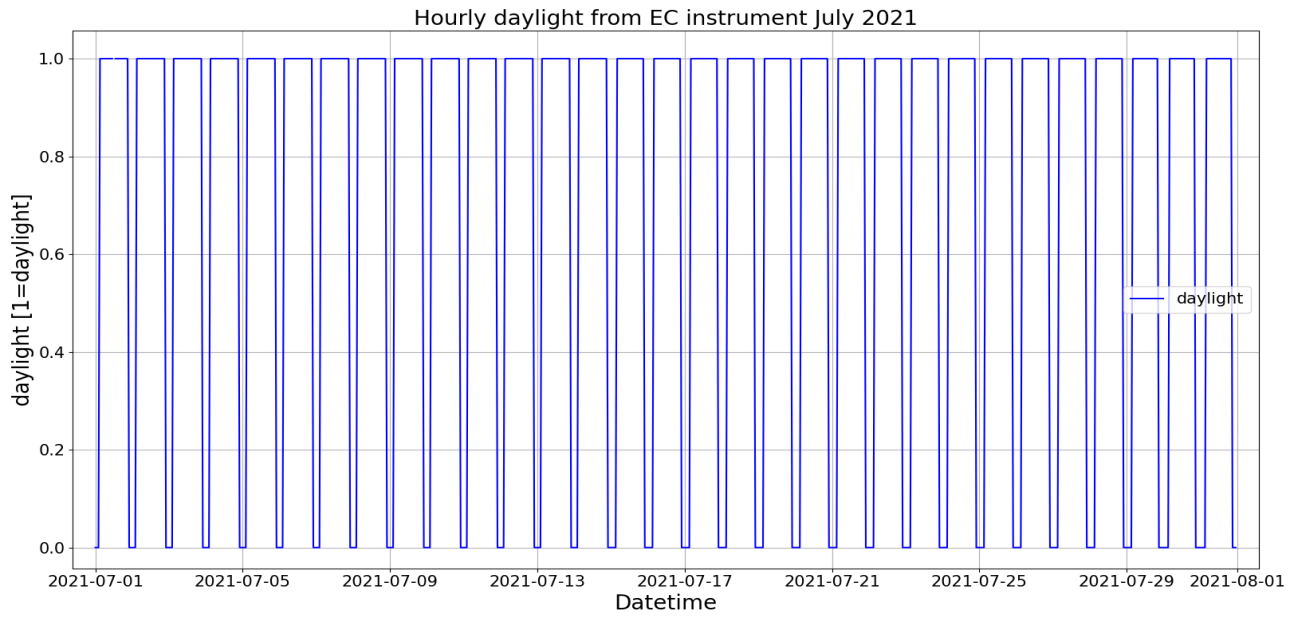


Figure 94: Hourly measurement of daylight in July 2021. Daylight at 1 and no daylight at 0.

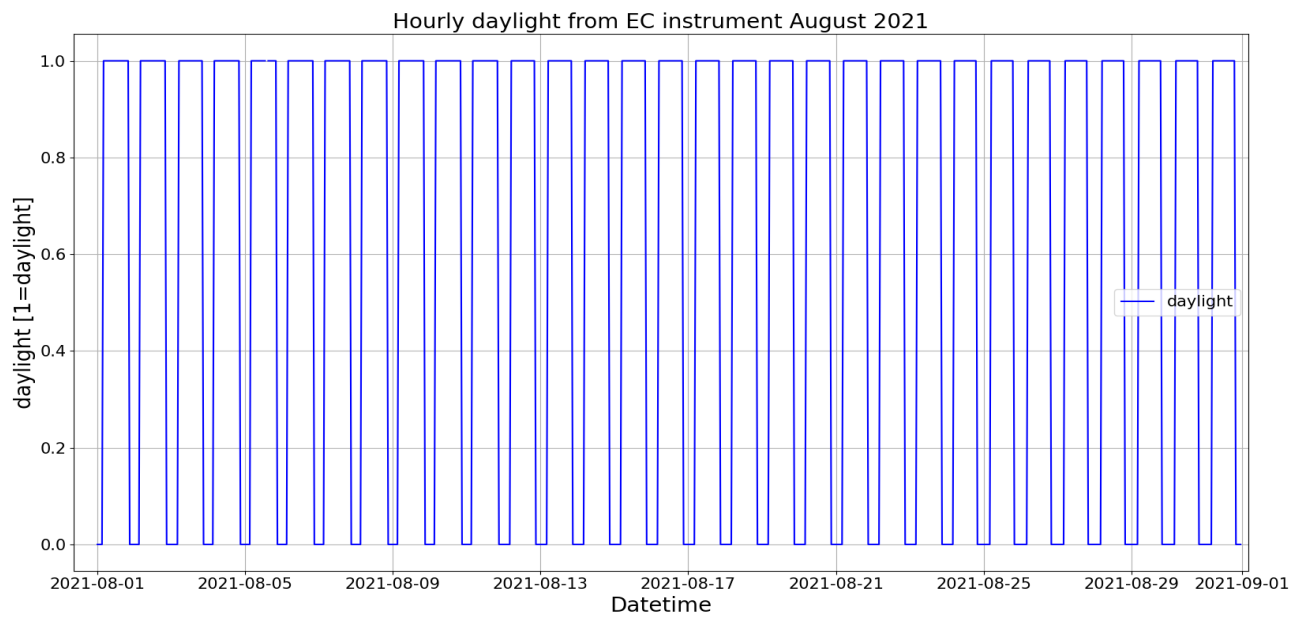


Figure 95: *Hourly measurement of daylight in August 2021. Daylight at 1 and no daylight at 0.*

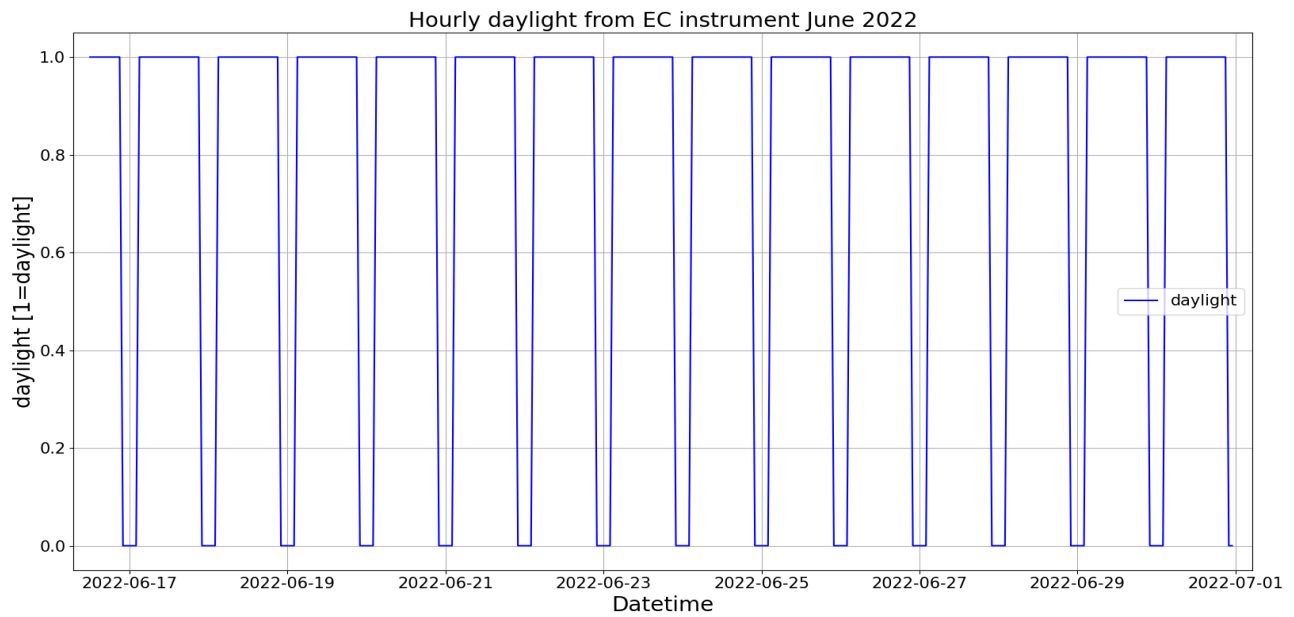


Figure 96: *Hourly measurement of daylight in June 2022. Daylight at 1 and no daylight at 0.*

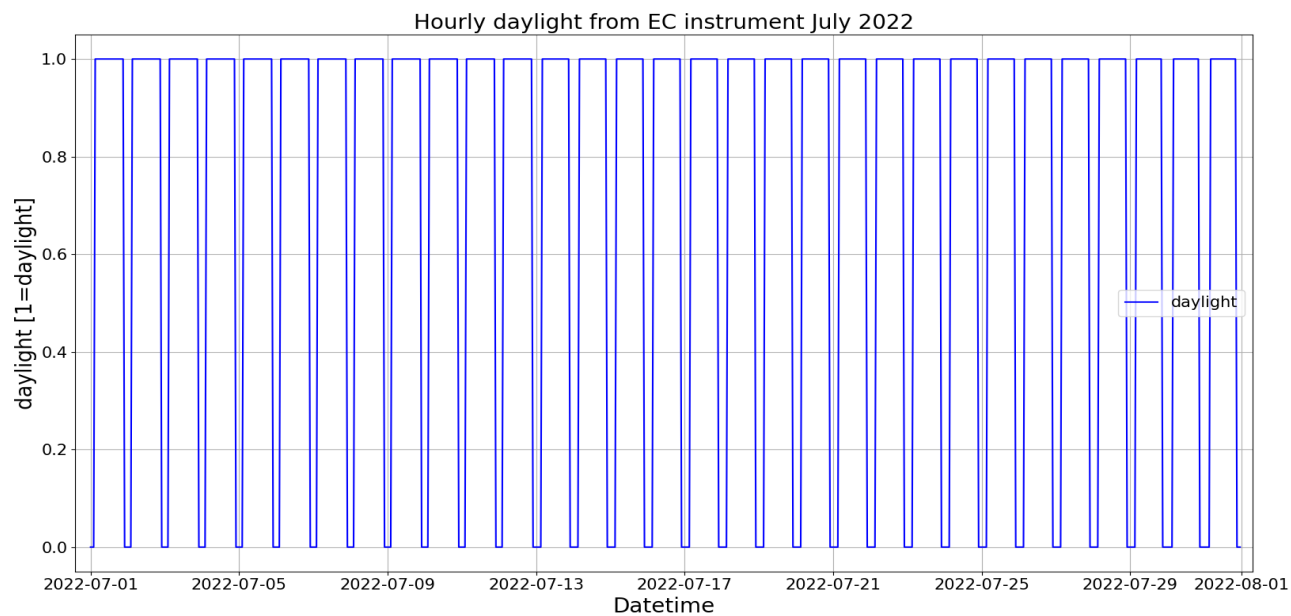


Figure 97: *Hourly measurement of daylight in July 2022. Daylight at 1 and no daylight at 0.*

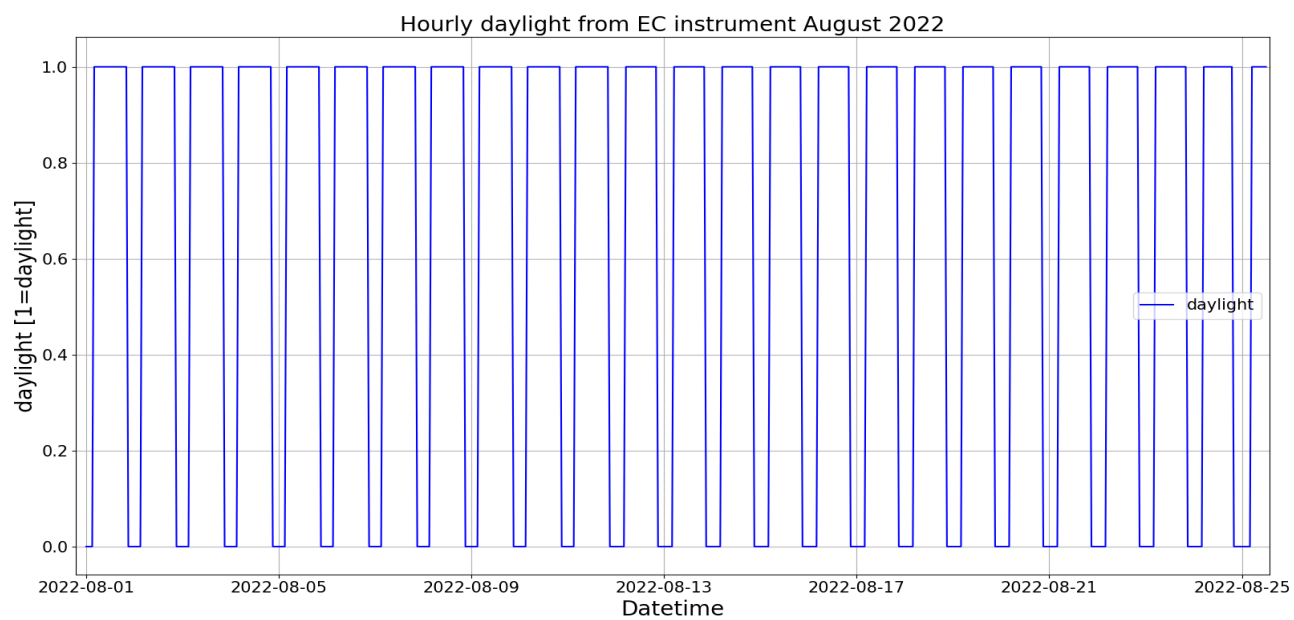


Figure 98: *Hourly measurement of daylight in August 2022. Daylight at 1 and no daylight at 0.*

Appendix B: ET models

B1: PT models

PT1

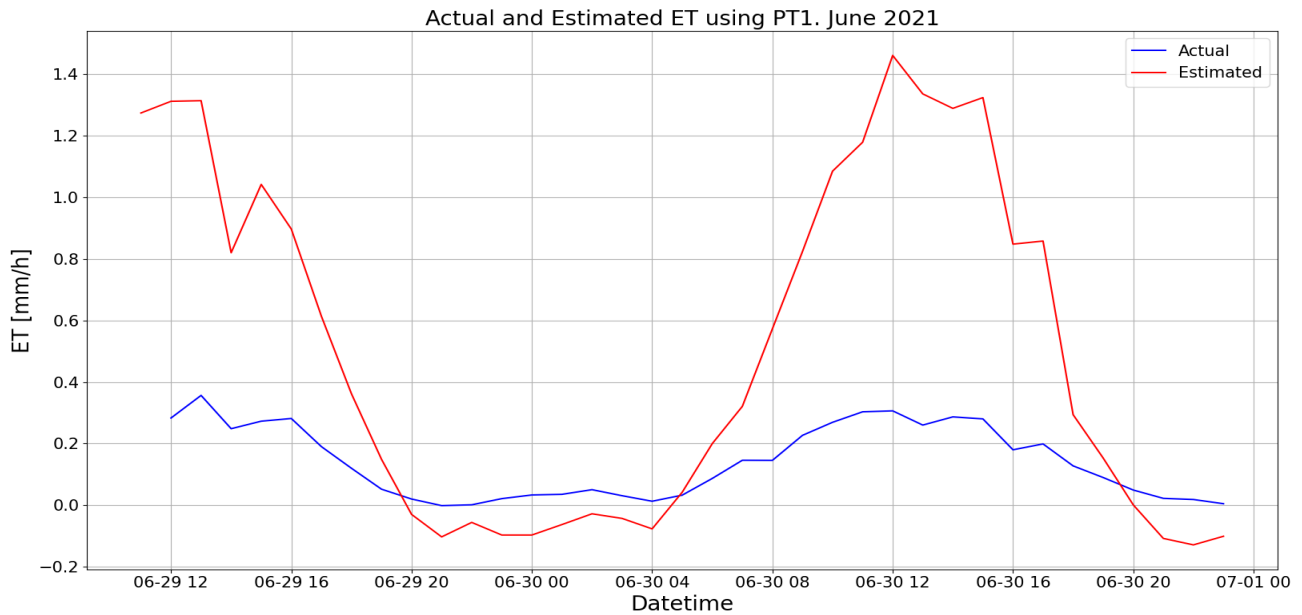


Figure 99: Hourly measured evapotranspiration (blue) and estimated evapotranspiration (red) using PT1 model in June 2021.

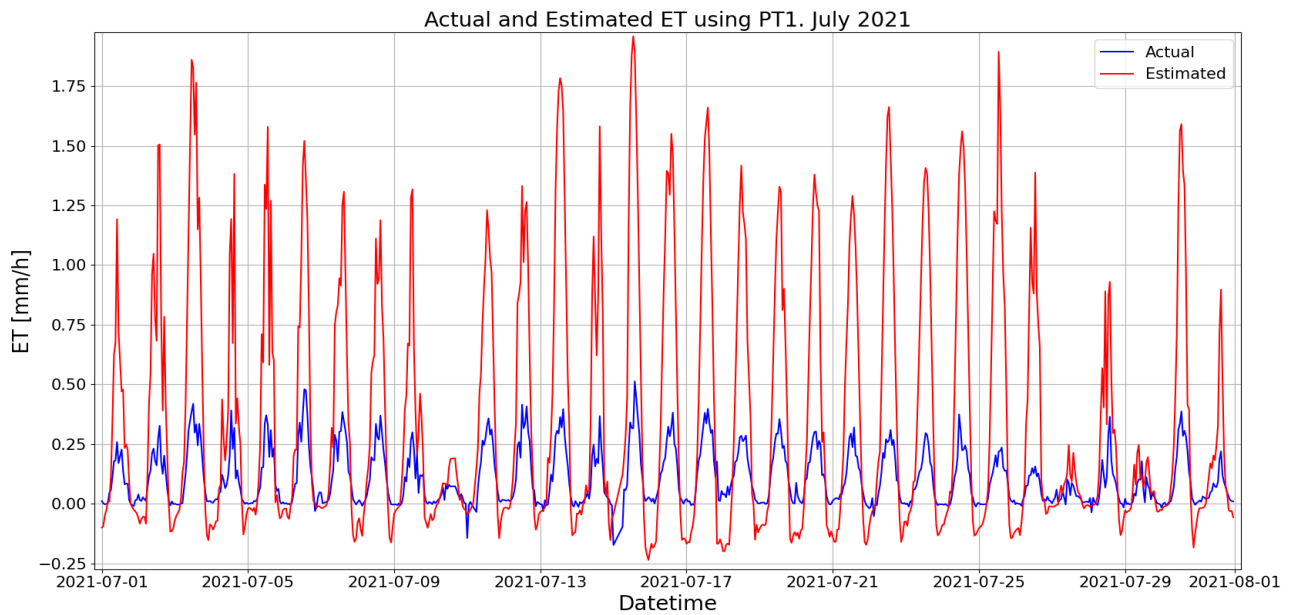


Figure 100: Hourly measured evapotranspiration (blue) and estimated evapotranspiration (red) using PT1 model in July 2021.

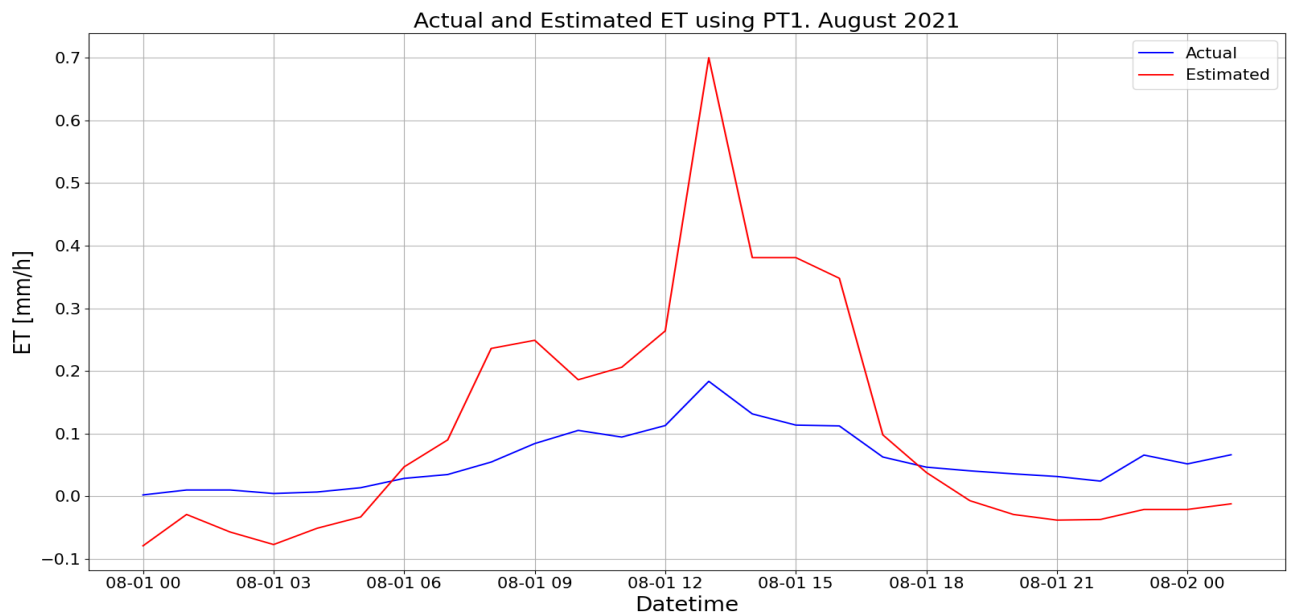


Figure 101: *Hourly measured evapotranspiration (blue) and estimated evapotranspiration (red) using PT1 model in August 2021.*

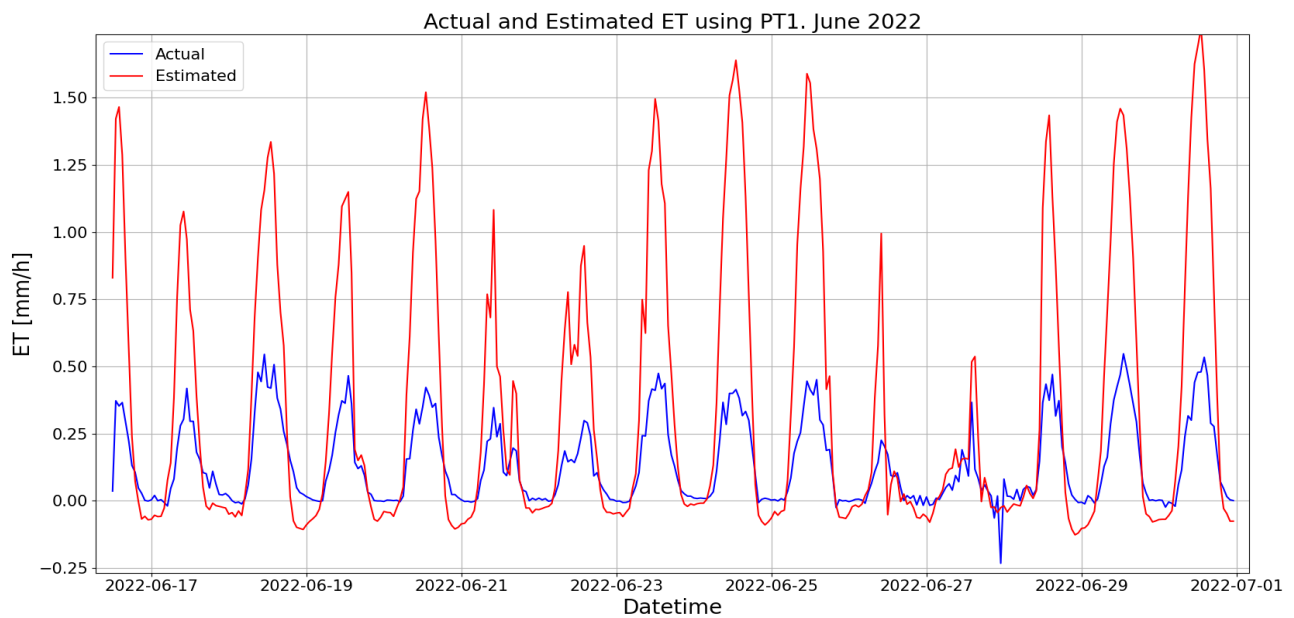


Figure 102: *Hourly measured evapotranspiration (blue) and estimated evapotranspiration (red) using PT1 model in June 2022.*

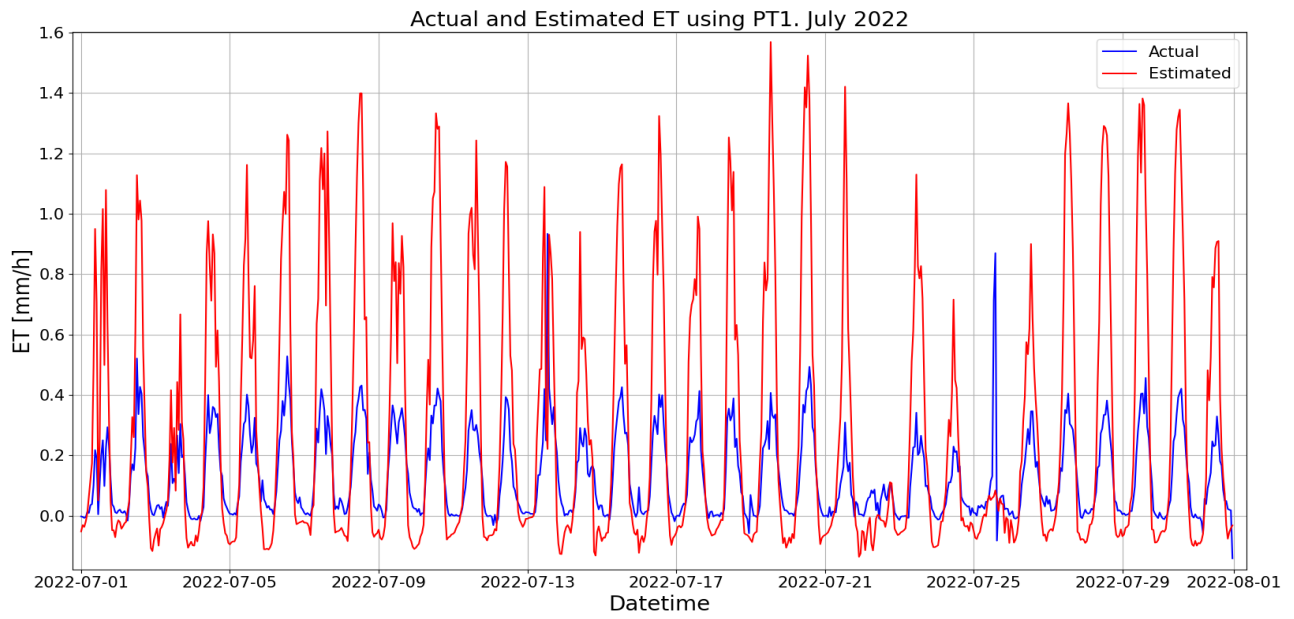


Figure 103: Hourly measured evapotranspiration (blue) and estimated evapotranspiration (red) using PT1 model in July 2022.

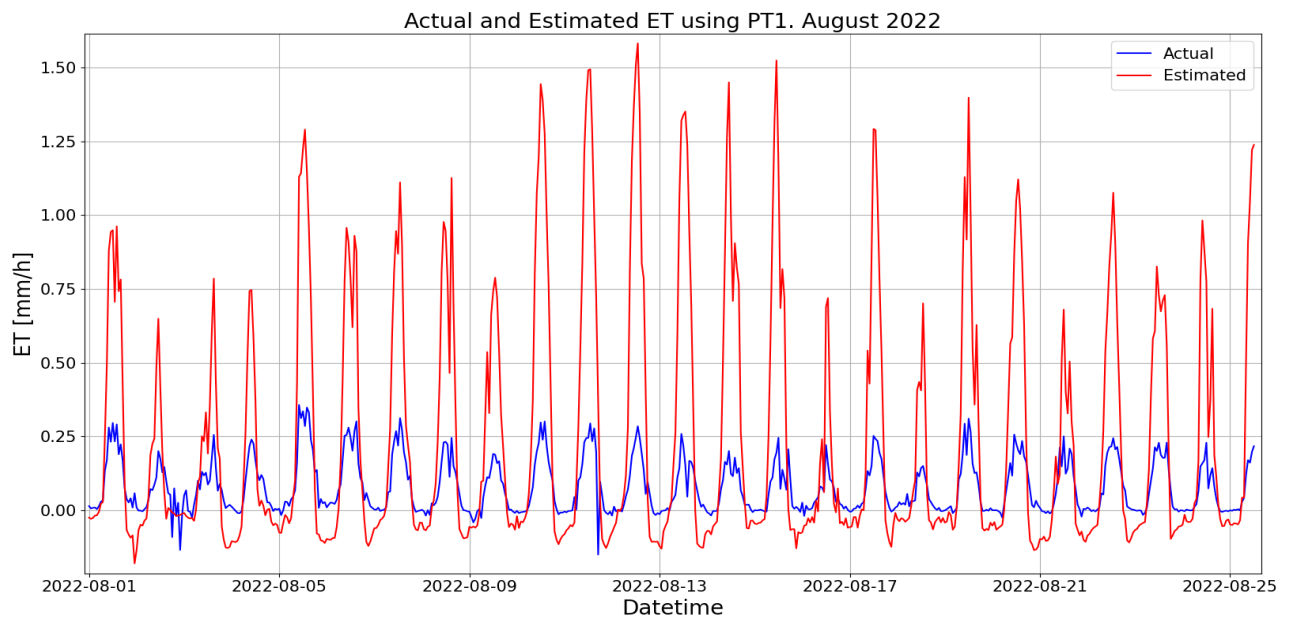


Figure 104: Hourly measured evapotranspiration (blue) and estimated evapotranspiration (red) using PT1 model in August 2022.

PT2

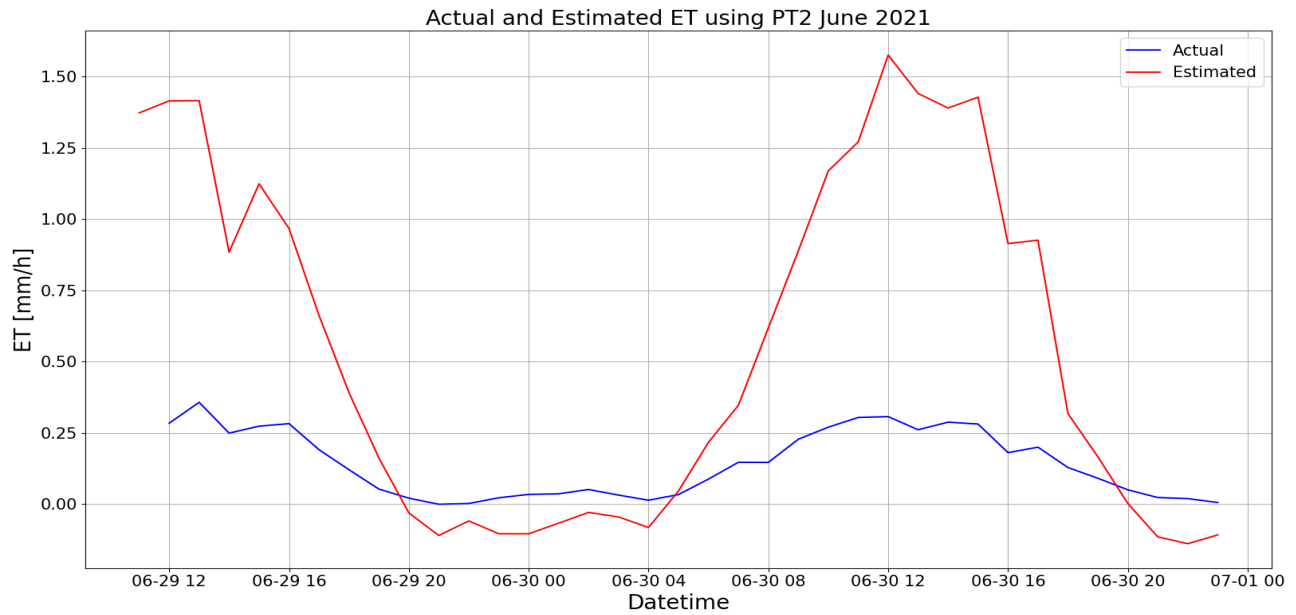


Figure 105: Hourly measured evapotranspiration (blue) and estimated evapotranspiration (red) using PT2 model in June 2021.

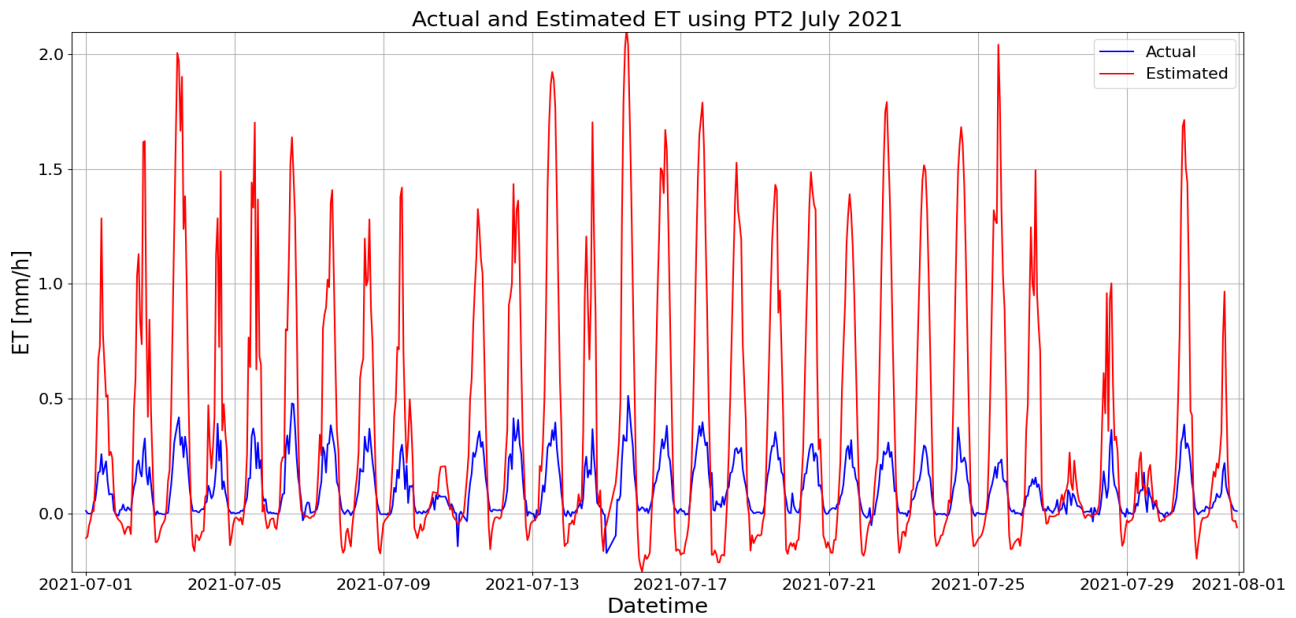


Figure 106: Hourly measured evapotranspiration (blue) and estimated evapotranspiration (red) using PT2 model in July 2021.

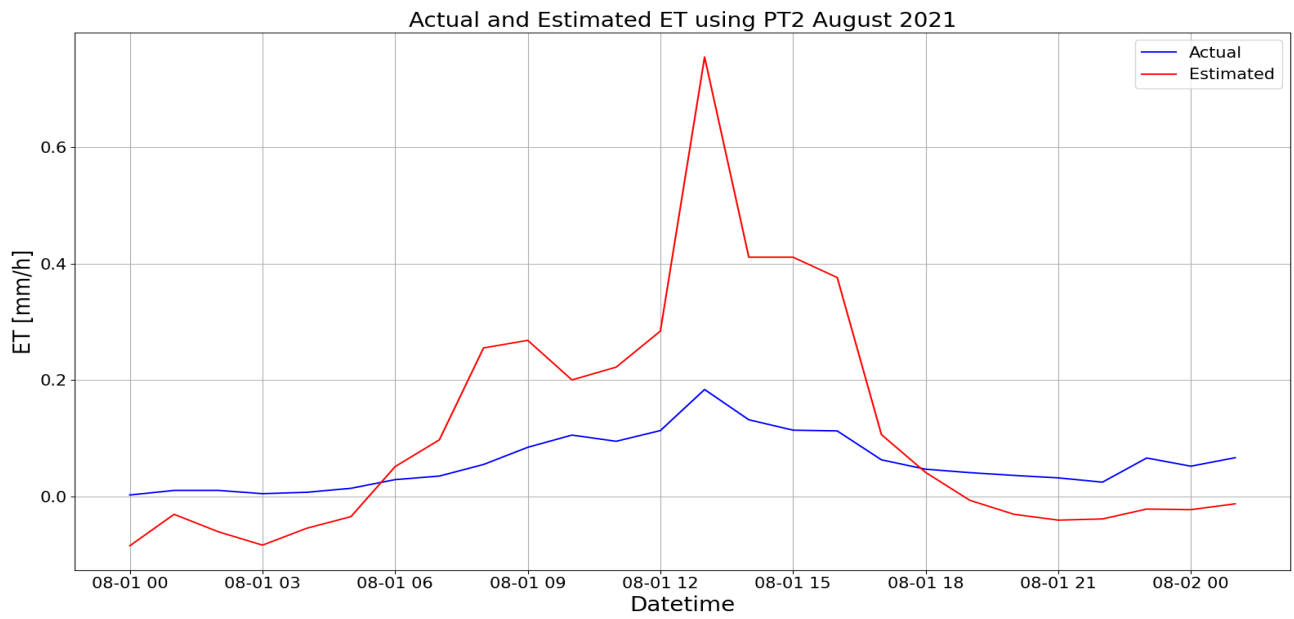


Figure 107: Hourly measured evapotranspiration (blue) and estimated evapotranspiration (red) using PT2 model in August 2021.

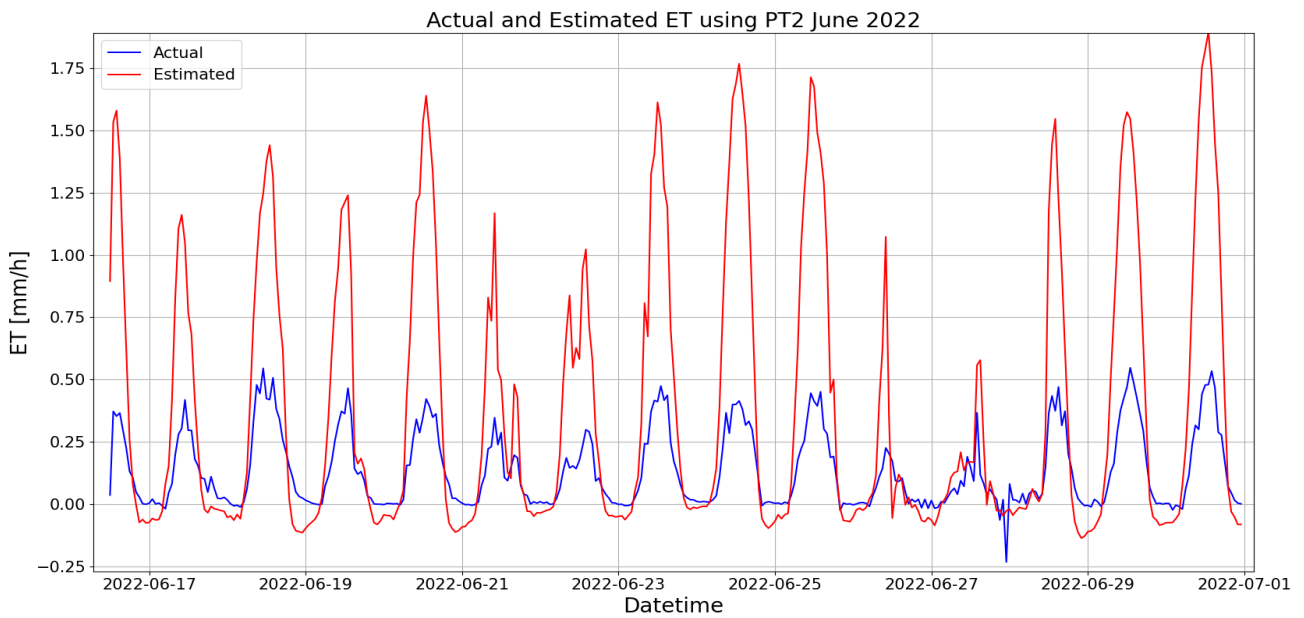


Figure 108: Hourly measured evapotranspiration (blue) and estimated evapotranspiration (red) using PT2 model in June 2022.

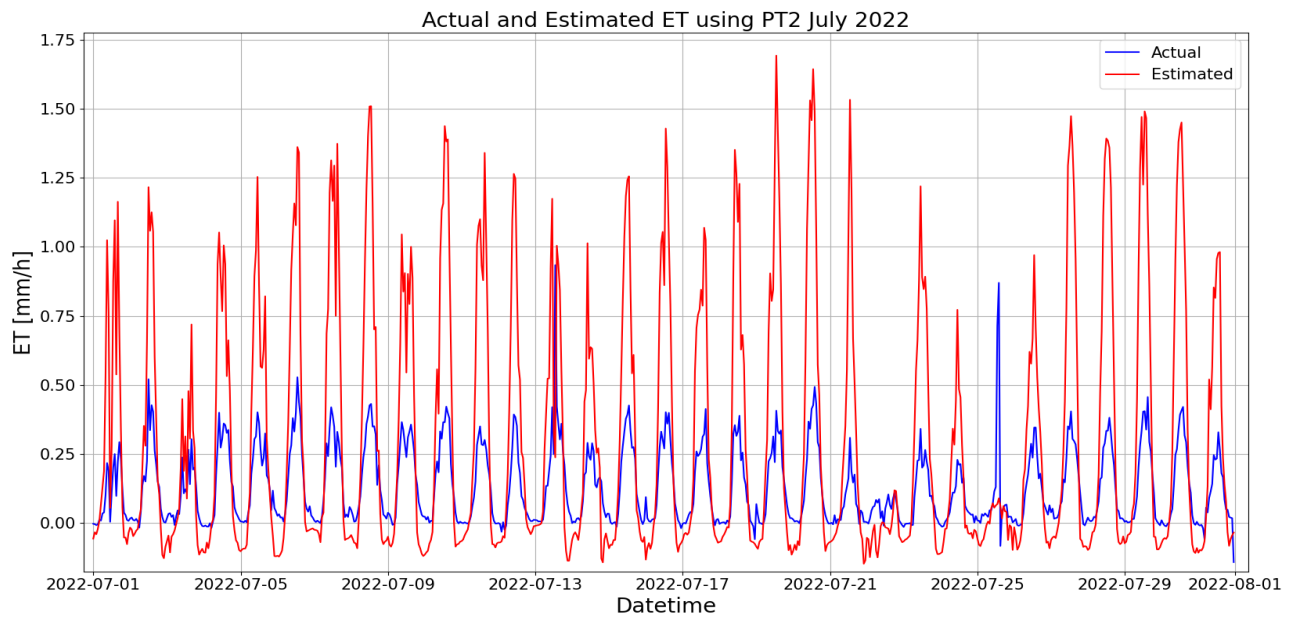


Figure 109: *Hourly measured evapotranspiration (blue) and estimated evapotranspiration (red) using PT2 model in July 2022.*

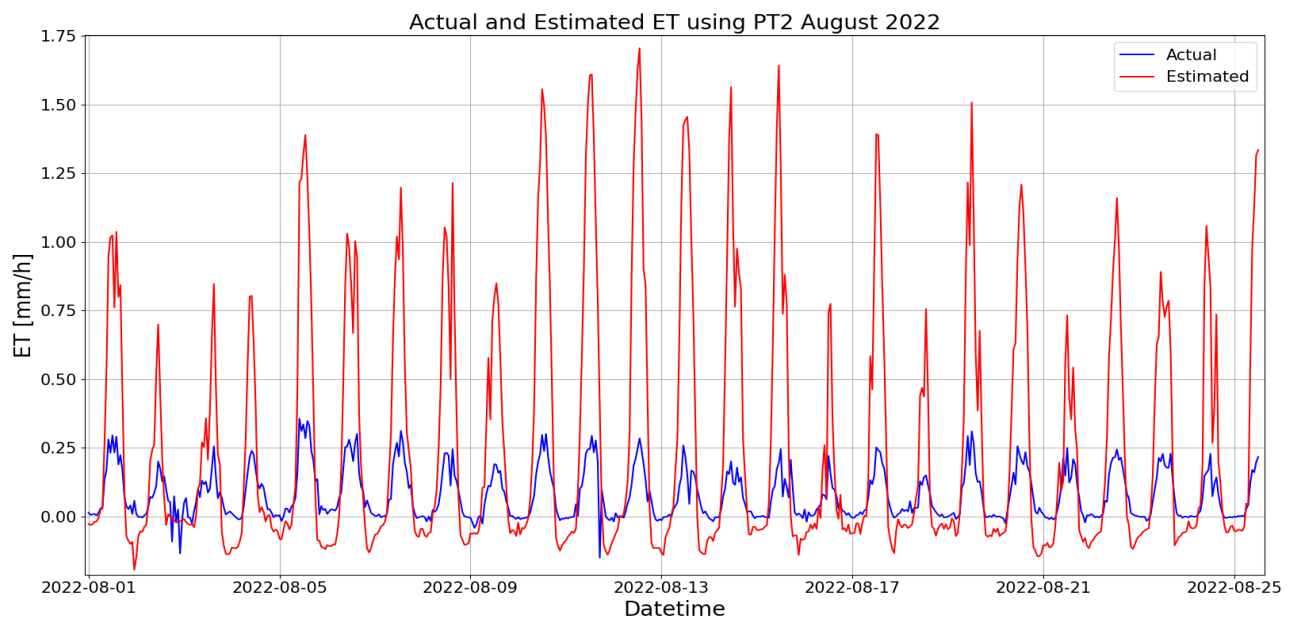


Figure 110: *Hourly measured evapotranspiration (blue) and estimated evapotranspiration (red) using PT2 model in August 2022.*

PT3

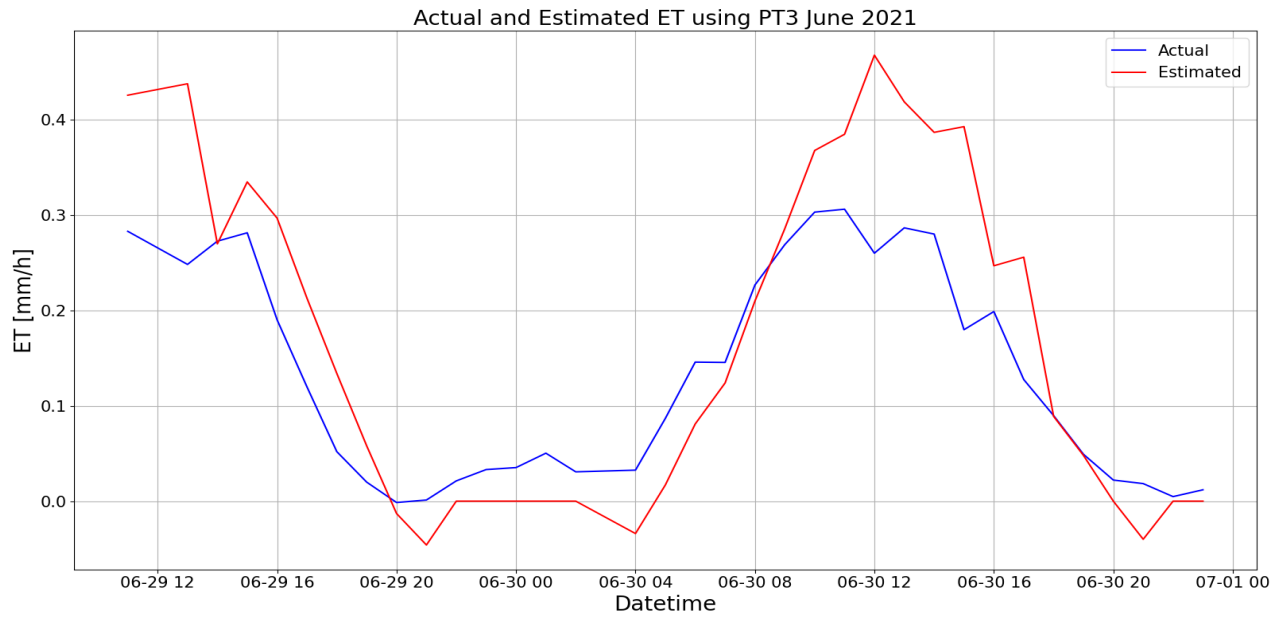


Figure 111: Hourly measured evapotranspiration (blue) and estimated evapotranspiration (red) using PT3 model in June 2021.

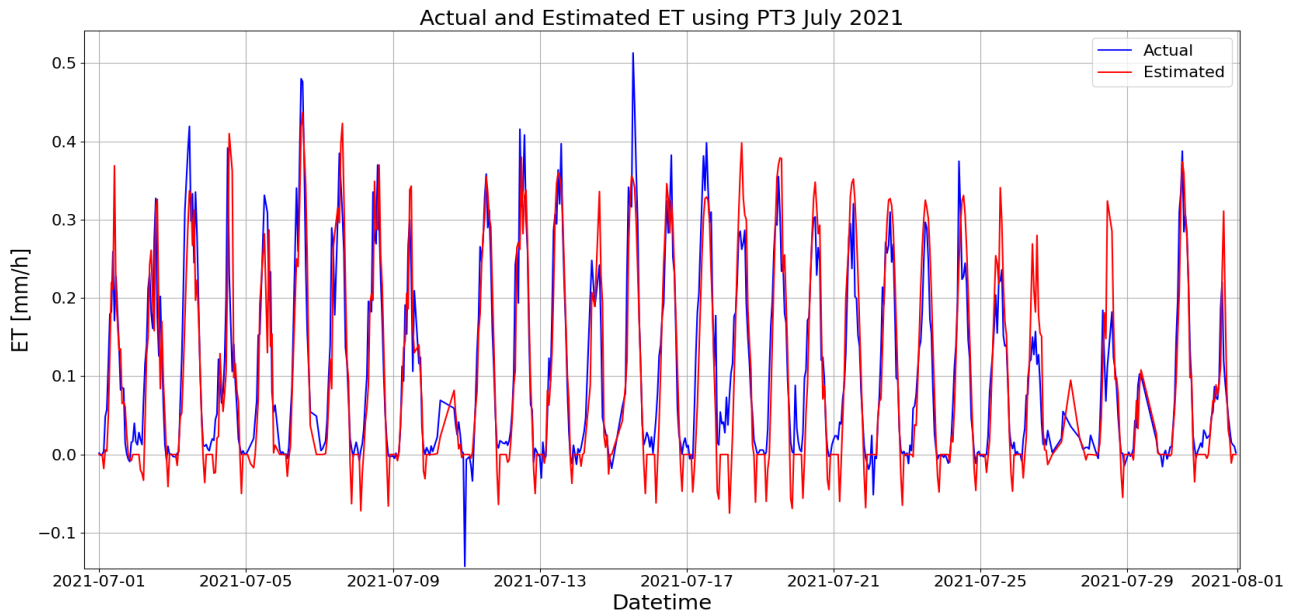


Figure 112: Hourly measured evapotranspiration (blue) and estimated evapotranspiration (red) using PT3 model in July 2021.

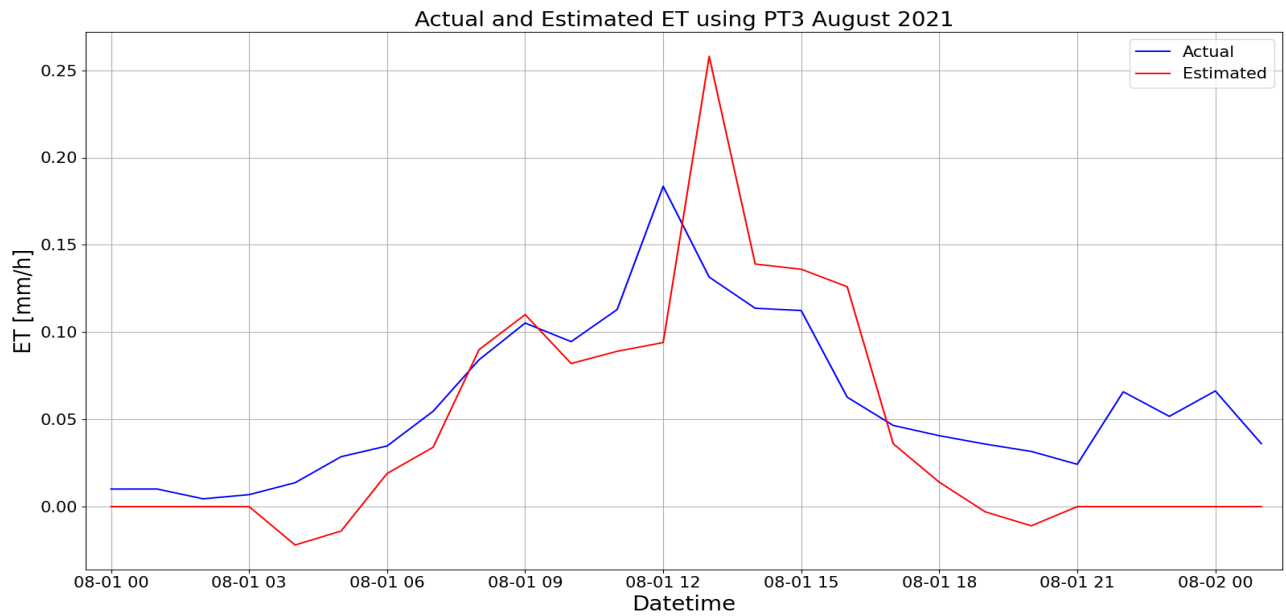


Figure 113: *Hourly measured evapotranspiration (blue) and estimated evapotranspiration (red) using PT3 model in August 2021.*

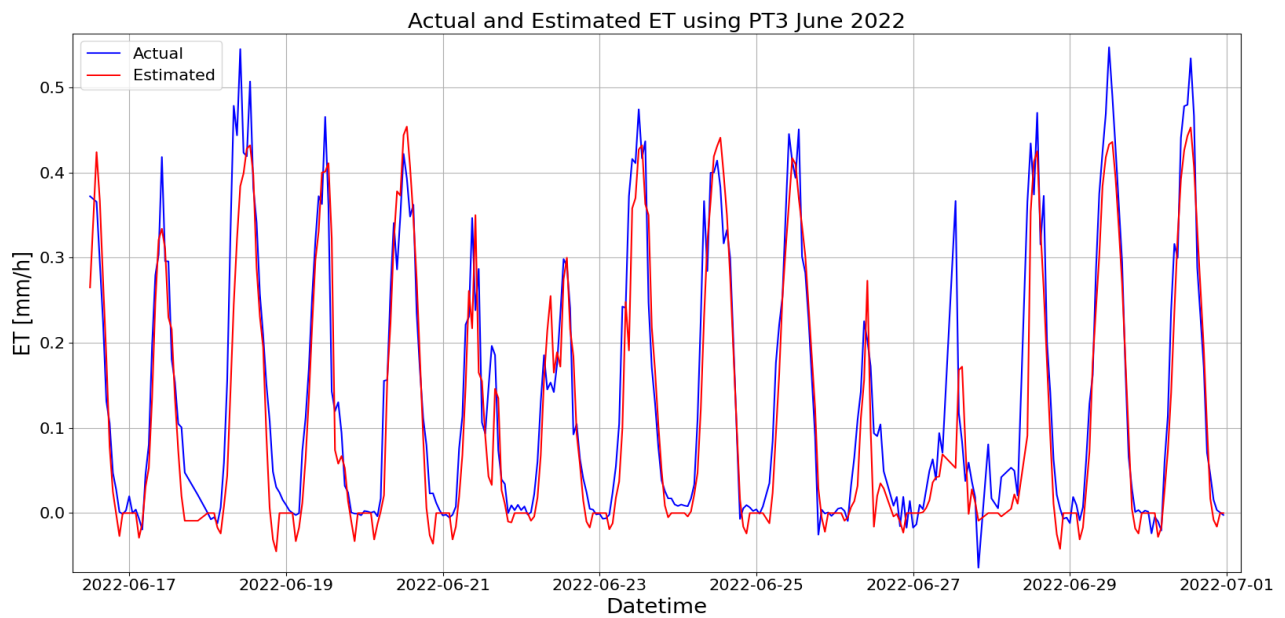


Figure 114: *Hourly measured evapotranspiration (blue) and estimated evapotranspiration (red) using PT3 model in June 2022.*

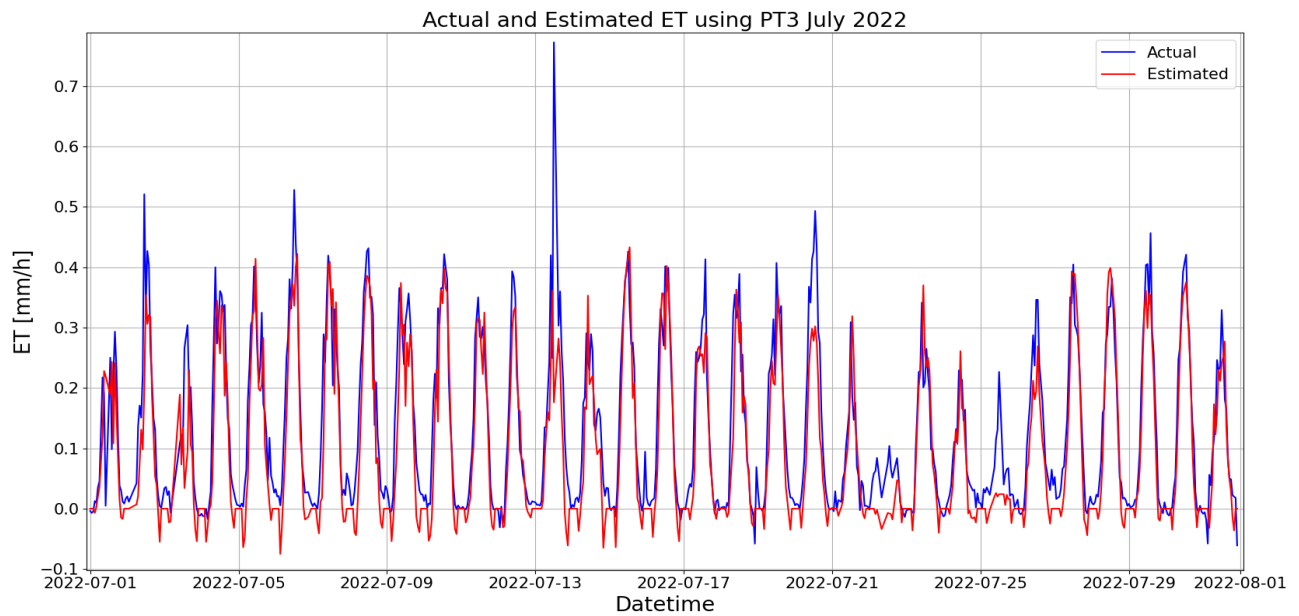


Figure 115: *Hourly measured evapotranspiration (blue) and estimated evapotranspiration (red) using PT3 model in July 2022.*

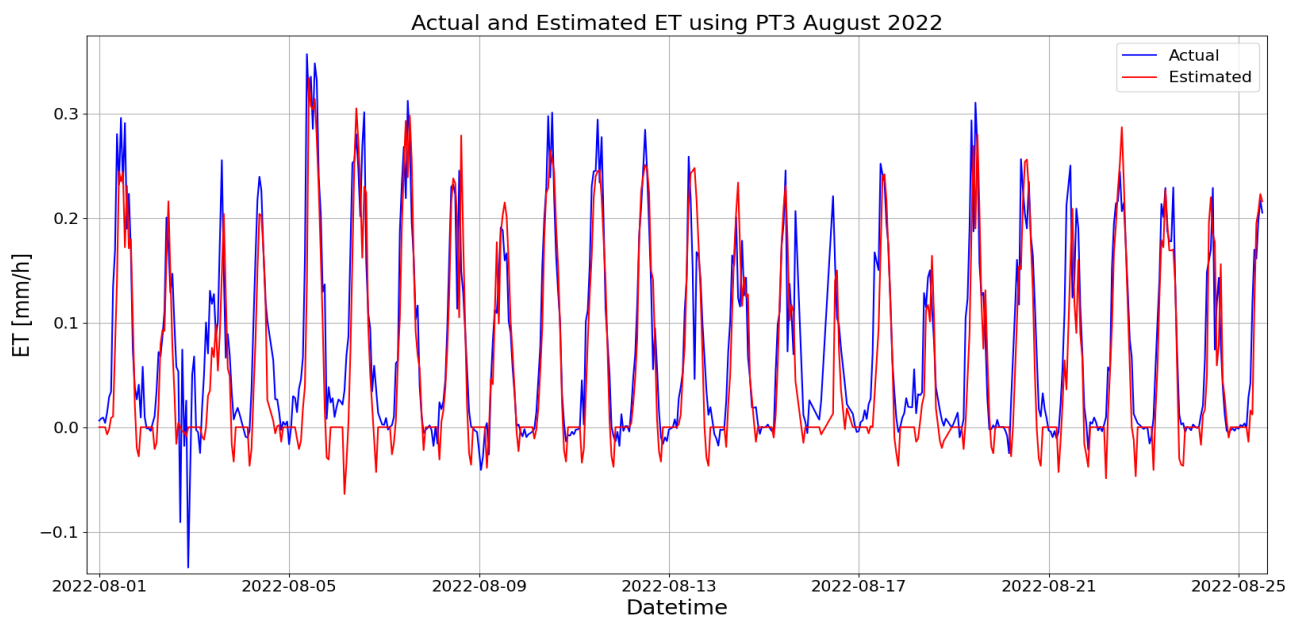


Figure 116: *Hourly measured evapotranspiration (blue) and estimated evapotranspiration (red) using PT3 model in August 2022.*

PT4

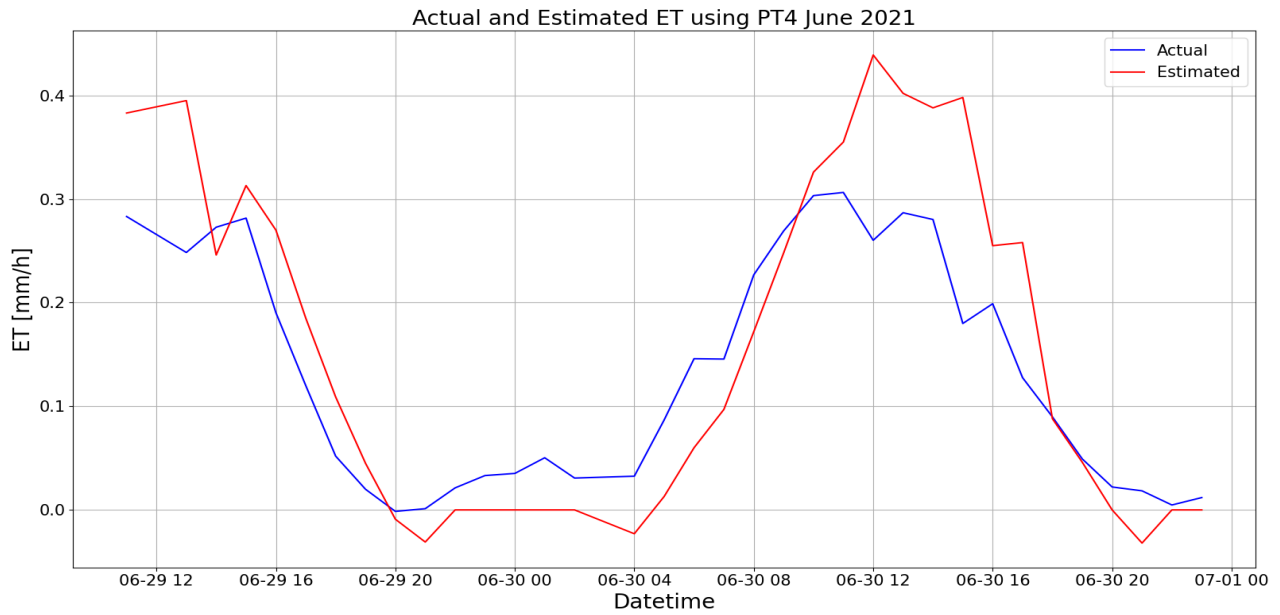


Figure 117: Hourly measured evapotranspiration (blue) and estimated evapotranspiration (red) using PT4 model in June 2021.

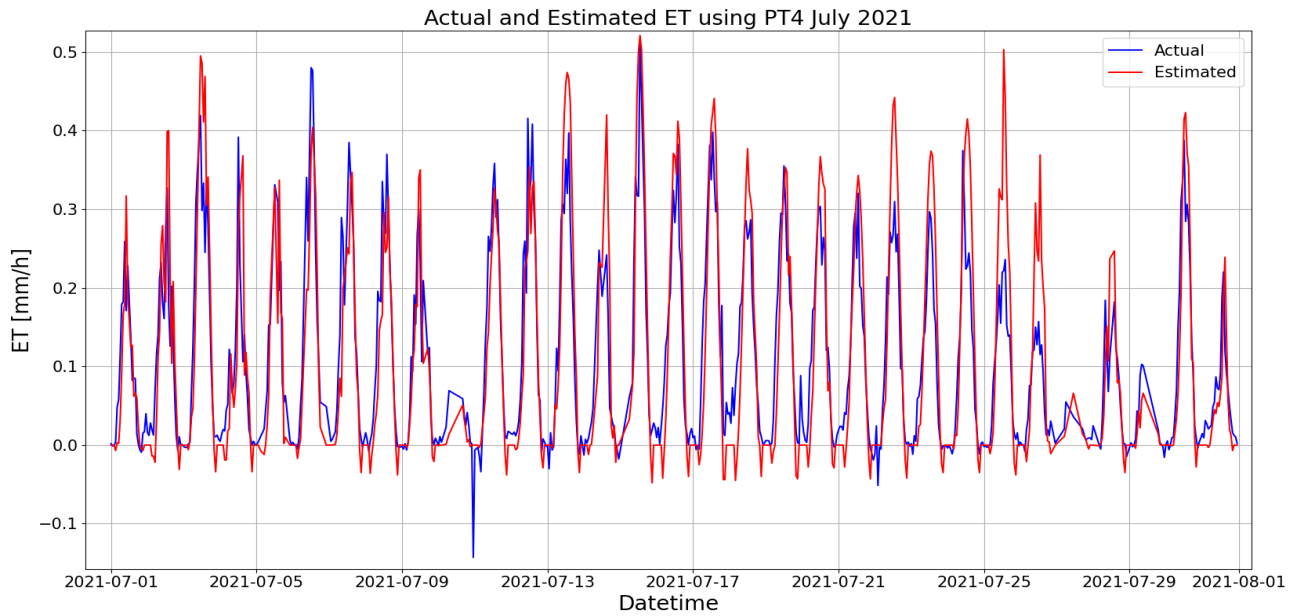


Figure 118: Hourly measured evapotranspiration (blue) and estimated evapotranspiration (red) using PT3 model in July 2021.

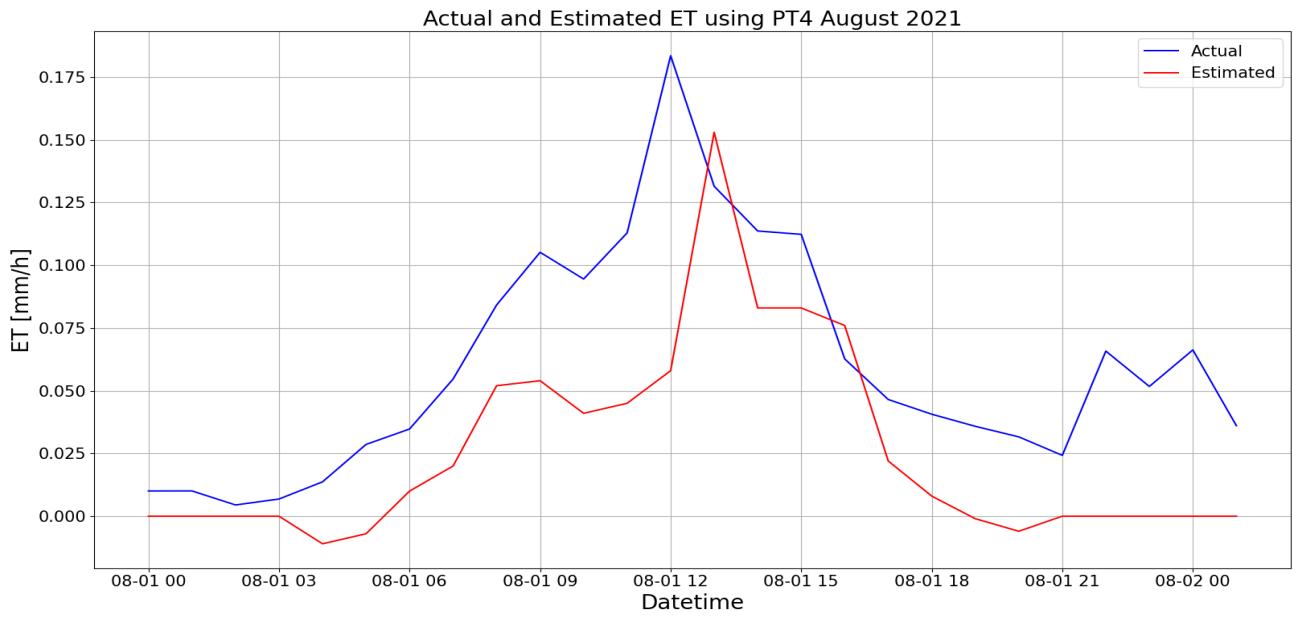


Figure 119: Hourly measured evapotranspiration (blue) and estimated evapotranspiration (red) using PT3 model in August 2021.

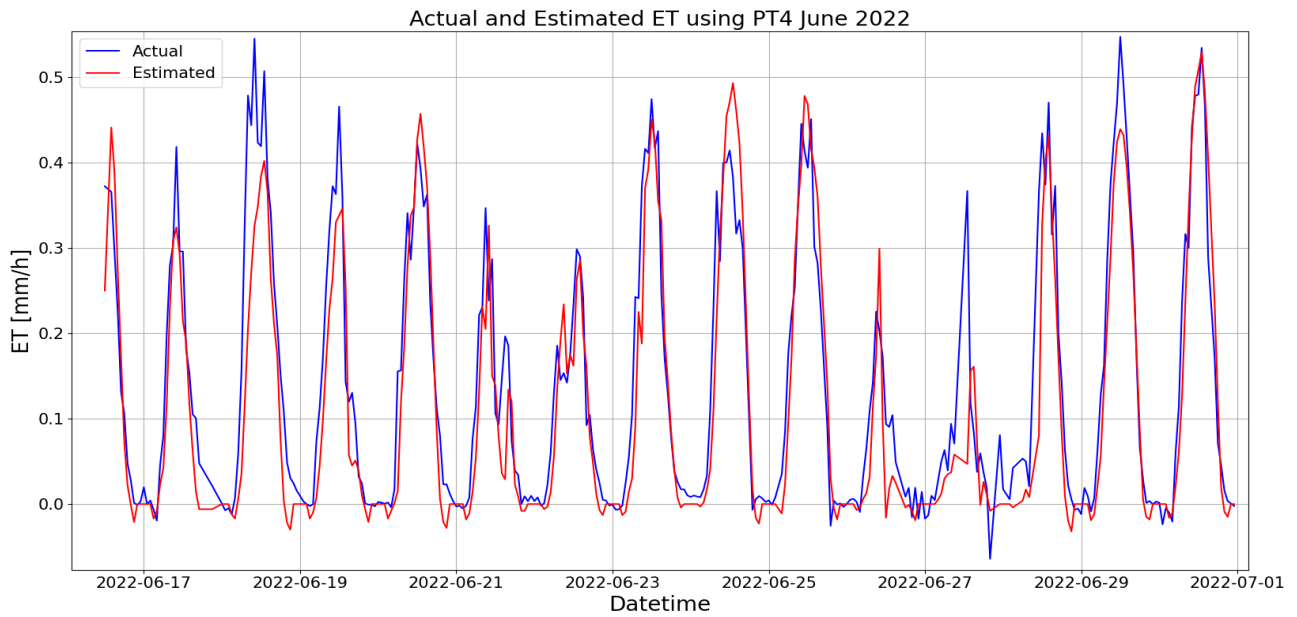


Figure 120: Hourly measured evapotranspiration (blue) and estimated evapotranspiration (red) using PT3 model in June 2022.

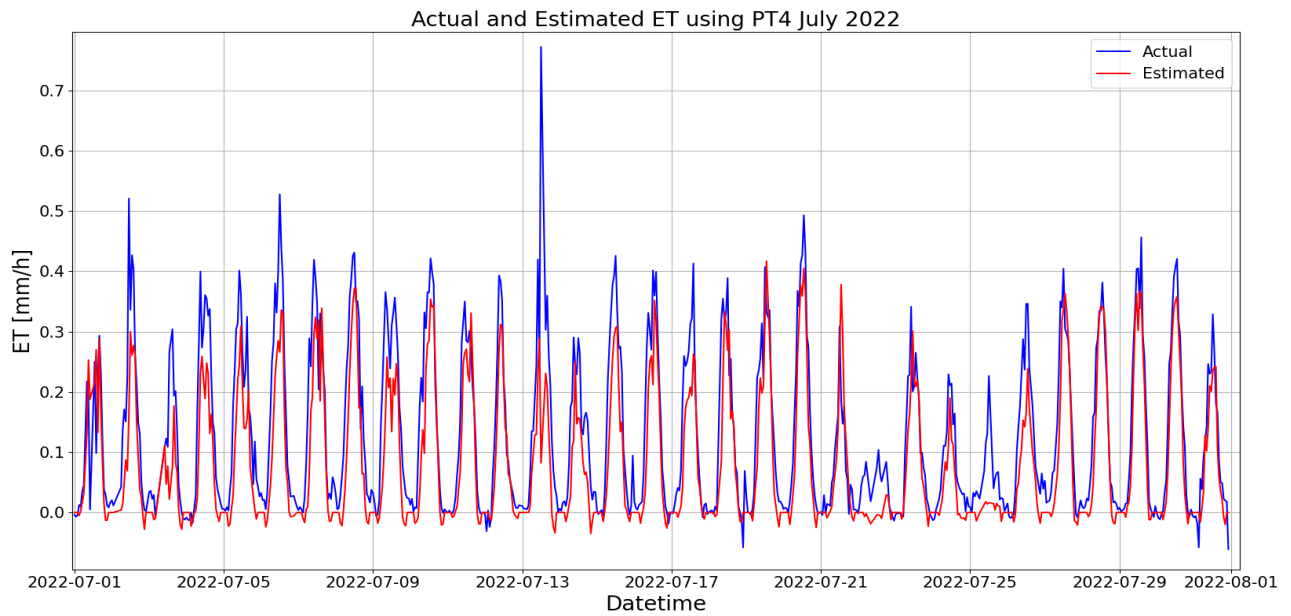


Figure 121: *Hourly measured evapotranspiration (blue) and estimated evapotranspiration (red) using PT3 model in July 2022.*

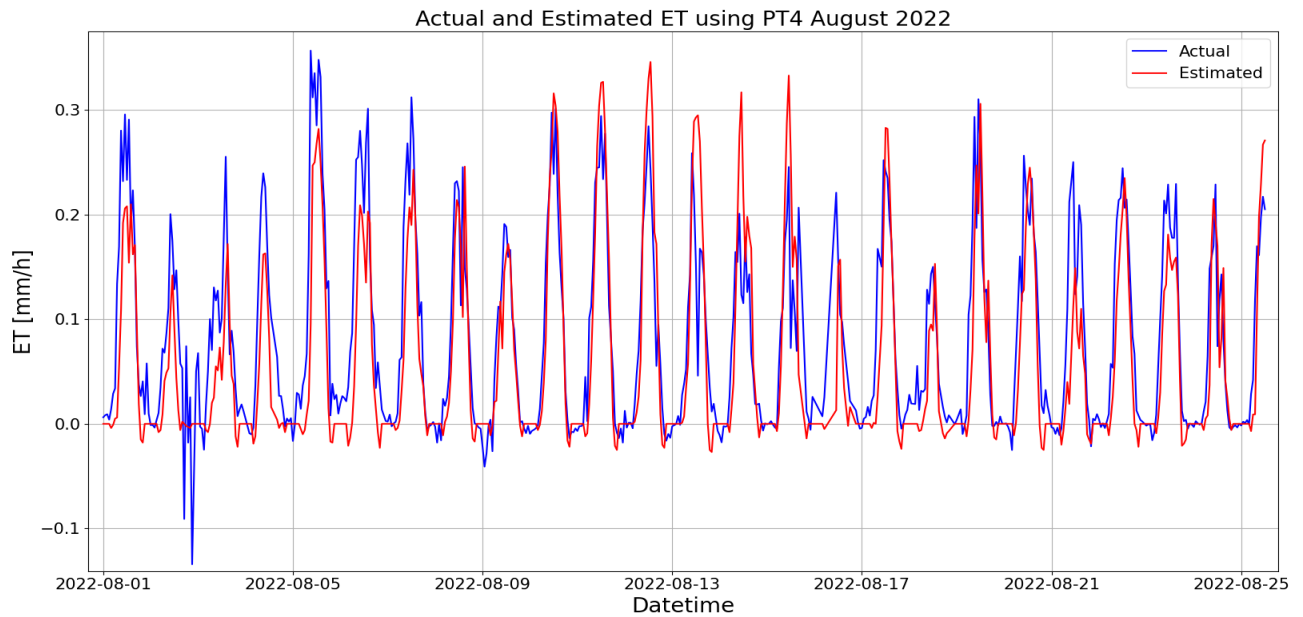


Figure 122: *Hourly measured evapotranspiration (blue) and estimated evapotranspiration (red) using PT3 model in August 2022.*

PT daily

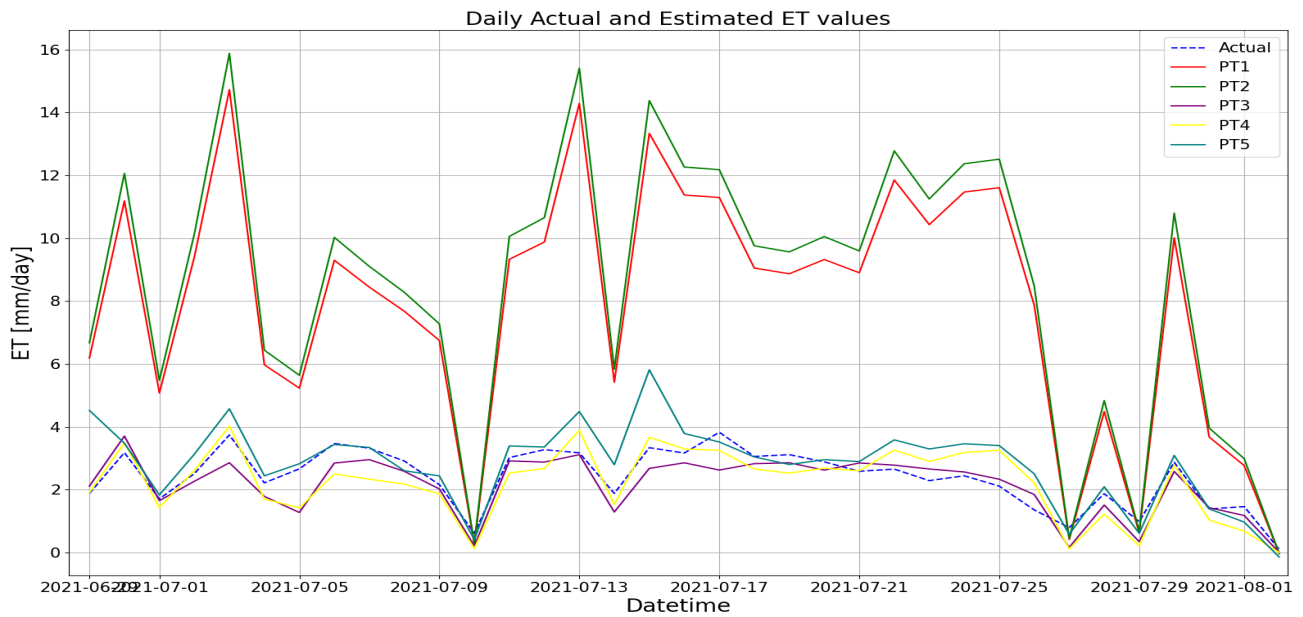


Figure 123: Daily measured (dashed blue), and estimated by PT1 (red), PT2 (green), PT3 (purple), PT4 (yellow) and PT5 (teal) evapotranspiration values in 2021.

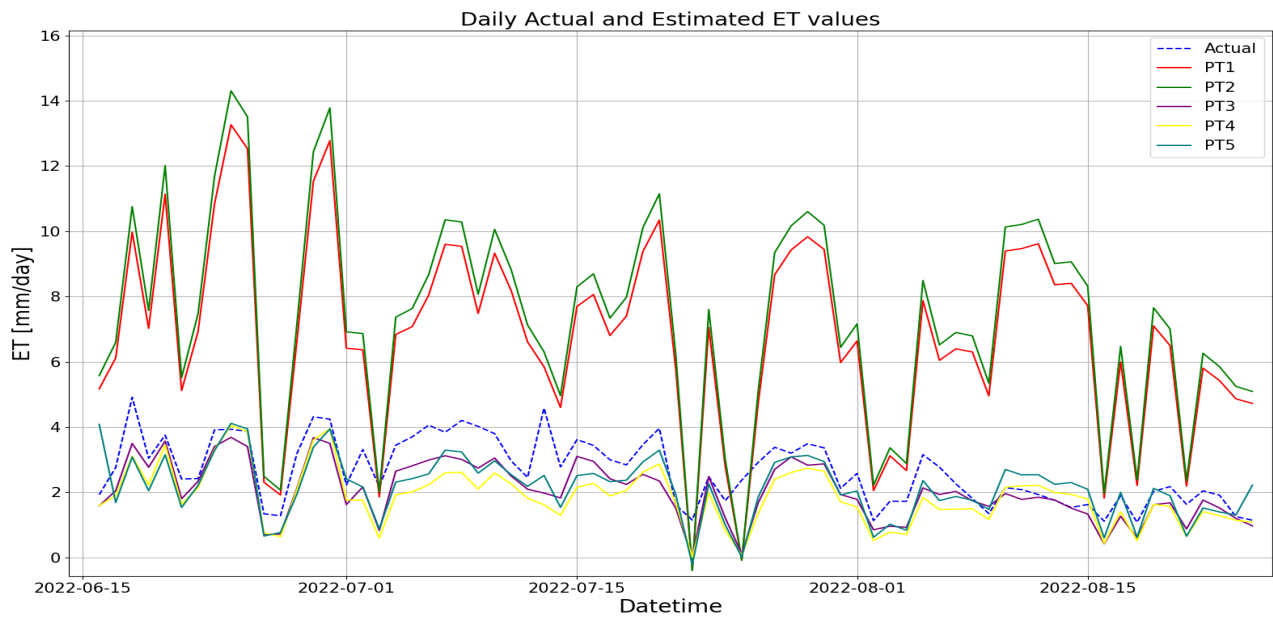


Figure 124: Daily measured (dashed blue), and estimated by PT1 (red), PT2 (green), PT3 (purple), PT4 (yellow) and PT5 (teal) evapotranspiration values in 2022.

B2: PM models

PMhourly1

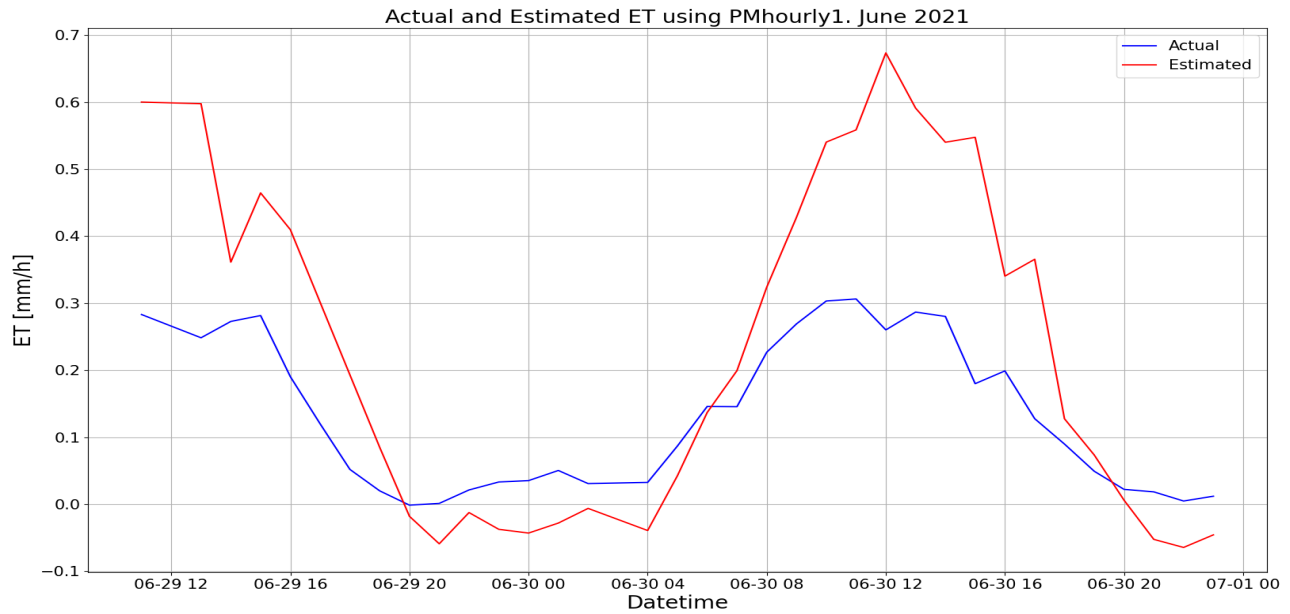


Figure 125: Hourly measured evapotranspiration (blue) and estimated evapotranspiration (red) using PMhourly1 model in June 2021.

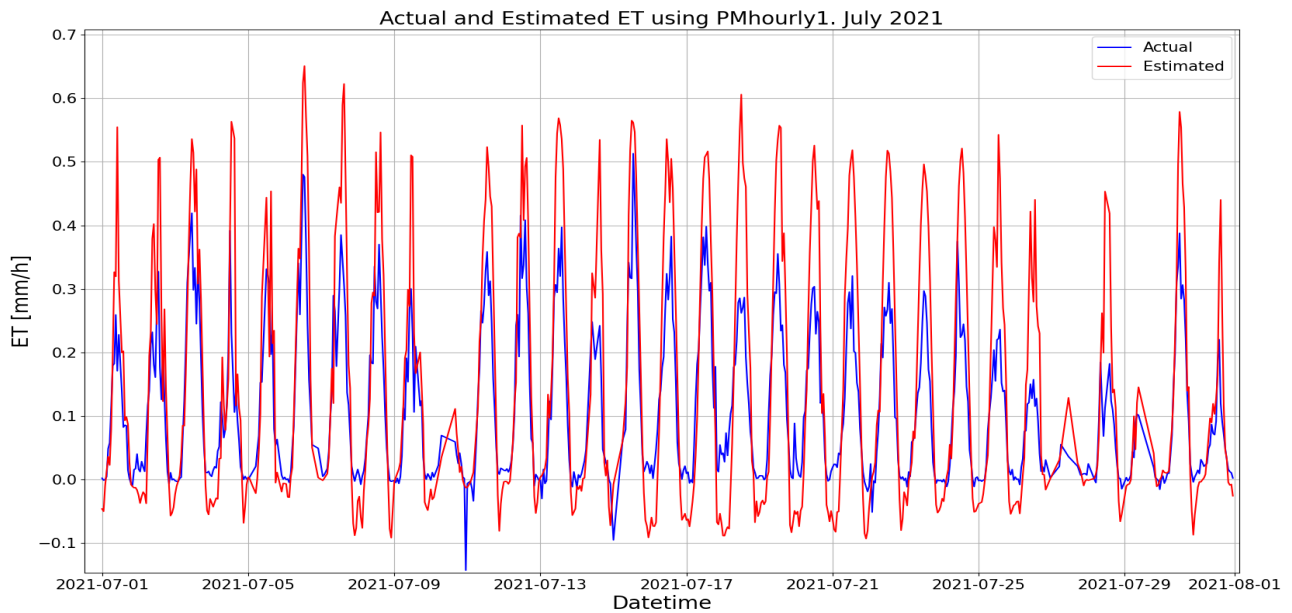


Figure 126: Hourly measured evapotranspiration (blue) and estimated evapotranspiration (red) using PMhourly1 model in July 2021.

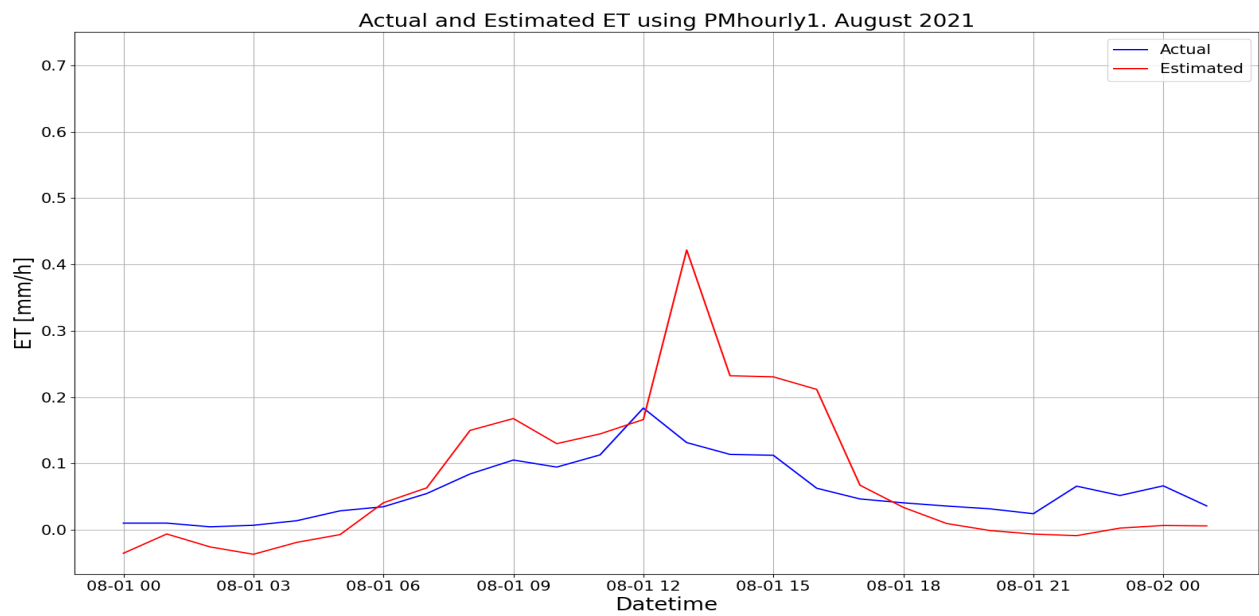


Figure 127: Hourly measured evapotranspiration (blue) and estimated evapotranspiration (red) using PMhourly1 model in August 2021.

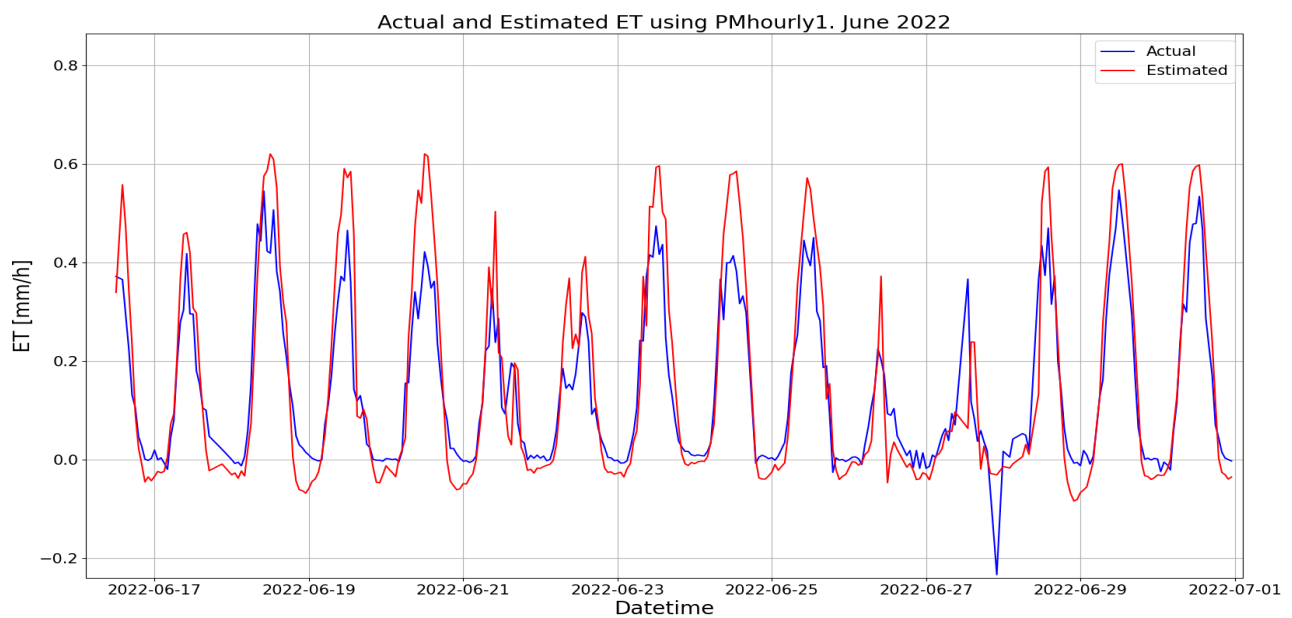


Figure 128: Hourly measured evapotranspiration (blue) and estimated evapotranspiration (red) using PMhourly1 model in June 2022.

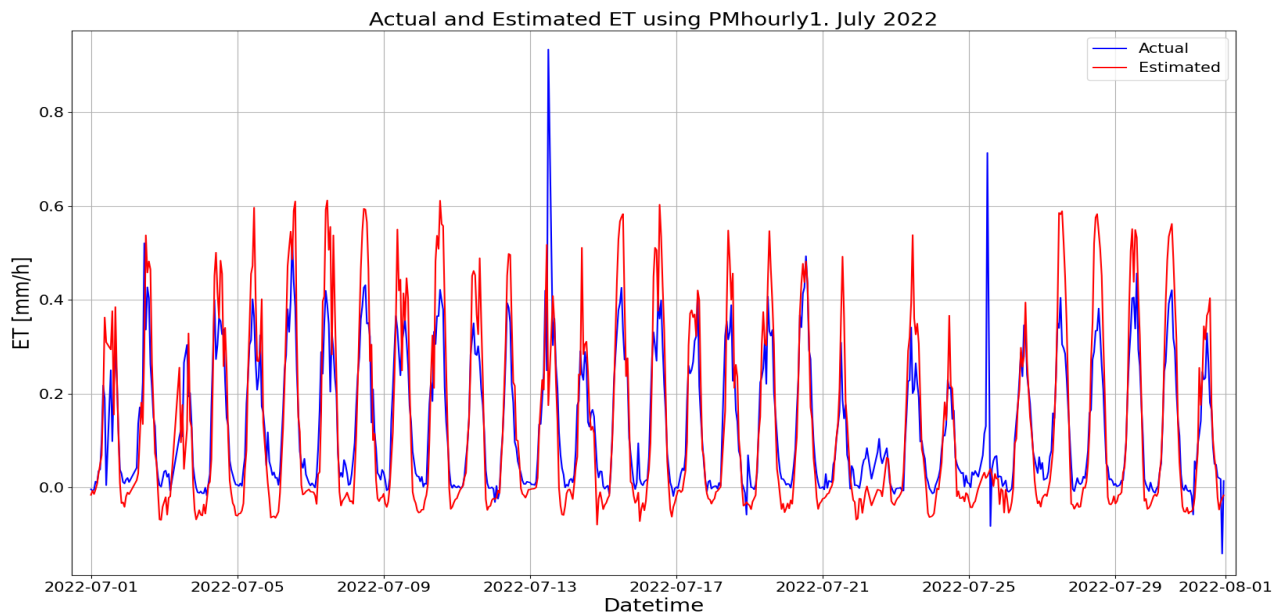


Figure 129: Hourly measured evapotranspiration (blue) and estimated evapotranspiration (red) using PMhourly1 model in July 2022.

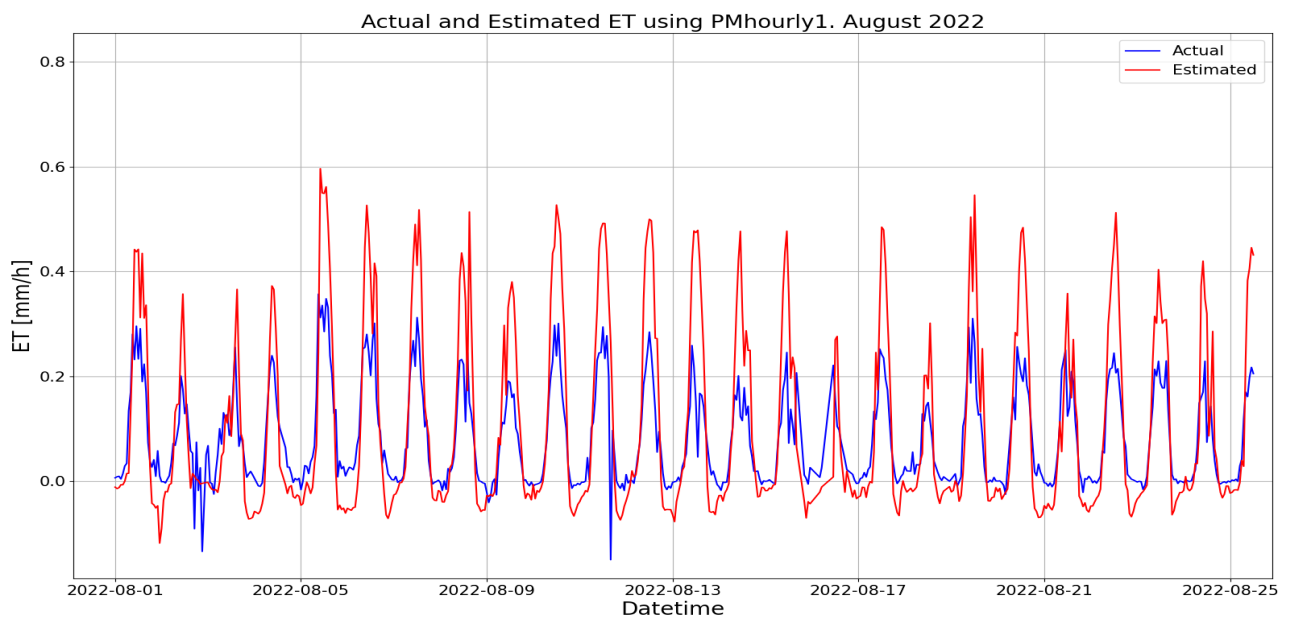


Figure 130: Hourly measured evapotranspiration (blue) and estimated evapotranspiration (red) using PMhourly1 model in August 2022.

PMhourly2

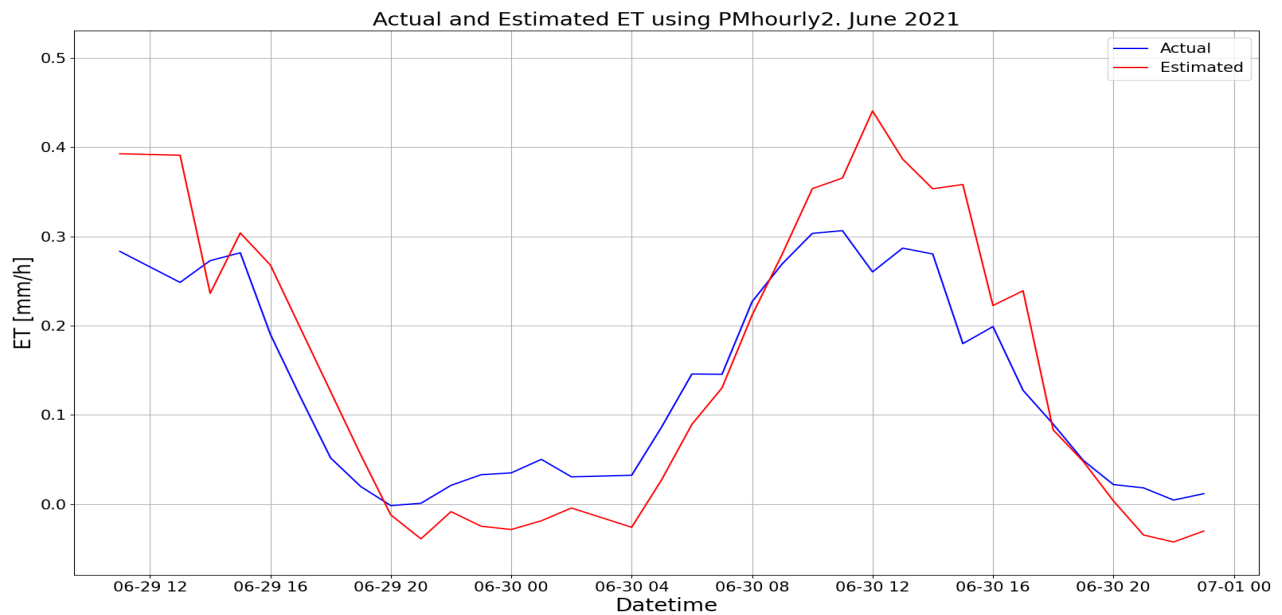


Figure 131: Hourly measured evapotranspiration (blue) and estimated evapotranspiration (red) using PMhourly2 model in June 2021.

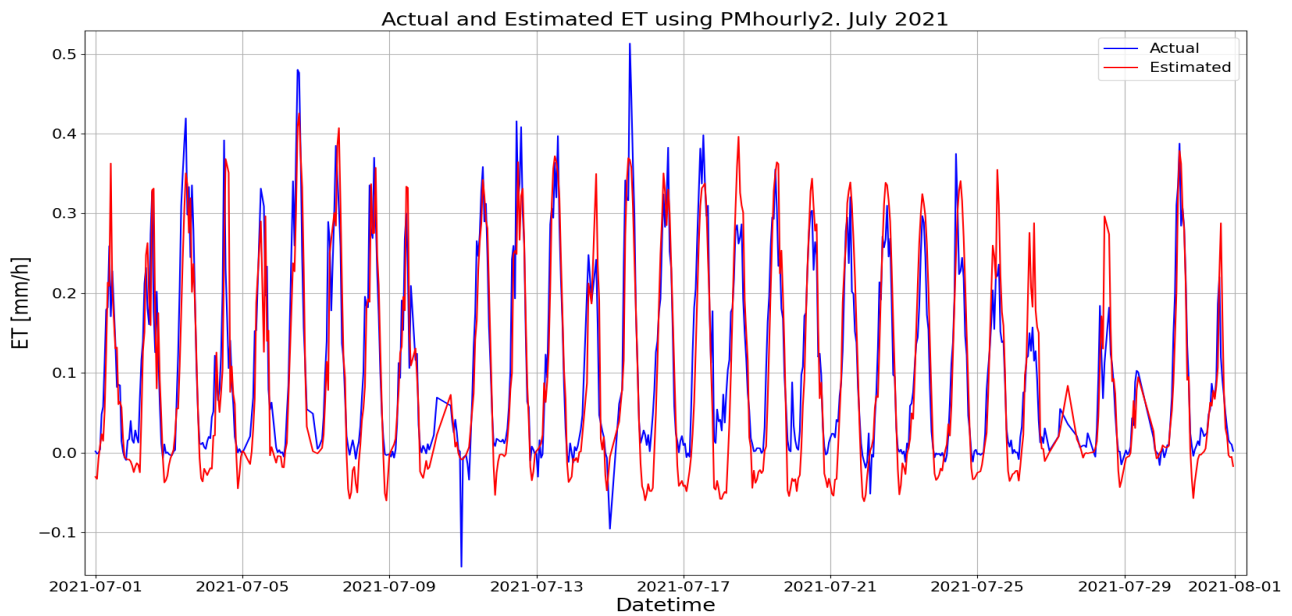


Figure 132: Hourly measured evapotranspiration (blue) and estimated evapotranspiration (red) using PMhourly2 model in July 2021.

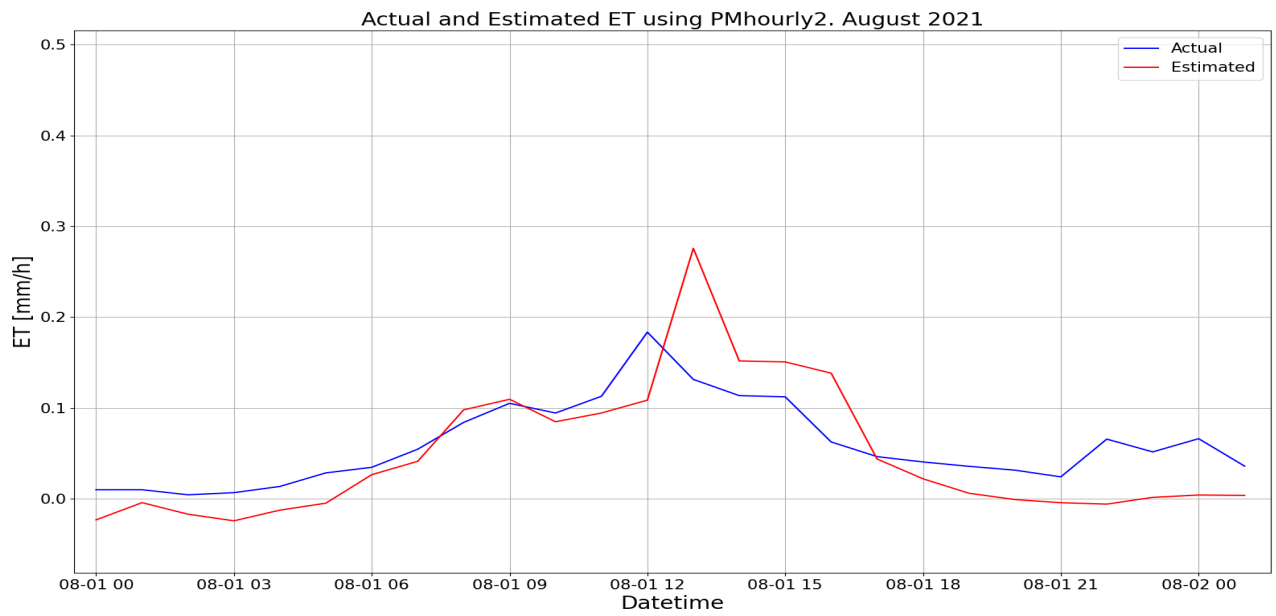


Figure 133: Hourly measured evapotranspiration (blue) and estimated evapotranspiration (red) using PMhourly2 model in August 2021.

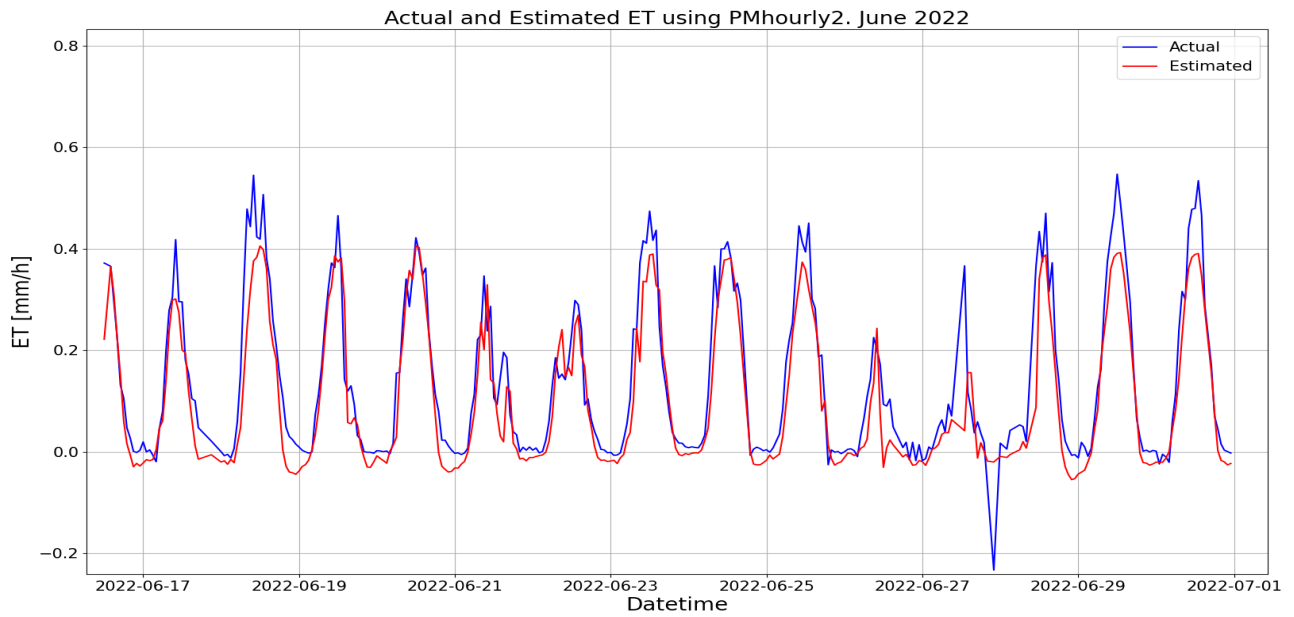


Figure 134: Hourly measured evapotranspiration (blue) and estimated evapotranspiration (red) using PMhourly2 model in June 2022.

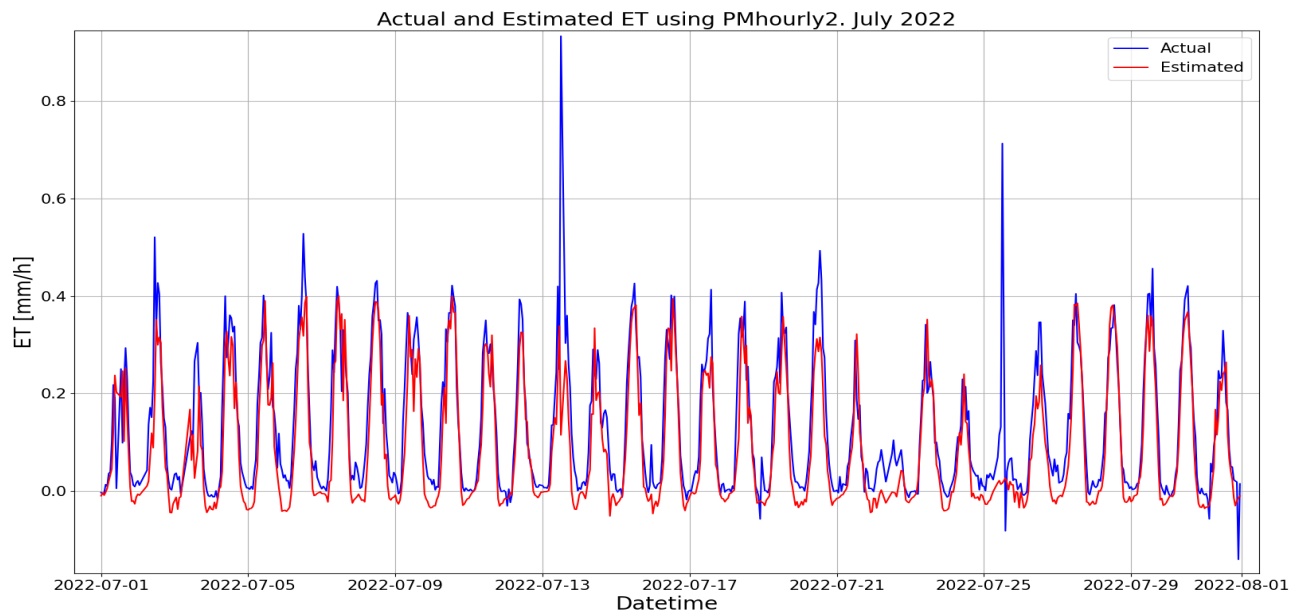


Figure 135: Hourly measured evapotranspiration (blue) and estimated evapotranspiration (red) using PMhourly2 model in July 2022.

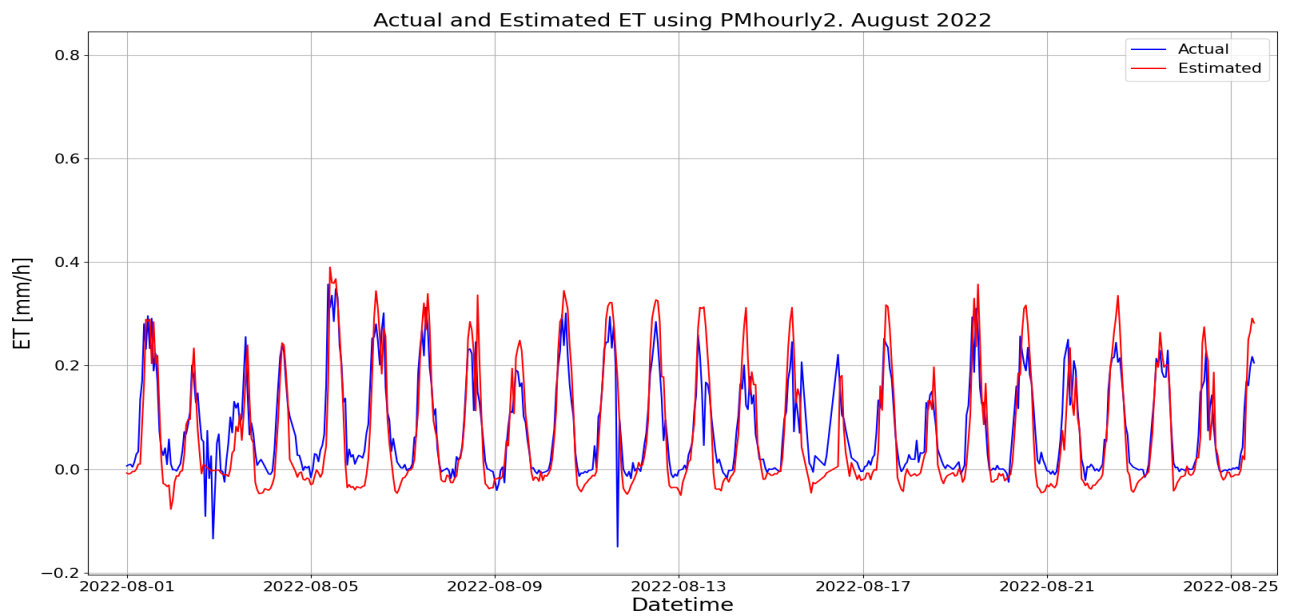


Figure 136: Hourly measured evapotranspiration (blue) and estimated evapotranspiration (red) using PMhourly2 model in August 2022.

PMdaily2 and daily resolution of PMhourly1 and PMhourly2

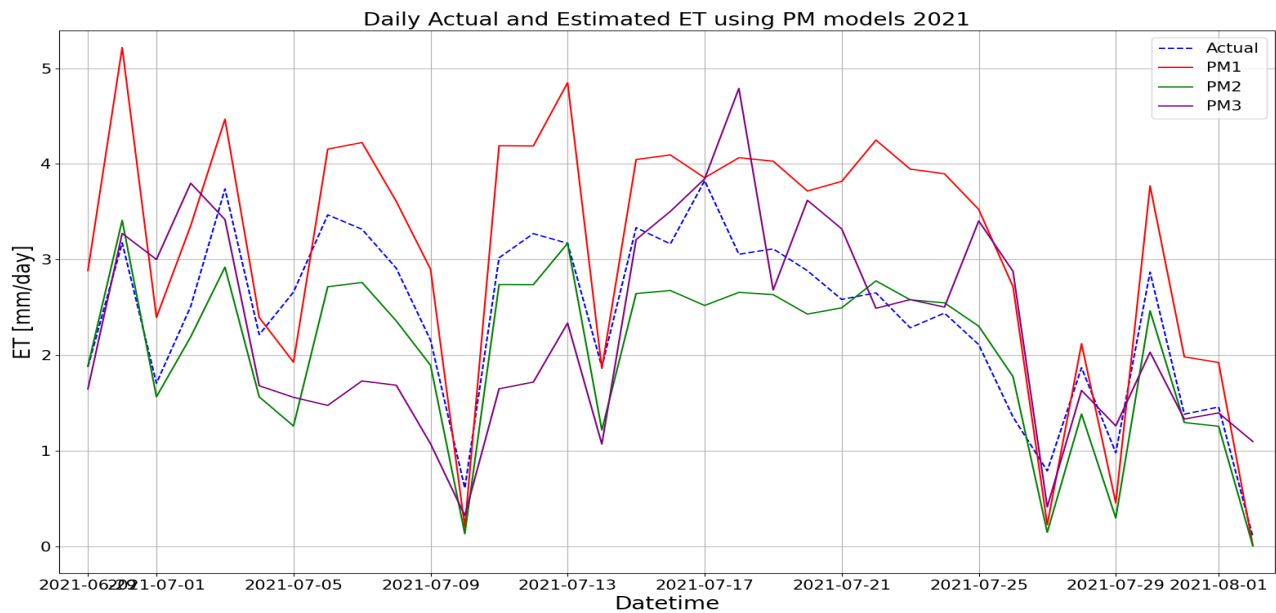


Figure 137: Daily measured (dashed blue), and estimated by PMhourly1 (red), PMhourly2 (green) and PMdaily2 (purple) evapotranspiration values in 2021.

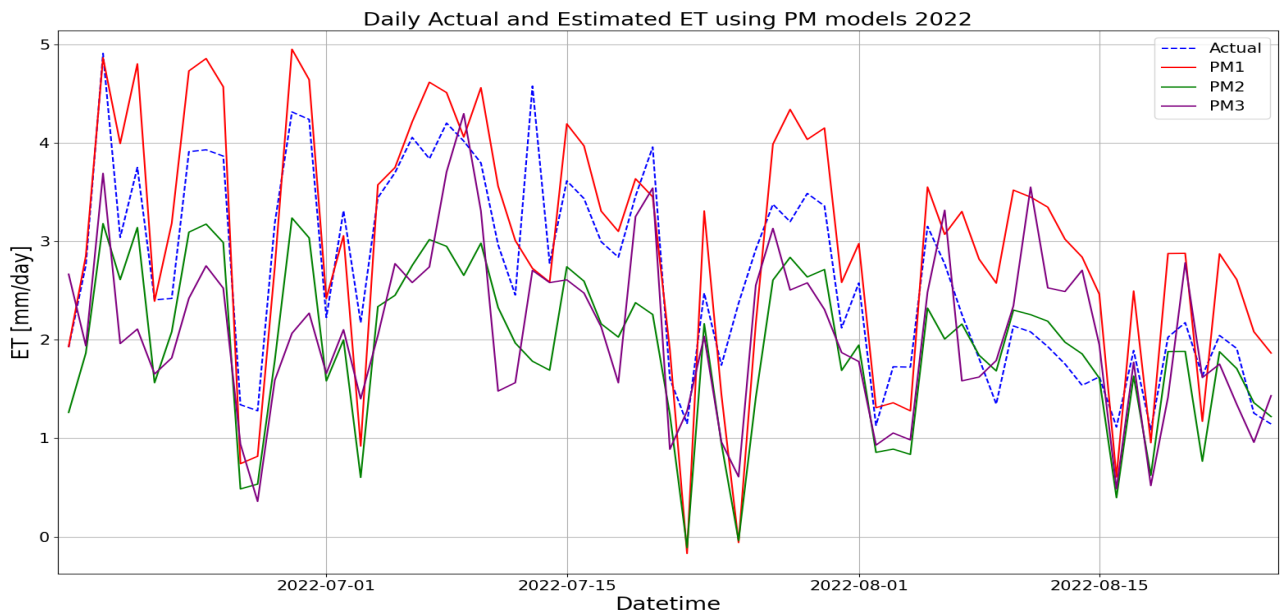


Figure 138: Daily measured (dashed blue), and estimated by PMhourly1 (red), PMhourly2 (green) and PMdaily2 (purple) evapotranspiration values in 2022.

PMdaily1

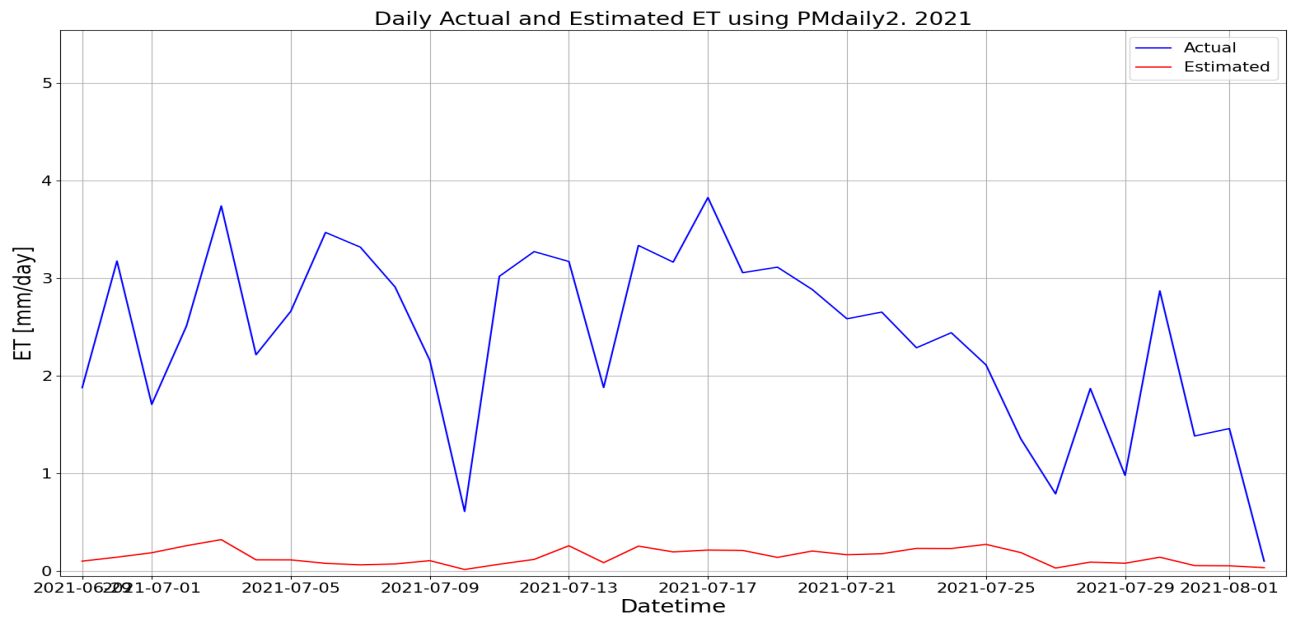


Figure 139: Daily measured (blue) and estimated by PMdaily1 (red) evapotranspiration values in 2021.

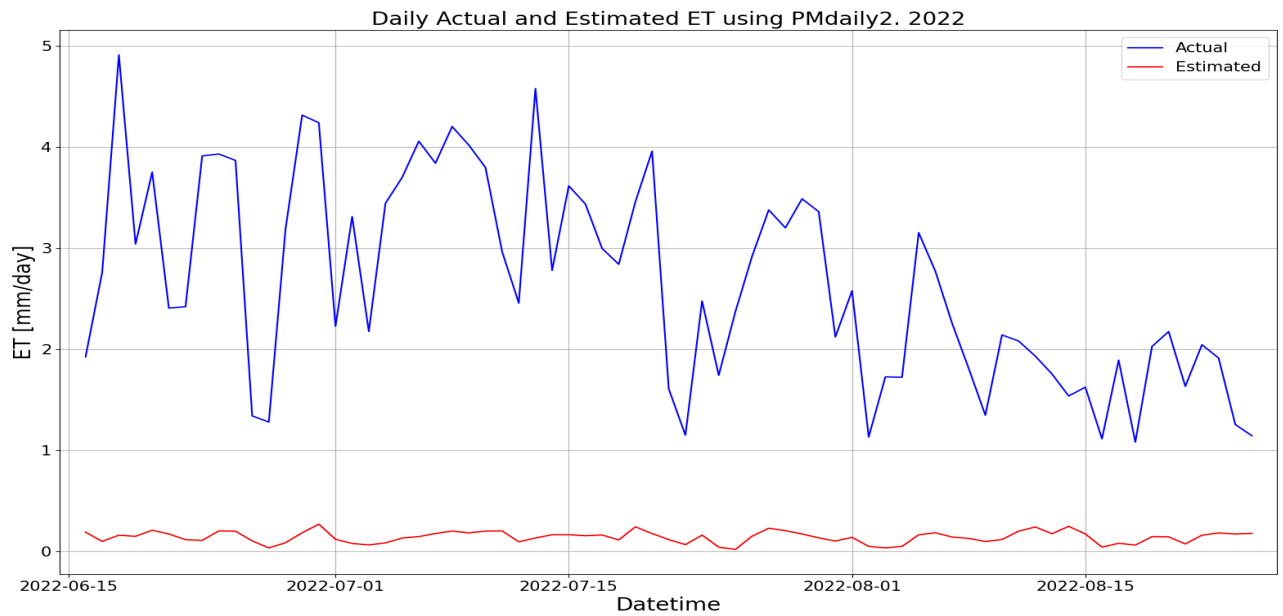


Figure 140: Daily measured (blue) and estimated by PMdaily1 (red) evapotranspiration values in 2022.

Appendix C: Pan vs EC

Pan evaporation hourly

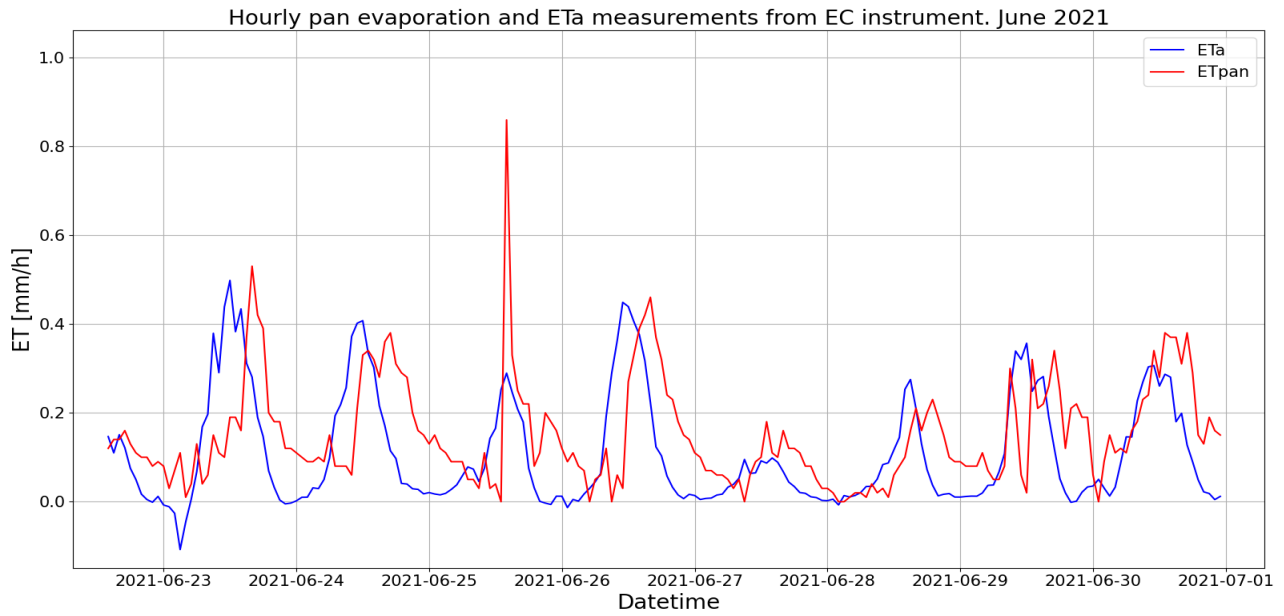


Figure 141: Hourly measured evapotranspiration (blue) and measured pan evaporation (red) in June 2021.

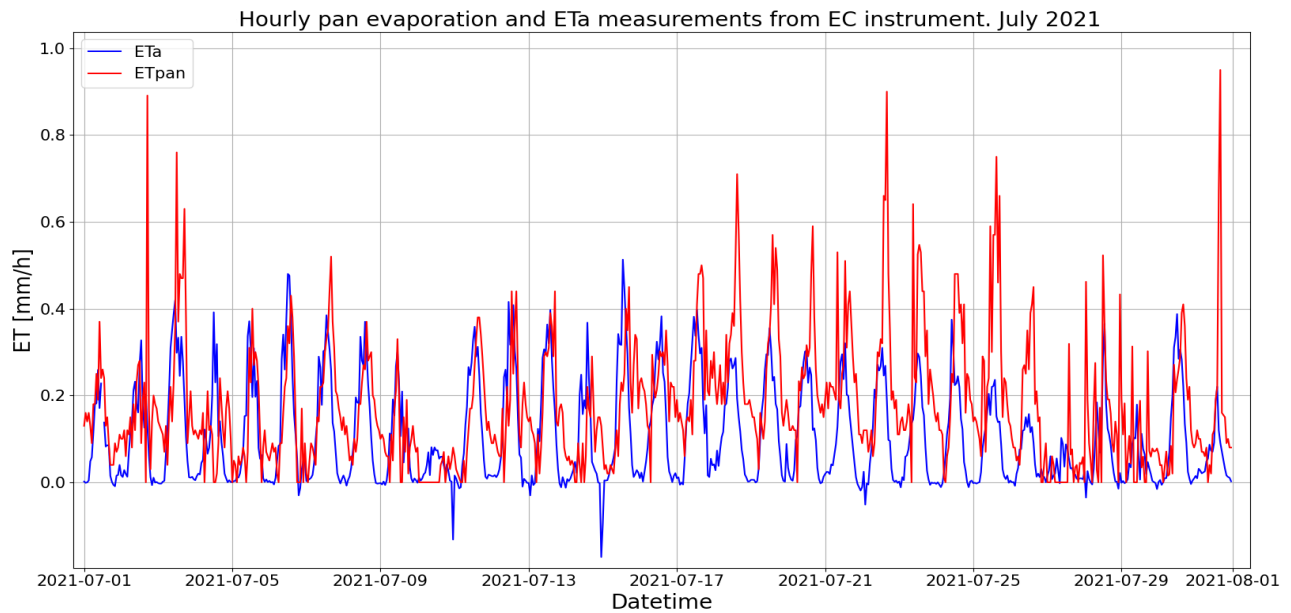


Figure 142: Hourly measured evapotranspiration (blue) and measured pan evaporation (red) in July 2021.

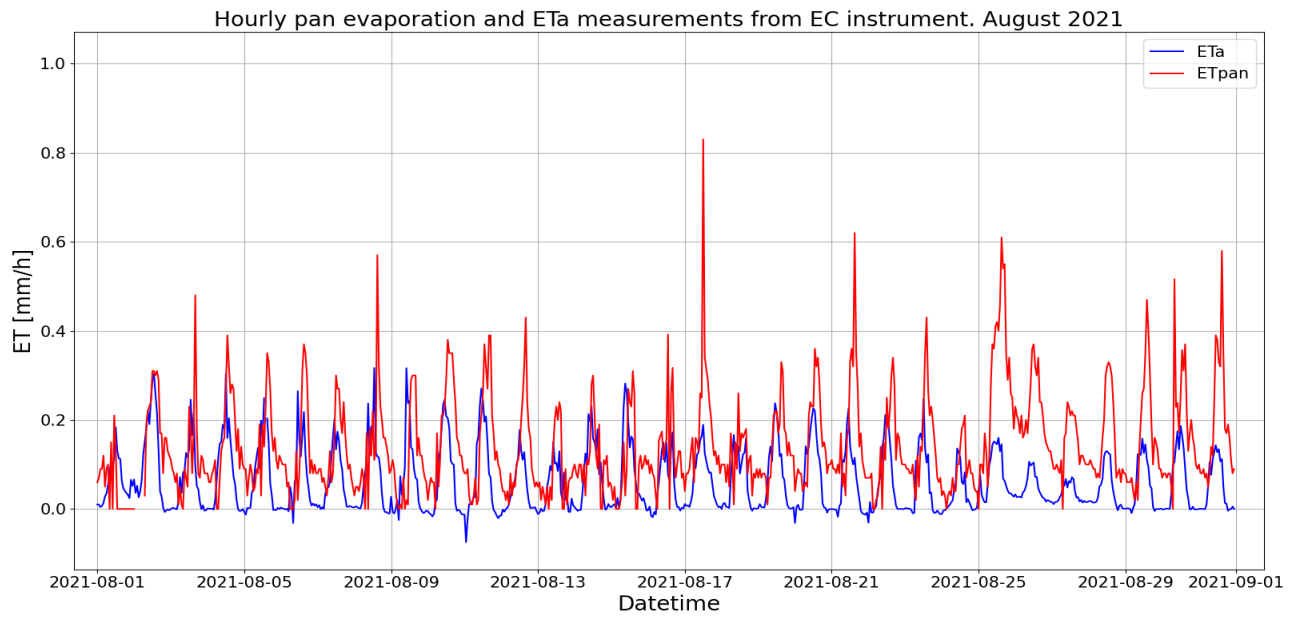


Figure 143: *Hourly measured evapotranspiration (blue) and measured pan evaporation (red) in August 2021.*

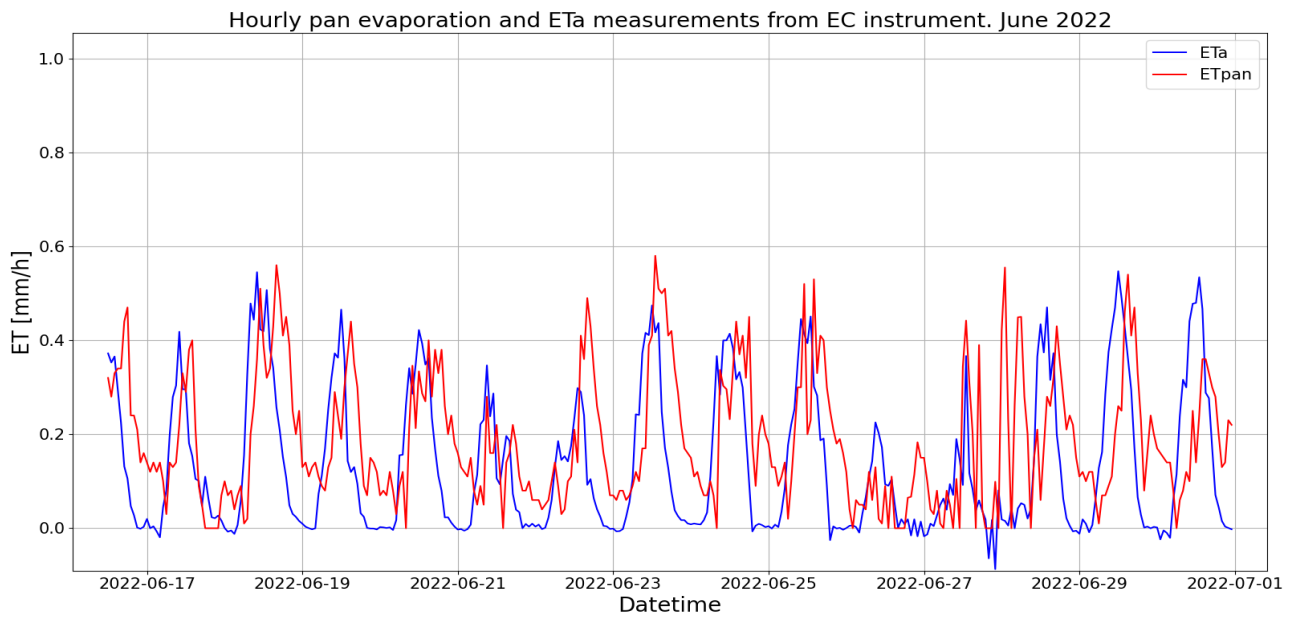


Figure 144: *Hourly measured evapotranspiration (blue) and measured pan evaporation (red) in June 2022.*

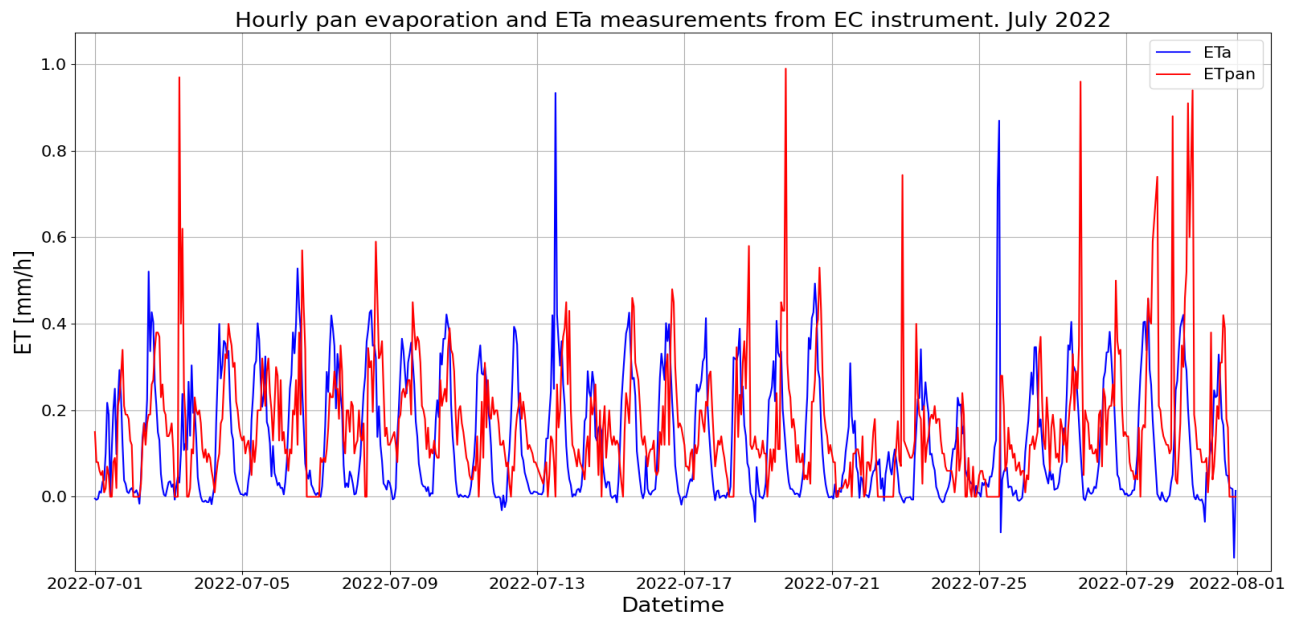


Figure 145: *Hourly measured evapotranspiration (blue) and measured pan evaporation (red) in July 2022.*

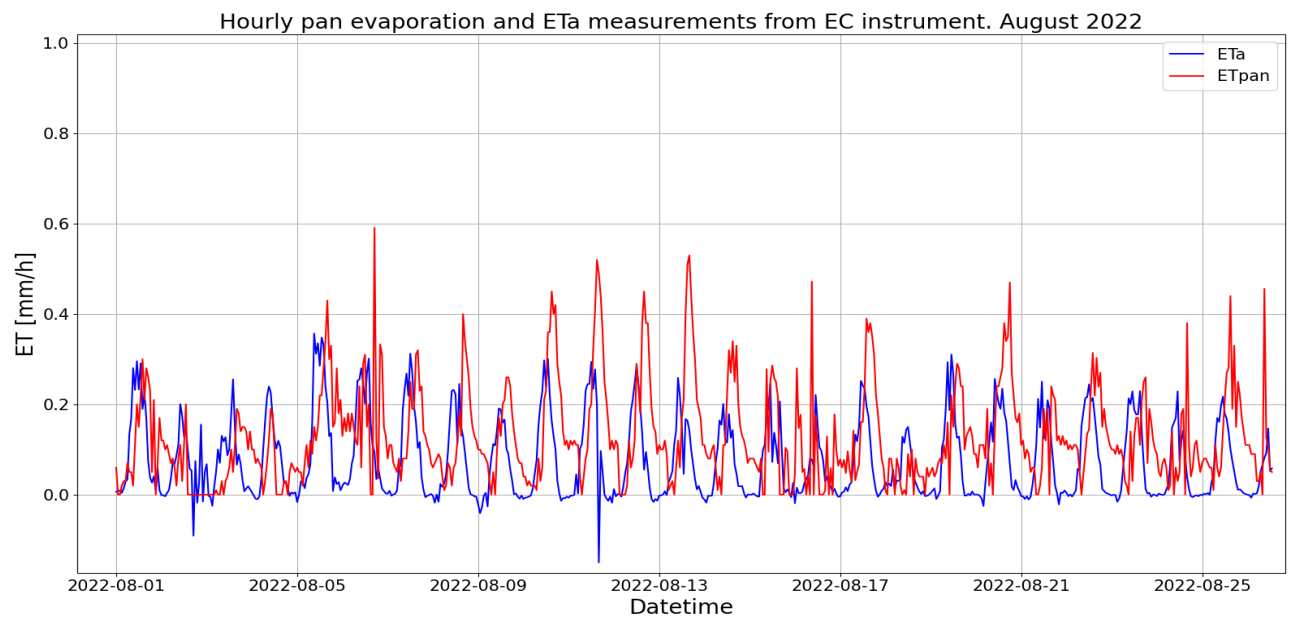


Figure 146: *Hourly measured evapotranspiration (blue) and measured pan evaporation (red) in August 2022.*

Reference evapotranspiration hourly

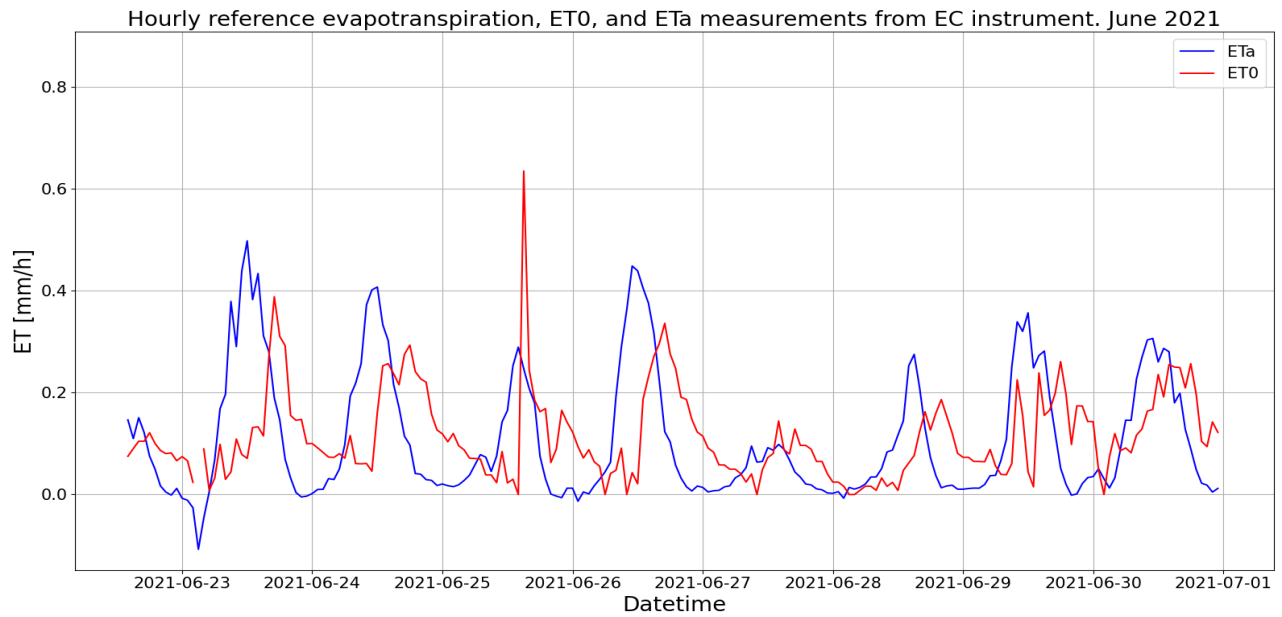


Figure 147: Hourly measured evapotranspiration (blue) and estimated reference evapotranspiration (red) in June 2021.

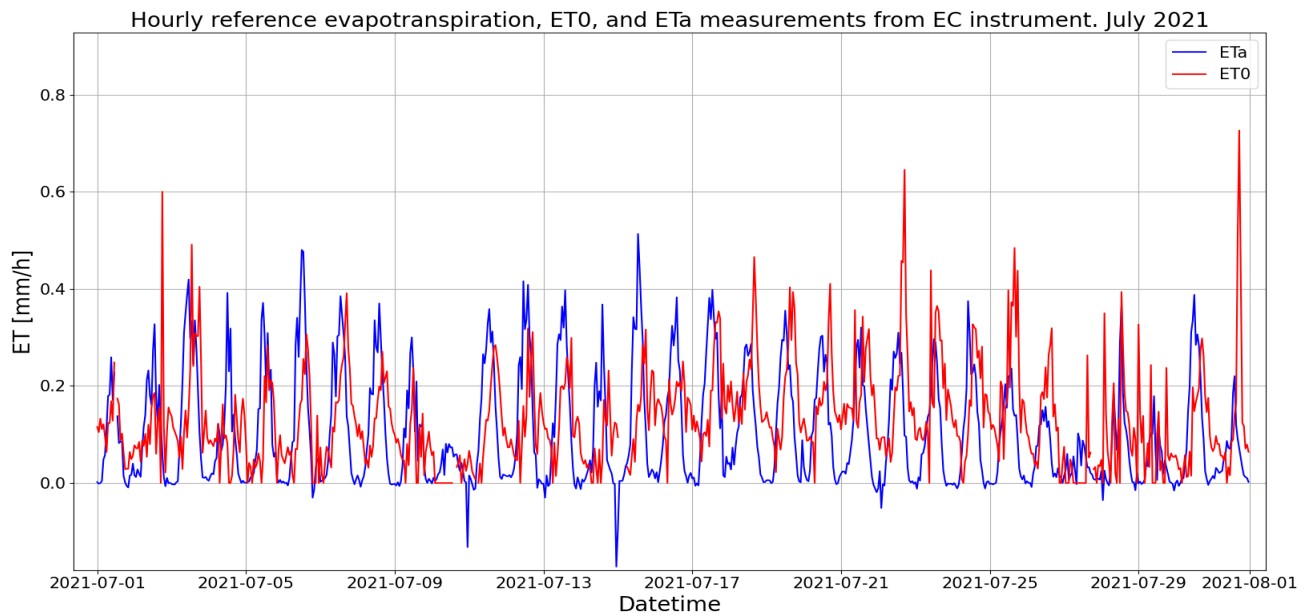


Figure 148: Hourly measured evapotranspiration (blue) and estimated reference evapotranspiration (red) in July 2021.

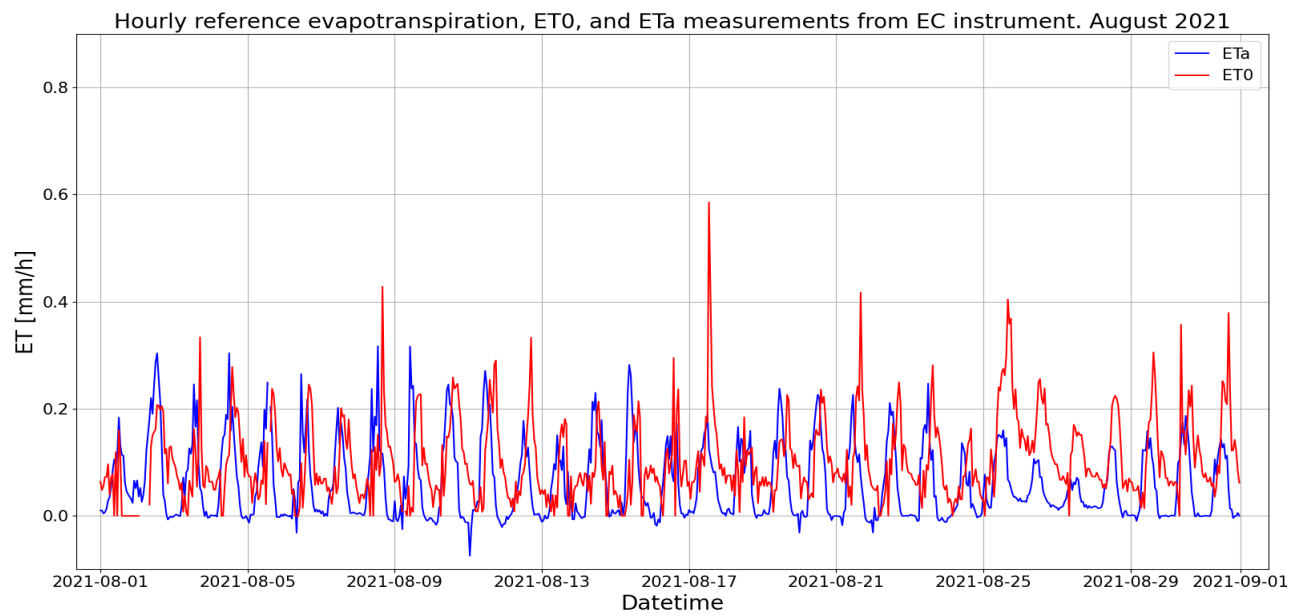


Figure 149: *Hourly measured evapotranspiration (blue) and estimated reference evapotranspiration (red) in August 2021.*

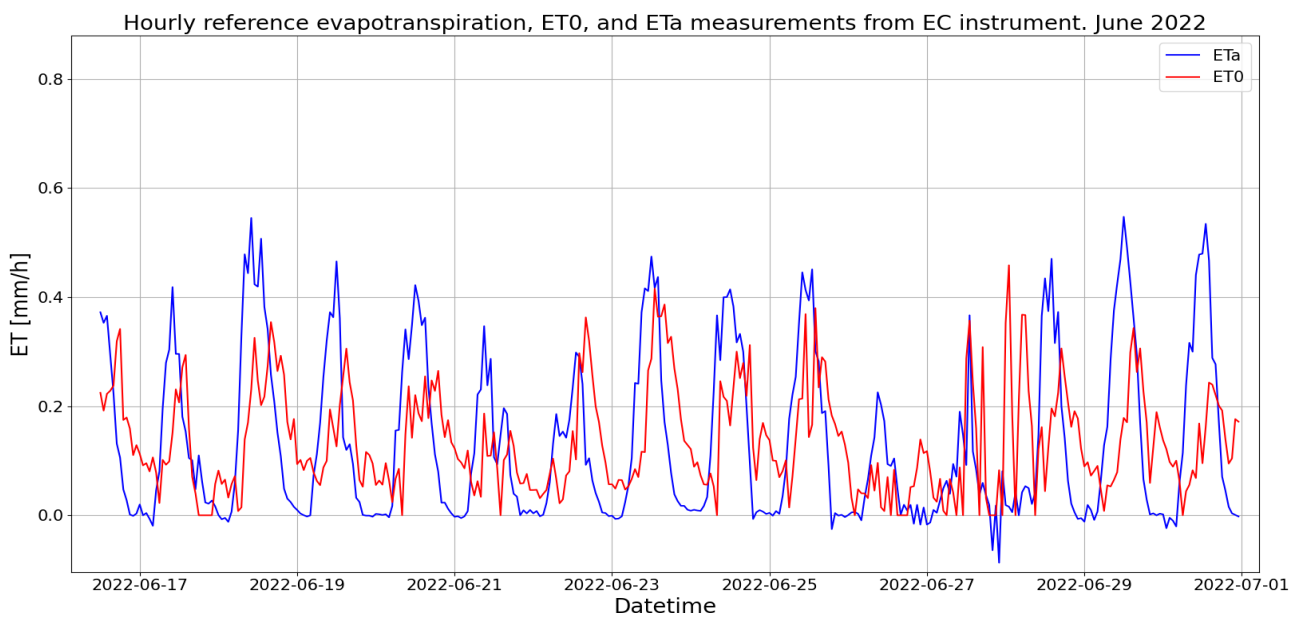


Figure 150: *Hourly measured evapotranspiration (blue) and estimated reference evapotranspiration (red) in June 2022.*

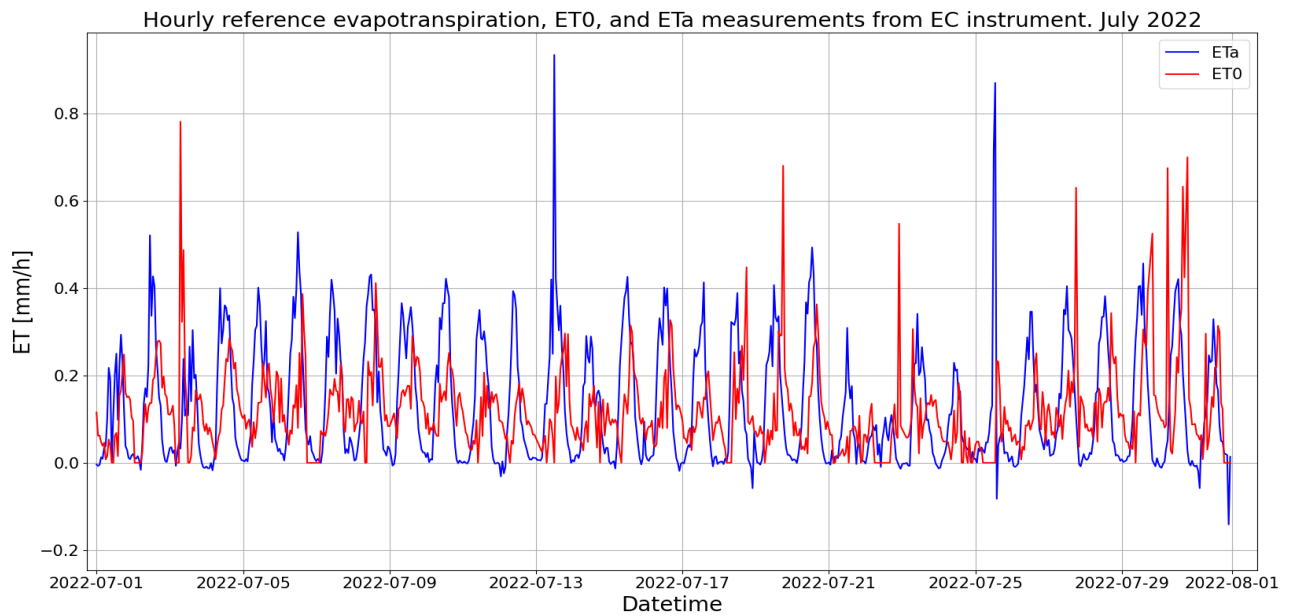


Figure 151: Hourly measured evapotranspiration (blue) and estimated reference evapotranspiration (red) in July 2022.

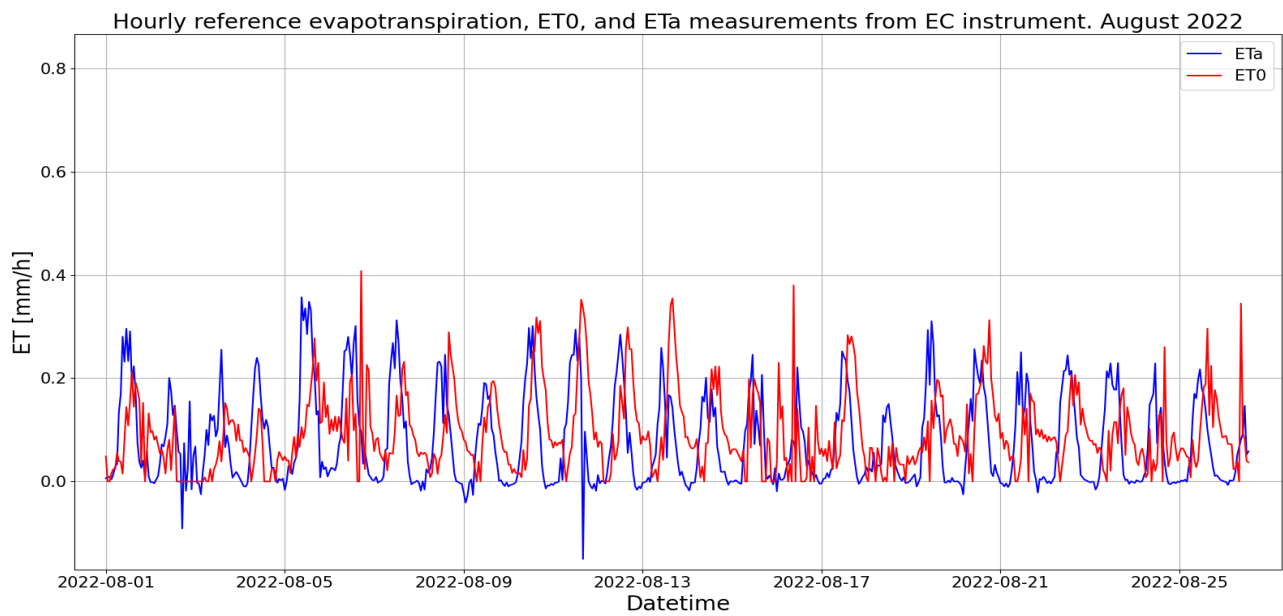


Figure 152: Hourly measured evapotranspiration (blue) and estimated reference evapotranspiration (red) in August 2022.

Actual evapotranspiration hourly, $k_c=0.9$

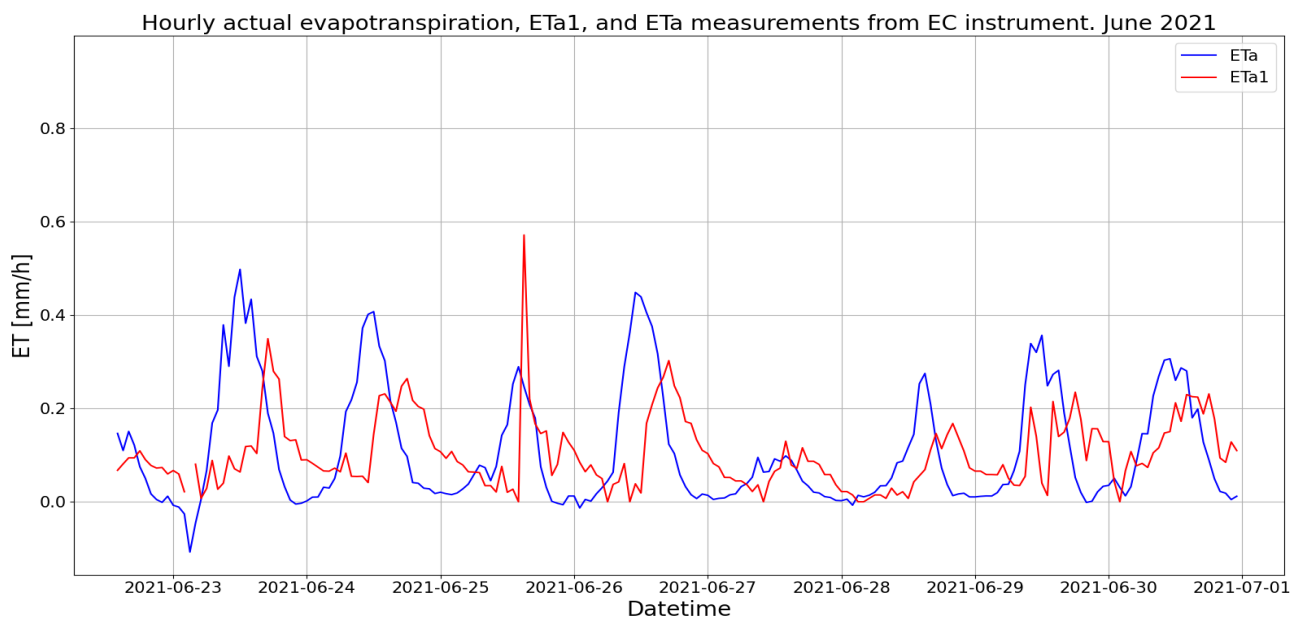


Figure 153: Hourly measured evapotranspiration (blue) and estimated evapotranspiration (red) using crop coefficient of 0.9 in June 2021.

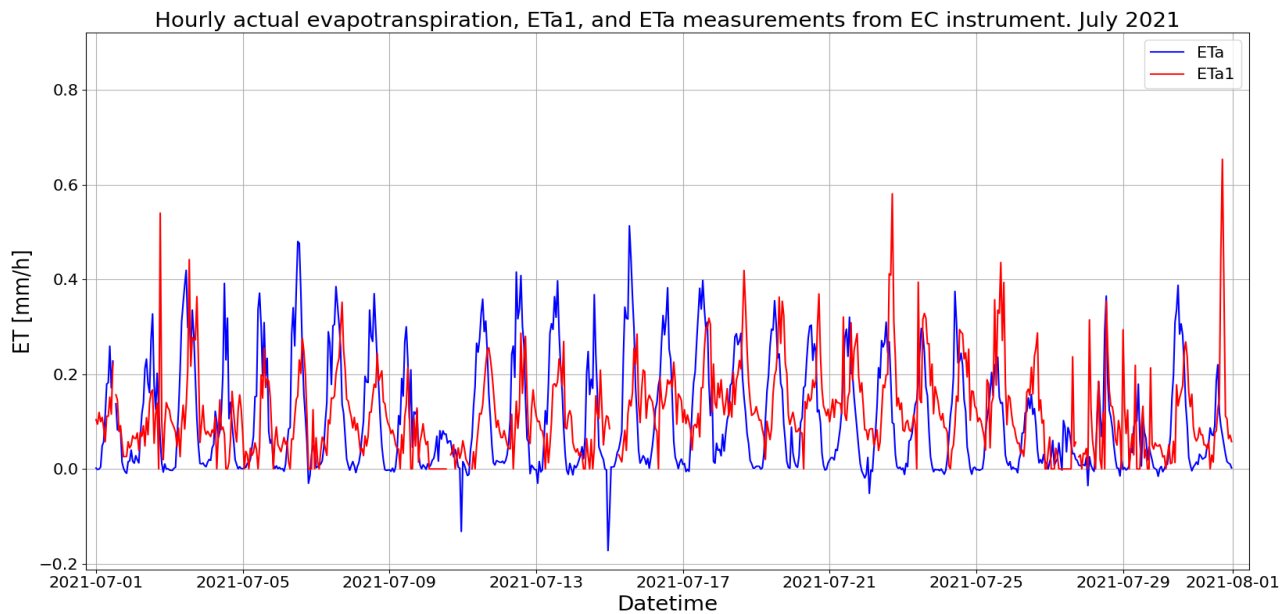


Figure 154: Hourly measured evapotranspiration (blue) and estimated evapotranspiration (red) using crop coefficient of 0.9 in July 2021.

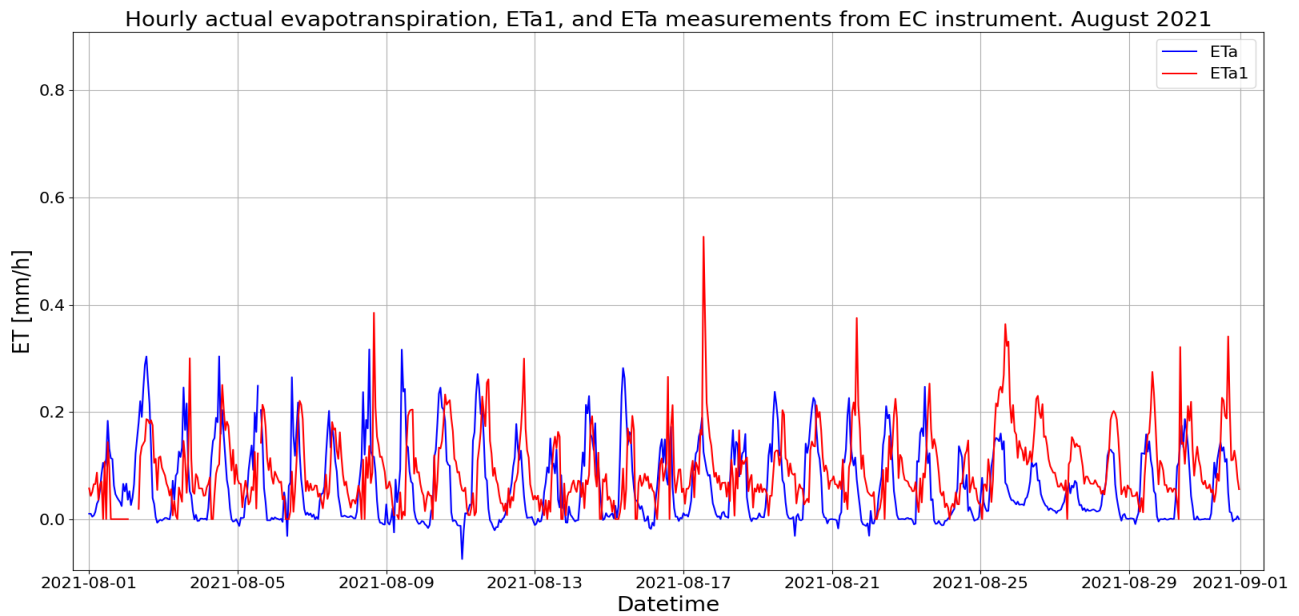


Figure 155: *Hourly measured evapotranspiration (blue) and estimated evapotranspiration (red) using crop coefficient of 0.9 in August 2021.*

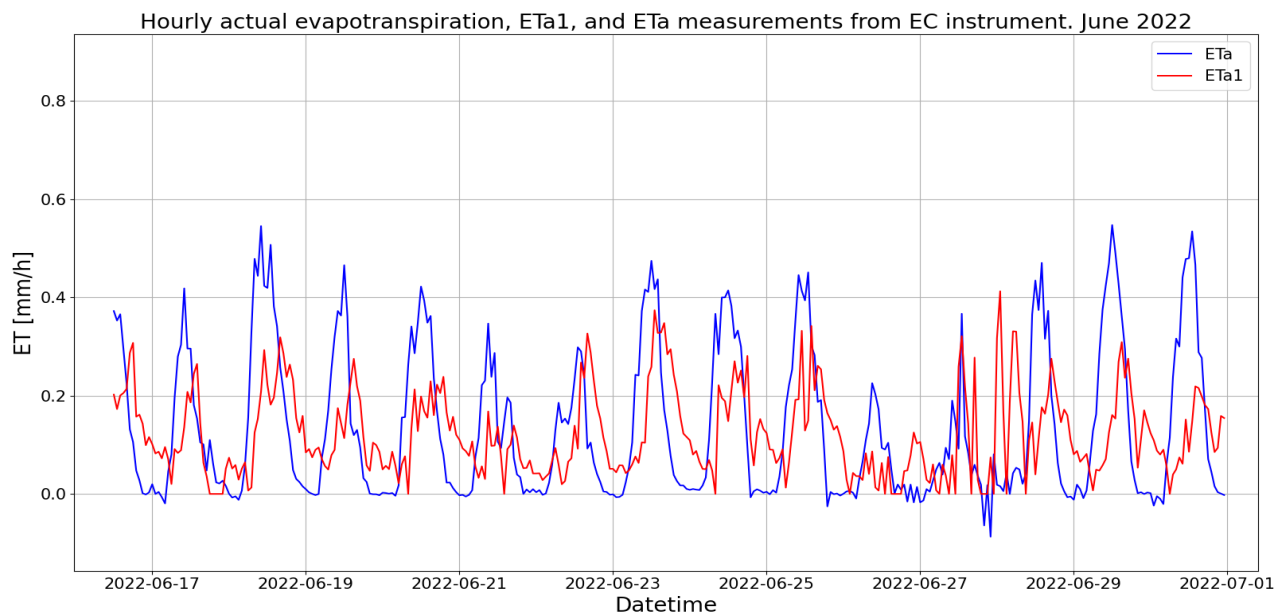


Figure 156: *Hourly measured evapotranspiration (blue) and estimated evapotranspiration (red) using crop coefficient of 0.9 in June 2022.*

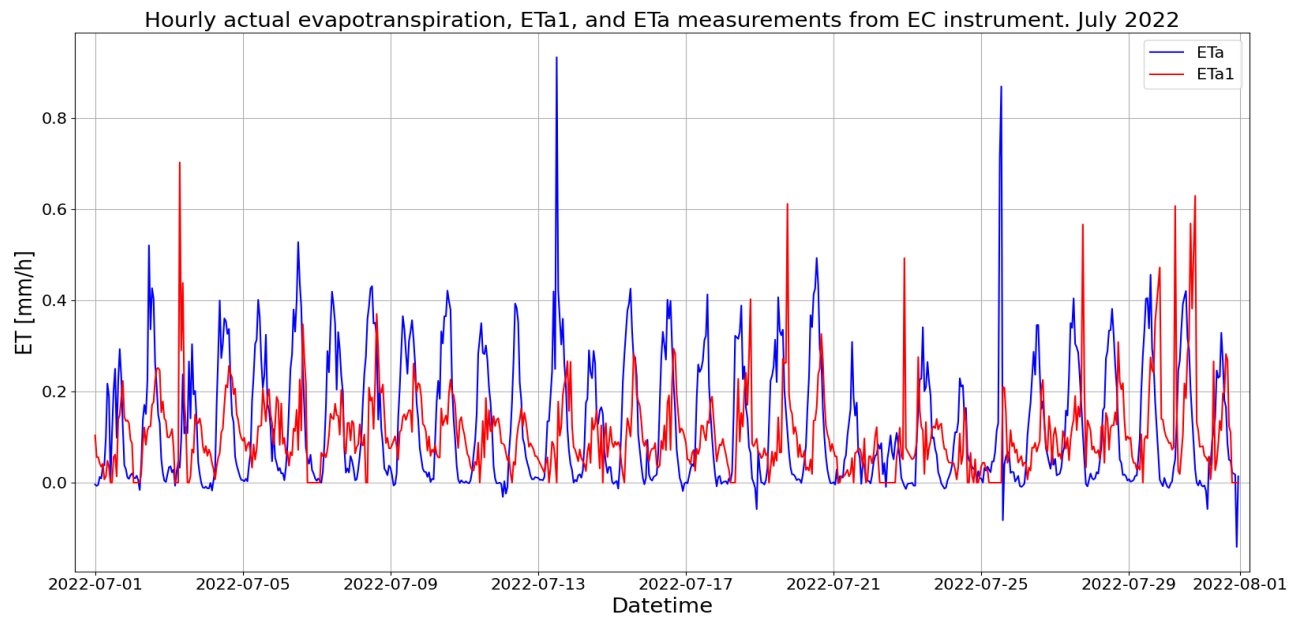


Figure 157: *Hourly measured evapotranspiration (blue) and estimated evapotranspiration (red) using crop coefficient of 0.9 in July 2022.*

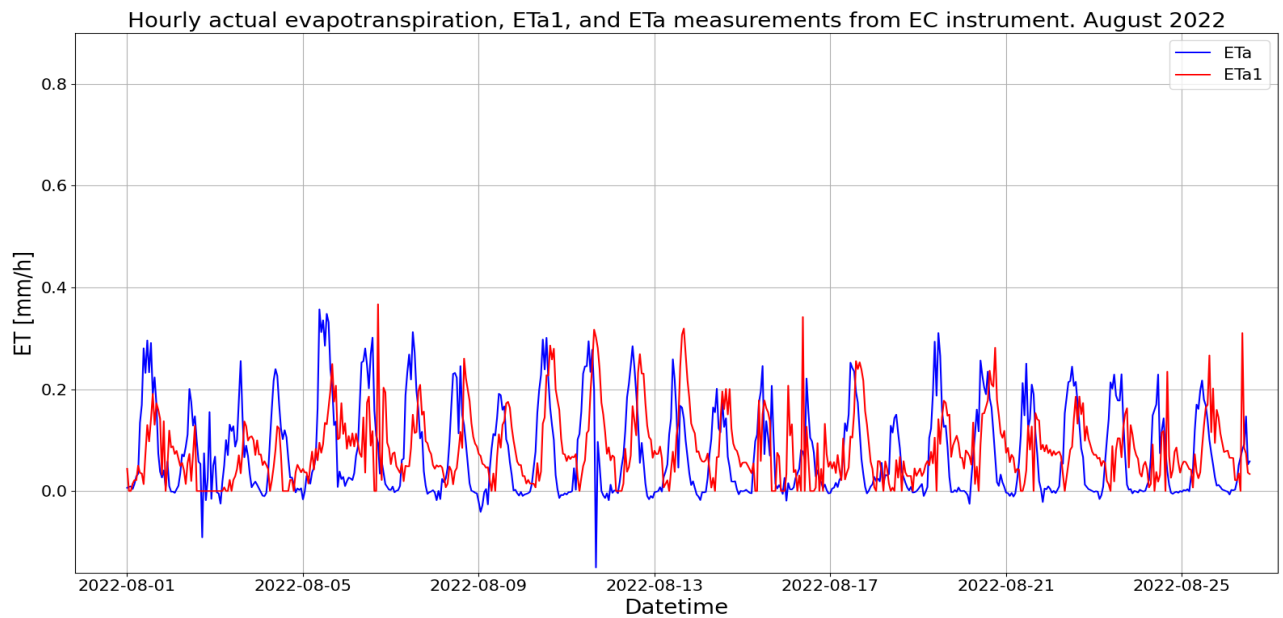


Figure 158: *Hourly measured evapotranspiration (blue) and estimated evapotranspiration (red) using crop coefficient of 0.9 in August 2022.*

Actual evapotranspiration hourly, $k_c=0.588$

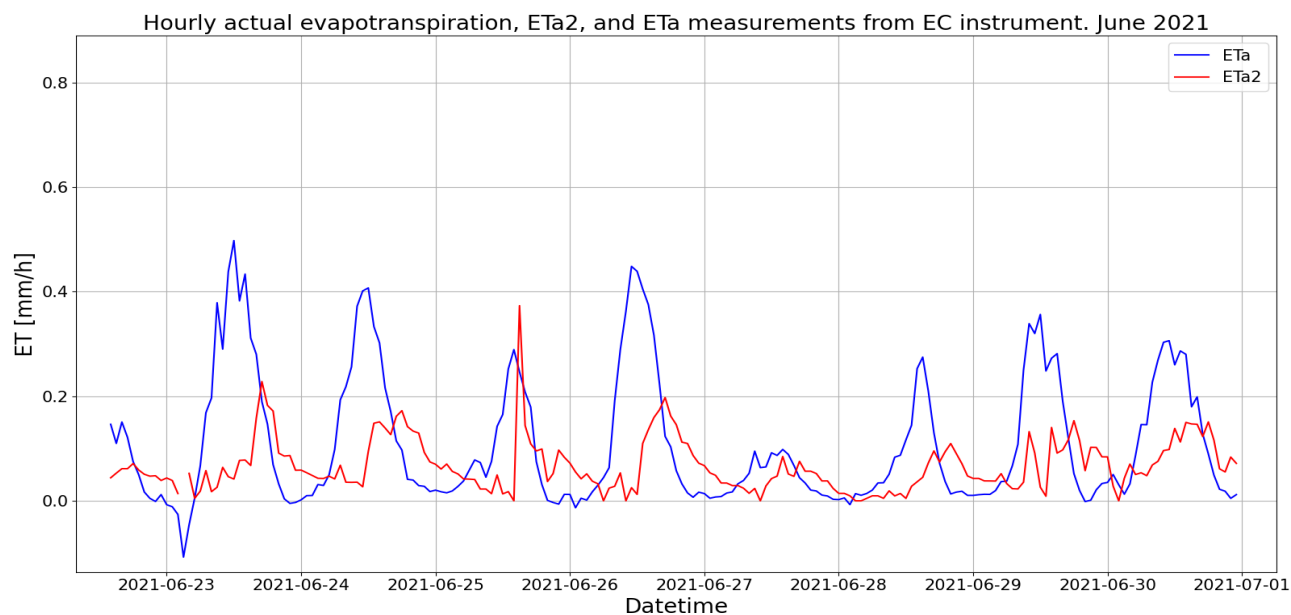


Figure 159: Hourly measured evapotranspiration (blue) and estimated evapotranspiration (red) using crop coefficient of 0.588 in June 2021.

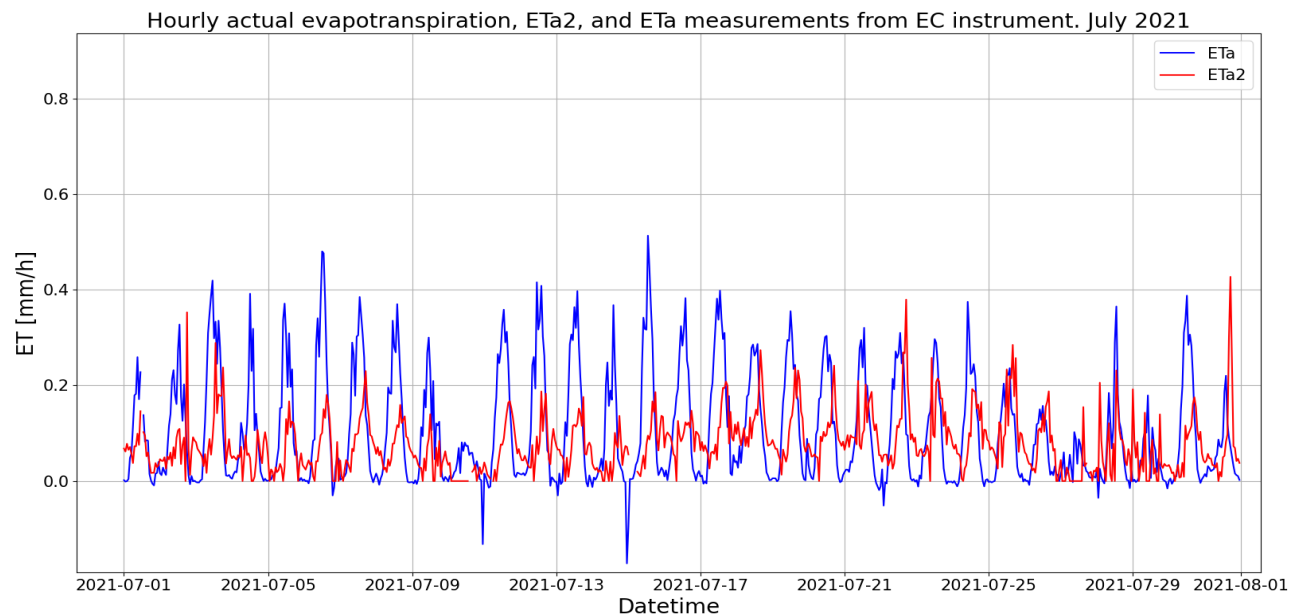


Figure 160: Hourly measured evapotranspiration (blue) and estimated evapotranspiration (red) using crop coefficient of 0.588 in July 2021.

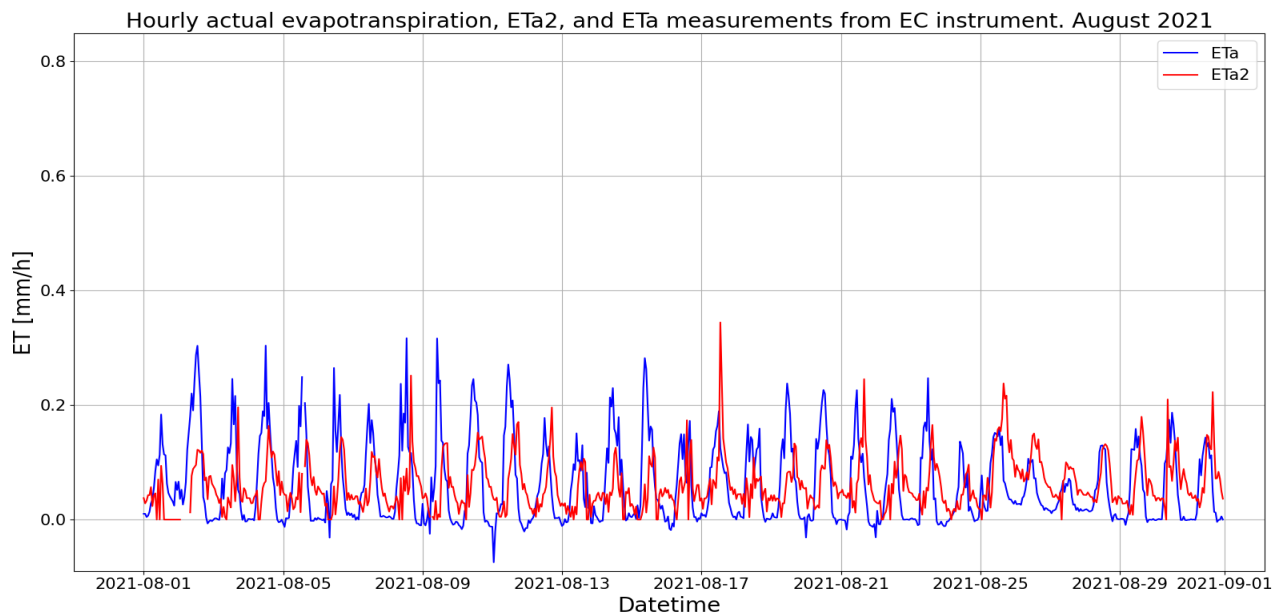


Figure 161: *Hourly measured evapotranspiration (blue) and estimated evapotranspiration (red) using crop coefficient of 0.588 in August 2021.*

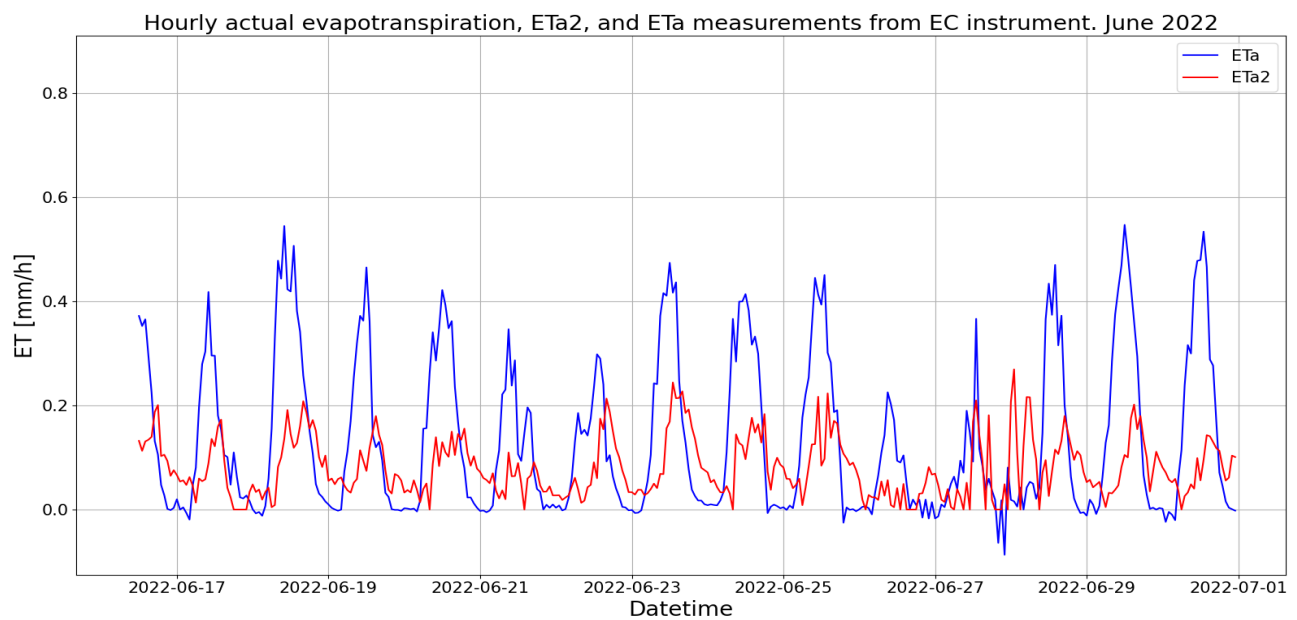


Figure 162: *Hourly measured evapotranspiration (blue) and estimated evapotranspiration (red) using crop coefficient of 0.588 in June 2022.*

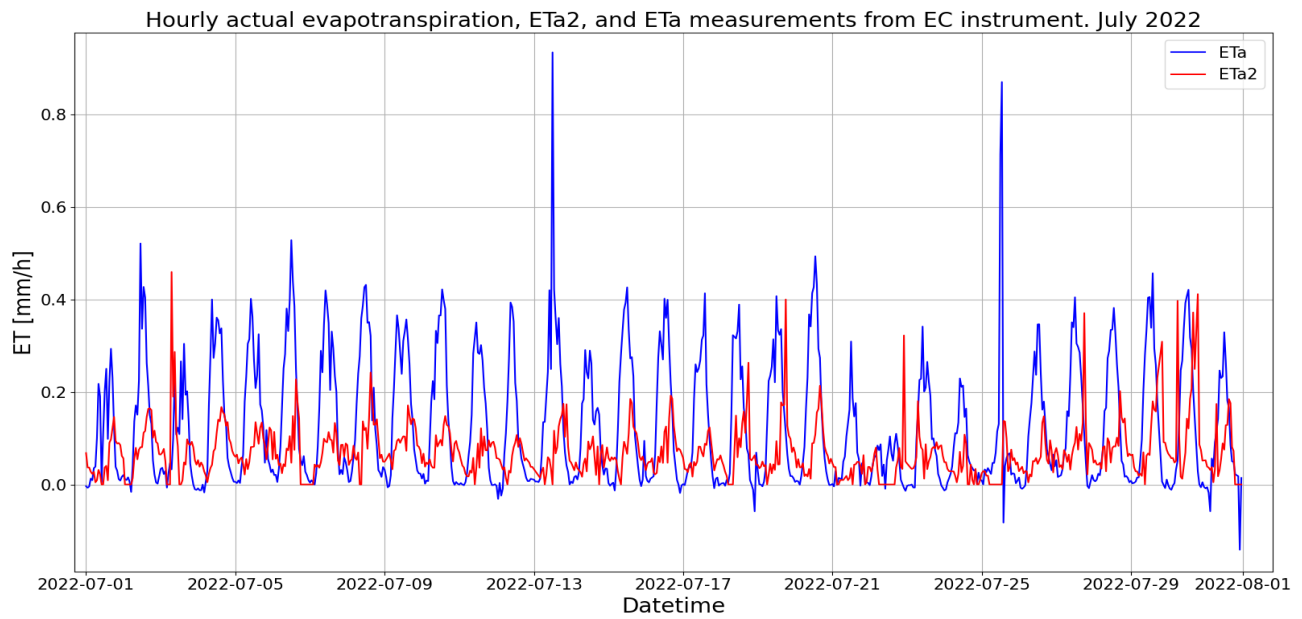


Figure 163: *Hourly measured evapotranspiration (blue) and estimated evapotranspiration (red) using crop coefficient of 0.588 in July 2022.*

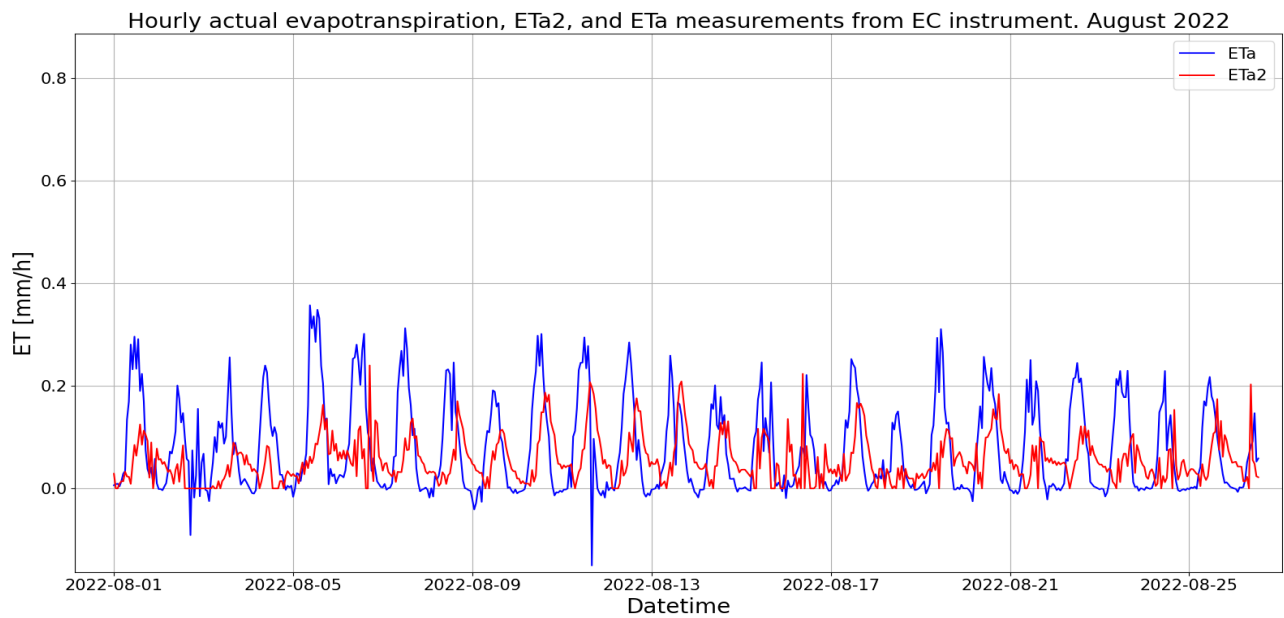


Figure 164: *Hourly measured evapotranspiration (blue) and estimated evapotranspiration (red) using crop coefficient of 0.588 in August 2022.*



Norges miljø- og biovitenskapelige universitet
Noregs miljø- og biovitenskapelige universitet
Norwegian University of Life Sciences

Postboks 5003
NO-1432 Ås
Norway